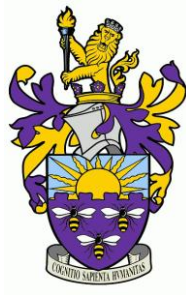# Efficient Methodologies for Single-Image Blind Deconvolution and Deblurring

Aftab Khan

School of Electrical and Electronic Engineering

The University of Manchester

A thesis submitted for the degree of

Doctor of Philosophy

May 2014

Abstract

The Blind Image Deconvolution/Deblurring (BID) problem was realised in the early 1960s but it still remains a challenging task for the image processing research community to find an efficient, reliable and most importantly a diversely applicable deblurring scheme. The main challenge arises from little or no prior information about the image or the blurring process as well as the lack of optimal restoration filters to reduce or completely eliminate the blurring effect. Moreover, restoration can be marred by the two common side effects of deblurring; namely the noise amplification and ringing artefacts that arise in the deblurred image due to an unrealizable or imperfect restoration filter. Also, developing a scheme that can process different types of blur, especially for real images, is yet to be realized to a satisfactory level.

This research is focused on the development of blind restoration schemes for real life blurred images. The primary objective is to design a BID scheme that is robust in term of Point Spread Function (PSF) estimation, efficient in terms of restoration speed, and effective in terms of restoration quality. A desired scheme will require a deblurring measure to act as a feedback of quality regarding the deblurred image and lead the estimation of the blurring PSF. The blurred image and the estimated PSF can then be passed on to any classical restoration filter for deblurring.

The deblurring measures presented in this research include blind non-Gaussianity measures as well as blind Image Quality Measures (IQMs). These measures are blind in the sense that they are able to gauge the quality of an image directly from it

without the need to reference a high quality image. The non-Gaussianity measures include spatial and spectral kurtosis measures; while the image quality analysers include the Blind/Reference-less Image Spatial QUality Evaluator (BRISQUE), Natural Image Quality Evaluator (NIQE) index and Reblurring based Peak Signal to Noise Ratio (RPSNR) measure. BRISQUE, NIQE and spectral kurtosis, are introduced for the first time as deblurring measures for BID. RPSNR is a novel full reference yet blind IQM designed and used in this research work. Experiments were conducted on different image datasets and real life blurred images. Optimization of the BID schemes has been achieved using a gradient descent based scheme and a Genetic Algorithm (GA). Quantitative results based on full-reference and non-reference IQMs, present BRISQUE as a robust and computationally efficient blind feedback quality measure.

Also, parametric and arbitrarily shaped (non-parametric or generic) PSFs were treated for the blind deconvolution of images. The parametric forms of PSF include uniform Gaussian, motion and out-of-focus blur. The arbitrarily shaped PSFs comprise blurs that have a much more complex blur shape which cannot be easily modelled in the parametric form. A novel scheme for arbitrarily shaped PSF estimation and blind deblurring has been designed, implemented and tested on artificial and real life blurred images. The scheme provides a unified base for the estimation of both parametric and arbitrarily shaped PSFs with the BRISQUE quality measure in conjunction with a GA.

Full-reference and non-reference IQMs have been utilised to gauge the quality of deblurred images for the BID schemes. In the real BID case, only non-reference IQMs can be employed due to the unavailability of the reference high quality image. Quantitative results of these images depict the restoration ability of the BID scheme. The significance of the research work lies in the BID scheme's ability to handle parametric and arbitrarily shaped PSFs using a single algorithm, for single-shot blurred images, with enhanced optimization through the gradient descent scheme and GA in conjunction with multiple feedback IQMs.

Dedicated to my loving parents for their endless love and care

and for

their selfless guidance, encouragement and support

Declaration

No portion of the work referred to in this thesis has been submitted in support of an application for another degree or qualification of this or any other university or other institution of learning.

Copyright Statement

[i]   The author of this thesis (including any appendices and/or schedules to this thesis) owns any copyright in it (the "Copyright") and he has given The University of Manchester the right to use such Copyright for any administrative, promotional, educational and/or teaching purposes.

[ii]   Copies of this thesis, either in full or in extracts, may be made only in accordance with the regulations of the John Rylands University Library of Manchester. Details of these regulations may be obtained from the Librarian. This page must form part of any such copies made.

[iii]   The ownership of any patents, designs, trademarks and any and all other intellectual property rights except for the Copyright (the "Intellectual Property Rights") and any reproductions of copyright works, for example graphs and tables ("Reproductions"), which may be described in this thesis, may not be owned by the author and may be owned by third parties. Such Intellectual Property Rights and Reproductions cannot and must not be made available for use without the prior written permission of the owner(s) of the relevant Intellectual Property Rights and/or Reproductions.

[iv]   Further information on the conditions under which disclosure, publication and exploitation of this thesis, the Copyright and any Intellectual Property Rights and/or Reproductions described in it may take place is available from the Head of School of Electrical and Electronic Engineering.

Acknowledgements

First and foremost, praises and thanks are to Allah Almighty, Who blessed me with a lot of great people and things. I owe everything to Him and for who I am today. I am especially thankful to Him for blessing me with the gift of knowledge, loving family and a beautiful life.

I am greatly thankful and can never forget the close support and guidance of my supervisor, Dr Hujun Yin, who guided me with devotion and dedication and continues to do so till today.

About three years ago when I first came to UK, I was welcomed by my elder brother Dr. Ashfaq Khan with great love. His love, encouragement, support and guidance helped me greatly through my studies and never made me feel away from home. Had he not been here, it would have been really difficult living in a new country and studying so well and it was through him that I found and met some really great friends. Thank you for everything my beloved brother.

After he completed his PhD studies and left back to Pakistan, I was joined by my eldest brother, Dr. Mushtaq Khan along with his family. Their love, support and care is a blessing that I greatly appreciate. I can never forget the fun time I had with them especially with my nephew, Bilal Khan.

I started as a nervous and naive researcher but I had the will and determination that I inherited from my loving parents. I would always, for my education and for my whole life, be thankful to them. It is through their guidance and prayers that I have reached to this level in my life. I missed them, their love and care greatly during my studies abroad. I am especially thankful to my father Dr. Nawar Khan for his supervision, advice and support throughout my educational career.

I am grateful to my grandparents, my uncles and aunts, my brothers and sister, my cousins, my fiancé and her family, and my friends here and thousands of miles away in Pakistan for their love, support, encouragement and prayers which made my resolve and determination stronger. I am especially thankful to my friends Moustafa

Contents

1 Introduction

3   The Spectral Kurtosis Based Non-Gaussianity Measure for Blind Image Deblurring

List of Figures

xviii

List of Tables

List of Research Publications

- Khan, A. and Yin, H., *Spectral Non-Gaussianity for Blind Image Deblurring*, in Proceedings of the **12th International Conference on Intelligent Data Engineering and Automated Learning (IDEAL)**. 2011, Norwich, UK. Springer-Verlag Berlin: Berlin. p. 144-151.

- Khan, A. and Yin, H., *Quality Measures for Blind Image Deblurring*, in **IEEE International Conference on Imaging Systems and Techniques (IST)**, 2012, Manchester, UK. p. 456-459

- Khan, A. and Yin, H., *Efficient Blind Image Deconvolution Using Spectral Non-Gaussianity*, **Integrated Computer Aided Engineering (ICAE)**, 2012. 19(4): p. 331-340.

- Khan, A. and Yin, H., *Efficient Blind Image Deblurring with Gradient Descent Based Kurtosis Maximization*, **IEEE Transactions on Image Processing (TIP)**, (under review), 2013.

List of Terms

This section lists terms specific to the thesis or used with a specific meaning. Compound terms based on these are not included here, but are explained in full where they first occur.

Scheme: It refers to a method or algorithm designed to perform a specific task and is usually in the form of a computer code.

Signal: A signal usually refers to a 1-D array of elements that represents a continuous signal in its discrete form.

Image: An image is a 2-D signal. The terms signal and image are used interchangeably in this thesis.

Noise: The term noise refers to the inherent degradation in image resulting from the recording medium's imprecision or corruption by the electronic circuitry present. The level of inherent noise cannot be gauged due to absence of a noise free source signal.

Noiseless: A noiseless image means no noise has been added to the source image apart from any inherent noise already present in the image.

Blur: A degradation of the image data due to its convolution with the impulse response of the capturing or recording medium. A blur maybe space invariant or space variant in the image.

Space Variant Blur: An image blur that is dependent on the spatial location of the image data and varies throughout the image.

Space-Invariant Blur: An image blur that is independent of the spatial location of the image data and is uniform throughout the image.

Parametric/Non-Parametric Blur: A blur that can be defined in a set of its

parameter(s) is regarded as parametric blur. A non-parametric blur, also termed as arbitrarily shaped blur, refers to blur that has a complex shape and cannot be modelled in parametric form.

Robustness: It is defined as the ability of a scheme in producing results as expected and over a wide range of source data.

Efficiency: Efficiency of a scheme is computed as the time it takes on average to produce a result from the moment the scheme starts performing its task. This is also referred to as computational efficiency which is calculated in seconds for an algorithm.

Quality: Quality of the image refers to the quantitative measurement of the image's appearance using a quality measure. The different factors that usually contribute to the image's appearance include its contrast, sharpness, brightness etc.

Abbreviations

BID	Blind Image Deconvolution/Deblurring
BRISQUE	Blind/Reference-less Image Spatial QUality Evaluator
BSS	Blind Source Separation
CLT	Central Limit Theorem
COC	Circle Of Confusion
DCA	Dependent Component Analysis
Eqn.	Equation
FDK	Frequency Domain Kurtosis
FFT	Fast Fourier Transform
Fig.	Figure
GA	Genetic Algorithm
GUI	Graphical User Interface
HVS	Human Visual System
IBD	Iterative Blind Deconvolution
ICA	Independent Component Analysis
iFFT	inverse Fast Fourier Transform
IQM	Image Quality Measure
MED	Minimum Entropy Deconvolution
MSE	Mean Square Error
MSSIM	Mean Structural SIMilarity index
NIQE	Natural Image Quality Evaluator

OTF	Optical Transfer Function
PCA	Principal Component Analysis
PSF	Point Spread Function
PSNR	Peak Signal to Noise Ratio
RPSNR	Reblurring based Peak Signal to Noise Ratio
SNR	Signal to Noise Ratio
SSIM	Structural SIMilarity Index
TV	Total Variation
UQI	Universal Quality Index

Nomenclature

φ	Angle of motion in degrees
g	Blurred image
C	Constant
$c(,)$	Contrast function
α	Convergence step size
$*$	Convolution operator
B	Entropy norm
J_1	First order Bessel function
G	Frequency domain blurred image
Y	Frequency domain deblurred image
H	Frequency domain point spread function
F	Frequency domain pristine image
∇	Gradient operator
r	Iteration/order number
L	Length of motion blur in pixels
$l(,)$	Luminance function
$S(,)$	MSSIM index function
δ	Noise to Signal Ratio
N	Number of image columns
M	Number of image rows
$\dfrac{\partial}{\partial()}$	Partial derivative function
h	Point spread function

f	Pristine image
f'	Pristine image estimate
p, P	Probability distribution
λ	PSF parameter
$\mu(p)$	p^{th} order central moment of data
R	Radius of out-of-focus blur
m, n	Spatial image coordinates
k	Spatial kurtosis function
v	Spatial noise
i, j	Spectral image coordinates
K	Spectral kurtosis function
V	Spectral noise
L	Spectral regularisation parameter
σ	Standard deviation
$s(,)$	Structural similarity function
$Q(,)$	UQI function
σ^2	Variance

Chapter 1

Introduction

1.1. Background

With the technological advances that have taken place over the past few decades, most of blurred image data is sourced from handheld and mobile phone cameras, satellites, CCTVs and other imaging sources. Images often suffer from degradation due to imperfection in the capturing and imaging process, with a recorded image inevitably emerging as a degraded version of the original image. These degradations are caused from various sources like lens defocus, optical imperfections in the case of a digital camera or atmospheric blurring in the case of satellite/aerial photography, etc. The use of handheld cameras, especially by amateur photographers, has resulted in blurred images caused mostly from camera shake or failure to focus the camera properly. Some examples of such blurred images are shown in Fig. 1.1. These images are deblurred in the later part of the thesis.

In addition to these blurring effects, noise may corrupt any recorded image. Noise can be introduced into the system by the creating medium or by the recording medium or simply because of measurement imprecision. Noise may appear due to the inability of the restoration filter to estimate the image data perfectly and is regarded as deblurring noise. Apart from noise, ringing may occur in the restored image due to the imperfect estimation of blur. Ringing occurs for a restoration filter

if it assumes the image's frequency sample is periodic which leads to high frequency drop-off at the image boundaries. Undoing these imperfections, in some cases, is crucial for many image processing and multidimensional signal processing tasks.

(a) (b)

(c)

(d)

(e)
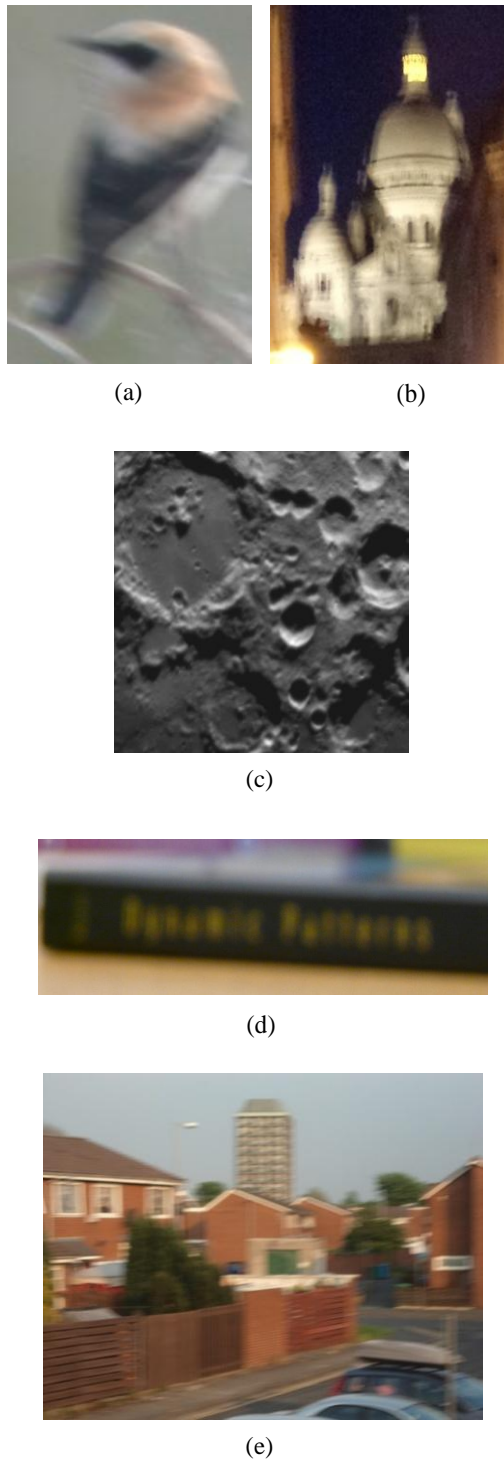
Fig. 1.1 Examples of real life blurred images.

Nowadays, cameras come fitted with image stabilization and auto-focusing techniques to handle the imperfections of camera handshake and improper focusing, respectively. They also include much faster shutters, more sensitive imaging sensors

and anti-camera shake mechanisms. Optical image stabilization systems usually contain either a moving image sensor or an optical element to reduce camera motion. Auto-focusing involves the estimation of correct focus by single or multiple sensors using light metering techniques, which in turn controls an electromechanical system that adjusts the focus of the optical system. These systems are technologically demanding as their goal is to remove blur without increasing noise level. This usually results in a higher cost, more weight and high energy consumption [1]. Even with these solutions provided by the digital camera industry, camera handshake blur can only be handled in a limited manner [2].

Other hardware solutions have been formulated to tackle the blurring problem by capturing much better images in the first place [3, 4]. Some of these mechanisms involve coded aperture [4-6], coded exposure [3, 7] and multiple camera based Point Spread Function (PSF) estimation [8, 9]. Numerous image processing algorithms provide effective solutions to post-process the blurred images, estimate the degradations and deblur the images to an acceptable level. The field of digital image processing which studies and handles the restoration process is called digital image restoration.

The field of image restoration can be dated back to the early 1960s problem of non-linear filtering of convolved signals. It refers to the estimation of the original image from a noisy, convolved version by using some prior information about the degradation phenomenon. The main goal of the restoration is to estimate the degradation and apply an inverse process in order to recover the original signal(s). Image restoration is an ill-posed inverse problem because in many cases prior information is either unavailable or very limited. Major work in the field is related to the restoration of astronomical images and still interests many researchers. Nonetheless it has now found applications in computer vision [10], remote sensing [11], medical imaging [12], etc, and particularly increased interests in law enforcement agencies. Image restoration solutions provided by Blind Image Deconvolution (BID) can be used for restoration of biomedical images [12-14], aerial and satellite photography [15, 16], handheld camera pictures and videos [17-20], audio and seismic signals [21, 22], remote sensing data [23], industrial tomography images [24], astronomical photos [25, 26] and other sources of signals and images as well.

A variety of Blind Image Deconvolution/Deblurring (BID) schemes and restoration filters have been proposed over the years that try to estimate the pristine image. This

collection of methods ranges from the time domain to the frequency domain, simultaneous or separate PSF estimation technique, parametric to non-parametric, etc. Examples include the Richardson-Lucy method [27], Total Variation [28], Maximum Likelihood (ML) method [29, 30], Minimum Entropy Deconvolution (MED) [31], Non-negativity And Support- constraint Recursive Inverse Filter (NAS-RIF) [32], simulated annealing [33], and multi-channel blind deconvolution [33].

Blind Signal Separation (BSS) is another area where the aim to recover original signals from a set of mixtures without any prior knowledge of the original signals themselves [34, 35]. Assuming statistical independence of the source signals, it implies that according to the Central Limit Theorem (CLT) the output signals of a linear system are closer to a Gaussian distribution. So a general scheme exists to find independent signals that are maximally non-Gaussian. This also forms the basis of Independent Component Analysis (ICA) [36], an active research topic [37].

These methods provide solutions to some extent to the BID problem but lacking in terms of robustness, computational efficiency and restoration quality. Mainly, the robustness of these schemes remains or becomes questionable when real-life blurred images are to be restored. This is because unlike artificial deblurring, real deblurring suffers heavily from deblurring noise and ringing effects. These effects hinder the restoration process by interfering with and changing the statistical properties of the image data leading to inefficient PSF estimation. Noise in the images can be caused by the recording device's sensitivity to different environmental factors like poor lighting condition. The other form of visual artefacts includes ringing that appears near strong edges in the image. Ringing was commonly believed to be Gibbs phenomenon occurring from the inability of finite Fourier basis in modelling step signals occurring in the images [38]. However, it has been demonstrated that ringing mainly occurs due to errors in the estimated PSF [39].

The blurred images may have been degraded by arbitrarily shaped PSFs that are complex and cannot be easily modelled by the usual parametric blur models [17, 18, 40-45]. Nowadays, most of the BID schemes focus mainly on deblurring images corrupted by arbitrarily shaped motion blur PSFs. Not only because it commonly occurs in real life image acquisition but also because it is more challenging. This type of blur ensues mainly from camera shakes or movement of objects or background in the focal range. The PSFs of such blurs are usually arbitrarily shaped and sometimes even space-invariant. Restoring such images requires more effort, with complex procedures being applied to approximate the blur kernel as well as to

4

restore the image to its pristine form while deterring occurrence of deblurring noise and ringing artefacts. This research addresses the problem of blind image restoration, and has developed image processing approaches to tackle the ill-posed deblurring problem.

1.2. Research Scope

The research deals with the blind deblurring of noiseless images corrupted by space invariant blurs. The space invariant blur includes both parametric and non-parametric (arbitrarily shaped) Point Spread Functions (PSFs). Images include both artificially blurred and real life blurred images from handheld camera.

The research does not deal with denoising (noise removal) from an image may it be either inherent, artificially added noise or deblurring noise. Ringing reduction is also out of scope in this research work.

1.3. Aims

To design and investigate efficient Blind Image Deblurring (BID) schemes for deblurring of real life blurred images with focus on: robustness in estimation of parametric and arbitrarily shaped Point Spread Function (PSF), computational efficiency and deblurring quality.

1.4. Objectives

The main objectives of this research were as follows:

- To review the existing BID schemes presented in the relevant literature and develop an understanding of existing spatial non-Gaussianity based BID schemes.
- To design and demonstrate the working of a robust quality measure for BID.
- To develop and test a BID scheme for the deblurring of space invariant parametric and non-parametric PSF blurred images.
- To test the proposed BID scheme(s) to restore naturally blurred images.
- To analyse the computational efficiency and deblurring quality of the BID scheme.
- To produce a user friendly Graphical User Interface (GUI) for the BID scheme(s).

1.5. Research Methodology

The research work started with an analysis of existing BID schemes covered in the literature study. New ideas to efficiently tackle the restoration problem were then proposed, designed, implemented and evaluated. Testing on both real and artificially blurred images was performed to evaluate the robustness and efficiency of the proposed scheme. MATLAB based computer simulations were carried out. Comparisons against some benchmark restoration schemes were performed to estimate the efficiency of the proposed BID schemes. Upon successful validation and verification of the results, some research work was published in peer reviewed international journals and disseminated at international conferences. A GUI toolbox was developed to allow for easily usable and fast deblurring of corrupted images.

1.6. Significance of Research Work

The research work is focused towards providing image restoration solutions. The developed BID scheme provides the ability to handle both parametric and arbitrarily shaped PSFs using a single algorithm. The new BID scheme does not require any prior knowledge about the image or the blurring process. It is completely blind and operates on only a single-shot of the blurred image for its recovery. Optimization in terms of computational efficiency for the BID scheme has been achieved using Genetic Algorithm (GA) and gradient decent scheme. Different Image Quality Measures (IQMs) and restoration filters are investigated to enhance the deblurring quality.

1.7. Thesis Structure

Chapter 2 introduces the blind deconvolution problem and discusses the commonly occurring blurring PSF types. Functionalities of some restoration filters and image quality measures used for restoration are also detailed. Chapter 2 also provides a review of some of the existing schemes and methods in the literature and provides information about the methodology of some of the schemes considered in this research. The literature study was subsequently used to identify gaps and limitations in the existing BID methodologies. The information gained was used to form a base for new ideas to tackle the restoration problem. The spatial non-Gaussianity based BID scheme was researched in depth as a motivation for seeking more robust and efficient deblurring measures.

Chapter 3 explains a new spectral non-Gaussianity based measure for BID and presents experimental results for both artificial and real blurred images. The measure was proposed as an efficient and robust alternative to the previously used spatial non-Gaussianity measures. Spectral kurtosis based BID schemes using gradient descent and GA based optimizations are provided. However, the new measure's sensitivity to deblurring noise and ringing artefacts led us to look for measures that can tackle these problems.

Chapter 4 introduces the use of non-reference or blind IQMs as possible substitutes to the higher order cumulant based non-Gaussianity measures. A novel full-reference but blind spatial domain IQM and a BID scheme based on the IQM were also proposed. BID schemes for these different IQMs were designed and evaluated using both real and artificially blurred images. The Blind/Reference-less Image Spatial Quality Evaluator (BRISQUE) depicts efficient performance among all other measures. The restoration of blurred images by parametric PSFs has been tackled to a degree where the PSF parameter values are reasonably well approximated and the deblurred images are of high quality as compared with other benchmark scheme.

Chapter 5 introduces a novel blind deblurring scheme visualized for deblurring images corrupted by non-parametric (arbitrarily) shaped PSF. The scheme using the existing deblurring measures is able to estimate arbitrarily shaped blurring PSFs. BRISQUE IQM was used to evaluate the performance of the BID scheme with experimental results on both synthetic and real life blurred images; presented and compared against other benchmark BID schemes.

Chapter 6 presents a GUI Toolbox developed to readily deploy and apply the proposed BID schemes. It encompasses all the feedback IQMs used in conjunction with the GA based optimization scheme. Its features are discussed in detail and the chapter presents a practical lab session worksheet format to guide the user.

Chapter 7 discusses and analyses all the IQMs and the proposed BID scheme based on them. It also discusses their advantages and limitations.

Chapter 8 summarizes and concludes the research and gives direction for further research. It also discusses the major contributions of this research study towards the field of BID.

Appendices provide comprehensive results of different schemes for the images used in experimentation of the deblurring measures over a wide range of blurring PSF parameter values and a large set of images. It also includes additional information on the MATLAB's optimization technique used.

Chapter 2

Image Deblurring: Concepts and Techniques

2.1. Introduction

The field of BID spans over a period of four decades and has applications in diverse fields. A wide range of mathematical and image processing techniques have been used to tackle the challenges involved. In this chapter a review of some basic concepts in the field of BID is presented. The degradation model, different blur types and a number of restoration filters are discussed. Past literature encompassing BID techniques is reviewed in depth. This chapter also provides a review of some of the existing techniques in literature, providing relevance or a comparison to the approach described in this research work.

2.2. Problem Formulation

Image restoration algorithms are usually based on some form of degradation model that establishes the relationship between an original and the blurred images of an imaging system. The blurred image is assumed to be the result of the convolution between the original image and the transfer function (degradation function) of the imaging system. The key to restoration is to estimate the degradation function. Any

imperfection of the imaging system or environment can induce degradation to the captured image.

If the image formation process can be modelled as a linear system, a recorded image can be represented as the output of the convolution of the spatial impulse response or Point Spread Function (PSF) of the linear blurring system with the original image (scene). Let m and n be the spatial image coordinates and f present the original image without any form of degradation, h be the PSF and the output of the system be given by g. Mathematically, for a stationary impulse response of the system across the image (i.e. a spatially invariant stationary PSF), the discrete form of the convolution according to [46, 47] is given by,

$$g = h * f + v \tag{2.1}$$

where * represents the 2-D convolution operator and v represents additive noise. Fig. 2.1 shows the blurring model of a camera. The frequency domain model obtained using the Fourier Transform is,

$$G = HF + V \tag{2.2}$$

$h = $ impulse response of the system

$f = $ observed scene (image)

$g = $ captured scene (image)
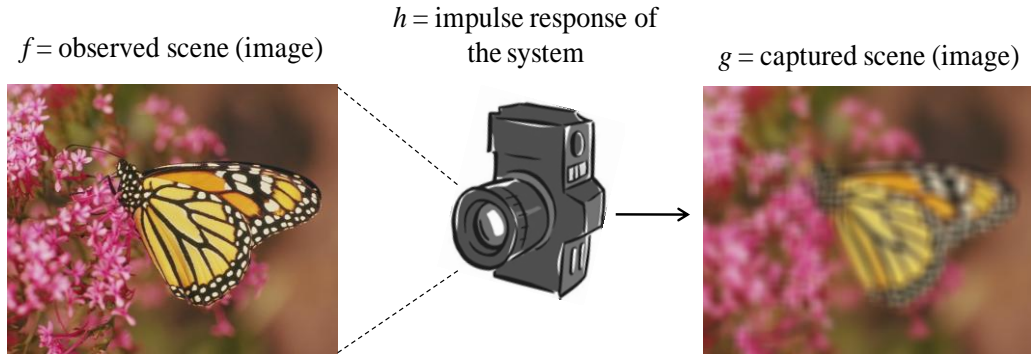
Fig. 2.1 Image blurring model of a camera.

The goal of deblurring is to produce a good approximation of the original image f'. This process is generally known as convolution filtering or deconvolution [46] and deblurring in the case of the restoration of blurred images.

In the noise free case, having prior knowledge of the PSF H, Eqn. 2.3 can be used to find F', an approximation of F, by,

$$F' = H^{-1}G \tag{2.3}$$

such that,

$$F' \approx F \qquad\qquad (2.4)$$

This is known as inverse filtering [48]. If the exact parameters for the convoluting signal are known, it is reasonably expected that the original signal can be recovered accurately.

In many cases, however, detailed information about the unwanted components of the signal is not available thus rendering the method of inverse filtering no longer feasible. Fig. 2.2 shows the deblurring model depicting restoration for real life blurred image. The original image and the blurring kernel are both unknown/ unavailable.
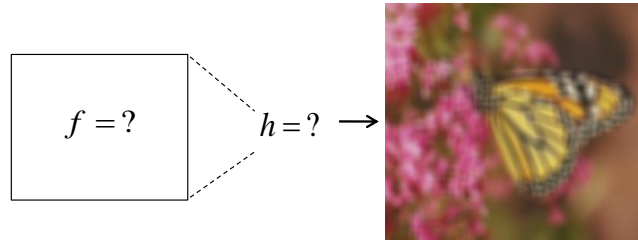
Fig. 2.2 Real life deblurring model. The original scene and the camera PSF information are not available.

Also, if the Fourier transform of the PSF contains zeros, the inverse filtering becomes a poor restoration technique. This predicament of deconvolution of the two signals when both are unknown is termed 'blind deconvolution' [49, 50]. Stockham et al. in [49] were the first to coin the term for this problem.

2.3. Blur Models

The following section briefly describes some of the common blur types. The blurring functions are usually related to the following two classes:

- **Space invariant**

    These constitute the general form of blur PSFs that are independent of image pixel location. The blurring function produces a uniform blurring effect during convolution for each pixel location.

- **Space variant**

    These constitute the blurring PSFs that create a different blurring effect depending on image pixel location. This results in the blurring effect being different for different pixels.

10

PSFs can be commonly distinguished in the following two groups based on their shape/form namely parametric and non-parametric:

- **Parametric form**

   These PSFs can be easily defined using a functional or parametric form. Usually an equation suffices to describe/generate the PSF. The PSF can be decomposed in a set of parameter(s) and can be reasonably approximated by these parameters.

- **Arbitrarily shaped (non-parametric form)**

   These PSFs usually have a complex shape and cannot be defined by an equation of their parameters. Decomposing the PSF in a set of parameters is not possible due to the complex shape of the PSF. Deblurring images corrupted by such PSFs is a very challenging task.

Although there have been some proposed methods for recovering space-variant blurring, the majority of existing deblurring methods were developed for tackling space-invariant blurring PSF [51-56]. Blind restoration of space-invariant degradations is still considered a rather challenging problem. This research focuses on space-invariant PSFs, and, in the context of this research work, "blur" refers to a linear, space-invariant degradation, i.e., a convolution, with or without noise, unless stated otherwise.

2.3.1. Gaussian Blur

The Gaussian blur (or Gaussian smoothing) is the result of filtering an image by a low pass filter estimated by a 2-D Gaussian function. The Gaussian filter in two dimensions over PSF rows and columns, m and n, according to [48] is given as

$$h(m,n) = \frac{1}{2\pi\sigma^2} e^{\frac{-(m^2+n^2)}{2\sigma^2}} \tag{2.5}$$

The PSF for atmospheric turbulence blur can be described by Eqn. 2.5 which can be regarded as a Gaussian blurring [57, 58]. Fig. 2.3 shows the Gaussian blur PSF of size 15x15 and its respective Optical Transfer Function (OTF). The OTF or Fourier transform approximation of the Gaussian PSF is also a Gaussian function. Fig. 2.4(a) shows the effect of atmospheric turbulence blur (approximated by Gaussian blur).

11

The low pass filter blurs the image especially the edges (high pass signal). The image when restored by deblurring becomes crisper with the edges recovered.

(a)

(b)
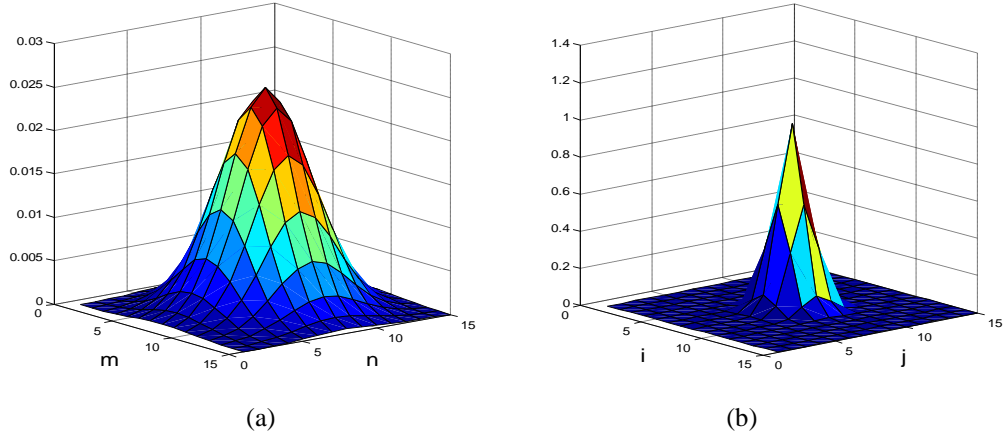
Fig. 2.3 Perspective plot of a Gaussian PSF of size 15x15 with variance σ=2.5 (a) and its respective frequency domain representation (b).

(a)

(b)

Fig. 2.4 (a) Blurred video frame (b) Deblurred using estimated atmospheric turbulence PSF.

2.3.2. Motion Blur

Motion blurs are due to relative motion between the recording device and the scene. This can be in the form of a translation, a rotation, a sudden change of scale, or some combinations of these. Here only the usual case of a global translation is considered.

(a)   (b)
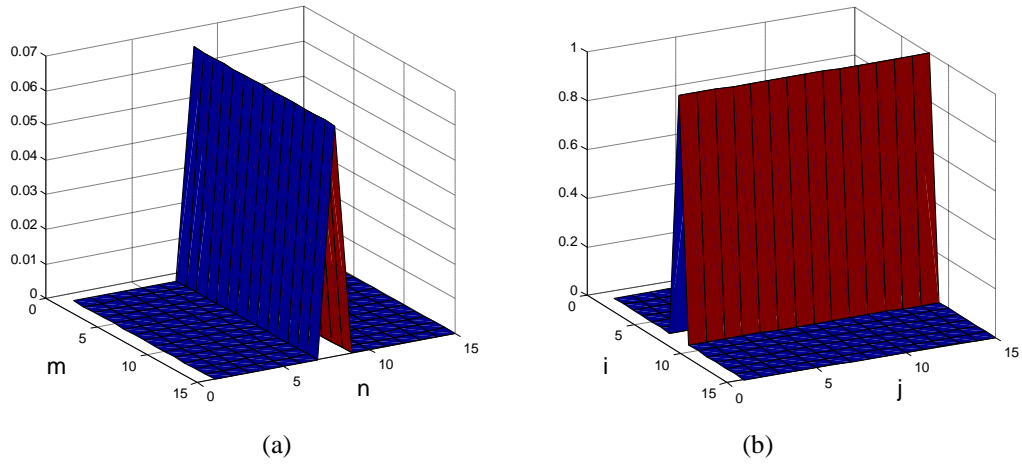
Fig. 2.5 Perspective plot for a PSF of linear motion blur of length 15 and angle 0 degrees (left) and its Fourier transform (right).

When the scene to be recorded translates relative to the camera at a constant velocity under an angle of φ radians with the horizontal axis during the exposure interval, the distortion is one-dimensional. Denoting the length of motion by L, the angle by φ, the PSF is given by Eqn. 2.6 with reference to [59]

$$h(m,n;L,\varphi) = \begin{cases} \dfrac{1}{L} & \text{if } \sqrt{m^2 + n^2} \le \dfrac{L}{2} \text{ and } \dfrac{m}{n} = -\tan\varphi \\ 0 & \text{elsewhere} \end{cases} \tag{2.6}$$

where m and n are the PSF pixel coordinates. Fig. 2.5(a) shows the PSF obtained with application of Eqn. 2.6 for linear motion for length of 15 pixels and at an angle of zero degrees while its spectral domain representation is shown in Fig. 2.5(b). Fig. 2.6 shows the effect of motion blurring on the book image. The filter spreads the effect of the neighbouring pixels in the direction of motion.
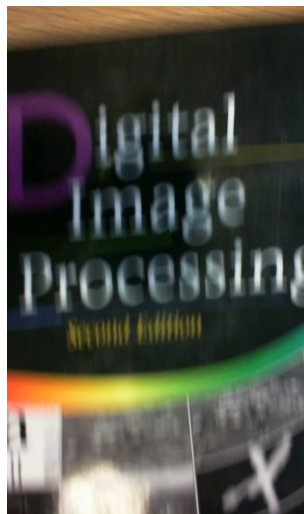
Fig. 2.6 Image of book depicting vertical motion blur. Video of the book being slid was captured using Microsoft Lifecam. This particular frame was extracted afterwards.

13

2.3.3. Camera Out-of-Focus Blur

When a camera takes a 3-D scene onto a 2-D imaging plane, some parts of the scene are in focus while other parts are not. If the aperture of the camera is circular, the image of any point source is a small disk, known as the Circle Of Confusion (COC). The degree of defocus (diameter of the COC) depends on the focal length and the aperture value of the lens, and the distance between the camera and object. An accurate model not only describes the diameter of the COC, but also provides the intensity distribution within the COC. However, if the degree of defocusing is large relative to the wavelengths considered, a geometrical approach can be followed resulting in a uniform intensity distribution within the COC. The spatially continuous out-of-focus blur of radius R, with PSF coordinates *m* and *n*, is given by Eqn. 2.7 with reference to [59]

$$b(m,n;R) = \begin{cases} \dfrac{1}{C\pi R^2} & \text{if } \sqrt{m^2 + n^2} \leq R^2 \\ 0 & \text{elsewhere} \end{cases} \tag{2.7}$$

where *C* is a constant that must be chosen so that energy conservation law is satisfied. Fig. 2.7 shows the original PSF (left) and its spectral domain representation (right). One can notice the low pass behaviour (in this case both horizontally and vertically) in Fig. 2.7 (left), as well as characteristic pattern of spectral zeros in Fig. 2.7 (right).
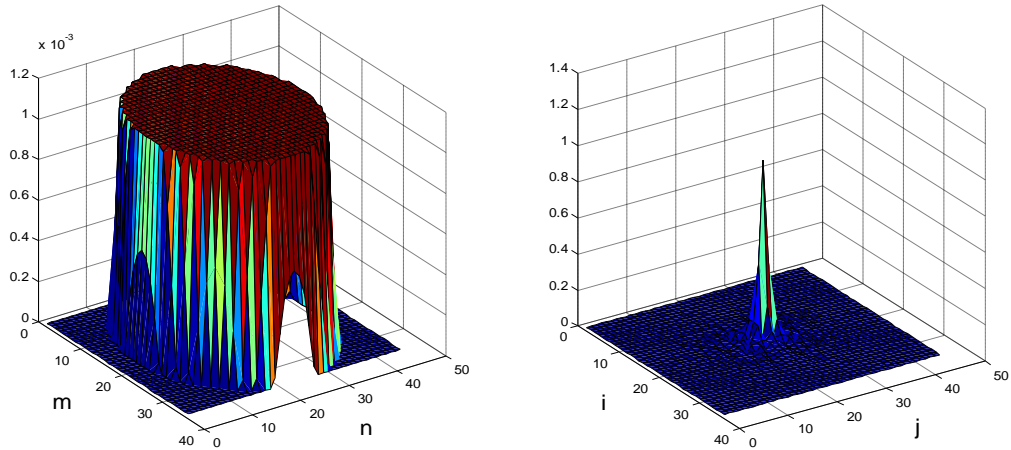
Fig. 2.7 Perspective plot of camera out of focus PSF for R=17 (left) and its Fourier transform (right).

Fig. 2.8 shows an image of the MATLAB book and its out of focus version captured by manually changing the focus away from the focal point on the Microsoft Lifecam. The small size text becomes unreadable as a result of defocusing.

14
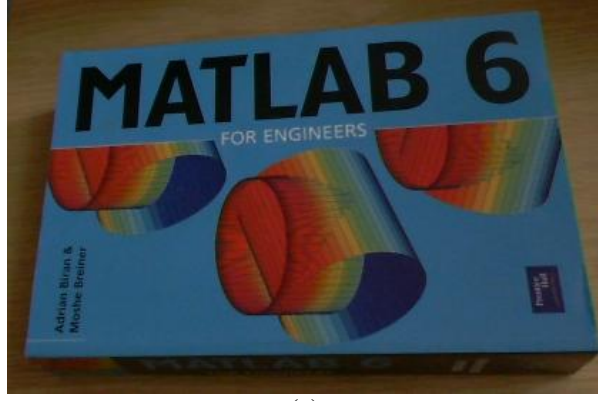
(a)

(b)

Fig. 2.8 (a) Original book image and (b) Out-of-focus blurred version captured using Microsoft LifeCam.

2.4. Restoration Filters

The following section introduces the reader to some of the classical restoration filters that were used or studied in this research work.

2.4.1. Inverse Filtering

The ideal approach to deblurring would be to estimate the inverse of the PSF that blurred the image and apply it to the blurred image and recover the original image. For a noiseless blurred image case, the direct inverse filtering can easily be applied in the spectral (frequency) domain [48], since the convolution process will be converted into multiplication. The inverse filtering process can be represented as.

$$F' = \frac{G}{H} \tag{2.8}$$

In most cases the blurring PSF is not available especially for real blurred images; however, there exist certain situations in which the blurring PSF may be

15

approximated. For example, in the case of motion blur, the blurring is due to linear movement or translation of the image pixels during exposure. The motion blur PSF can be represented by a sinc function in the spectral domain [60]. This leads to a straightforward approach to deblurring by multiplying the blurred image with the inverse of the PSF in the frequency domain. Though the inverse filtering method seems very simple in principle, estimating the correct values of the constants or coefficients of the corresponding PSF may be difficult in practical deblurring cases. The problem of estimating the correct coefficient values arises due to the presence of frequency domain zeros and noise amplification during deblurring. Since an inverse filter is generally a high pass filter, it amplifies the high frequency therefore the noise may get amplified significantly in the process. The presence of frequency domain zeros produces adverse effects in the deblurring process due to inaccurate filter estimation at these points. These issues limit the filter from being utilised in many deblurring applications.

2.4.2. Wiener Filtering

As inverse filtering is very sensitive to additive noise which gets amplified during this process, a simple approach is to reduce single degradation at a time. Thus, the method allows us to develop a restoration algorithm for each type of degradation which can simply be combined afterwards. The Wiener filtering is a linear estimation of the original image. The approach is based on a stochastic framework. The Wiener filter in Fourier domain can be expressed as follows [48]:

$$F' = \left[\left(\frac{H^*}{|H|^2 + \delta} \right) \right] \text{ where } \delta = \frac{|V|^2}{|F|^2} \tag{2.9}$$

The Wiener filtering executes an optimal trade off between inverse filtering and noise smoothing [61]. It removes the additive noise and inverts blurring simultaneously. The Wiener filtering is optimal in terms of the Mean Squared Error (MSE) [48]. In other words, it minimizes the overall MSE in the process of inverse filtering and noise smoothing.

2.4.3. Iterative Blind Deconvolution Method

The Iterative Blind Deconvolution (IBD) method makes use of the Fast Fourier Transform (FFT) and the deterministic constraints in the form of non-negativity and finite support constraints. The algorithm is shown in Fig. 2.9, as given by [29, 32, 62]. The image estimate is denoted by f', the PSF estimate by h', and the linearly

degraded image by g. Capital letters represent FFT versions of the corresponding signals. Subscript r denotes the iteration number of the algorithm.

The iterative process can be summarised as follows:

1. First, a non-negative valued initial estimate f_0 is input to the process.
2. This is Fourier transformed to give F'_r which is then inverted to form an inverse filter and used to form a new estimate of G, G'_r.
3. G'_r is then transformed by inverse Fourier Transform (iFFT) to give g_r.
4. Then image non-negativity constraints are imposed to reveal a positive constrained estimate of g_r.
5. g_r is then Fourier transformed to give the spectrum of G'_r.
6. The spectrum G'_r is then inverted to form an inverse filter and multiplied by H'_r to estimate F'_r.
7. F'_r is then inverse Fourier transformed to give f_r.
8. Image constraints are applied and an estimate of the image f'_r is achieved, this completes single iteration of the algorithm.

The iterative loop is repeated until two positive functions with the required convolution have been found.

Unfortunately, the IBD algorithm suffers from two main problems:

- The inverse filter is difficult to define in regions where the inverted function possesses regions with low values.
- Spectral zeros at frequencies in either F'_r and G'_r provide no information about that spatial frequency being a part of the blurring process.

Implementation of this basic algorithm differs on the assumption on the true image and PSF, implementation of the assumptions and application in mind [62, 63]. The IBD method is popular because of its low complexity [29, 32]. Another advantage of this technique is its robustness to noise which results from the ill-posed nature of the blind image deconvolution problem. IBD algorithm also suffers from uncertain uniqueness, convergence, instability and sensitivity to initial image estimate [62].
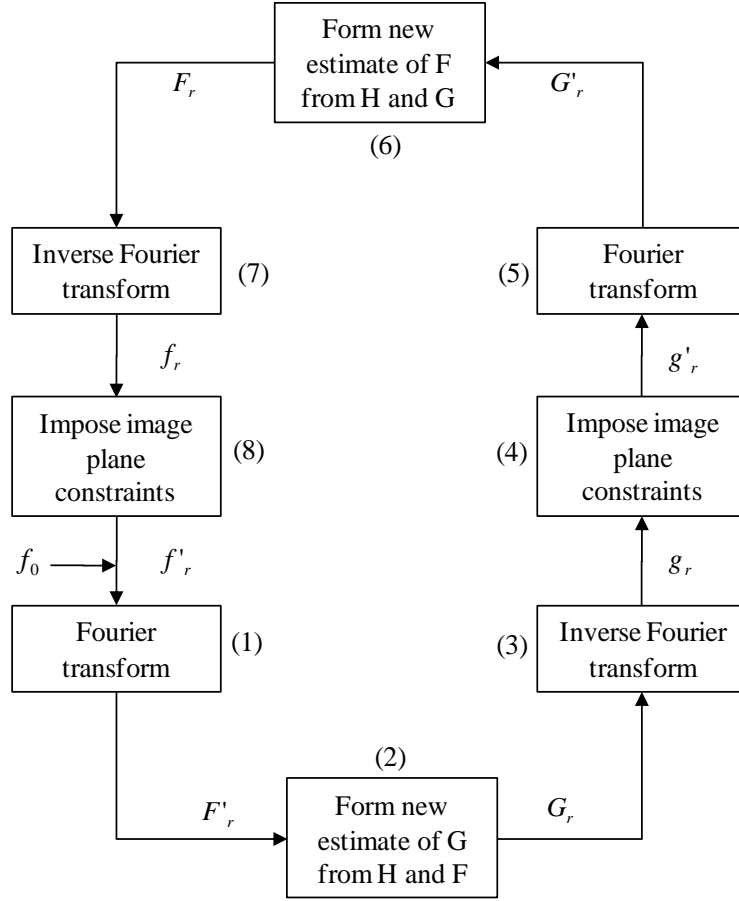
Fig. 2.9 Block diagram of Iterative Blind Deconvolution (IBD) algorithm [29, 32, 62] .

2.4.4. **Richardson-Lucy Algorithm**

Richardson presented an iterative method of restoring degraded images in [27] based on Bayes' theorem of conditional probability, by considering the image, PSF and degraded image probability functions. For an original image *F*, the PSF *H*, the degraded image presented by *G*, and the iteration *k*, Bayes' theorem may be employed as follows

$$P(F \mid G_k) = \frac{P(G_k \mid F)P(F)}{\sum\limits_{i,j} P(G_k \mid F)P(F)} \tag{2.12}$$

Also considering G_k with respect to its dependence on *F*

$$P(F) = \sum\limits_{i,j} P(FG_k) = \sum\limits_{i,j} P(F \mid G_k)P(G_k) \tag{2.14}$$

and

$$P(F \mid G_k) = P(F \mid G_k) / P(G_k) \tag{2.15}$$

18

Substituting Eqn. 2.12 in Eqn. 2.14, we get

$$P(F) = \sum_{i,j} \frac{P(G_k \mid F)P(F)}{\sum_{i,j} P(G_k \mid F)P(F)} P(G_k) \tag{2.16}$$

$$P(F) = P(F) \sum_{k} \frac{P(G_k \mid F)P(G_k)}{\sum_{i.j} P(G_k \mid F)P(F)} \tag{2.17}$$

The term $P(F)$ on the right hand side is also the desired term. An initial estimate of it was suggested using Eqn. 2.12 which results in the iterative restoration method given in Eqn. 2.18

$$P_{k+1}(F) = P_k(F) \sum_{k} \frac{P(G_k \mid F)P(G_k)}{\sum_{i,j} P(G_k \mid F)P(F)} \tag{2.18}$$

The main problem of blind Richardson-Lucy algorithm is that it requires an initial guess for the support size of blurring kernel. Although the blurring kernel is incorporated in the block-circulant matrix form, the support size must be either known or estimated, thus making the algorithm non-blind.

2.4.5. Regularization Based Deblurring Algorithm

Looking into the convolution model of blurring presented in Eqn. 2.2, the image estimate through inverse filtering is given by Eqn. 2.19 as follows

$$F' = \frac{G}{H} = F + \frac{V}{H} \tag{2.19}$$

The restoration error for this model is given by Eqn. 2.20

$$\left\| F' - F \right\| = \left\| \frac{V}{H} \right\| = \sqrt{\left| \frac{V}{H} \right|^2} \tag{2.20}$$

Due to the ill-posed inverse problem, the restoration error will take very large values, particularly amplifying the high frequency noise [64]. Due to this problem, the system defined in Eqn. 2.19 yields solutions at points where the amplified high frequency noise masks the desired solution F. In accordance with the regularization theory [65], if prior information about the noise or original data can be incorporated, physically meaningful solutions to the ill-posed problem can be achieved. If we represent a regularization operator in the frequency domain by L then the regularized

restored image can be obtained by minimizing the cost function in Eqn. 2.20 in accordance with [66]

$$\|LF'\| \tag{2.21}$$

provided the norm of the noise is known, the term is given in Eqn. 2.22

$$\|G - HF'\| = \|V\| \tag{2.22}$$

The above constrained minimization problem leads to the constrained least-squares or Tikhonov-Miller regularized solution [65, 66] , given by Eqn. 2.23

$$\|G - HF'\| = \|V\| \tag{2.23}$$

2.5. Image Quality Measures (IQMs)

For BID, quality measures have been developed to evaluate the effectiveness of individual schemes or to evaluate different image processing algorithms. The performance of BID schemes in the past has been mainly subjected to error based performance measures that are already used by the existing signal processing community [48]. Most of these measures use an original and deblurred image pair to compute the error among them in order to construct a quantitative quality analysis. The original/uncorrupted image serves as a reference for high quality. In the past decade efforts were directed towards development of such quantitative image quality measures (IQMs) [67]. Error measures require both the original/reference and the observed/distorted image to be stationary with reference to each other; hence they do not allow any translational or rotational motion between the required images. Since the error measures require a reference image to compute the quality against it, they are regarded as full-reference quality measures in this research work.

In contrast to error based measures, perceptual quality measures try to incorporate Human Visual System (HVS) characteristics; this is because the quantitative measure is mathematical only and hence may not be truly representative of the perceived quality [68]. However, by no means are the perceptual quality measures able to outdo the simplicity of error based measures, and thus offer a suitable alternative. HVS based quality measures are calculated from the image or its characteristics without the use of a reference image. Therefore they are usually regarded as non-reference or blind quality measures. In recent years, blind image quality measures (IQMs) have been the centre of attention in the field of image processing especially in BID. In

BID they can be used to estimate the blurring PSF. The quality measure used would optimize at or around the point where the true PSF is located. These quality measures are independent of a reference image and in this research work are regarded as non-reference or blind IQMs.

The field of image restoration lacks a promising comparison base for judging the effectiveness of competing algorithms. Until recently by far the most widely adopted quantitative measurement of image restoration performance used variants of error based measures, for example, Mean Squared Error (MSE), Signal to Noise Ratio (SNR) and Peak Signal to Noise Ratio (PSNR) etc. Lack of an effective performance evaluation measure exclusively for images has hampered the robust assessment of competing algorithms [67], with users of the community generally resorting to very generic or algorithm specific evaluation techniques. While others propose modification to quantitative performance criterion based on qualitative (visual) criterion to bring the error measures in-line with the HVS. HVS is subjective in itself in providing measureable as well as visual effect results.

IQMs as described above can be divided into two types, namely full-reference and non-reference quality measures. A full-reference IQM relies on the availability of the original image as a reference for comparison against its distorted version, while non-reference (blind or reference-less) IQM quantitatively determines the quality of the image directly from it or from its attributes. The list of both full-reference and non-reference quality measures is quite long [69].

IQMs were employed during the research work to judge the deblurred image quality, and include both full-reference and non-reference IQMs. Full-reference IQMs include: the Peak Signal to Noise Ratio (PSNR), Mean Structural SIMilarity (MSSIM) index [70-72] and the Universal Quality Index (UQI) [67]. Non-reference IQMs include: spatial kurtosis [36, 73] , spectral kurtosis [74-76], Blind/Reference-less Image Spatial QUality Evaluator (BRISQUE) [77, 78] and Natural Image Quality Evaluator (NIQE) [79, 80]. These IQMs were selected with respect to their performance and robustness as detailed in the literature. A brief description of these quality measures is given below.

2.6. Full-reference IQMs

In error based performance evaluations, the restoration is evaluated by measuring the amount of improvement in image quality. To measure that improvement, one needs to have the original, the distorted and the restored images available in the measuring

process. Extent of restoration performance can generally be regarded as a process that takes in the original image *f*, the distorted image *g* and the restored image *f'*, and returns a scalar value. This output value is thus a measure to indicate how much the image quality has been improved from the blurred image *g* to the restored image *f'* with respect to the original image *f*. Listed below are the variants of the error based performance measures, these measures are still employed and in fact the majority of the image processing schemes base their quality performance on these measures [81]. This is simply because these measures are easy to use and readily give a numerical value to match up, which in many cases, is quite well-liked, comprehensible, and reciprocal with signal processing community terminologies, e.g. decibel (dB).

2.6.1. Peak Signal to Noise Ratio (PSNR)

Evaluating deblurred image quality necessitates a measure. MSE is a very commonly employed quantitative measure in the signal and image processing community [48]. The MSE between two images *f* and *g* is given by,

$$MSE = \frac{1}{MN}\left(\sum_{m=1}^{N}\sum_{n=1}^{M}\left(f(m,n)-g(m,n)\right)^2\right)$$
(2.24)

PSNR provides quantitative image quality results by scaling the MSE according to the image range. For grayscale images with a pixel intensity range from 0 to 255, the PSNR is defined as,

$$PSNR = -10\log_{10}\left(\frac{\sum_{m=1}^{N}\sum_{n=1}^{M}\left(f(m,n)-g(m,n)\right)^2}{255^2}\right) dB$$
(2.25)

PSNR is measured in decibels (dBs). A higher value of PSNR represents an image of high quality. The PSNR measure is not ideal, but is in common use. Its main failing is that the signal strength is estimated as maximum signal value, rather than the actual signal strength for the image. PSNR is a good measure for comparing restoration results for the same image, but PSNR comparison with different images may be meaningless. For example, an image with 15 dB PSNR may seem visually much superior to another image with 20 dB PSNR.

2.6.2. Mean Structural SIMilarity Index (MSSIM)

Structural SIMilarity (SSIM) index is an objective image quality metric that measures the structural similarity between two images by comparing of local patterns

of pixel intensities that have been normalized for luminance and contrast [71]. Assuming two images f and g, the SSIM is a function of the luminance $l(f,g)$, contrast $c(f,g)$ and structural similarity $s(f,g)$ of the images.

$$S(f,g) = t(l(f,g), c(f,g), s(f,g)) \tag{2.26}$$

$$l(f,g) = \frac{2\mu_f \mu_g + C1}{\mu_f^2 + \mu_g^2 + C1} \tag{2.27}$$

$$c(f,g) = \frac{2\sigma_f \sigma_g + C2}{\sigma_f^2 + \sigma_g^2 + C2} \tag{2.28}$$

$$s(f,g) = \frac{\sigma_{fg} + C3}{\sigma_f \sigma_g + C3} \tag{2.29}$$

where μ is the mean, σ is the standard deviation of the image signal and $C1, C2, C3$ are constants. SSIM has been successfully used for denoising and classification [82, 83]. A higher value of MSSIM represents an image of high quality.

2.6.3. Universal Quality Index (UQI)

The next IQM, UQI, analyses the loss of correlation, luminance and contrast distortion among the two images as the base for quality perception. The UQI for two image signals f and g is defined in Eqn. 2.30 as,

$$Q(f,g) = \frac{4\sigma_{fg} \mu_f \mu_g}{(\sigma_f^2 + \sigma_g^2)(\mu_f^2 + \mu_g^2)} \tag{2.30}$$

Rearranging Eqn. 2.30 we obtain,

$$Q(f,g) = \frac{\sigma_{fg}}{\sigma_f \sigma_g} \cdot \frac{2\mu_f \mu_g}{\mu_f^2 + \mu_g^2} \cdot \frac{2\sigma_f \sigma_g}{\sigma_f^2 + \sigma_g^2} \tag{2.31}$$

The first term is the correlation coefficient of the two signals, whereas the second and third terms measure mean luminance and structural similarity. A higher value of UQI represents an image of high quality.

Error based performance measures are usually applied to evaluate restoration performance, and have become a de-facto standard in the comparative study of

restoration algorithms. However, it is well known that such measures which are based on the MSE criterion, do not agree with HVS properties. This implies that performance assessment by means of SNR improvement is, to a certain extent, of a poor representation with respect to the HVS. Besides, it is found that the SNR improvement is of low precision in evaluating restoration performance. Therefore, apart from accuracy and precision, the SNR improvement as a measurement of restoration performance expresses an indistinct message.

Every performance measure has its own set of advantages and drawbacks and cannot be used globally on every image under every condition, as demonstrated by Eskicioglu and Fisher in [69]. They carried out a suitability analysis on different objective quality measures for grayscale image compression. They argued about the sufficiency of a single scalar value to describe a variety of impairments. They further demonstrated that a set of numerical measures might reliably be used to specify magnitude of degradation in reconstructed images; however, the same evaluation scheme across different techniques may not bear the same optimal results. They suggested using a combination of numerical and graphical measures for a better image quality performance comparison.

2.7. Non-Reference IQMs

Over the last few years, the image and signal processing community have focused on the design of IQMs especially for the blind evaluation of image quality based on HVS. Two of the IQMs used in this research work are BRISQUE and NIQE. The other two IQMs, spatial and spectral kurtosis, are based on higher order cumulants of the data. The main advantage of such IQMs is that not only are they independent of a reference image, they are also independent of distortion specific features, such as ringing, noise, blur, or blocking. They have shown to compete well with top performing non-reference image quality analysers trained on human judgements of known distorted images.

2.7.1. Non-Gaussianity as a Quality Measure

Conventional image performance measures work on the principle of subjective (qualitative) performance measures or quantitative quality measures which are based on error/difference image. These conventional measures, both subjective and error based, tend to have their own pros and cons. Even a combination of subjective and error based objective measures, like HVS based performance systems, fall short in applicability, simply because of the very complex nature, limited knowledge and

implementation difficulties of human eye behaviour. These error based techniques are dependent on relational matching between two images; the observed and the reference. Therefore, relational based performance evaluation techniques require a reference image in addition to the observed and the restored image, which may not be available in any real life scenario, like digital camera photography. Hence, these performance indexes cannot be used as a performance maximization criterion or act as a feedback parameter.

If the blur/noise and the image are assumed as two distinct independent sources, i.e. Gaussian and non-Gaussian respectively, one can rely on the basic approach of the BSS [73] to look for non-Gaussianity in the recovered signals. Non-Gaussianity has been used in [84, 85] for image denoising.

As the image and degrading/distortion function on a distorted image are all distinct processes, they thus have a direct bearing on the information content of the image as the result of any restoration algorithm. The clear advantage offered by basing the performance index on the information content of the image rather than the reference image is that the original image is not required. Therefore associating performance index with the non-Gaussianity is associating it with an observed image or only the available blurred image itself.

The obvious question of how it works can be answered as follows: the information content of a noise free and undistorted image is unique which does not remain the same when it is subjected to any degrading or distortion function. Hence, when any blurred image is treated by any deblurring algorithm, all it tries to do to bring the blurred image to its pristine form is to eradicate the distortions. From the perspective of the blurred image's information content or the space of non-Gaussianity, the algorithm tries to restore the image to its "original" information content or to non-Gaussianity, which otherwise happens to be at its minimum when it is blurred.

Thus non-Gaussianity of the data can be employed as a performance measure, with or without the need of the original image as required by other measures, where it can serve as a feedback performance measure for the BID scheme. The quality index for comparing the performance of improvement/deterioration of any image can then be defined as,

$$
Q_{NG} = \begin{cases} \dfrac{J_o}{J_1} & if \quad J_1 \geq J_o \\[3mm] \dfrac{J_1}{J_0} & otherwise \end{cases}
\tag{2.32}
$$

25

where, J_I and J_O, are non-Gaussianity of the original and the distorted image respectively. The advantage of using a non-Gaussianity based performance measure is not only that it works for both blind and non-blind situations, but also that it is robust against translational, orientation deviations etc.

Various measures can be used for computing the Gaussianity/non-Gaussianity of the image, with kurtosis and negentropy being the main ones used. Spatial domain non-Gaussianity measures were used for blind image deblurring and denoising by Yin and Hussain in [86] . The measure and scheme based on it are defined in Section 2.9. Non-Gaussianity measure in the frequency domain, termed spectral non-Gaussianity measure, has been investigated in this research work as an alternate, more robust and computationally efficient IQM as compared to spatial kurtosis. The new frequency domain non-Gaussianity IQM, spectral kurtosis, is presented in the research work illustrated in chapter 3.

2.7.2. Blind/Reference-less Image Spatial QUality Evaluator (BRISQUE)

BRISQUE is a spatial domain natural scene statistic based distortion-generic non-reference IQM model. Rather than computing distortion specific features such as ringing, blur or blocking, it instead uses scene statistics of locally normalized luminance coefficients to quantify possible losses of 'naturalness' in the image due to the presence of distortions; thereby leading to a holistic measure of quality. The BRISQUE model uses mapping from feature space to quality scores using a regression model that yields a measure of image quality. The features comprise the statistic measures of a generalized Gaussian distribution fitting of mean subtracted contrast normalized coefficients. For the distorted image g, mean subtracted contrast normalized coefficient at each pixel is obtained by subtracting the local mean signal value μ_g and then dividing by the local contrast function σ_g such that,

$$\hat{g}(m,n) = \frac{g(m,n) - \mu_g(m,n)}{\sigma_g(m,n) + C} \tag{2.33}$$

where,

$$\mu_g(m,n) = \sum_{k=-U}^{U} \sum_{l=-V}^{V} w_{k,l} g_{k,l}(m,n) \tag{2.34}$$

$$\sigma_g(m,n) = \sqrt{\sum_{k=-U}^{U} \sum_{l=-V}^{V} w_{k,l}(g_{k,l}(m,n) - \mu_g(m,n))^2} \qquad (2.35)$$

and *C* is a constant. *w={w_{k,l}|k=-U,....U,l=-V,....V}* is a 2-D circular-symmetric Gaussian weighting function and *U=V=3* was used to calculate the measure. A lower value of BRISQUE represents an image of high quality.

2.7.3. Natural Image Quality Evaluator (NIQE)

The next IQM measure, the non-reference NIQE, is a completely blind image quality analyzer that only makes use of measurable deviations from statistical regularities observed in natural images, without training on human-rated distorted images, and without any coverage of distorted images. The same model for image quality computation as in BRISQUE is used with the exception that NIQE uses natural scene statistics features from a staple of natural images unlike BRISQUE, which is trained on features obtained from both natural and distorted images as well as human judgment of image quality. A lower value of NIQE represents an image of high quality.

2.8. Review of Image Deblurring Techniques

Blind deconvolution is the process of estimating both the true image and the blurred image using partial information available/deduced from the blurred image and a study of the characteristics of the blurring system. Blind deconvolution is not a new area and various approaches have been proposed to solve the problem depending upon the particular degradation and image models [29, 33, 48, 62, 64, 87, 88].

In blind deconvolution, a convoluted version of an original signal is observed, without knowing whether it is the true signal or the convolution kernel or PSF. The problem is then to find a separating filter that can deconvolve the blurred image and give a good approximation of the real image. If the convolution blur is assumed to be known prior to deblurring, one of the classical image restoration techniques such as inverse filtering, least-squares filtering, or iterative filtering can be employed. In practical imaging situations, this however is almost never the case because the image capturing device's transfer function is unknown. Therefore, the true image must be estimated directly from the blurred image by using partial or no information about the blurring process and the true image, and thus becomes a case of blind deconvolution.

Over the past few years, several methods have been developed for image deblurring.

27

These methods range from the spatial to the spectral domain, parametric to non-parametric, and adaptive to batch operation. Examples include the Richardson-Lucy method [27], Total Variation [28], Maximum Likelihood (ML) method [29, 30], Minimum Entropy Deconvolution (MED) [31], Non-negativity And Support-constraint Recursive Inverse Filter (NAS-RIF) [32], simulated annealing [33], and multi-channel blind deconvolution [33]. These methods do provide, to some extent, solutions to the BID problem; however many are not satisfactory in terms of robustness, computational efficiency and restoration quality. Mainly, the robustness of these schemes remains or becomes questionable when real-life blurred images are to be restored.

The problem of blind deconvolution can be tackled in the spatial or spectral domain. The spectral domain approach offers a valuable insight into image and noise properties. The solutions provided by the existing deconvolution methods are not satisfactory in terms of stability, robustness, noise amplification and ringing artefacts [33]. For instance, the Richardson-Lucy method is iterative in nature, it estimates the blurring function during the deblurring process, and is computationally complex and intensive. The method also requires a good initial estimate of the blurring kernel in order to operate the algorithm.

Categorizing the different approaches given over the years by many researchers is a difficult task. Schemes can be divided into parametric or non-parametric, iterative and non-iterative, spatial and spectral etc. Most of the blind deconvolution approaches can be divided into parametric and non-parametric. In applications where the blurring function can be assumed in advance (e.g. motion blur or defocus), it is possible to use a parametric model of the PSF instead, and then one can try to estimate the model's parameters. The main advantage is a small number of estimation parameters, however, in real life scenarios it is often difficult to derive a good model for the PSF [17, 18, 40-45].

Blind deconvolution approaches on the basis of implementation strategy can be divided into two main constituent classes [29].

- The first class identifies the blurring kernel (PSF) separately from the true image, which is to be used later with any of the classic image restoration algorithms. This class employs blur identification methods, which first estimate the blurring kernel and then utilize any non-blind deconvolution algorithm to find the source estimate. Examples of this class of algorithms

include methods like the zero-sheet separation method and identification by frequency domain zeros [89-92].

- The second class incorporates the estimation of the source image and the blurring kernel simultaneously. This class includes methods based on statistical or deterministic priors of the source image, the blurring kernel and noise. Using the mentioned priors, estimation of the source image is performed by some use of the maximization approach; total variation based deblurring is an example for this class of algorithms [28]. Since the source image and the blurring kernel are now variables in the problem, computational complexity is a major problem.

The zero-sheet separation method and identification by frequency domain zeros method are briefly explained as follows. The identification by frequency domain zeros method utilises visual information acquired from investigating the zeros of the blurred image in the frequency domain for the cases of motion and out-of-focus blurred image. Zeros in the frequency domain result at points where the inverse of the blurring kernel does not exist. For a specific PSF they are in relation to its parameter(s). In the case of motion blurred image blurred by a PSF of length L, the zeros appear in the frequency domain at a length of L pixels away from the centre of the image spectrum. By observing the zeros, length of the blurring PSF is identified and then the blurred image is deblurred using the estimated PSF. Similarly, in the case of out-of-focus blurred image blurred by an out-of-focus PSF of radius R, the zeros form a ring at a length of R pixels from the centre of the image spectrum. The blurring PSFs radius is estimated from observing the zeros, the deblurring PSF is calculated for it and the blurred image is deblurred using the estimated deblurring PSF.

The zero-sheet separation method relies on estimating the PSF from the zeros of the polynomial that defines the blurring PSF. The 2-D discrete transform of the blurred image is represented as a 2-D polynomial and then factored to yield all the transform components (zeros of the polynomial) up to an arbitrary complex scale factor and linear phase terms. Once the zeros of the polynomial are identified, the deblurring PSF is formed from it and then the image is deblurred. Both these schemes deal with blind deblurring of images in the noiseless case and are prone to rounding errors resulting from the mathematical algorithms.

Images constitute two main components, namely illumination and object reflectance [48, 50]. If $i(m,n)$ presents the illumination and $r(m,n)$ the reflectance component at

each pixel location *(m,n)*, then the image pixel *f(m,n)* can be presented as,

$$f(m,n) = i(m,n)r(m,n) \qquad (2.36)$$

$$0 < i(m,n) < \infty$$

$$0 < r(m,n) < 1 \qquad (2.37)$$

Spatial or homomorphic filtering reduces illumination variations. By attenuating the low spatial frequencies relative to high frequencies, the contrast of the image is enhanced and the details are preserved [50]. Images are transformed to the log domain before processing where the log image is equivalent to the sum of the logs of illumination and reflectance components. In [46], Oppenheim et al. demonstrated the use of spatial filtering [93] in image enhancement with application to bandwidth reduction. They also suggested the use of convolutional filtering for restoring blurred images without prior information, thus providing the general concept of blind deconvolution. For an input $x=x_1*x_2$ (* denotes convolution), taking the z-transform results in,

$$X(z) = X_1(z)X_2(z) \qquad (2.38)$$

Taking the logarithm transform of Eqn. 2.38, one gets,

$$\ln(X(z)) = \ln(X_1(z)) + \ln(X_2(z)) \qquad (2.39)$$

Eqn. 2.39 shows the transformation from a convolution space to an additive space, thus enhancing simplicity in separating mixed (convolved) signals [94]. Oppenheim et al. [46] proposed the use of homomorphic filtering for deconvolution by separating the minimum phase and maximum phase signal from the input signal. Ulrych et al. [94] used homomorphic filtering for deconvolution of seismic signals by approximating a better wavelet to effectively separate the signal into a crustal and mantle response. Stockham et al. also suggested a homomorphic filtering based approach for deconvolving the signal by approximating the true signal directly [49]. In the noiseless case, the logarithm of Eqn. 2.2 can be presented as,

$$\log(G) = \log(H) + \log(F) \qquad (2.40)$$

In accordance with the Central Limit Theorem (CLT), if there are many samples

available, the right hand side of the equation converges to log(*H*). Since only a single observation of the blurred signal is available, Stockham proposed segmenting the signal for this purpose. The idea was also extended to the power spectrum, although the results appear to be affected by unknown phase distortion.

MED is another scheme that employs minimizing the entropy of the resulting signal. Originally proposed by Wiggins in [31] for the deconvolution of seismic data, it was modified by Ulrych et al. in [95] to include complex reflection coefficients, phase distortions and time delays related to seismic activity. The basic scheme involved separating the components of the system into a smooth wavelet and a series of impulses. The MED iteration as by [95] can be given as,

$$F_{x+1}^n = B_x^{n-1} y + F_x \qquad (2.41)$$

F_x is the initial estimate of the image and F_{x+1}^n is the new estimate of the image. Convergence of the scheme depends upon the entropy norm *B* that is minimized in successive iterations. Different entropy norms have been suggested based on their convergence and error minimization properties. Wiggins in [31] proposed the varimax norm while Ulrych and Walker used a kurtosis norm in [95]. Cabrelli used a D norm for the same purpose [96]. Extending the scheme to the frequency domain, Sacchi et al. in [97] proposed applying frequency domain constraints over the mid frequency ranges of the convolved signal, to provide a dominant signal spectrum, thus avoiding heavy distortion by noise. Their algorithm is named as the frequency-domain MED.

If the Fourier transform of the PSF contains zeros, the inverse filtering becomes a poor restoration technique. Sondhi reviewed the digital image restoration methods of his era in [47]. In [47], Sondhi suggested a modification to the inverse filtering to overcome this difficulty.

In [93], Gennery suggested determining the OTF, the Fourier Transform of the PSF, by looking at the zeros in the Fourier transform of a blurred image which might provide sufficient information about the parameters of the OTF. The method is limited to only certain usual forms of degradation and in the absence or low presence of noise in the image. In [89] Cannon proposed using the power spectrum as it provided a better identification of the zeros even in the presence of noise.

Simultaneous deconvolution of the unknown PSF and the blurred image was first proposed by Ayers and Dainty in [62]. It suggests alternately iterating on each of the unknowns to estimate the true image and the PSF, thus making it a blind

deconvolution scheme. But the scheme suffers from noise amplification in successive iterations and depends on the initial estimates of both unknowns as well.

The work undertaken by Schafer et al. in [98] marks the birth of deblurring algorithms that impose various constraints in order to converge on the true solution. Prior information about the signal and the blurring kernel can be incorporated in the algorithm in the form of a constraint operator. The iteration as in [98] is given by,

$$F_{x+1} = \lambda y + F_x \qquad (2.42)$$

$$y = DCx \qquad (2.43)$$

where λ is the convergence operator that can be a constant or a function of the independent variables and F_x is the initial estimate of the image. y is the original signal with the convolution signal D and the constraint operator C.

Principal Component Analysis (PCA) is a mathematical procedure that uses an orthogonal transformation to convert a set of observations of possibly correlated variables into a set of values of uncorrelated variables called principal components. The number of principal components is less than or equal to the number of original variables. This transformation is defined in such a way that the first principal component has variance as high as possible (that is, it accounts for as much of the variability in the data as possible), and each succeeding component in turn has the highest variance possible under the constraint so it is orthogonal to the preceding components. So, PCA can be seen as a linear mixture that defines most variation of the data. Independent Component Analysis (ICA) is a much more powerful technique; capable of finding the underlying factors or sources when these classic methods fail completely. ICA forms the basis for the non-Gaussianity based BID scheme and is thus presented in detail in the following section.

Recent focus in the image deblurring domain is towards the deblurring of images corrupted by arbitrarily shaped PSFs resulting from camera handshake. Parametric blurs can be estimated by finding the original values of the blurring parameter(s) but arbitrarily shaped PSFs usually have a complex shape that cannot be modelled in a mathematical or parametric form thus making the PSF estimation difficult. Some of the BID schemes that deal with such PSFs include the BID of Shan et al. [39], Fergus et al. [17] and Whyte et al. [18].

Shan et al. BID scheme deals with the blind deconvolution of images corrupted by motion PSFs both linear and arbitrarily shaped. It uses a single blurred image for

estimating the blurring PSF and deconvolution through a unified probabilistic model for kernel estimation and unblurred image restoration. Their BID model focuses on handling inherent image noise effectively and reducing ringing artefacts by shrinking kernel errors during the estimation phase of the BID scheme. Image structures such as edges and sharpness of the deblurred image are utilised for ringing reduction.

Their technique benefits from three main contributions. Firstly it uses a new model of the spatially random distribution of image noise which helps in reducing the kernel errors that arise during image noise reduction and blurring PSF estimation. Secondly a new smoothness constraint is imposed on low contrast areas in the latent image. This constraint suppresses ringing artefacts not only in smooth areas but also on textured ones in the near vicinity. The constraint in turn affects the kernel refinement stage as well. Thirdly an efficient optimization algorithm based on variable substitutions and Plancherel's theorem is utilised, that allows for computationally intensive optimization steps to be performed in the frequency domain.

The scheme from Fergus et al. [17] estimates the blurring PSF and then the image is deconvolved using a Richardson-Lucy filter. The PSF estimation process depends on image statistics, especially pixel colour/ image gradients. Their scheme was designed to estimate in-plane motion PSF while neglecting out-of-plane (rotational) motion blur. The second scheme by Whyte et al. [18] extends the scheme of Fergus et al. by incorporating rotational blur constraints as well as employing it for two deblurring cases. In the first deblurring case their scheme has been used to deblur a single-shot image, while in the second deblurring case, it utilizes information from a noisy pair of blurred image along with a single-shot blurred image to estimate the blurring PSF.

Many digital camera hardware assisted approaches to BID are also suggested. Coded aperture techniques use a patterned mask placed in the camera lens aperture to change the frequency features of out-of-focus blur in order to facilitate blur estimation and removal [5, 6]. These methods provide minimal modifications to the conventional camera resulting in portable imaging systems. They depend on scene depth information to perform shift-variant BID. Several hardware designs have been proposed and incorporated in the camera to estimate scene depth using out-of-focus cues, which can also be viewed as out-of-focus blurring PSF estimation methods. A modified multiple pinhole camera was used by Hiura and Matsuyama in [8] to estimate scene depth in different image textures and superimposing the image textures in a depth-dependent manner.

Coded exposure techniques have been utilised for motion blur reduction by opening

and closing the shutter during exposure, attenuation of high frequencies due to motion blur can be prevented. Raskar et al. in [7] developed a coded exposure technique that opens and closes the shutter during exposure according to a pseudo-random binary code. Agrawal and Xu in [3] presented another technique for code selection in order to make the resulting point spread function (PSF) invertible. Their technique presents a trade-off between PSF estimation and PSF invertiblity for the code selected. Levin et al. in [5] showed that sensor motion can render motion blur invariant to 1-D linear object motion by proposing to move the camera image sensor with a constant 1-D acceleration during exposure. Ben-Ezra and Nayar in [9] attached a low resolution video camera to a main camera, in order to estimate camera shake PSF from video frames, and then to remove blur from the main camera image. Some researchers proposed to move sensors for different purposes. Ben-Ezra et al. moved the sensor by a fraction of a pixel size between exposures for video super-resolution [99]. Mohan et al. [100] moved the lens and sensor to deliberately introduce motion blur that acts like out-of-focus blur. Nagahara et al. [101] moved the sensor along the optical axis to make defocus blur depth-invariant.

2.9. Independent Component Analysis (ICA)

ICA is another technique based on the independency concepts of Blind Signal Separation (BSS), which provides a framework for deconvolution. Assuming the source and blurring signal to be independent and non-Gaussian, it tries to estimate the source signal as the most independent one. According to the CLT, this is the most non-Gaussian signal. ICA as a multivariate data analysis method has gained wide spread use in the image processing community [36, 102-104]. ICA has successfully been applied as the solution to the BSS problem [105]. But its application is not limited to BSS only, and many signal and image processing fields like image denoising, image segmentation and recognition and others have also benefited from this [85, 106].

Independent Component Analysis (ICA) is a statistical and computational technique for revealing hidden factors that underlying sets of random variables, measurements, or signals. ICA defines a generative model for the observed multivariate data, which is typically given as a large database of samples. In the model, the data variables are assumed to be linear or nonlinear mixtures of some unknown latent variables, and the mixing system is also unknown. The variables are assumed to be non-Gaussian and mutually independent and they are called the independent components of the

observed data. These independent components (also called sources or factors) can be estimated by ICA. ICA can be seen as an extension to PCA and factor analysis [104]. ICA is one of the increasingly important tools in signal processing. It has gained its novelty in the successful solution of BSS problems [102, 103, 106]. It was initially proposed to provide a solution to the BSS problem [34] which aims at recovering a set of unobserved sources mixed in an unknown manner from a set of observations. Since its inception, numerous algorithms based on the ICA concept have been employed successfully in various fields of multivariate data processing, from biomedical signal applications and communications to financial data modelling and text retrieval. While linear mixtures of unknown sources have been examined thoroughly in the literature, the case of nonlinear ones remains an active field of research.

2.9.1. ICA Problem Formulation

The source separation problem was formulated around 1982 by Herault and Jutten et al. in [107] for motion decoding of vertebrates while the underlying ICA technique was first rigorously developed by Comon in [102] as a generalization of the PCA technique. ICA is one method for performing BSS that aims to recover unknown source signals from a set of their observations, in which they are mixed in an unknown manner. By minimizing the mutual information between the components of the output vectors of the demixing system, ICA tries to estimate both the mixing function and a coordinate system in which the source signal estimates become as mutually statistically independent as possible.

For a source signal s, consider its recorded/captured version x as follows

$$x = A.s \tag{2.44}$$

where A is a matrix of some unknown coefficients that define the representation and is known as the mixing matrix. In most cases, only linear functions are considered, because then the interpretation of the representation is simpler, and so is its computation. Both the mixing matrix A and the source signals are unknown.

In this framework, one can determine the matrix A by the statistical properties of the transformed components y. In order to estimate the inverse of A, some basic assumptions are made such as the source signals are assumed to hold mutual statistical independence i.e. the knowledge of one element does not provide any information about other elements and that the source signals are not Gaussian.

The goal of ICA is to find the original signal s from the mixture x. This is the BSS

problem [108]. Blind means that we know very little if anything about the original sources or we do not have any knowledge at all.

ICA offers a simple solution to this BSS problem by considering just the statistical independence of the signals [73, 106]. If the signals are not Gaussian, it is even simpler to determine the inverse mixing coefficients *W* so that the source signals are statistically independent.

$$y = W.x$$
$$y \approx s$$

$$(2.45)$$

So, the ICA problem is now reduced to finding a linear representation in which the components are statistically independent. Also, one must keep in mind that ICA model holds strictly under the assumption that components are non-Gaussian and the mixing matrix *A* is orthogonal.

2.9.2. **Maximum Non-Gaussianity Principle**

Another very intuitive and important principle of ICA estimation is maximum non-Gaussianity [73]. The idea is that according to the CLT, sums of non-Gaussian random variables are closer to Gaussian than the original ones. Therefore, if we take a linear combination $y=\sum b_i x_i$ of the observed mixture variables, this will be maximally non-Gaussian if it equals to one of the independent components. This is because if it were a real mixture of two or more components, it would be closer to a Gaussian distribution, due to CLT. Thus, the principle can be quoted as follows

"Find the local maxima of non-Gaussianity of a linear combination $y=\sum b_i x_i$ under the constraint that the variance of y is constant. Each local maximum gives one independent component." [36]

Higher order cumulants have been used for BSS problem before [109]. Kurtosis, a fourth order cumulant, and negative entropy are two measures used in ICA to calculate the non-Gaussianity of a signal [73].

2.9.3. **Limitations of ICA**

Although ICA-based schemes provide a framework to apply statistical independency concepts to blind deconvolution problems; their performance remains limited because of lack of observation samples, a prerequisite for BSS problems. Applying ICA on BSS or blind deconvolution problem requires fulfilling its pre-conditions,

which essentially means providing as many observations as underlying sources and independency among all observations.

Further, only one underlying source or observation can have a Gaussian distribution. As the convoluted signal is reverberate of its own adjacent samples or pixels (in case of an image) which are mixed as per the proportion defined by the PSF; thus resulting in single observation only. In order to have multi-channel representation as required by ICA, one has to resort to some alternate representation technique. Recently a framework was developed under which a blurred image was redefined as multi-channel observations and thus the ICA based concept was applied to the problem of Blind Image Deconvolution (BID) [110].

These ICA based algorithms do provide a feasible solution to the image deconvolution problem, however these methods fail to address the signal independency issues which have impeded exploration of real potentials of ICA in successful separation of underlying sources [111-113]. Further, existing ICA-based solutions have limited scope for image deconvolution problems because of small blurring kernel support, and very limited noise handling capacity along with deblurring. Also the independency assumption of ICA may not hold true in some practical situations. A new scheme that uses ICA with relaxed independency known as Dependent Component Analysis (DCA) was proposed by [114] to overcome this limitation. Its uniqueness and novelty is further marred by the fact that it is not completely blind at this moment as it requires an initial estimate of the blurring kernel to initialize the algorithm; therefore blind deconvolution still remains an exciting field of study.

2.10. Spatial Non-Gaussianity Based Blind Image Deblurring (BID) Scheme

The ICA-based algorithms have limited applicability in restoring the single frame blurred images. Therefore, either one has to provide multiple frame of the blurred images or to use some method to generate independent multi-channel observation from a single image for successful ICA-based deblurring.

Yin & Hussain in [115] proposed a non-Gaussianity based single frame image deblurring scheme based on the principles of ICA. It uses a Wiener filter to deblur and denoise the image while the optimization procedure is based on GA. The methodology uses independency concept of ICA, in the sense that the independent nature of the original image over the blurred one is exploited. By utilizing this fact,

blurred image is tried to be restored by the application of any of the non-Gaussianity measures, i.e. kurtosis or negentropy, just like ICA employs them in BSS to separate the signals. As per CLT, images becoming more Gaussian as a result of increasing values of the blur, so using a non-Gaussianity measure, one can estimate the original image. Fig. 2.11 verifies this claim for the Barbara image in Fig. 2.10 for Gaussian blur of varying kernel width, σ.

Fig. 2.10 Barbara image used for non-Gaussianity analysis.
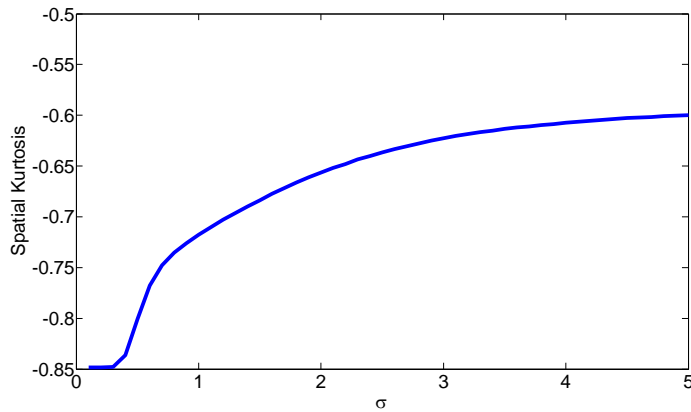
Fig. 2.11 Gaussianity behaviour of Barbara image depicted by spatial kurtosis. The image becomes more Gaussian due to blurring.

Spatial non-Gaussianity measures were used by this scheme to differentiate between the correlated (blurred image) and intermediate stages of recovery process till the time an uncorrelated (independent) image is achieved. During the restoration process the estimated PSF was optimized by a simple fixed point algorithm in an iterative manner. Their BID scheme uses GA based optimization of the fitness function. GAs have been widely used as an effective optimization algorithm for solving complex problems [116, 117]. A restored image is the one that has maximum possible independency. Fig. 2.12 presents the overview of the blind single frame image deblurring technique.
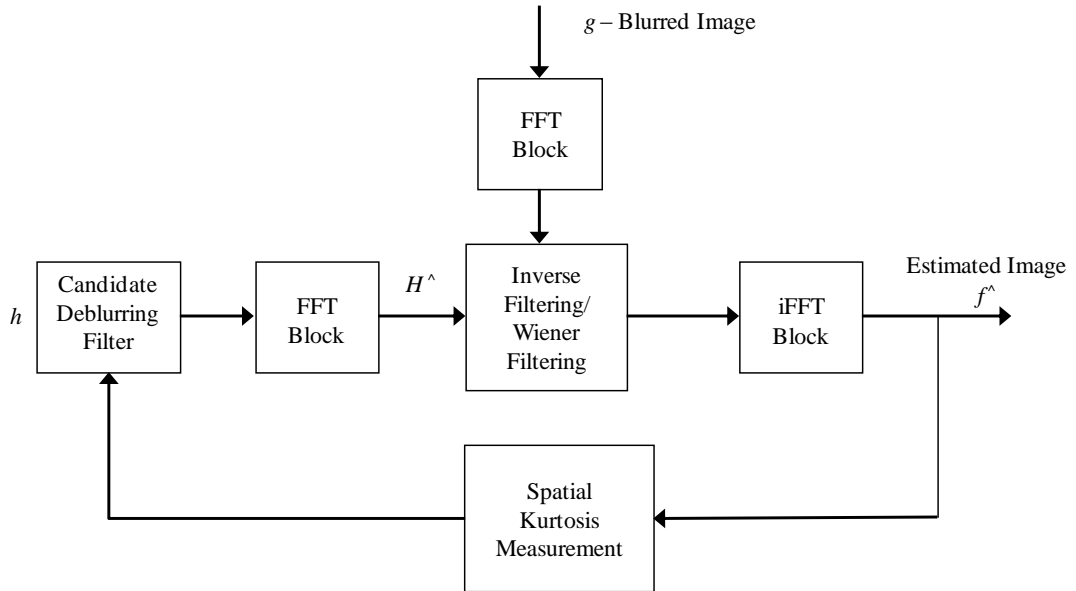
Fig. 2.12 Overview of the spatial non-Gaussianity based blind deconvolution scheme

2.11. Summary

An introduction to the topic of BID was provided with focus on the restoration filters and techniques used in this research work. Some of the classical restoration filters including Wiener, Richardson-Lucy and regularised filters were examined and their functionality discussed. A critical analysis of the existing BID techniques in literature was provided and schemes relevant to the research work were reviewed. The spatial non-Gaussianity based scheme, which forms the base for the spectral non-Gaussianity measure, was discussed in detail and its limitations reviewed. This leads the need to find more efficient and robust deblurring measures. The following chapter presents the spectral non-Gaussianity measure as an efficient alternate to the spatial non-Gaussianity measure.

Chapter 3

The Spectral Kurtosis Based Non-Gaussianity Measure for Blind Image Deblurring

3.1. Introduction

This chapter proposes the spectral kurtosis non-Gaussianity measure for BID and presents experimental results on both artificial and real blurred images. Spatial non-Gaussianity measures suffer from deblurring noise and ringing artefacts which makes the robustness of the BID scheme based on them questionable, especially when real life blurred images are to be deblurred. This leads the need to develop new measure(s) or investigate other existing measures, those that are more robust and preferably computationally simple. The spectral kurtosis measure is presented as an efficient and robust alternative to the previously used spatial non-Gaussianity measures. The spectral kurtosis based BID schemes for gradient descent and GA based optimization are provided. Full-reference and non-reference IQMs have been used to quantitatively evaluate the quality of the deblurred images.

The principle of ICA is used in BSS and deconvolution problems. In image restoration, such methods are often computationally intensive, and ringing and noise amplification artefacts from the deblurring process greatly affect the image statistics,

varying the calculated non-Gaussianity measures. The spatial kurtosis measure was previously used by Yin and Hussain in [115] as a fitness function for the GA to measure non-Gaussianity in the time domain. The spatial kurtosis measure maximizes/minimizes in the vicinity of true PSF parameter values indicating that the deblurring estimate is closest to the pristine image. It uses a Wiener filter in each iteration to generate a deblurred image estimate from the blurred one using a candidate PSF. This makes the spatial kurtosis based BID scheme computation-intensive due to the transformation of the deblurred image in the frequency domain, estimated by the Wiener filter, back to the time domain to calculate the spatial kurtosis. The spatial kurtosis measure is also very sensitive to, and suffers from, ringing and noise degradations generated as a result of deblurring. To overcome these problems, an enhanced scheme is proposed that employs the non-Gaussianity principle of ICA on the spectral data rather than the image data itself. That is, spectral kurtosis is used as a measure of non-Gaussianity during the deblurring process. The deblurring process measures the non-Gaussianity of the image spectrum of the estimated images and the measure maximizes for the true blurring kernel. The spectral kurtosis measure, unlike the spatial kurtosis measure, is calculated in the frequency domain thus omitting the use of iFFT.

3.2. The Spectral Kurtosis Based Non-Gaussianity Measure

The blurring process makes the image more Gaussian by producing correlation among adjacent pixels. This trend follows for increasing value of blur, and was demonstrated by Hussain in [115, 118]. As a consequence of the CLT, the original image to be recovered from a mixed/degraded signal would be the one that has minimum Gaussianity or maximally non-Gaussian properties. Kurtosis, a fourth order cumulant, is generally employed to measure the non-Gaussianity of a signal. Mathematically the normalized spatial kurtosis of image data f is defined in Eqn. 3.1 as,

$$k(f) = \frac{E\{f^4\}}{(E\{f^2\})^2} - 3 \tag{3.1}$$

When f has unit variance, spatial kurtosis is estimated as,

$$k(f) = E\{f^4\} - 3 \qquad\qquad (3.2)$$

Optimizing kurtosis function is not a trivial problem and resulting learning algorithms can be difficult to implement or become easily trapped in local minima. Spatial kurtosis is highly sensitive to outliers, and due to noise amplification and ringing effects from the restoration filter during the deblurring process, the measured non-Gaussianity varies, thus leading to a less precise approximation of PSF parameters. To increase the computational efficiency of the BID scheme and seek a more robust non-Gaussianity measure, spectral kurtosis is proposed as an alternative. Spectral kurtosis measures a signal's non-Gaussianity in the frequency domain.

The spectral kurtosis measure resembles the Frequency Domain Kurtosis (FDK) of Dwyer [74], where the magnitude of the signal's spectrum is used to calculate the kurtosis value of the signal in the frequency domain. Though initially used to detect random signals, the measure has been widely used to detect bearing faults, noise in underwater signals and even subterranean termite detection [119-123].

The spectral kurtosis measure is defined by Eqn. 3.3,

$$K(F) = \frac{E\{F^4\}}{(E\{F^2\})^2} - 3 \qquad\qquad (3.3)$$

where F is the magnitude frequency domain value of signal f. It has been noted empirically that taking the logarithm to the base 10 of F, prior to calculating the spectral kurtosis, and during deblurring, provides a more distinct maximum. The measure has been shown to be more prone to the deblurring artefacts and much better pristine image estimates were obtained. The initial results of the spectral non-Gaussianity based deblurring scheme developed by Khan and Yin were reported in [75, 76] .

3.3. Spectral Kurtosis Based Non-Gaussianity Analysis For Blurred Images

As per the CLT, the output of a linear system is more Gaussian compared to the input signal. In accordance, the image blurring process is assumed to make the blurred images more Gaussian than the pristine ones by producing correlation among the adjacent pixels of the image. If independency is assumed for the original signals, the same fact can be related in the frequency domain. Then the deblurring problem can be considered as separation of the convolved signals' spectrum by the use of

frequency domain non-Gaussianity measure. In order to perform deblurring based on frequency domain non-Gaussianity measure, an analysis of the image's blurring pattern is observed to substantiate that image's non-Gaussianity lessens as it is blurred more and more. Fig. 3.2, 3.3 and 3.4 verify this behaviour in the frequency domain of the image by using the spectral kurtosis measure. Images in Fig. 3.1 were blurred with Gaussian PSF of increasing variance (from 0.1 to 5). Also noted here is that spatial kurtosis for sub-Gaussian and super-Gaussian image shows an increasing and decreasing kurtosis value respectively while spectral kurtosis is always increasing. This makes the spectral kurtosis independent of the statistical nature of the image and the deblurring scheme easily automatable.
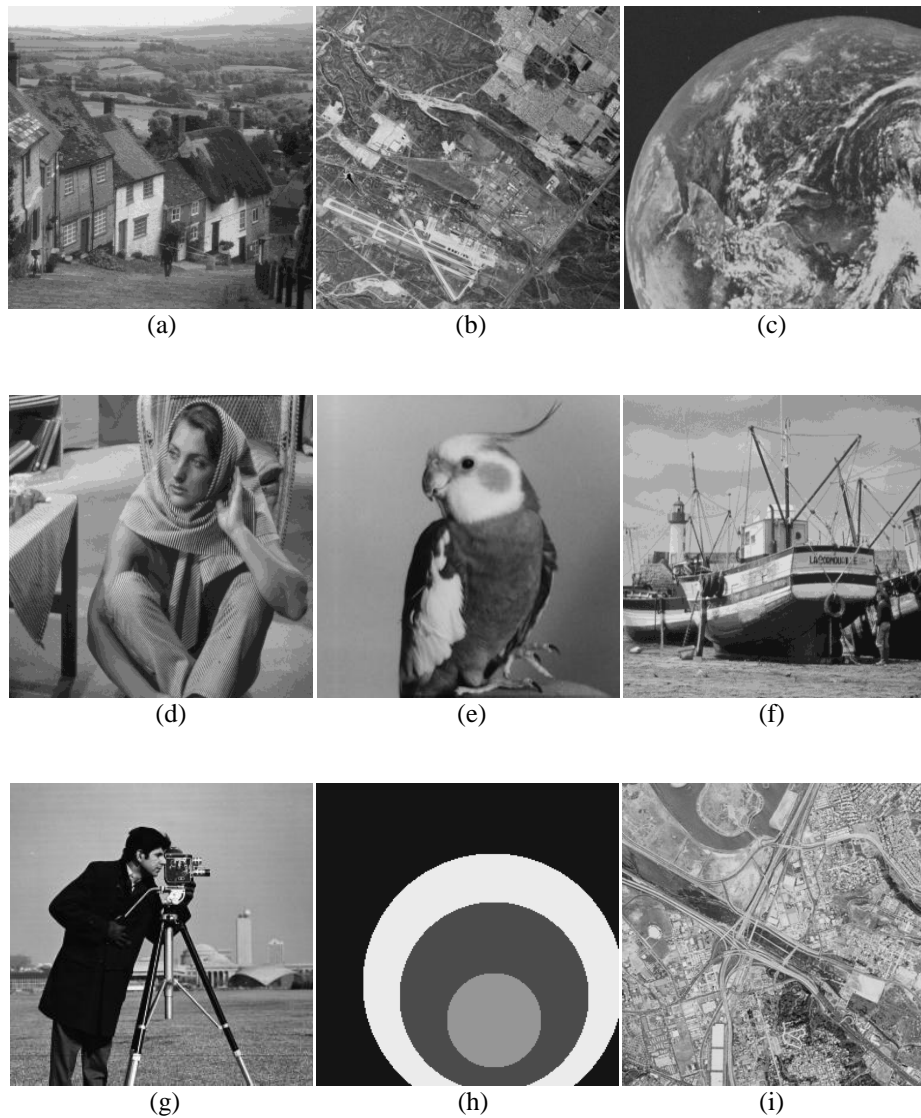
Fig. 3.1 Test images used for non-Gaussianity analysis (a) Goldhill (b) Aerial-1 (c) Earth (d) Barbara (e) Parrot (f) Boat (g) Cameraman (h) Circles (i) Aerial-2.
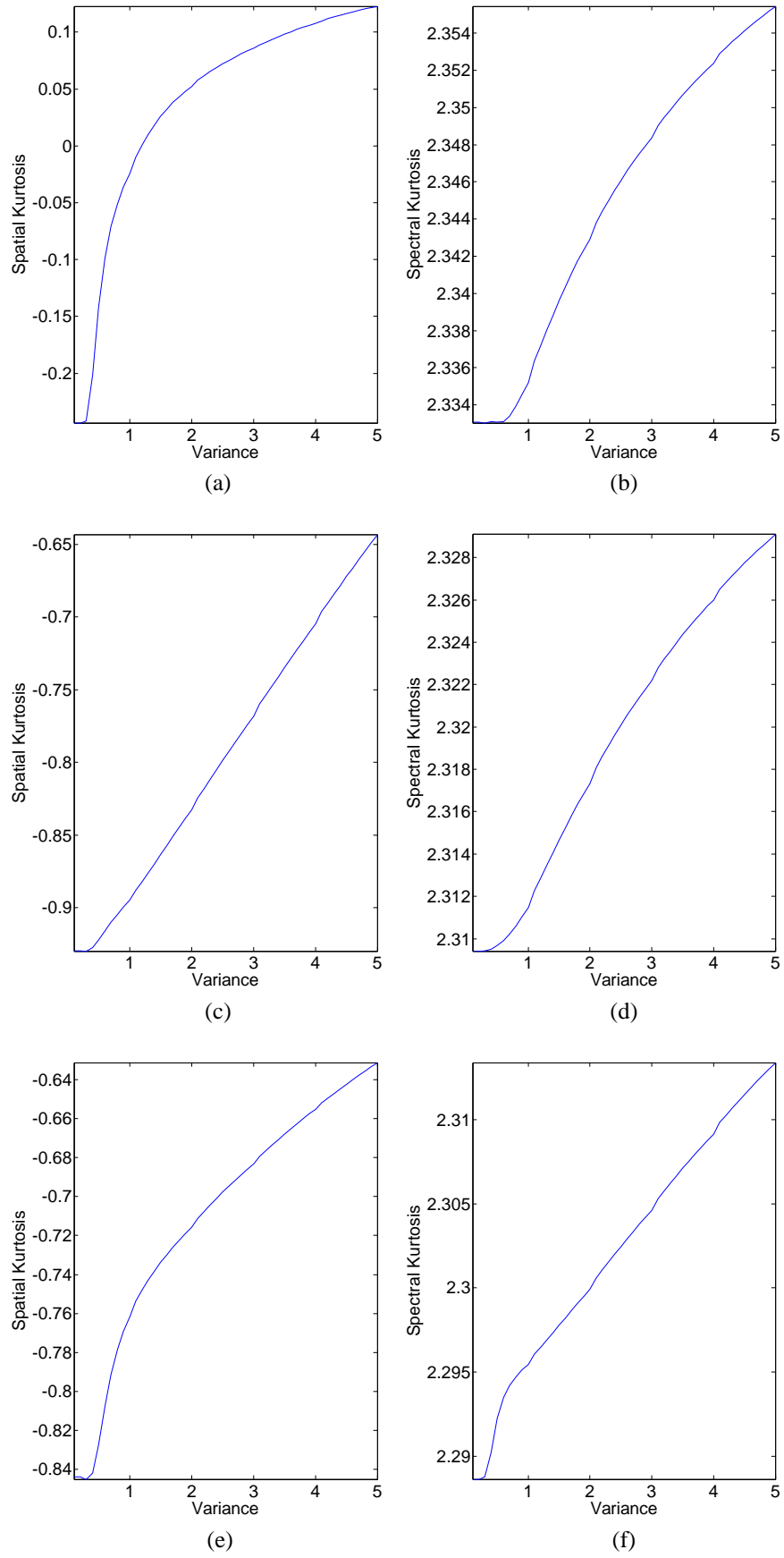
Fig. 3.2 Gaussianity analysis for Goldhill, Aerial-1 and Earth images. (a), (c), (e) spatial kurtosis and (b), (d), (f) spectral kurtosis plots.

44
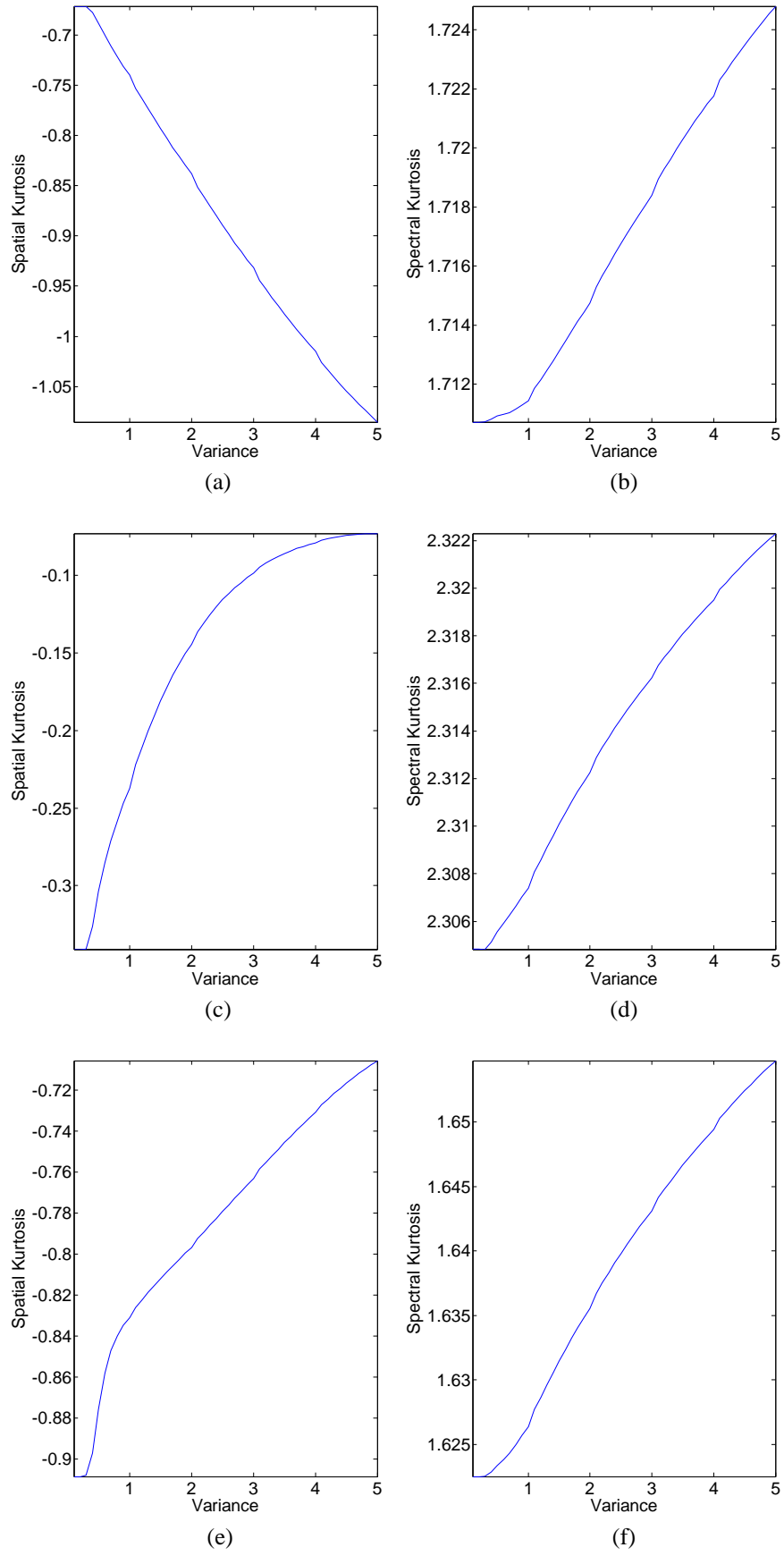
Fig. 3.3 Gaussianity analysis for Barbara, Parrot and Boat images. (a), (c), (e) spatial kurtosis and (b), (d), (f) spectral kurtosis plots.
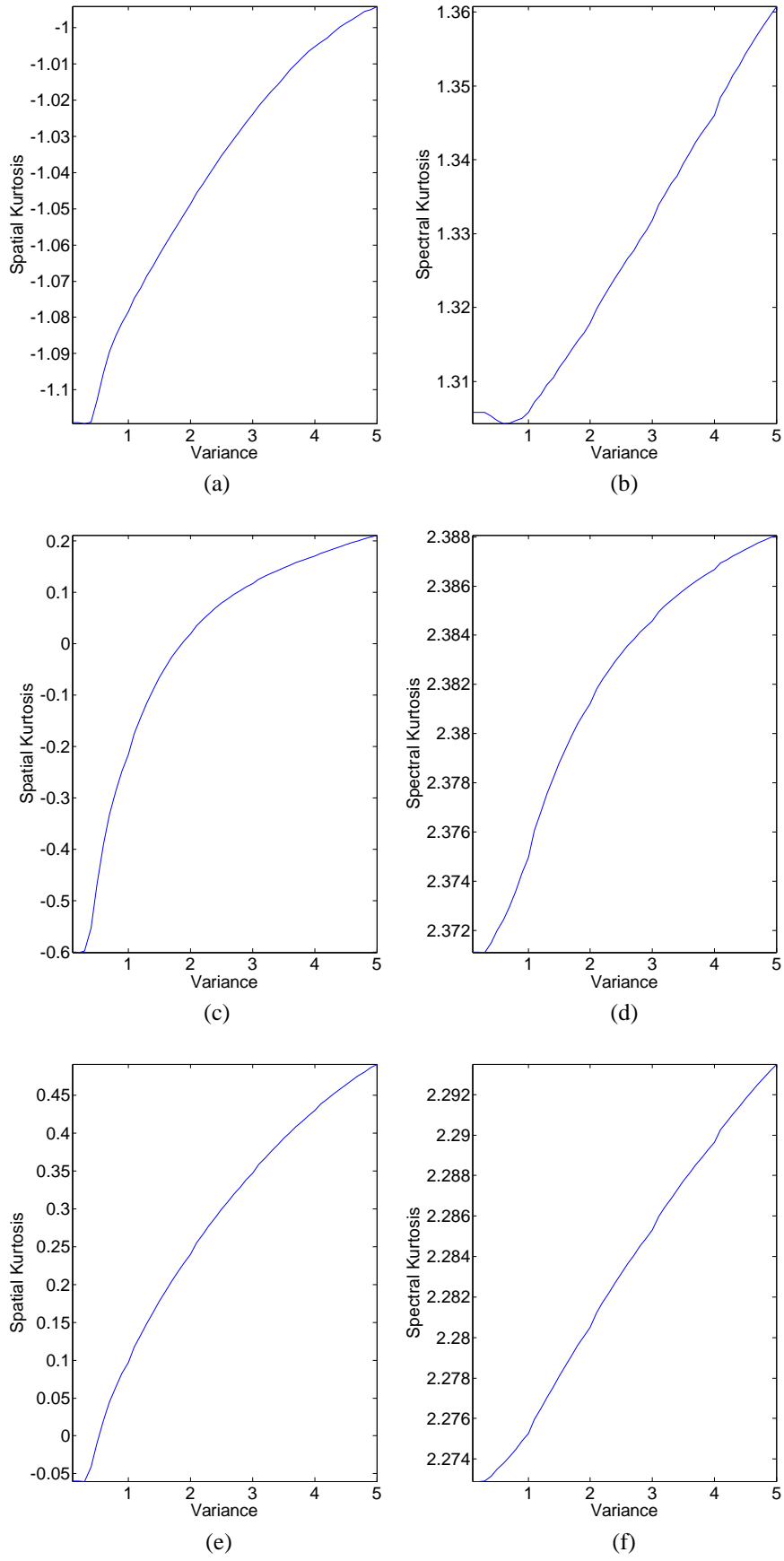
Fig. 3.4 Gaussianity analysis for Cameraman, Circles and Aerial-2 images. (a), (c), (e) spatial kurtosis and (b), (d), (f) spectral kurtosis plots.

3.4. Spectral Kurtosis in Relation to Spatial Kurtosis

Let f represent a zero mean signal with normal distribution and k its spatial kurtosis value, σ_f its standard deviation, σ^2_f its variance and $\mu_f(r) = \mu^r_f$ its rth central moment or mean. Their frequency domain counterparts are depicted as F, K, σ_F, σ^2_F and $\mu_F(r) = \mu^r_F$ respectively. Signal f's normal distribution in the time domain and frequency domain are given by Eqns. 3.4 and 3.5, respectively

$$p(f) = \frac{1}{\sigma^2_f \sqrt{2\pi}} e^{\frac{-f^2}{2\sigma^2_f}} \qquad (3.4)$$

$$P(F) = \frac{1}{\sigma^2_F \sqrt{2\pi}} e^{\frac{-F^2}{2\sigma^2_F}} \qquad (3.5)$$

The relation between σ^2_f and σ^2_F can be expressed according to [124] in Eqn. 3.6 as,

$$\sigma^2_f \sigma^2_F = 1 \qquad (3.6)$$

The relationship between the spatial and the spectral kurtosis for the two cases of normalized and non-normalized kurtosis is evaluated as follows.

3.4.1. Non-Normalized Spatial and Spectral Kurtosis

The non-normalized kurtosis in time domains is given by Eqn. 3.7

$$k = \frac{\mu_f(4)}{\sigma^4_f} = \frac{\mu^4_f}{\sigma^4_f} \qquad (3.7)$$

and in frequency domain by Eqn. 3.8

$$K = \frac{\mu_F(4)}{\sigma^4_F} = \frac{\mu^4_F}{\sigma^4_F} \qquad (3.8)$$

Multiplying Eqn. 3.7 and Eqn. 3.8 we get

$$kK = \frac{\mu^4_f}{\sigma^4_f} \frac{\mu^4_F}{\sigma^4_F} = \frac{\mu^4_f \mu^4_F}{(\sigma^2_f \sigma^2_F)^2} \qquad (3.9)$$

from Eqn. 3.6 we have $\sigma^2_f \sigma^2_F = 1$. Putting this in Eqn. 3.9, we obtain

$$kK = \mu_f{}^4 \mu_F^4 \qquad (3.10)$$

The rth central moment for normal distribution is given by

$$E[(f - \mu_f)^r] = \begin{cases} 0 & \text{if } r \text{ is odd} \\ \sigma_f^r (r-1)!! & \text{if } r \text{ is even} \end{cases} \qquad (3.11)$$

We calculate the fourth central moment which is in order used to calculate kurtosis.

$$\mu_f^4 = E\left[(f - \mu_f)^4\right] = \sigma_f^4 (4-1)!! = 3\sigma_f^4 \qquad (3.12)$$

Similarly

$$\mu_F^4 = 3\sigma_F^4 \qquad (3.13)$$

Multiplying Eqn. 3.12 and Eqn. 3.13 we get

$$\mu_f^4 \mu_F^4 = (3\sigma_f^4)(3\sigma_F^4) = 9\sigma_f^4 \sigma_F^4 \qquad (3.14)$$

But $\sigma_f^2 \sigma_F^2 = 1$ from Eqn. 3.6. So

$$\mu_f^4 \mu_F^4 = 9 \qquad (3.15)$$

Putting this in Eqn. 3.10, we get

$$kK = 9 \qquad (3.16)$$

3.4.2. Normalized Spatial and Spectral Kurtosis

The normalized kurtosis in time domain is given by Eqn. 3.17 as follows

$$k = \frac{\mu_f^4}{\sigma_f^4} - 3 \qquad (3.17)$$

and in frequency domain by Eqn. 3.18

$$K = \frac{\mu_F^4}{\sigma_F^4} - 3 \qquad (3.18)$$

Rearranging them, we get

$$\sigma_f^4 = \frac{\mu_f^4}{k+3} \tag{3.19}$$

$$\sigma_F^4 = \frac{\mu_F^4}{K+3} \tag{3.20}$$

Multiplying Eqn. 3.19 and Eqn. 3.20 we obtain

$$\sigma_f^4 \sigma_F^4 = \frac{\mu_f^4 \mu_F^4}{(k+3)(K+3)} \tag{3.21}$$

Replacing $\sigma_f^4 \sigma_F^4$ and $\mu_f^4 \mu_F^4$ with their respective values from Eqn. 3.6 and Eqn. 3.15 and through further manipulation, we get

$$k = \frac{9}{K+3} - 3 \tag{3.22}$$

So, in general, for non-normalized and normalized kurtosis, the relationship between their time and frequency counterparts can be approximated by Eqn. 3.23 as

$$k \propto \frac{1}{K} \tag{3.23}$$

3.5. Proposed Spectral Kurtosis Based BID Scheme Using Gradient Descent Optimization

A steepest descent BID scheme for spectral kurtosis maximization is presented. Assuming that uniform blur can be modelled by a parametric form, the scheme tries to estimate the true blurring parameters for the absolute maximum value of spectral kurtosis the deblurred image. The scheme is devised to handle any type of blur that can be modelled in a parametric form such as Gaussian, motion and out-of-focus blur. Gradient is computed against the parameter(s) of the blurring PSF, which is optimized in the direction of increasing kurtosis value till the pristine image is estimated. The scheme is simple and efficient and does not require any prior knowledge about the image or the blurring process. The algorithms and gradients are derived for a number of blurs, and the performance improvements are corroborated through a set of simulations. The benefit of using such a model of estimation is that it provides a united/single base for the BID scheme, allowing it to estimate any of the mentioned uniform blur types using the same scheme. The parametric model of blur

helps us simplify the search for the blurring PSF's parameter(s) value by optimizing the spectral kurtosis with respect to the blurred parameter until the desired result is obtained.

Assume that Y is the deblurred image resulting from the deconvolution of the blurred image G with the Wiener restoration filter, given by Eqn. 3.24

$$\frac{H^*}{|H|^2 + \delta} \tag{3.24}$$

where δ is the noise to signal ratio. For simplicity of future derivation, w.r.t magnitude of the spectral data, we rewrite the above equation as

$$\frac{H}{H}\left(\frac{H^*}{|H|^2 + \delta}\right) = \left(\frac{HH^*}{|H|^2 H + H\delta}\right) = \frac{H^2}{H^3 + H\delta} \tag{3.25}$$

The kurtosis of the deblurred image Y is given by Eqn. 3.26

$$K(Y) = \frac{\mu_Y(4)}{\mu_Y(2)^2} - 3 \tag{3.26}$$

Eqn. 3.27 gives the expected value or mean of Y represented by $\mu_Y(0)$

$$\mu_Y(0) = \frac{1}{M - Q_1} \frac{1}{N - Q_2} \sum_{i=Q_1+1}^{M} \sum_{j=Q_2+1}^{N} Y(i, j) \tag{3.27}$$

Here M and N are the number of rows and columns of the image Y. Q_1 and Q_2 represent the row and column number at which blurring starts occurring for actual image data and not the padded data around the rows and columns. The derivation of the gradient based BID algorithm scheme starts with differentiation of the cost function with respect to the parameter of the blurring function. In the proposed method a kurtosis based cost function for the deblurred image is employed. The parameter is updated iteratively using the steepest descent method, as shown in Eqn. 3.28

$$\lambda_{r+1} = \lambda_r + \alpha \nabla \left| K_{\lambda_r}(Y) \right| \tag{3.28}$$

under the constraint given in Eqn. 3.29

$$\left| K_{\lambda_{r+1}}(Y) \right| > \left| K_{\lambda_r}(Y) \right| \tag{3.29}$$

Where λ is the blurring PSF parameter, such as kernel width, length, or radius in case of Gaussian, motion or out-of-focus blur respectively, r is the iteration number, $K_{\lambda_r}(Y)$ is the kurtosis of the deblurred image for the current parameter, $\nabla\left|K_{\lambda_r}(Y)\right|$ represents the gradient matrix for the absolute kurtosis value and α is the convergence step size.

Since

$$\left|K_\lambda(Y)\right| = K_\lambda(Y)\,\mathrm{sgn}(K_\lambda(Y)) \tag{3.30}$$

Eqn. 3.28 can be rewritten as

$$\lambda_{r+1} = \lambda_r + \alpha\nabla K_{\lambda_r}(Y)\,\mathrm{sgn}(K_{\lambda_r}(Y)) \tag{3.31}$$

For α, a fixed scalar value can be used e.g. $a=p^r$ where r is the iteration number and $0<p\leq1$. For faster convergence, more efficient step computation schemes can also be employed. The gradient matrix is derived as follows.

$$\nabla K_\lambda(Y) = \frac{\partial}{\partial\lambda}K(Y) = \frac{\partial}{\partial\lambda}\left(\frac{\mu_Y(4)}{\mu_Y(2)^2}\right) \tag{3.32}$$

$$\nabla K_\lambda(Y) = \frac{\partial}{\partial\lambda}\left(\frac{\dfrac{1}{M-Q_1}\dfrac{1}{N-Q_2}\displaystyle\sum_{i=Q_1+1}^{M}\sum_{j=Q2+1}^{N}[Y(i,j)-\mu_Y(0)]^4}{\left(\dfrac{1}{M-Q_1}\dfrac{1}{N-Q_2}\displaystyle\sum_{i=Q_1+1}^{M}\sum_{j=Q2+1}^{N}[Y(i,j)-\mu_Y(0)]^2\right)^2}\right) \tag{3.33}$$

$$\begin{aligned}
\nabla K_\lambda(Y) \\
= 4\left(\frac{1}{\mu_Y(2)^2}\frac{1}{M-Q_1}\frac{1}{N-Q_2}\sum_{i=Q_1+1}^{M}\sum_{j=Q2+1}^{N}\eta[Y(i,j)-\mu_Y(0)]^3\right) \\
- 4\left(\frac{\mu_Y(4)}{\mu_Y(2)^3}\frac{1}{M-Q_1}\frac{1}{N-Q_2}\sum_{i=Q_1+1}^{M}\sum_{j=Q2+1}^{N}\eta[Y(i,j)-\mu_Y(0)]\right)
\end{aligned} \tag{3.34}$$

where

$$\eta = \frac{\partial}{\partial\lambda}(Y-\mu_Y(0)) = \frac{\partial}{\partial\lambda}(Y) - \frac{\partial}{\partial\lambda}(\mu_Y(0)) \tag{3.35}$$

$\frac{\partial}{\partial\lambda}(\mu_Y(0))$ is equivalent to the mean value of $\frac{\partial}{\partial\lambda}Y$ and

51

$$\frac{\partial}{\partial\lambda}Y = \frac{\partial}{\partial\lambda}\left(G\left(\frac{H^2}{H^3 + H\delta}\right)\right) = G\frac{\partial}{\partial\lambda}\left(\frac{H^2}{H^3 + H\delta}\right) \tag{3.36}$$

Through further manipulations, we get

$$\frac{\partial}{\partial\lambda}Y = G\left(\left(\frac{2H}{H^3 + H\delta}\right) + H^2\left(\frac{-(3H^2 + \delta)}{(H^3 + H\delta)^2}\right)\right)\frac{\partial}{\partial\lambda}H \tag{3.37}$$

The term $\dfrac{\partial}{\partial\lambda}H$ needs to be calculated for specific types of blur.

3.5.1. Gradient Matrix Derivation for Gaussian Blur Optical Transfer Function

The derivation for the Gaussian blurring PSF is as follows. In case of Gaussian blur, the OTF for parametric model is given by Eqn. 3.38

$$H(i,j) = \frac{1}{2\pi\sigma_F^2}e^{\left(\frac{-\left(i^2+j^2\right)}{2\sigma_F^2}\right)} \tag{3.38}$$

with the σ_F of the OTF being reciprocal to σ_f of the PSF. For simplicity σ_F will be just represented by σ in future calculations. Differentiating the OTF with respect to σ of the OTF as given in Eqns. 3.39 - 3.43, we get $\dfrac{\partial}{\partial\sigma}H$

$$\frac{\partial}{\partial\sigma}H(i,j) = \frac{\partial}{\partial\sigma}\left(\frac{1}{2\pi\sigma_F^2}e^{\left(\frac{-\left(i^2+j^2\right)}{2\sigma_F^2}\right)}\right) \tag{3.39}$$

$$\frac{\partial}{\partial\sigma}H(i,j) = \frac{-2}{2\pi\sigma^3}e^{\left(\frac{-\left(i^2+j^2\right)}{2\sigma^2}\right)} + \frac{1}{2\pi\sigma^2}\frac{\partial}{\partial\sigma}\left(e^{\left(\frac{-\left(i^2+j^2\right)}{2\sigma^2}\right)}\right) \tag{3.40}$$

$$= \frac{-2}{2\pi\sigma^3}e^{\left(\frac{-\left(i^2+j^2\right)}{2\sigma^2}\right)} + \frac{\left(i^2+j^2\right)}{2\pi\sigma^5}e^{\left(\frac{-\left(i^2+j^2\right)}{2\sigma^2}\right)} \tag{3.41}$$

$$= \frac{-2}{2\pi\sigma^3} e^{\left(\frac{-\left(i^2+j^2\right)}{2\sigma^2}\right)} + \frac{\left(i^2+j^2\right)}{2\pi\sigma^5} e^{\left(\frac{-\left(i^2+j^2\right)}{2\sigma^2}\right)} \tag{3.42}$$

$$\frac{\partial}{\partial\sigma} H(i,j) = H(i,j)\left(\frac{-2}{\sigma} + \frac{(i^2+j^2)}{\sigma^3}\right) \tag{3.43}$$

3.5.2. Gradient Matrix Derivation for Motion Blur Optical Transfer Function

The linear motion modelled here is the result of translation in the horizontal direction. In order to simplify the search for true blur parameters using the steepest descent scheme, we rotate the image until the blur can be assumed horizontal. This simplifies the case from two parameters i.e. length (L) and angle (φ) of blur. Now only the length of blur (L) needs to be optimized. The OTF for motion blur according to [87] is given by Eqn. 3.44

$$H(i,j) = \frac{1}{L+1} e^{-ki\pi L} \frac{\sin(\pi(L+1)i))}{\sin(\pi i)} \forall j \tag{3.44}$$

Differentiating the OTF with respect to the length parameter (L) of the OTF as given in Eqns. 3.45 – 3.50, we get

$$\frac{\partial}{\partial\lambda} H(i,j) = \frac{\partial}{\partial L} H(i,j) = \frac{\partial}{\partial L}\left(\frac{1}{L+1} e^{-ki\pi L} \frac{\sin(\pi(L+1)i))}{\sin(\pi i)}\right) \tag{3.45}$$

$$\begin{aligned}\frac{\partial}{\partial L} H(i,j) &= \left(e^{-ki\pi L} \frac{\sin(\pi(L+1)i))}{\sin(\pi i)}\right) \frac{\partial}{\partial L}\left(\frac{1}{L+1}\right) \\ &+ \left(\frac{1}{L+1}\right) \frac{\partial}{\partial L}\left(e^{-ki\pi L} \frac{\sin(\pi(L+1)i))}{\sin(\pi i)}\right)\end{aligned} \tag{3.46}$$

$$\begin{aligned}\frac{\partial}{\partial L} H(i,j) &= \left(e^{-ki\pi L} \frac{\sin(\pi(L+1)i))}{\sin(\pi i)}\right)(-1)\frac{1}{(L+1)^2} \\ &+ \left(\frac{1}{\sin(\pi i)}\right)\left(\frac{1}{L+1}\right)\frac{\partial}{\partial L}\left(e^{-ki\pi L} \sin(\pi(L+1)i))\right)\end{aligned} \tag{3.47}$$

$$\frac{\partial}{\partial L} H(i,j) = \frac{-1}{(L+1)^2} \left(e^{-ki\pi L} \frac{\sin(\pi(L+1)i)}{\sin(\pi i)} \right)$$
$$+ \left(\frac{\sin(\pi(L+1)i)(-ki\pi)e^{-ki\pi L} + (e^{-ki\pi L})(\pi i)\cos(\pi(L+1)i)}{(L+1)\sin(\pi i)} \right) \quad (3.48)$$

$$\frac{\partial}{\partial L} H(i,j) = \frac{-1}{(L+1)} H(i,j) - k\pi i H(i,j) + (\pi i)\cot(\pi(L+1)i)H(i,j) \quad (3.49)$$

$$\frac{\partial}{\partial L} H(i,j) = H(i,j)\left(\frac{-1}{(L+1)} - k\pi i + (\pi i)\cot(\pi(L+1)i) \right) \quad (3.50)$$

3.5.3. Gradient Matrix Derivation for Out-of-Focus Blur Optical Transfer Function

The OTF for out-of-focus blur according to [87] is given by Eqn. 3.51

$$H(i,j) = \frac{J_1(Rp)}{(Rp)}, \qquad p^2 = i^2 + j^2 \quad (3.51)$$

where J_1 is the first order Bessel function. The Bessel function can be approximated by an exponential for sufficiently large data [125].

$$H(i,j) = \frac{e^{Rp}}{\sqrt{2\pi Rp}} \quad (3.52)$$

Differentiating the OTF with respect to the radius parameter (R) of the OTF, Eqn. $3.53 - 3.57$

$$\frac{\partial}{\partial R} H(i,j) = \frac{\partial}{\partial R}\left(\frac{e^{Rp}}{\sqrt{2\pi Rp}} \right) \quad (3.53)$$

$$\frac{\partial}{\partial R} H(i,j) = e^{Rp} \frac{\partial}{\partial R}\left(\frac{1}{\sqrt{2\pi Rp}} \right) + \frac{1}{\sqrt{2\pi Rp}} \frac{\partial}{\partial R}\left(e^{Rp} \right) \quad (3.54)$$

$$\frac{\partial}{\partial R} H(i,j) = 2\pi p e^{Rp} \frac{-(1/2)}{\sqrt{2\pi Rp}} + \frac{e^{Rp}}{\sqrt{2\pi Rp}} Rp \quad (3.55)$$

$$\frac{\partial}{\partial R} H(i, j) = \frac{e^{Rp}}{\sqrt{2\pi Rp}}(-\pi p + Rp) \tag{3.56}$$

$$\frac{\partial}{\partial R} H(i, j) = H(i, j)(-\pi p + Rp) \tag{3.57}$$

The parameter of the blurring PSF model is optimized in the direction of increasing value of the absolute kurtosis till the gradient shows a flat point or the difference of kurtosis between successive iterations falls below a specified tolerance value.

A conjugate gradient algorithm may be formed by reformulation the gradient optimization iterations to achieve a much higher convergence rate [126]. Expectation-minimization based algorithms can also provide an attractive alternative to the standard gradient-based searches [127, 128].

3.5.4. **Experimental Setup for Gradient Based BID scheme**

The proposed scheme has been tested on various images degraded with different degrading functions. Experiments were conducted on both artificial and real blurred images for the three different types of blur. Several image quality measures were employed to evaluate the quality of the deblurred images. The full reference IQMs include the MSSIM index and the UQI. The blind\no-reference based IQMs used were BRISQUE and NIQE. Images from the Desktop Nexus image wallpaper database [129] were used in the experiments on the artificial blur case. The test images are shown in Appendix A in Fig. A.1. Real blurred natural images, captured by either the author or others, were used in the case of real blind image deblurring. Fig. 3.6 depicts some of the example images used in the experiments. The proposed scheme has been compared with Shan et al.'s BID scheme [39]. A brief summary of their scheme is provided in chapter 2, section 2.8.

3.5.5. **Deblurring Results for Artificially Blurred Images**

The estimated PSF parameters and comparisons of different quality measures for Gaussian deblurring using the proposed BID scheme are given in Table 3.1. As it can be seen that the estimated values of Gaussian blur width parameter (σ) are closer to its original values. For MSSIM and UQI a higher value is desirable, whereas for BRISQUE and NIQE a lower value indicates improvement in the image quality as explained earlier in Chapter 2. The proposed BID scheme shows higher MSSIM value which shows an improvement in the quality of the deblurred image as

compared to the original blurred image. The same behaviour is validated by higher values of UQI and lower values of BRISQUE and NIQE. Fig. 3.5 shows some examples of the restoration of Gaussian blurred images using the proposed BID scheme.

Table 3.1. True PSF parameter estimation for Gaussian blurred images and quantitative comparison of the deblurred image using MSSIM, UQI, BRISQUE and NIQE quality measures.

Image	Original Sigma	Estimated Sigma	MSSIM		UQI		BRISQUE		NIQE	
			Blurred	Proposed Scheme	Blurred	Proposed Scheme	Blurred	Proposed Scheme	Blurred	Proposed Scheme
Img-01	1.63	1.85	0.85	0.90	0.99	0.99	56.69	18.28	7.28	8.40
Img-02	4.98	4.76	0.73	0.81	0.95	0.97	77.15	70.69	10.84	7.97
Img-03	5.13	5.26	0.62	0.68	0.94	0.96	79.32	73.12	11.85	9.05
Img-04	3.88	4.05	0.78	0.86	0.97	0.98	72.87	55.30	10.64	7.65
Img-05	0.71	0.68	0.88	0.95	0.99	1.00	25.45	19.06	3.80	3.88
Img-06	0.94	1.21	0.97	0.88	1.00	1.00	52.71	38.15	7.00	7.21
Img-07	2.07	2.18	0.52	0.74	0.94	0.97	61.24	40.69	7.40	7.76
Img-08	2.63	2.50	0.69	0.80	0.95	0.97	67.06	34.43	9.10	6.99
Img-09	3.45	3.32	0.67	0.76	0.97	0.98	67.54	54.20	10.28	6.86
Img-10	2.44	2.24	0.75	0.86	0.97	0.98	64.76	36.55	8.56	6.45
Img-11	1.64	1.82	0.75	0.88	0.98	0.99	54.33	26.65	6.56	6.59
Img-12	0.98	0.99	0.93	0.94	0.99	1.00	47.88	11.99	5.48	3.85
Img-13	1.38	1.53	0.89	0.96	0.99	0.99	45.66	24.88	6.66	5.94
Img-14	3.13	3.26	0.62	0.80	0.93	0.97	72.01	49.99	9.79	6.85
Img-15	4.18	4.13	0.79	0.81	0.97	0.98	80.98	58.73	10.61	8.11
Img-16	5.47	5.39	0.45	0.55	0.93	0.95	82.44	70.65	10.77	9.02
Mean			0.75	0.82	0.97	0.98	63.00	42.71	8.54	7.04
Variance			1.985E-02	1.069E-02	5.239E-04	1.956E-04	2.218E+02	3.685E+02	4.962E+00	2.172E+00
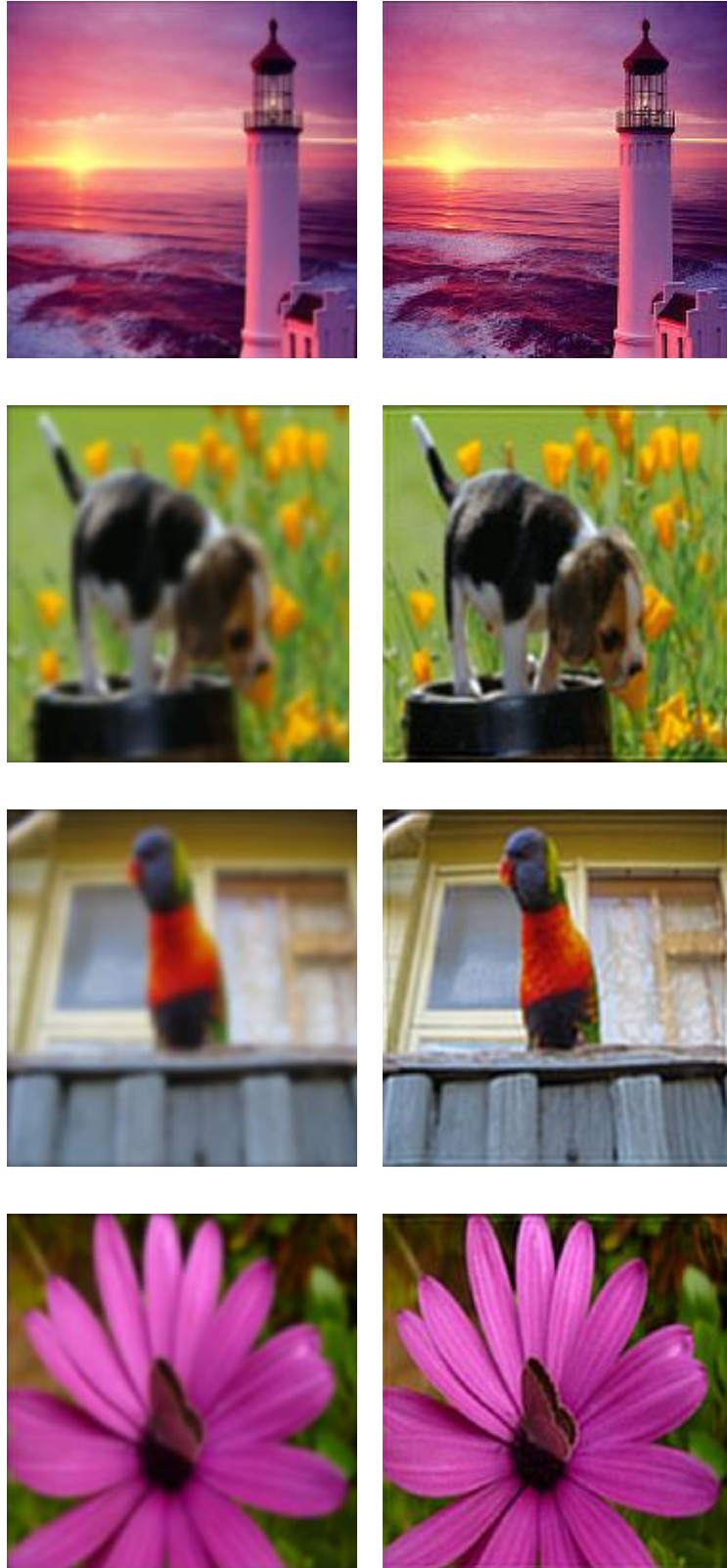
Fig. 3.5 (left) Gaussian blurred images and (right) their respective pristine image estimates using the proposed gradient based BID scheme.

Table 3.2 summarizes the results for out-of-focus deblurring along with the comparison of different image quality measures. Estimated values of out-of-focus blur radius parameter are in the near vicinity of original blurring parameter values. The proposed BID scheme shows higher MSSIM value which depicts the proposed BID scheme results in better quality deblurred images as compared to the blurred images with lower MSSIM values. The same behaviour is validated by higher values of UQI and lower values of BRISQUE and NIQE. Fig. 3.6 shows some examples of out-of-focus blurred images and their respective deblurred counterparts using the proposed scheme.

Table 3.2. True PSF parameter estimation for out-of-focus blurred images and quantitative comparison of the deblurred image using MSSIM, UQI, BRISQUE and NIQE quality measures.

Image	Original Radius	Estimated Radius	MSSIM		UQI		BRISQUE		NIQE	
			Blurred	Proposed Scheme	Blurred	Proposed Scheme	Blurred	Proposed Scheme	Blurred	Proposed Scheme
Img-01	7.00	6.84	0.70	0.81	0.96	0.98	69.52	27.22	10.24	4.32
Img-02	8.85	9.20	0.70	0.76	0.94	0.97	76.69	44.17	10.42	5.34
Img-03	10.00	9.40	0.59	0.70	0.93	0.95	77.68	39.09	11.99	4.97
Img-04	11.50	11.47	0.69	0.84	0.93	0.97	76.05	32.21	12.35	5.55
Img-05	1.00	0.74	0.95	0.97	1.00	1.00	22.08	12.82	3.29	2.70
Img-06	2.50	2.46	0.97	0.93	1.00	1.00	60.49	14.96	8.15	5.54
Img-07	4.00	3.91	0.48	0.83	0.93	0.98	57.52	10.78	6.92	3.77
Img-08	5.50	4.72	0.64	0.59	0.94	0.94	68.54	29.01	9.56	5.19
Img-09	13.00	12.58	0.63	0.68	0.96	0.97	67.17	39.76	10.84	4.61
Img-10	14.50	14.14	0.63	0.61	0.93	0.95	73.93	45.10	12.12	5.31
Img-11	16.00	15.27	0.51	0.58	0.93	0.95	76.35	43.96	11.36	5.20
Img-12	17.50	18.74	0.73	0.79	0.96	0.98	77.13	37.51	11.19	4.75
Img-13	19.00	18.82	0.40	0.70	0.86	0.95	80.40	45.59	11.93	5.96
Img-14	20.50	20.03	0.42	0.65	0.82	0.93	83.63	46.97	11.43	5.83
Img-15	22.00	21.58	0.68	0.64	0.93	0.93	86.56	56.11	12.76	7.12
Img-16	23.50	22.89	0.38	0.47	0.89	0.91	84.80	57.47	11.57	7.85
Mean			0.63	0.72	0.93	0.96	71.16	36.42	10.38	5.25
Variance			2.785E-02	1.706E-02	1.928E-03	5.539E-04	2.229E+02	1.919E+02	5.614E+00	1.348E+00
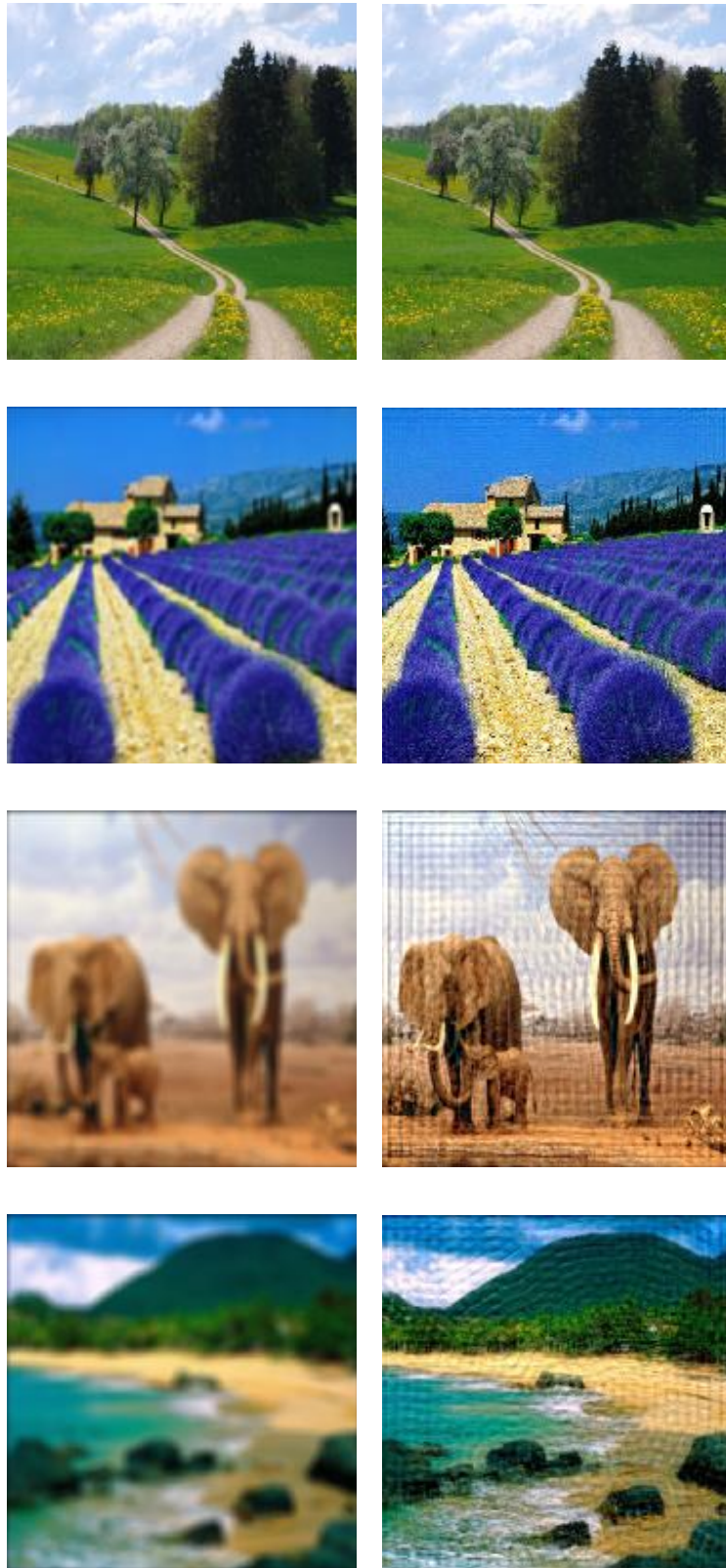
Fig. 3.6 (left) Out of focus blurred images and (right) their respective pristine image estimates using the proposed gradient based BID scheme.

Fig. 3.7 shows the deblurring result for motion blurred images. The results for motion deblurring are summarized in Table 3.3 and Table 3.4. Estimated values of motion blur length parameter are in the near vicinity of original blurring parameter values. The proposed BID scheme shows higher MSSIM value which depicts the proposed BID scheme results in better quality deblurred images as compared to the blurred images with lower MSSIM values. The same behaviour is validated by higher values of UQI and lower values of BRISQUE and NIQE. The proposed scheme in the case of motion deblurring are also compared to the BID scheme of Shan et al. [39]. Shan et al. BID scheme deals with the estimation of arbitrarily shaped motion blur PSF and deblurring of images by such PSF. The proposed BID scheme depicts higher MSSIM and UQI and lower BRISQUE and NIQE values as compared to Shan et al. BID scheme. This depicts the proposed scheme's efficiency in producing high quality deblurred images as compared to Shan et al. BID scheme. With reference to Tables 3.1-3.4, BRISQUE IQM shows an improvement of 32, 49 and 41 percent for Gaussian, motion and out-of-focus blur respectively. While NIQE IQM shows an improvement of 18, 49 and 38 percent for Gaussian, motion and out-of-focus blur respectively.

Table 3.3. True PSF parameter estimation for motion blurred images and quantitative comparison of the deblurred image using MSSIM and UQI quality measures.

Image	Original Length	Estimated Length	MSSIM			UQI		
			Blurred	Shan	Proposed Scheme	Blurred	Shan	Proposed Scheme
Img-01	7	8	0.92	0.87	0.94	0.99	0.98	0.99
Img-02	8	8	0.87	0.89	0.93	0.99	0.99	0.99
Img-03	9	9	0.76	0.81	0.89	0.98	0.98	0.99
Img-04	10	10	0.86	0.82	0.93	0.98	0.98	0.99
Img-05	11	12	0.74	0.73	0.83	0.98	0.97	0.99
Img-06	12	12	0.92	0.89	0.92	0.99	0.99	1.00
Img-07	13	13	0.54	0.62	0.81	0.93	0.93	0.97
Img-08	14	13	0.77	0.86	0.86	0.96	0.98	0.98
Img-09	15	14	0.72	0.76	0.83	0.97	0.97	0.98
Img-10	16	15	0.73	0.79	0.83	0.96	0.97	0.97
Img-11	17	17	0.57	0.53	0.80	0.94	0.94	0.98
Img-12	18	19	0.78	0.77	0.83	0.97	0.97	0.99
Img-13	19	19	0.51	0.72	0.81	0.92	0.96	0.98
Img-14	20	21	0.55	0.67	0.77	0.89	0.95	0.97
Img-15	21	21	0.75	0.68	0.59	0.97	0.96	0.96
Img-16	22	24	0.50	0.55	0.67	0.93	0.93	0.96
Mean			0.72	0.75	0.83	0.96	0.97	0.98
Variance			1.923E-02	1.216E-02	8.268E-03	7.672E-04	3.581E-04	1.123E-04

Table 3.4. True PSF parameter estimation for motion blurred images and quantitative comparison of the deblurred image using BRISQUE and NIQE quality measures.

Image	Original Length	Estimated Length	BRISQUE			NIQE		
			Blurred	Shan	Proposed Scheme	Blurred	Shan	Proposed Scheme
Img-01	7	8	34.76	24.06	33.44	6.36	5.66	5.99
Img-02	8	8	64.96	36.54	30.68	7.06	5.15	3.91
Img-03	9	9	56.47	42.72	27.88	6.48	5.26	4.22
Img-04	10	10	65.95	38.15	21.61	8.99	5.66	4.38
Img-05	11	12	52.71	44.81	16.76	8.39	5.92	4.31
Img-06	12	12	67.19	21.62	30.10	9.37	6.35	4.47
Img-07	13	13	39.98	24.53	8.27	7.17	7.69	5.63
Img-08	14	13	39.23	35.90	26.18	7.28	8.69	6.29
Img-09	15	14	27.37	26.92	18.34	7.15	5.48	4.77
Img-10	16	15	26.16	24.41	25.42	7.26	4.84	4.84
Img-11	17	17	13.19	53.31	26.65	7.94	6.07	3.84
Img-12	18	19	27.51	26.16	28.34	9.07	5.33	3.99
Img-13	19	19	26.61	46.49	38.10	9.24	6.06	4.45
Img-14	20	21	25.01	45.83	34.55	8.10	5.23	4.31
Img-15	21	21	58.33	55.45	27.37	8.40	6.49	5.46
Img-16	22	24	49.09	45.29	44.78	6.07	5.92	5.62
Mean			42.16	37.01	27.40	7.77	5.99	4.78
Variance			2.794E+02	1.173E+02	7.024E+01	1.068E+00	9.149E-01	5.616E-01

Fig. 3.7 (left) Motion blurred images and (right) their respective pristine image estimates using the proposed gradient based BID scheme.

3.5.6. Deblurring Results for Real Blurred Images

The proposed deblurring scheme has also been performed on real images with motion blur, a typical problem facing amateur photographers, as well as atmospheric turbulence blur, a typical degradation in remote sensing. The deblurred images using the proposed scheme have been compared with pristine image estimates using the blind deconvolution scheme by Shan et al. in [39].

(a)   (b)

(c)
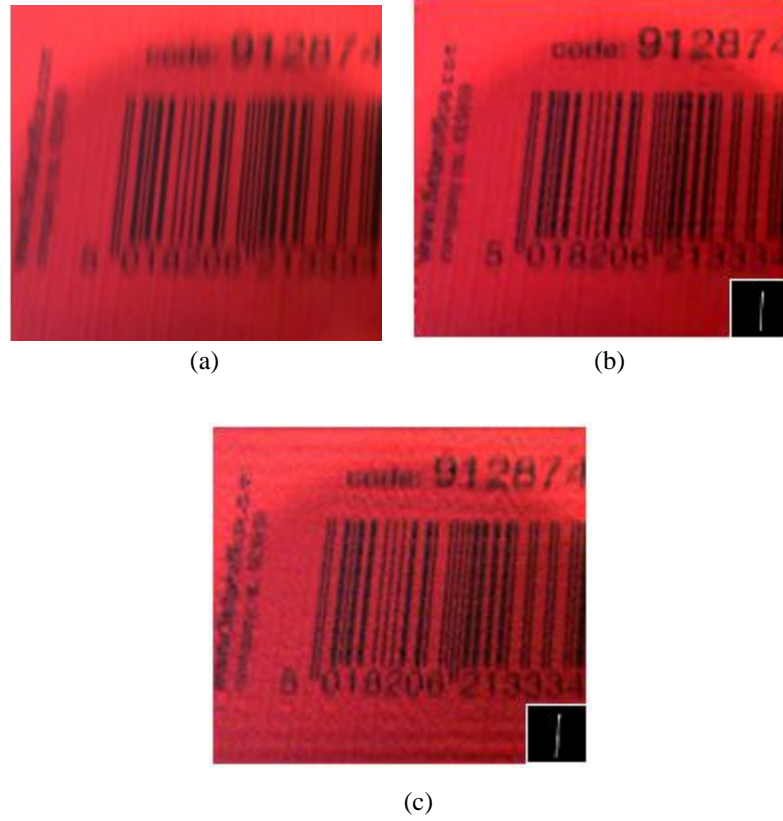
Fig. 3.8 (a) Real motion blurred LABEL image (b) Deblurred using the proposed BID scheme (c) Deblurred using Shan et al. BID scheme

In the first case, a video was captured by a low quality camera. A blurred image frame, depicted in Fig. 3.8 (a), shows an approximate vertical motion blur with the small numbers at the bottom becoming unreadable. The blurred image contains a certain amount of noise due to poor lighting, one of the most difficult issues in deblurring. Fig. 3.8(b) shows the deblurred image estimate using the proposed scheme with the estimated blur kernel visible. Fig. 3.8(c) shows the deblurred image and the corresponding PSF estimated using the blind deconvolution scheme by Shan et al. The image in Fig. 3.8(c) seems to have recovered well; however, the text on the left is still unreadable since the PSF estimate using this scheme does not completely follow a uniform motion blur. Using the proposed scheme, a uniform motion PSF of length 21 pixels and angle zero degree was estimated. In Fig. 3.8(b), the digits in the

deblurred image have become clear and easily readable. MATLAB's *edgetaper* function was used to reduce the ringing effect caused, by using the discrete Fourier Transform.

Fig. 3.9 and Fig. 3.10 show the deblurring of motion blurred images resulting from object movement and camera handshake, respectively. The motion blur is almost linear at a certain angle. The images seem to have recovered well.

(a)

(b)

(c)

Fig. 3.9 (a) Real motion blurred MATLAB_BOOK image (b) Deblurred using the proposed BID scheme (c) Deblurred using Shan et al. BID scheme.

(a)

(b)

(c)

Fig. 3.10 (a) Real motion blurred BUILDINGS image (b) Deblurred using the proposed BID scheme (c) Deblurred using Shan et al. BID scheme.

Another motion blurred image taken by an ordinary digital camera along with its deblurred versions is shown in Fig. 3.11. Fig. 3.11(b) shows the pristine image estimate using the proposed scheme with the corresponding estimated PSF. Fig. 3.11(c) shows the deblurred image and the corresponding PSF estimated using the blind deconvolution scheme by Shan et al. The image seems to have recovered well, with the main and sub-title text of the book more readable for our proposed scheme. However, some ringing is present for the deblurred image in Fig. 3.11(b) as ringing reduction apart from edge-taping is not utilized because it affects the image sharpness and statistics which in turn affect the IQM.

(a)
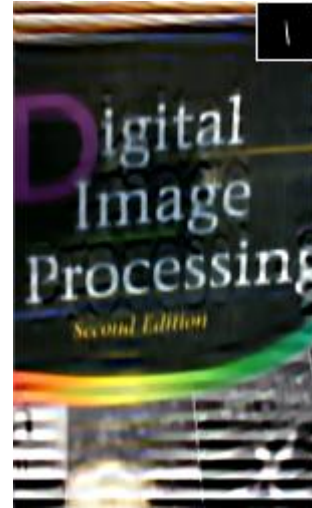
(b)
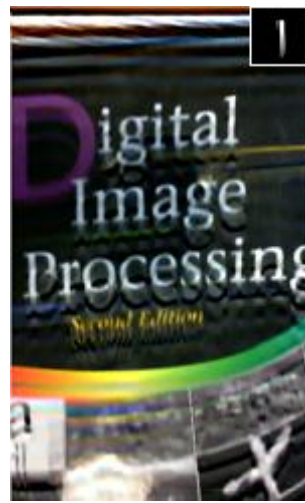
(c)

Fig. 3.11 (a) Real motion blurred DIP_BOOK image (b) Deblurred using the proposed BID scheme (c) Deblurred using Shan et al. BID scheme.

Table 3.5 shows the deblurring results for real life motion blurred images using the proposed BID scheme. Quality of the deblurred images is compared using BRISQUE and NIQE IQMs of proposed BID scheme with Shan et al. BID scheme. A low value of BRISQUE and NIQE shows a better quality image. For the LABEL image, both the proposed scheme and Shan et al. scheme shows improvement in the quality of image after deblurring. For the DIP_BOOK and MATLAB_BOOK image, both the schemes fail to estimate the blur correctly. This is depicted by high values of BRISQUE for the two schemes as compared to that of the original blurred image. For the BUILDINGS image, the proposed scheme depicts a better quality deblurred image as compared to Shan et al. BID scheme and an overall improvement as compared to the original image.

The proposed scheme shows better quality for LABEL image depicted by NIQE as compared to Shan et al. BID scheme. NIQE values for the deblurred images of Shan et al. BID scheme are relatively lower as compared to the proposed BID scheme for DIP_BOOK, MATLAB_BOOK and BUILDINGS image. This depicts better image quality but in the case of DIP_BOOK NIQE value is more for the deblurred image than the original image which shows the deblurred image deteriorates. However, visual inspection of the deblurred images of Shan et al. scheme are compromised by ringing artefacts resulting from errors in kernel estimation. It can be concluded that, although BRISQUE and NIQE are a true representation of the deblurred image quality, they are independent of the ringing artefacts occurring in the deblurred images.

Table 3.5 Quantitative comparison of pristine image estimates for real motion blurred images using BRISQUE and NIQE quality measures

Image	BRISQUE			
	Original	Manual	Shan	Proposed Scheme
LABEL	56.080	27.350	52.000	54.070
DIP_BOOK	29.770	17.780	40.210	45.680
MATLAB_BOOK	5.480	15.490	28.840	48.550
BUILDINGS	39.850	25.960	41.170	39.580

Image	NIQE			
	Original	Manual	Shan	Proposed Scheme
LABEL	7.110	6.230	8.100	7.680
DIP_BOOK	5.780	4.530	6.310	6.510
MATLAB_BOOK	5.760	5.530	4.070	6.310
BUILDINGS	7.010	5.440	6.410	6.850

3.6. Proposed Spectral Kurtosis Based BID Scheme Using Genetic Algorithm Optimization

The proposed scheme is an extension of a previous blind image deconvolution approach using ICA and GA [115] but operates in the frequency domain. The estimated (deblurred) image is obtained using a Wiener filter as the deblurring filter. The spectral kurtosis based fitness function is used in the GA to find the blur parameters in an iterative manner. As the spectral kurtosis is calculated in the frequency domain, it limits the need to transform the signal backward and forward between the spatial and spectral domains during each iteration. This greatly improves

the efficiency of the algorithm, especially when multiple PSF parameters are simultaneously searched.

Fig. 3.12 depicts the schematic diagram of the proposed spectral non-Gaussianity based deblurring scheme. The PSF parameter estimation block updates the candidate PSF's parameters for increasing spectral non-Gaussianity until no more improvement is possible. The deblurring block of the algorithm then deblurs the image with the candidate PSF using a suitable restoration filter such as Wiener or Richardson-Lucy.

The BID scheme is summarized as follows.

- Initialize the GA parameters i.e. population, size, crossover rate, mutation rate etc. Initial population consists of chromosomes represented in binary encoding.
- Perform an iteration and for different values of optimizing parameter (e.g. sigma in case of Gaussian blur, theta in case of motion blur etc); find the restored image through inverse/Wiener filtering in the spectral domain and calculate its spectral kurtosis (i.e. the fitness function) for different population samples.
- Generate the child population for the next iteration by evolving from the parents on the basis of the fitness function in subsequent iterations (generations), through mutations and crossover.
- Repeat the process again till the algorithm converges for the deblurring measure.

For estimating motion blur parameters, 11-bit chromosomes were used to search the angle from 0 to 180 degrees. The blur angles from 180 to 360 are similar to blur angles 0 to 180 and can be estimated using the 11-bit chromosome. The radius of out-of-focus PSF was approximated by 8-bit chromosomes in the range of 0 to 31 pixels. It was noted empirically that out-of-focus blur with radius above 23 pixels causes severe blurring and a lot of information is lost. The parameters (variance, angle and radius) were approximated to the precision of 0.125. In all cases, the population size was set to 100, while up to 3 bits of the chromosomes were randomly mutated every iteration.
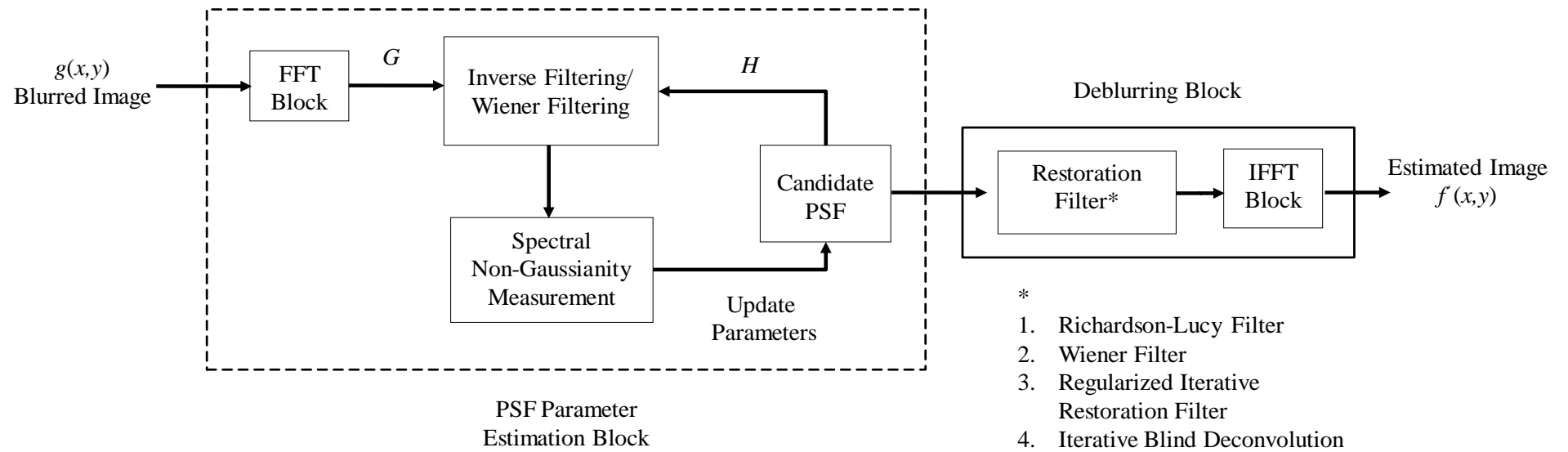
Fig. 3.12 Schematic diagram of the spectral non-Gaussianity based deblurring scheme.

In the diagram:

$g(x,y)$ Blurred Image → FFT Block → G → Inverse Filtering/Wiener Filtering

H → Inverse Filtering/Wiener Filtering

Inverse Filtering/Wiener Filtering → Spectral Non-Gaussianity Measurement → Update Parameters → Candidate PSF → H

Candidate PSF → Deblurring Block → Restoration Filter* → IFFT Block → Estimated Image $f(x,y)$

PSF Parameter Estimation Block

Deblurring Block

*
1. Richardson-Lucy Filter
2. Wiener Filter
3. Regularized Iterative Restoration Filter
4. Iterative Blind Deconvolution

Selection, crossover and mutation are performed as "pseudo-random" walk through search space. Search space is defined by all possible encodings of solutions. Crossover includes combining two individuals to create new individuals for possible inclusion in next generation. Each crossover is performed with probability p_c {0.5,…,0.8} and cross over points are selected at random. Mutation involves modification of components of the individual chromosomes with probability p_m. p_m is usually a small number usually assumed in the range of {0.001,….,.0.01}. Roulette wheel selection is used to select the best fitting individuals among the population. The proposed scheme is easy to implement and often only few parameters need to be searched or optimized, e.g. variance in the case of Gaussian blur, angle and length of PSF in the case of motion blur, while radius in the case of out-of-focus blur. Apart from the GA based algorithm, other optimization procedures can also be used in the BID scheme to efficiently seek for the PSF parameters.

3.6.1. Experimental Setup for GA based BID Scheme

The proposed scheme has been tested on various images degraded with different degrading functions. Common blurring kernels or PSFs are Gaussian or atmospheric turbulence, motion and out-of-focus [57, 115].

In the artificial deblurring case, the images were blurred without the presence of noise, while the real blurred images had a low level of noise present. In case of Gaussian PSF estimation, 6-bit chromosomes were used in the GA to represent and approximate the blur width within values of 0.5 to 5.5. Below 0.6 variance value, the spatial and spectral kurtosis values do not change much suggesting that the image has almost no blur effect. Above 5.5 variance value, the image is too blurred and does not recover well even if true PSF value is input. For estimating motion blur parameters, 11-bit chromosomes were used to search the angle from 0 to 180 degrees. The blur angles from 180 to 360 are similar to blur angles 0 to 180 and can be estimated using the 11-bit chromosome. The radius of out-of-focus PSF was approximated by 8-bit chromosomes in the range of 0 to 31 pixels. It was noted empirically that out-of-focus blur with radius above 23 pixels causes severe blurring and a lot of information is lost. The parameters (variance, angle and radius) were approximated to the precision of 0.125. In all cases, the population size was set to 100, while up to 3 bits of the chromosomes were randomly mutated every iteration.

3.6.2. Restoration of Gaussian Blurred Images

The 2-D Gaussian PSF for PSF pixel coordinates *(m,n)* is given by,

$$g(m,n) = \frac{1}{2\pi\sigma^2} e\left(\frac{-(m^2+n^2)}{2\sigma^2}\right) \tag{3.58}$$

where σ is the width of the blurring kernel. Fig. 3.13 shows the restoration of Gaussian blurred Peppers image using spectral kurtosis. Fig. 3.14 displays the spatial and spectral kurtosis curves. Both non-Gaussianity curves optimize around the true variance of 2.8. Estimated PSF parameters, the PSNR values and comparison with various methods are given in Table 3.6. Estimated values for the Gaussian blur parameter, variance, are in the near vicinity of the true values. Once the parameter has been estimated, different restoration filters were used to assess their deblurring quality. The PSNR values show that the proposed BID scheme, with the highest PSNR values, in conjunction with the Wiener filter produce deblurred images with the highest deblurring quality. MATLAB based BID scheme is second in order of deblurred image quality however this scheme requires an initial PSF estimation and cannot be regarded as totally blind.

(a)   (b)
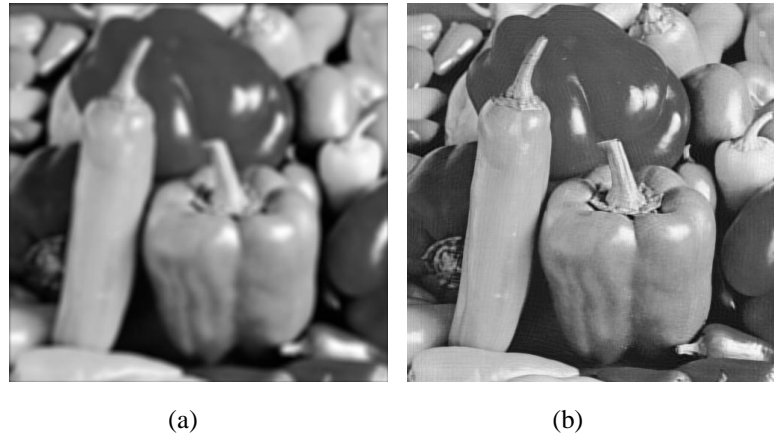
Fig. 3.13 (a) Gaussian blurred Peppers image (b) Deblurred image using spectral kurtosis based scheme.

(a)   (b)
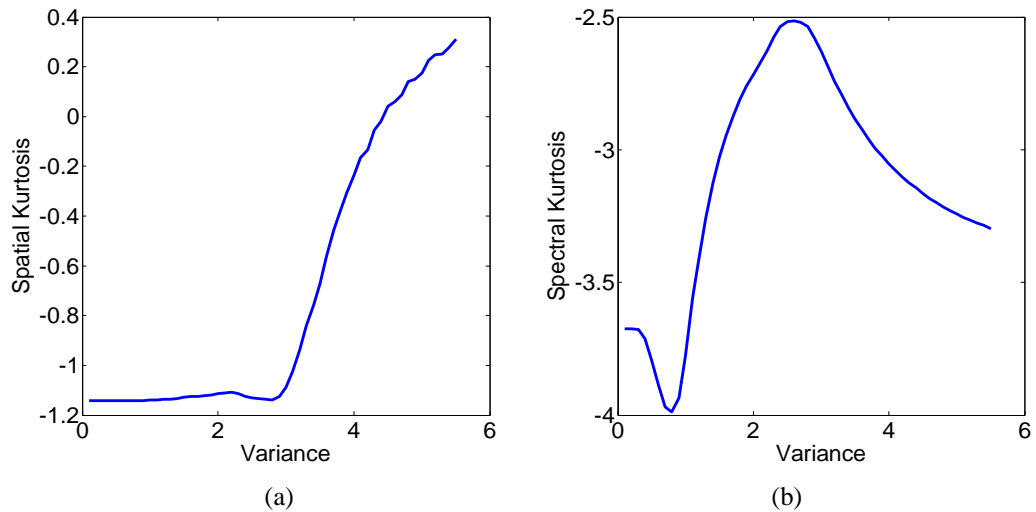
Fig. 3.14 (a) Spatial kurtosis (b) Spectral kurtosis plot for Gaussian blurred Peppers image.

71

Table 3.6 Parameter estimation for Gaussian blurred images and PSNR of various deblurring methods.

Image	Original Variance	Estimated Variance	PSNR (dB)				
			Blurred	Regularized Filtering	Richardson-Lucy Filter	MATLAB Blind Deconvolution	Proposed scheme with Wiener Filter
Barbara	2.3	2.35	22.25	26.13	24.22	24.22	26.55
Washsat	1.2	1.10	13.68	19.84	21.25	21.26	19.79
Boat	3.9	3.88	24.46	26.64	24.68	24.69	28.07
Cameraman	2.9	2.97	21.94	24.51	25.73	25.73	25.84
Goldhill	3.5	3.75	22.88	23.09	23.66	23.66	24.08
Lena	4.2	4.23	23.54	26.33	27.03	27.04	27.72
Mandrill	5.3	5.35	19.66	24.07	20.81	20.81	25.02
Peppers	2.8	2.70	27.92	26.20	26.42	26.42	29.18

Fig. 3.14(b) shows an important point to observe regarding the Gaussian blur based non-Gaussianity analysis. The graph depicts a non-Gaussian behaviour in the early stages of blurring (up to 0.5 PSF variance) before the image starts to become more Gaussian as a result of further blurring. This is due to the finite PSF matrix which for small variances (usually from 0.1 up to .9) has unnecessary zero elements that during convolution result in smaller values than the expected average value. This in turn affects the image statistics.

3.6.3. **Restoration of Motion Blurred Images**

Fig. 3.15 shows a motion blurred Cameraman image and its deblurred result using the proposed method. The image was blurred with motion blur at an angle of 47 degrees. The motion blur for PSF pixel coordinates *(m,n)* is described by [57, 115],

$$h(m,n;L,\varphi) = \begin{cases} \dfrac{1}{L} & \text{if } \sqrt{m^2+n^2} \leq \dfrac{L}{2} \text{ and } \dfrac{m}{n} = -\tan\varphi \\ 0 & \text{elsewhere} \end{cases} \qquad (3.59)$$

The true parameters were identified using the proposed scheme. In this case both the length of the blur and angle were estimated correctly. Fig. 3.16 depicts the spatial and spectral kurtosis curves. Both curves optimize near the angle of 47 degrees, correctly identifying the motion blur PSF parameter.
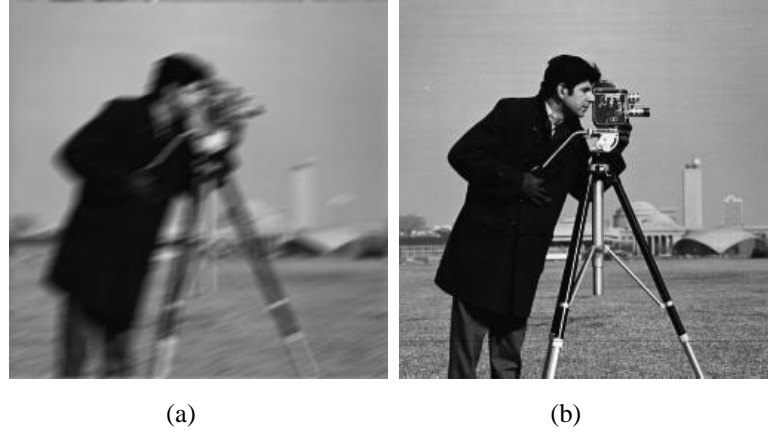
Fig. 3.15 (a) Motion blurred Cameraman image (b) Deblurred image using the spectral kurtosis based scheme.
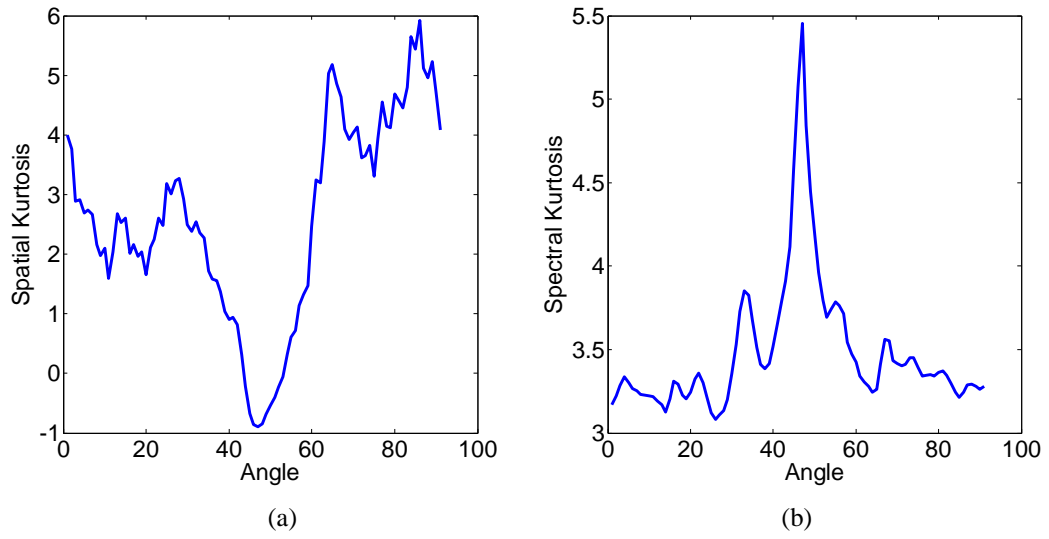
Fig. 3.16 (a) Spatial kurtosis (b) Spectral kurtosis plot for motion blurred Cameraman image.

Table 3.7 presents the estimated parameters and the PSNR values of the motion blurred and deblurred images. Estimated values for motion blur angle parameter, theta, are in the near vicinity of the true values. Once the parameter has been estimated, different restoration filters were used to assess their deblurring quality. The PSNR values show that the proposed BID scheme, with the highest PSNR values, in conjunction with the Wiener filter produce deblurred images with the highest deblurring quality. MATLAB based BID scheme is second in order of deblurred image quality however this scheme requires an initial PSF estimation and cannot be regarded as totally blind.

Image	Original Theta	Estimated Theta	PSNR (dB)				
			Blurred	Regularized Filtering	Richardson-Lucy Filter	MATLAB Blind Deconvolution	Proposed Scheme with Wiener Filter
Barbara	32.35	32.48	18.72	21.56	22.06	22.06	23.12
Washsat	63.13	63.13	19.16	20.75	23.63	23.55	24.12
Boat	123.21	123.63	18.92	21.28	22.03	22.03	23.23
Cameraman	47.45	47.38	15.29	19.53	20.87	20.90	20.88
Goldhill	11.19	11.25	19.20	19.66	20.25	20.34	20.45
Lena	111.21	110.38	19.74	21.37	22.08	21.97	22.17
Mandrill	175.67	175.13	17.14	18.99	19.86	19.75	21.98
Peppers	85.36	85.50	18.43	23.35	21.97	21.97	23.87

3.6.4. **Restoration of Out-of-Focus Blurred Images**

Fig. 3.17 presents the out-of-focus Barbara image and its restoration using the spectral kurtosis scheme. The spatially continuous out-of-focus blur of radius R is given by,

$$h(m,n;R) = \begin{cases} \dfrac{1}{C\pi R^2} & \text{if} \ \ \sqrt{m^2+n^2} \leq R^2 \\ 0 & \text{elsewhere} \end{cases} \tag{3.60}$$

where C is a constant that conserves the PSF energy. The Barbara image was blurred with blur radius of 12.3 pixels. Both non-Gaussianity curves optimize at the true blur radius. Fig. 3.18 shows the spatial and spectral kurtosis curves for the deblurring processes. Table 3.8 summarizes the results for the out-of-focus blur restoration.

(a)   (b)
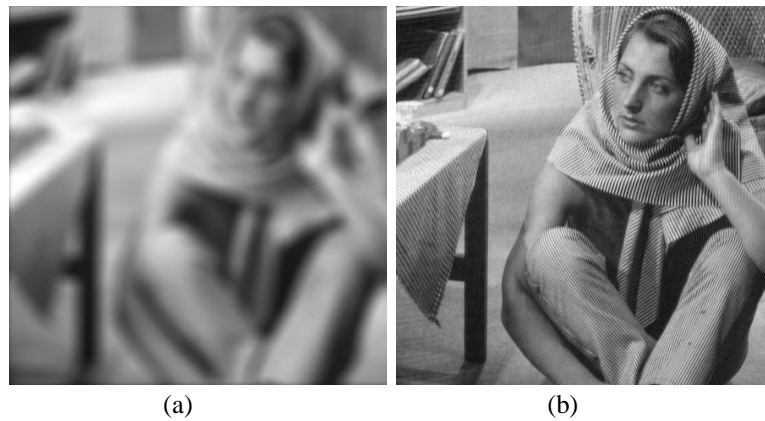
Fig. 3.17 (a) Out-of-focus blurred Barbara image (b) Deblurred image using the spectral kurtosis based scheme.

74
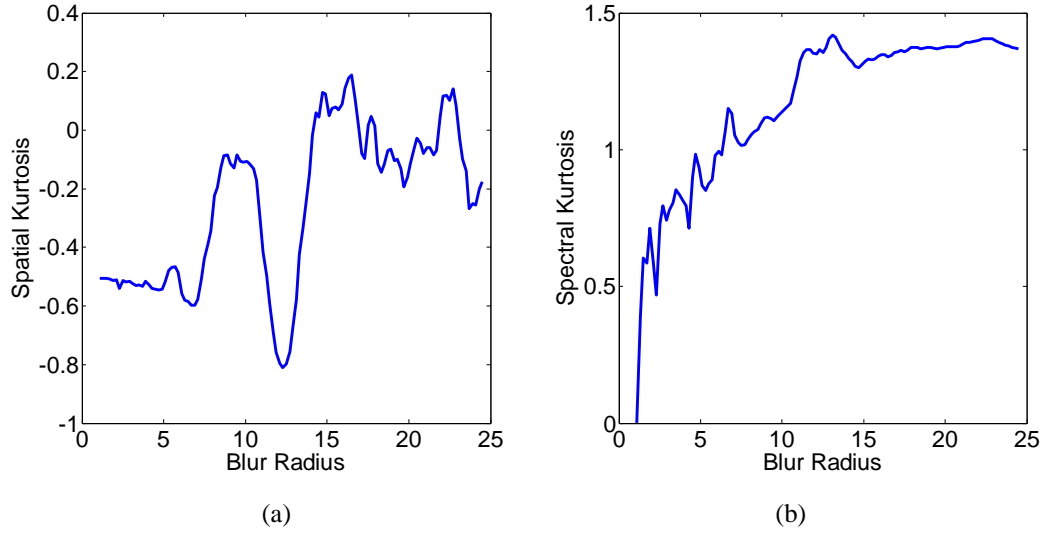
Fig. 3.18 (a) Spatial kurtosis (b) Spectral kurtosis plot for out-of-focus blurred Barbara image.

Detailed results for artificial deblurring of the three blurring types can be found in Appendix A. Images from the Desktop Nexus image database were used in the experiments and full reference quality measures, PSNR, MSSIM, UQI and non-reference image quality measures BRISQUE and NIQE, were used to evaluate the quality of the deblurred image.

Table 3.8 presents the estimated parameters and the PSNR values of the out-of-focus blurred and deblurred images. Estimated values for out-of-focus blur radius are in the near vicinity of the true values. Once the parameter has been estimated, different restoration filters were used to assess their deblurring quality. The PSNR values show that the proposed BID scheme, with the highest PSNR values, in conjunction with the Wiener filter produce deblurred images with the highest deblurring quality. MATLAB based BID scheme is second in order of deblurred image quality however this scheme requires an initial PSF estimation and cannot be regarded as totally blind.

Table 3.8: Parameter estimation for out-of-focus blurred images and PSNR of various deblurring methods.

Image	Original Radius	Estimated Radius	PSNR (dB)				
			Blurred	Regularized Filtering	Richardson-Lucy Filter	MATLAB Blind Deconvolution	Proposed Scheme with Wiener Filter
Barbara	12.35	12.25	18.07	16.48	20.17	20.20	20.81
Washsat	9.71	9.75	6.50	11.12	12.40	12.41	11.45
Boat	15.10	15.13	17.78	18.53	19.26	19.34	20.79
Cameraman	17.45	17.38	13.64	14.25	17.10	16.99	17.02
Goldhill	22.25	21.50	14.94	13.53	15.54	15.67	16.10
Lena	17.30	17.25	15.97	14.80	17.70	17.73	18.74
Mandrill	19.70	19.75	16.05	15.77	15.75	15.76	17.45
Peppers	27.79	27.75	15.85	12.78	16.40	16.40	16.77

3.6.5. Deblurring Results for Real Blurred Images

The proposed deblurring scheme has also been tested on several real images. The two blurring cases studied here include motion blur, a typical problem faced by amateur photographers, as well as atmospheric turbulence blur, a typical degradation in remote sensing.

In the first case of motion deblurring, a video was captured by a low quality camera. A blurred image frame, depicted in Fig. 3.19 (a), shows an approximate vertical motion blur with the small numbers at the bottom becoming almost unreadable. The blurred image also contains certain amounts of noise due to poor lighting which is one of the most difficult issues in deblurring.

Parameters were approximated by using a Wiener filter as the base for calculating both spatial and spectral non-Gaussianity values. Different restoration algorithms were compared for restoration quality. Fig. 3.19 (b) to (d) show the restoration results of different filters such as regularized, Wiener and Richardson-Lucy. The digits appear much more readable.

(a)   (b)

(c)   (d)
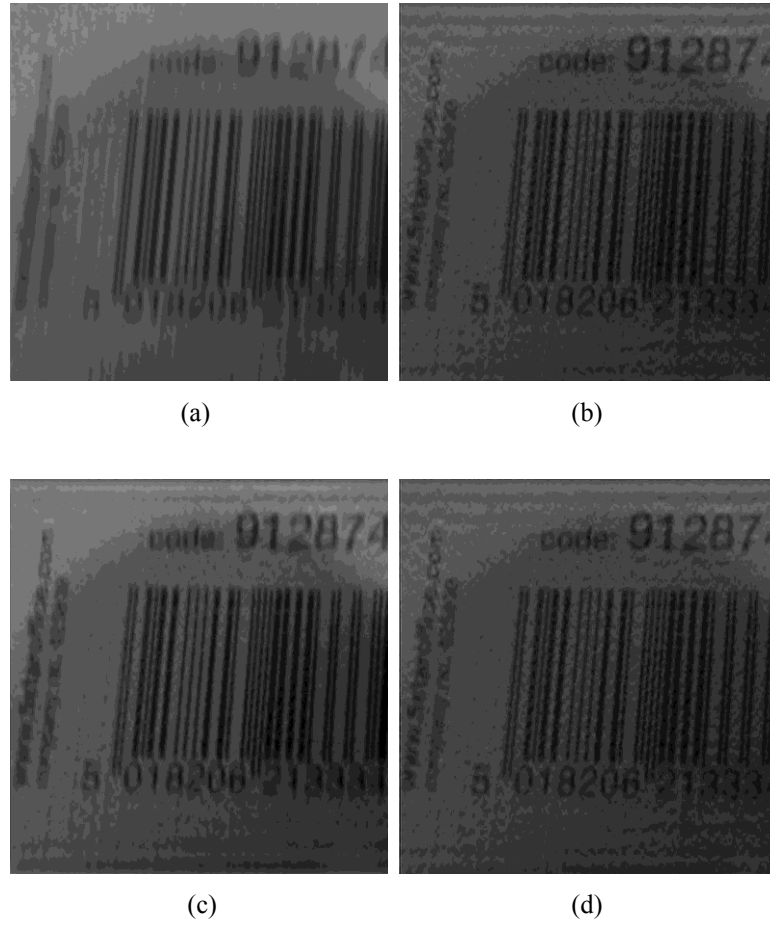
Fig. 3.19 (a) Blurred image, (b) Deblurred using the proposed scheme with the regularized filter, (c) with the Wiener filter, (d) with the Richardson-Lucy.

Fig. 3.20 (a) and (b) shows the spatial and spectral kurtosis plots vs. different angle values and PSF lengths. Results for three different PSF lengths are shown. The minimum kurtosis value in case of the spatial kurtosis measure was approximated as 85 degree and length of 30 pixels. In case of spectral kurtosis, the blur angle was approximated as 84.75 degree with a PSF length of 30 pixels at the point of maximum spectral kurtosis.
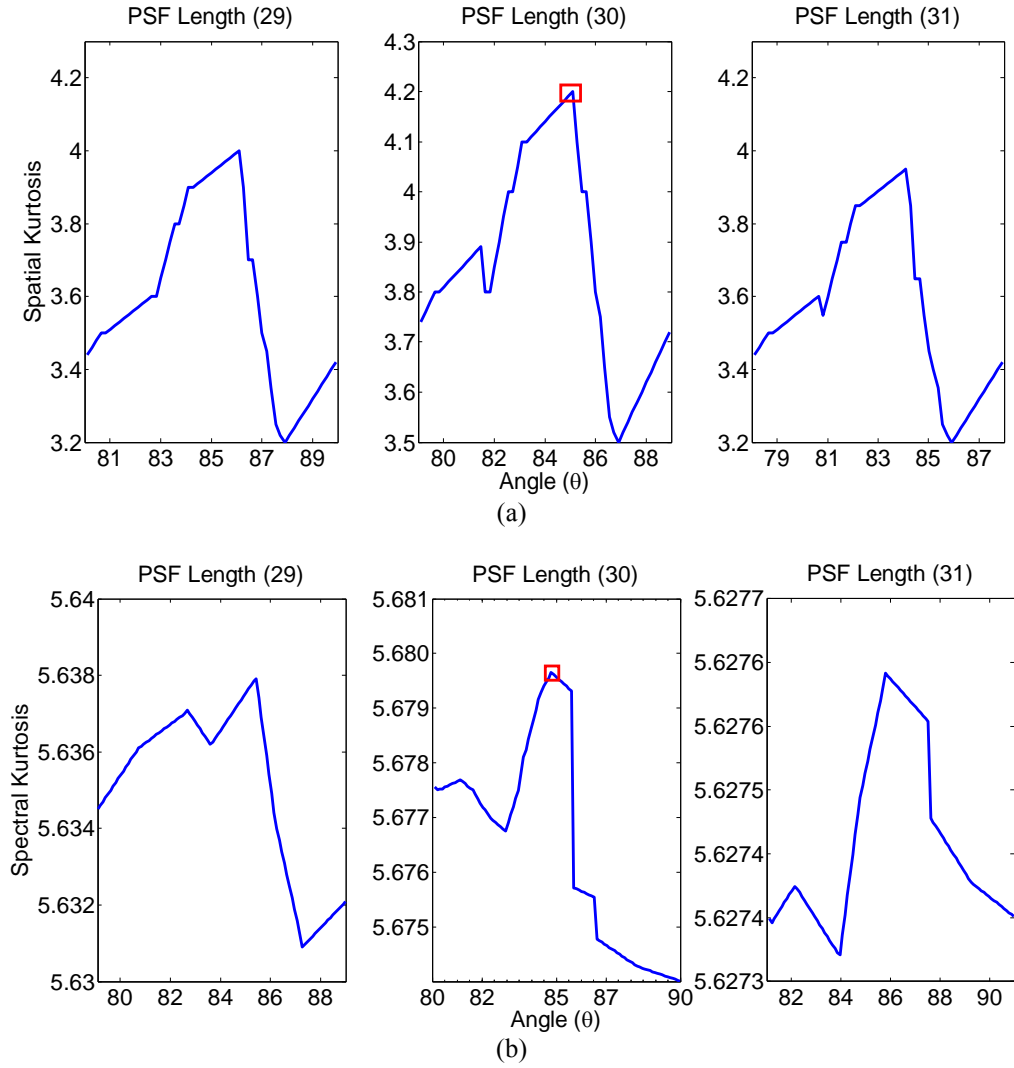
Fig. 3.20 (a) Spatial kurtosis curves with maximum value of 4.21 for PSF length of 30 pixels, (b) Spectral kurtosis curves with maximum value of 5.6797 for PSF length of 30 pixels.

Another motion blurred image taken by an ordinary digital camera and its deblurred version are shown in Fig. 3.21. Fig. 3.21(b) shows the deblurred image and the corresponding PSF (rescaled) estimated using the blind deconvolution scheme by Shan et al. in [39] . The image seems to have recovered well; however, the title of the book is still unreadable since the PSF estimated using this scheme does not completely follow a uniform motion blur. In the case of spectral kurtosis based deconvolution a uniform motion PSF of length 21 pixels and angle zero degree was estimated. In Fig. 3.21 (c), the text in the deblurred image becomes clear and easily readable. MATLAB's *edgetaper* function was used to reduce the ringing effect caused by using the discrete Fourier Transform. Fig. 3.21 (d) shows the ringing effect if edgetaping is not used for the proposed scheme.
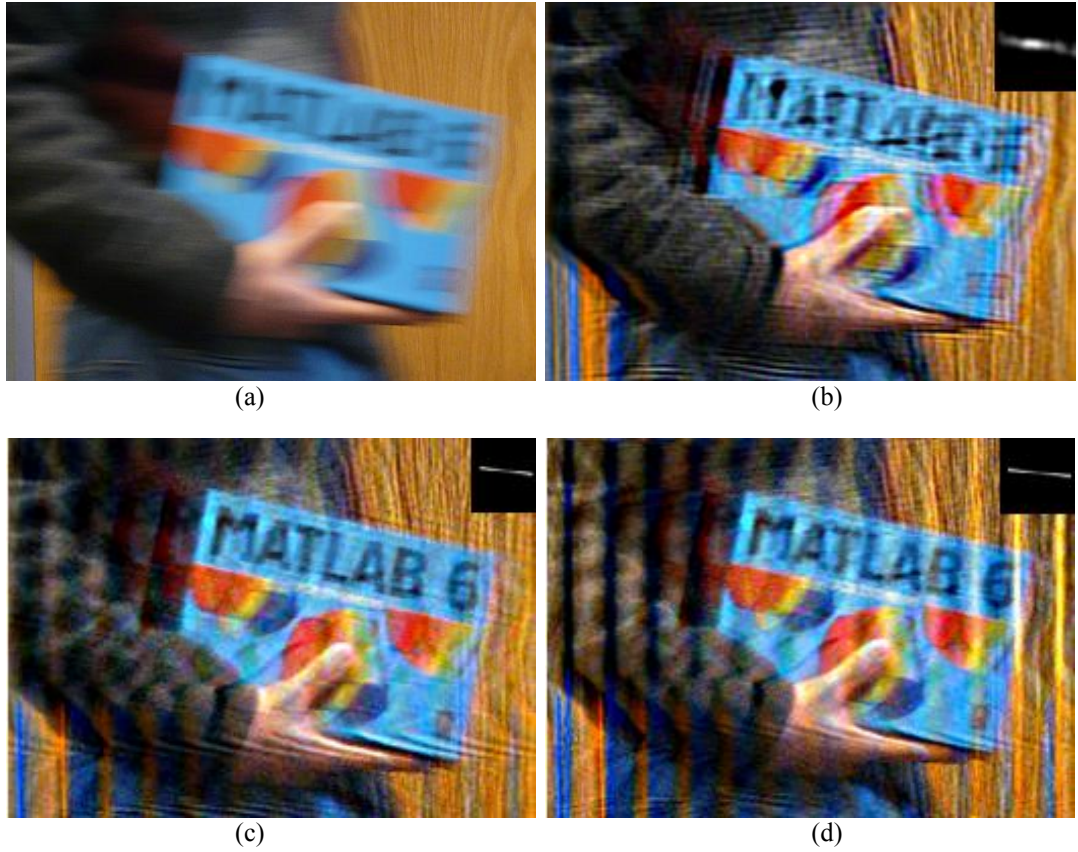
Fig. 3.21 (a) Blurred image, (b) Deblurred using blind deconvolution scheme of Shan et al. (estimated PSF is also shown) (c) Deblurred using the proposed spectral kurtosis based scheme (estimated PSF is also shown) (d) Ringing effect is visible in the deblurred image when edgetaping is not used.

Fig. 3.22 (a) and (b) shows the result of the proposed scheme on the NASA Moon Surface image. The blur can be modelled as atmospheric turbulence, which is given by Eqn. 3.61 according to [57] as follows,

$$h(m,n;\sigma) = Ce^{-\frac{(m^2+n^2)}{2\sigma^2}} \tag{3.61}$$

where C is a constant, σ is the burring width and m,n are PSF pixel coordinates. The proposed scheme using spectral kurtosis estimated the variance of 0.7 for the blurred image.

79

<div align="center">(a)   (b)</div>
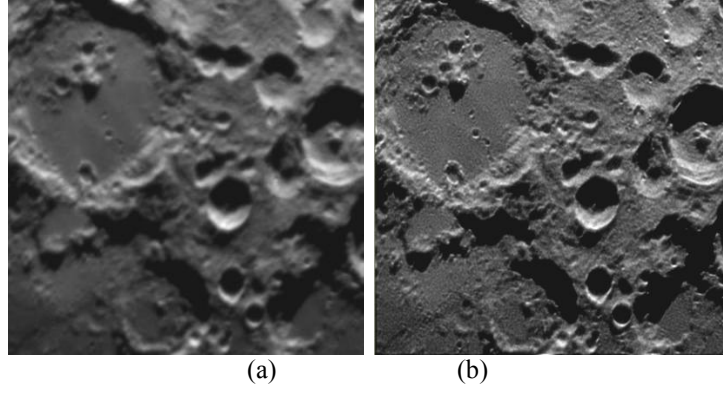
Fig. 3.22 (a) Blurred moon surface image (courtesy of NASA), (b) Spectral kurtosis based deblurring.

3.7. Evaluation and Discussion

3.7.1. Limitations

The proposed scheme has been evaluated for noiseless blurred images. Its performance for noisy blurred images needs to be investigated. The scheme highly depends on ideal restoration filter (no noise amplification and ringing during deblurring). At present, a functional form of the PSF is assumed which is a limited form model of real PSFs. The real images deblurred using the proposed scheme here had an almost uniform shape which could be estimated by PSFs with functional form as given in [57]. These real blurred images were assumed to be noise free but manual adjustment of the NSR (Noise-to-Signal Ratio) parameter δ was still needed for the restoration filter. Real blurred images in many cases appear corrupted by PSFs that are usually arbitrarily shaped and may be space variant.

3.7.2. Computational Efficiency of the Spectral Kurtosis Measure

Unlike the spatial kurtosis measure, the spectral kurtosis measure is calculated in the frequency domain thus omitting the need to transform the data back into the time domain. This saves valuable computation time during the deblurring process. For an image with N elements or MxM dimensions, the FFT algorithm by Cooley and Tukey reduces the number of computations from N^2 (or M^4) to $N \log_2 N$ [130]. A single iteration for calculating the spatial kurtosis measure takes about twice the time as compared to the spectral kurtosis measure. This is shown in Table 3.9 for the FFT-iFFT cycle.

However, the MATLAB's Wiener filter implementation also has other severe overheads losing per iteration efficiency. The average percentage efficiency in computation time per iteration for the FFT-iFFT cycle is 44 percent and for the

MATLAB's Wiener filter based deblurring it is 8 percent. The execution time depicted for the Wiener filter show deblurring schemes for both measures takes almost the same time per iteration. The spectral kurtosis with a low overhead deblurring filter will have low execution time especially when deblurring large size images or when multiple parameters need to be estimated. This is very important, especially when the deblurring is done online where the resources are very limited.

Table 3.9: Comparison of per iteration execution speeds for spatial and spectral kurtosis measures.

Image Dimensions	Execution Time (ms)					
	FFT-iFFT Cycle			Wiener Filter Iteration		
	Spatial Kurtosis	Spectral Kurtosis	Ratio	Spatial Kurtosis	Spectral Kurtosis	Ratio
32x32	12	8	1.50	6	6	1.00
64x64	13	8	1.63	15	13	1.15
128x128	19	13	1.46	48	44	1.09
256x256	35	20	1.75	204	189	1.08
512x512	229	87	2.63	848	771	1.10
1024x1024	779	332	2.35	3817	3427	1.11

3.7.3. Discussion

Spectral kurtosis is introduced as an alternate to spatial kurtosis for the estimation of parametric blur parameters. Spectral kurtosis is also independent of the statistical nature of an image. The absolute value of spectral kurtosis is maximised at or in the near vicinity of the true values of PSF parameters. To search for this optimum point, initially a gradient based search algorithm was used which was later replaced by GA. Results for the artificial and real blurred images using both search algorithms shows that spectral kurtosis serves as a suitable alternative to the spatial kurtosis measure. The spectral kurtosis measure is able to estimate blurring parameter values for the parametric Gaussian, motion and out-of-focus blur. The IQMs used for computing the deblurred image quality shows that the quality of blurred images improves using the estimated PSFs.

The spectral kurtosis measure was investigated for parametric blurs only. Deblurring was performed on noise free images in the artificial blurring case and with inherent image noise in the real blurred case.

The spectral kurtosis is computationally efficient with the deblurring speed almost doubled for the FFT-iFFT cycle for images larger than 256 x 256 pixels. However, the overall improvement in computational speed was marred by the MATLAB based implementation of Wiener filter employed in the proposed BID scheme.

In comparison with Shan et al. BID scheme, which can estimate parametric and

arbitrarily shaped PSFs, the proposed BID scheme is designed for the estimation of parametric blurs only. In the artificial deblurring case for parametric blurs i.e. Gaussian, motion and out-of-focus blur, the proposed scheme produced better quality deblurred images as compared to the Shan et al. BID scheme. This is shown by high values of MSSIM and UQI and low values of BRISQUE and NIQE in Table 3.1-3.4. For the deblurring of real life motion blurred images, the proposed BID scheme shows better quality deblurred images for the BUILDINGS and LABEL image for BRISQUE IQM as compared to the original blurred image. The proposed scheme showed even better result as compared to Shan et al. for the BUILDINGS image. For the LABEL image, Shan et al. scheme showed better result as compared to the proposed scheme. However, for DIP_BOOK and MATLAB_BOOK images both the proposed and Shan et al. scheme further deteriorated the original blurred images.

In most of the real deblurring cases, Shan et al. BID scheme shows lower quality as compared to the original blurred image. The deblurred images of Shan et al. are marred by ringing artefacts due to kernel errors in the PSF estimation stage.

For the NIQE IQM, the proposed scheme shows better result for the BUILDINGS image.

The proposed scheme was enhanced by using a GA based optimization technique instead of the gradient based optimization technique. This improved the overall convergence of the BID scheme in estimating the PSF parameter values. The GA based BID scheme was used to compare the deblurring results for multiple filters including Wiener filter, Richardson-Lucy filter, Regularization filter and MATLAB Iterative Blind Deconvolution (IBD) filter. Wiener filter based estimates show high PSNR values as compared to other filters showing the deblurred images are of high quality.

3.8. Summary

In this chapter, the spectral kurtosis based BID scheme was investigated as an alternative to the spatial kurtosis based BID scheme. Its performance was systematically evaluated and compared with a spatial kurtosis based BID scheme using artificially blurred and real life blurred images. Spectral kurtosis is computationally efficient and independent of the statistical nature of the image. The proposed BID scheme is simple, efficient, easy to implement and operates on a single blurred image for restoration. A comparison with spatial kurtosis and other blind restoration filters indicates the efficiency and improved performance of the proposed

scheme. The proposed scheme was enhanced by using a GA based optimization technique in conjunction with Wiener filter.

Chapter 4 investigates BRISQUE, NIQE and RPSNR measures as alternative IQMs to spatial and spectral kurtosis.

Chapter 4

Image Quality Measures for Blind Image Deblurring

4.1. Introduction

This chapter introduces the use of non-reference (reference-less or blind) Image Quality Measures (IQMs) as possible substitutes to the non-Gaussianity based deblurring measures. In simulated blurring cases the pristine image and deblurred image can be used to calculate quality measures such as PSNR, MSSIM, UQI etc. However, in the BID case, the source image is unavailable and an error image among the source and deblurred image cannot be calculated. This in turn leads to the impossibility of measuring the improvement in terms of error based or full-reference quality measures. It therefore raises the need to look for quality measures that can judge the deblurred image's quality without the need for a reference pristine image, or in other words, a measure that does not require a reference. In this research work, the existing blind IQMs BRISQUE and NIQE have been investigated as alternate deblurring measures for BID. A novel full-reference yet blind quality measure is also proposed as IQM for blind deblurring.

4.2. BRISQUE and NIQE as Deblurring Measures

As discussed in Section 2.6.2 and Section 2.6.3 , BRISQUE and NIQE are two non-reference quality measures recently proposed by Mittal et al. in [77] and [79]. Since neither of these quality measures require a reference image, it makes them good candidates by which to judge the quality of the deblurred image in BID. Using these measures, a deblurred image can be regarded as the best approximation of the original image at the point where the measures minimize. Fig. 4.1(a) shows the deblurring result of the motion blurred Barbara image. The image was blurred with a motion blur PSF of length 11 pixels and angle 25 degrees. Fig. 4.1(b) and Fig. 4.1(c) show the BRISQUE and NIQE plots for different angles of motion blur. Both these measures minimize in the near vicinity of the true blurring PSF parameters. The angles estimated by BRISQUE and NIQE are 26 and 25 degrees, respectively.

(a)
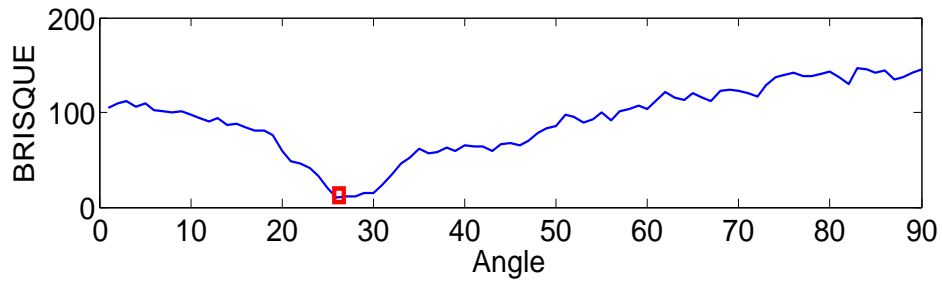
(b)
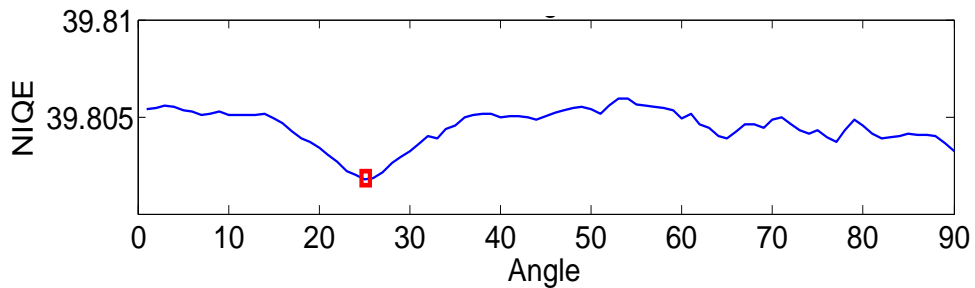
(c)

Fig. 4.1 Deblurring result for motion blurred Barbara image (a) Blurred image (b) BRISQUE plot (c) NIQE plot.

85

4.3. Reblurring Based Quality Measure for Blind Image Deblurring

Fig. 4.2 shows the schematic overview of the reblurring based blind deblurring scheme. Detailed explanation along with mathematical formulation is given in Section. 4.3.1. The blurred image g is passed onto the restoration filter where it is deblurred to obtain the original image estimate f'. A candidate restoration PSF h from a list of PSFs is passed onto the deblurring filter and the image is restored. The original image estimate f' is then reconvolved with the candidate PSF h to re-enact blurring in the image and get the reblurred image g'. If the restoration filter produces a noise-free and ringing-free image or a near approximate; only the candidate PSF, similar to the actual PSF h, will be able to reproduce the same blur. To measure the similarity between the original blurred and reblurred images, full-reference IQMs can be employed. Any of the full-reference IQMs PSNR, MSSIM, UQI, etc can be employed. In this research, the PSNR measure has been utilized for comparison thus naming the proposed measure Reblurring based PSNR (RPSNR).
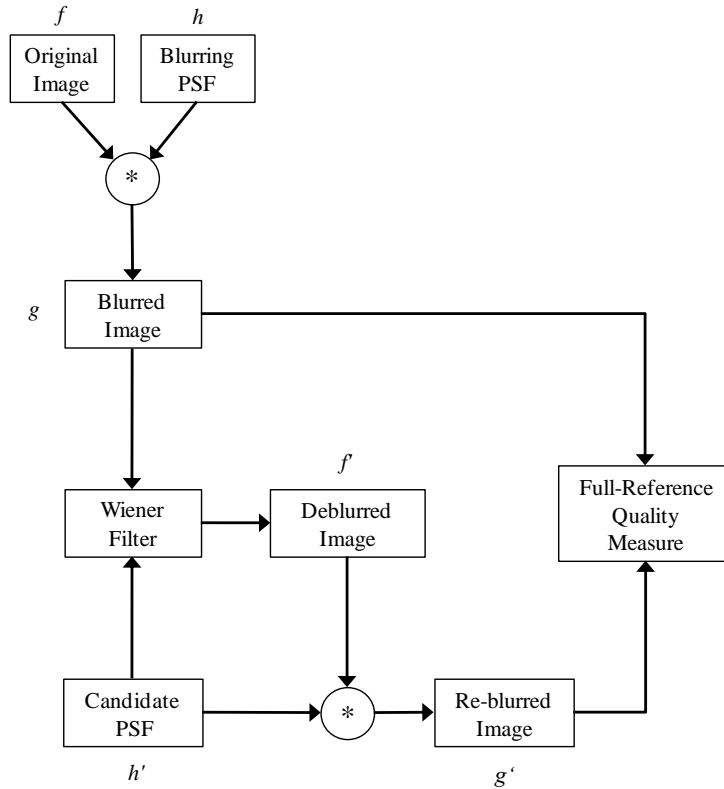
Fig. 4.2 Schematic diagram of the reblurring based BID scheme.

4.3.1. Mathematical Formulation

The mathematical derivation for the reblurring based BID scheme using the Wiener filter is presented as follows. The frequency domain blurring model in noiseless case

is given by Eqn.4.1,

$$G = HF \tag{4.1}$$

The goal of deblurring is to find *F'*, an approximation of *F*, by using Wiener filter, such that,

$$F' \approx F \tag{4.2}$$

The Wiener restoration filter, given by Eqn. 3.24

$$W = \frac{H*}{|H|^2 + \delta} \tag{4.3}$$

where δ is the NSR. For simplicity of future derivation, w.r.t magnitude of the spectral data, we rewrite Eqn. 4.3 as

$$\frac{H}{H}\left(\frac{H*}{|H|^2 + \delta}\right) = \left(\frac{HH*}{|H|^2 H + H\delta}\right) = \frac{H^2}{H^3 + H\delta} = \frac{H}{H^2 + \delta} \tag{4.4}$$

Restoration by Wiener filter results in the original image estimate *F'* which is equivalent to the original image with some Wiener filter approximation error/noise, ξ_δ.

$$F' = F + \xi_\delta \tag{4.5}$$

ξ_δ depends on the NSR value, δ. A low NSR value results in a sharper image with more noise and a higher value of ξ_δ while a high value NSR results in smooth image with more residual blur. The trade-off between image noise/sharpness and smoothness/residual blur is subjective to the user and can be achieved by adjusting the NSR parameter.

Let $\hat{H}$ represent the candidate deblurring filter. The candidate filter can be assumed as different version of the true PSF *H* with some error defined by Δ*H*, such that,

$$\hat{H} = H + \Delta H \tag{4.6}$$

or alternatively

$$H = \hat{H} - \Delta H \tag{4.7}$$

$$\Delta H = \hat{H} - H \tag{4.8}$$

The deblurring estimate *F'* is approximated using the Wiener filter in Eqn. 4.9

$$F' = GW = (FH)\left(\frac{\hat{H}}{\hat{H}^2 + \delta}\right) \tag{4.9}$$

Replacing $H = \hat{H} - \Delta H$ from Eqn. 4.7, we get

$$F' = GW = \left[F\left(\hat{H} - \Delta H\right)\right]\left(\frac{\hat{H}}{\hat{H}^2 + \delta}\right) \tag{4.10}$$

The deblurring result can be categorized into two different scenarios. In the first case, Wiener filter restoration is performed for a candidate filter similar to the original blurring PSF. In the other scenario where the Wiener filter is provided with a candidate PSF different from the original blurring PSF. The functionality of the reblurring based BID scheme is explained for the two scenarios as follows

CASE A

If the candidate filter is similar enough to the original blurring PSF, $\hat{H}=H$, the kernel error among them becomes zero. i.e. $\Delta H=0$. Replacing $\hat{H}=H$ and $\Delta H=0$ in Eqn.4.10, we get

$$F' = GW = \left(F\left(H - 0\right)\right)\left(\frac{H}{H^2 + \delta}\right) \tag{4.11}$$

or

$$F' = GW = \left(FH\right)\left(\frac{H}{H^2 + \delta}\right) \tag{4.12}$$

The deblurring simplifies to the blurred image, $G=F.H$, being treated by the Wiener filter with the candidate filter similar to the original blurring PSF. In this case the deblurred image is a mixture of the original image and the restoration filter error ξ_δ.

$$F' = F + \xi_\delta \tag{4.13}$$

The restoration error occurs more at spectral zeros of the candidate filter. The restored image in the case of $\hat{H}=H$ is a near estimate of the actual un-blurred image. Reblurring Eqn.4.13 results in achieving the original blurred image with an additive noise/error

$$F'H = F'H = (F + \xi_\delta)H = G + H\xi_\delta \tag{4.14}$$

The reblurred image in this case is the best approximate of the original blurred image. When the candidate filter $\hat{H}$ is similar to original blurring filter H, the Wiener

filter error ξ_δ is less, for a specific NSR value. Low ringing is also achieved in the deblurred image due to less kernel error [39].

CASE B

If the candidate filter is different from the original blurring PSF i.e. $\hat{H} \neq H$, the kernel error among them is equal to $\Delta H = \hat{H} - H$. Replacing $\hat{H} = H + \Delta H$ in Eqn. 4.10, we get

$$F' = GW = \left(F(H + \Delta H - \Delta H)\right)\left(\frac{H + \Delta H}{(H + \Delta H)^2 + \delta}\right) \tag{4.15}$$

$$F' = GW = (F.H)\left(\frac{H + \Delta H}{(H + \Delta H)^2 + \delta}\right) \tag{4.16}$$

$$F' = \underbrace{(FH)\left(\frac{H}{(H + \Delta H)^2 + \delta}\right)}_{\xi_H} + \underbrace{(FH)\left(\frac{\Delta H}{(H + \Delta H)^2 + \delta}\right)}_{\xi_{\Delta H}} \tag{4.17}$$

The two parts of the Wiener restoration in Eqn.4.17 result in erroneous deblurring due to a difference between the approximated PSF and the original blurring PSF. The erroneously deblurred image is given by $F_\xi = \xi_H + \xi_{\Delta H}$. The complete deblurring output is given by Eqn. 4.17

$$F' = F_\xi + \xi_\delta \tag{4.20}$$

The restored image in this case is a mixture of the estimated image error $F_\xi = \xi_H + \xi_{\Delta H}$ and the usual restoration filter error ξ_δ. The presence of kernel error results in an erroneous restoration and more ringing. Reblurring in this case by the candidate filter results in a blurred image different than the original blurred image

$$F'\hat{H} = (F_\xi + \xi_\delta)H \tag{4.21}$$

$$\hat{G} \neq G \tag{4.22}$$

As an example of the functioning of the scheme, we look into Fig. 4.3. Fig. 4.3(a) shows the original image which was blurred with motion PSF at an angle of 37 degrees, shown in Fig. 4.3(b). Fig. 4.3(c) shows the image deblurred with PSF of angle 37 degrees. The deblurred image is similar to the original image with negligible level noise and ringing. Fig. 4.3(e) and (g) shows the deblurred image for motion PSFs of angle 16 and 52 degrees respectively. The deblurred images are corrupted by noise and ringing artefacts. The image deblurred with a blur kernel

similar to the true PSF shown in Fig. 4.3(c) is the one which will reproduce a similar blur when reblurred.

(a)

(b)

(c)

(d)

(e)

(f)

(g)

(h)

Fig. 4.3 (a) Original image (b) Blurred image (c)(e)(g) Images deblurred with PSF angle 37, 16 and 52, with their respective reblurred images in (d),(f) and (h).
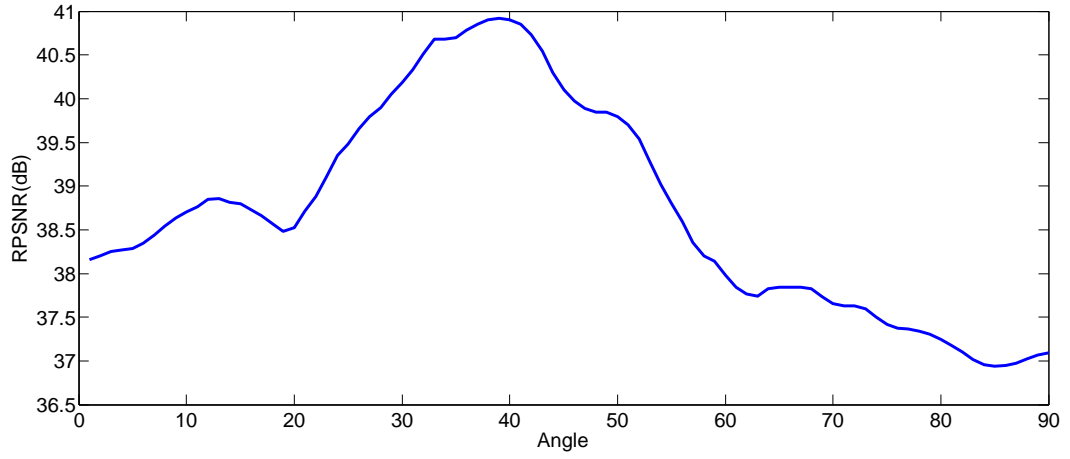
Fig. 4.4 RPSNR plot for deblurring of motion blurred Barbara image with PSF angle 37 degrees. The RPSNR measure estimates the true blurring angle as 38 degrees at its maxima.

Fig. 4.4 shows the RPSNR plot for the deblurring of the blurred Barbara image in Fig. 4.3(b), blurred with a motion PSF angle of 37 degrees. The RPSNR measure during deblurring estimates the true blurring angle as 38 degrees at its maxima.

(a)   (b)
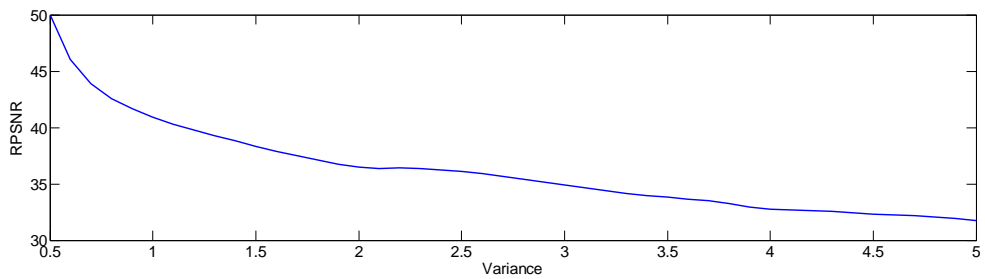
(c)

Fig. 4.5 RPSNR plot for deblurring of Gaussian blurred image with true blur variance of 2. The RPSNR measure incorrectly identifies the true blur variance as 0.5 .

The reblurring based BID scheme is limited to the deblurring of motion blurred images. The deblurring results for artificially blurred Gaussian and out-of-focus images shows that the RPSNR measure fails to depict a global maximum value near

91

the true blur parameters. Fig. 4.5 and Fig. 4.6 show the deblurring results in case of Gaussian and out-of-focus blurred images. The most probable reason being that the blurred image which presents a smooth version of the image, depicts less difference to the original image especially at low levels of blur. This is wrongly perceived by the error based PSNR measure and thus results in an incorrect PSF parameter estimation.

(a)   (b)

(c)
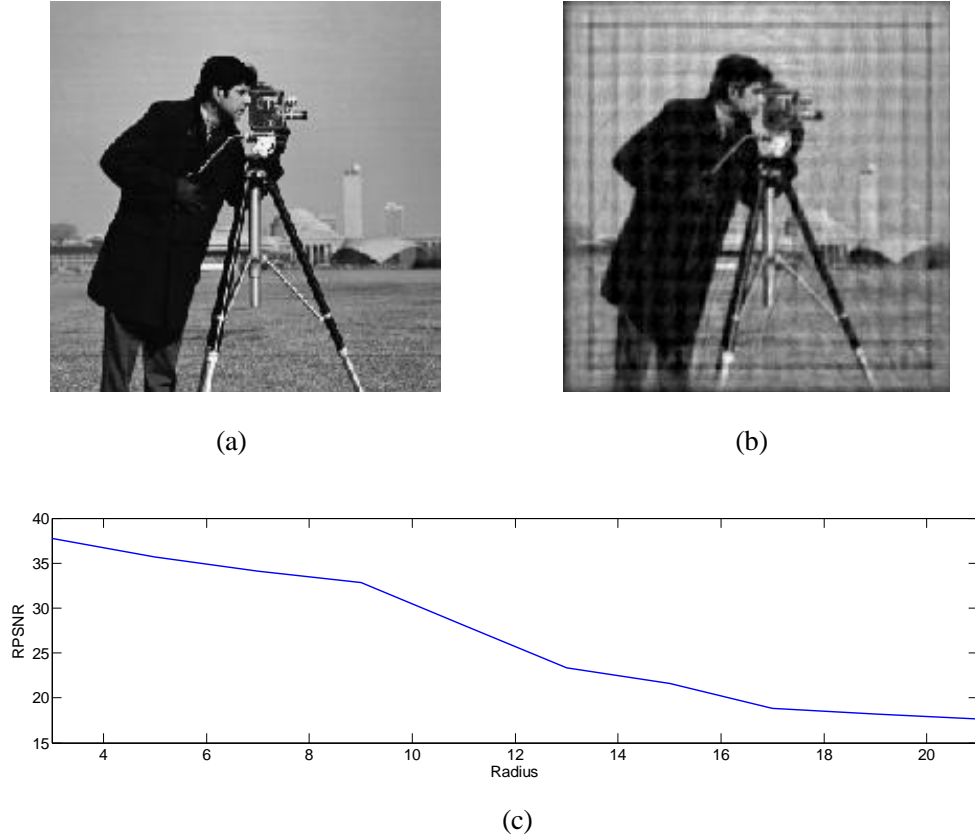
Fig. 4.6 RPSNR plot for deblurring of out-of-focus blurred image with true blur radius of 11. The RPSNR measure incorrectly identifies the true blur radius as 1.

4.4. Experimental Setup

Simulations were carried out to test the efficiency of the blind IQMs BRISQUE and NIQE and the full-reference blind IQM RPSNR. BRISQUE, NIQE and RPSNR have been tested as alternative deblurring measures. Experiments include testing of artificially blurred images as well as real blurred images. In the artificial blurring case the three types of parametric blurs, Gaussian, motion and out-of-focus blur, have been considered. RPSNR based BID was tested using the scheme shown in Fig. 4.2. BRISQUE and NIQE measures were directly employed to estimate the blurring PSF parameters at their minima.

4.5. Deblurring Results for Artificially Blurred Images

Fig. 4.7 shows the Cameraman image with blur at an angle of 35.35 degrees. The corresponding RPSNR, spatial and spectral kurtosis plots for deblurring are also shown. The RPSNR error measure estimated the angle as 32.5 degrees while spatial and spectral kurtosis estimated 32.25 as the blur angle. Angle step size in this case was 0.25 degrees. This shows that the RPSNR measure maximizes in the near vicinity of the true blurring parameter value.

(a)

(b)

(c)

(d)
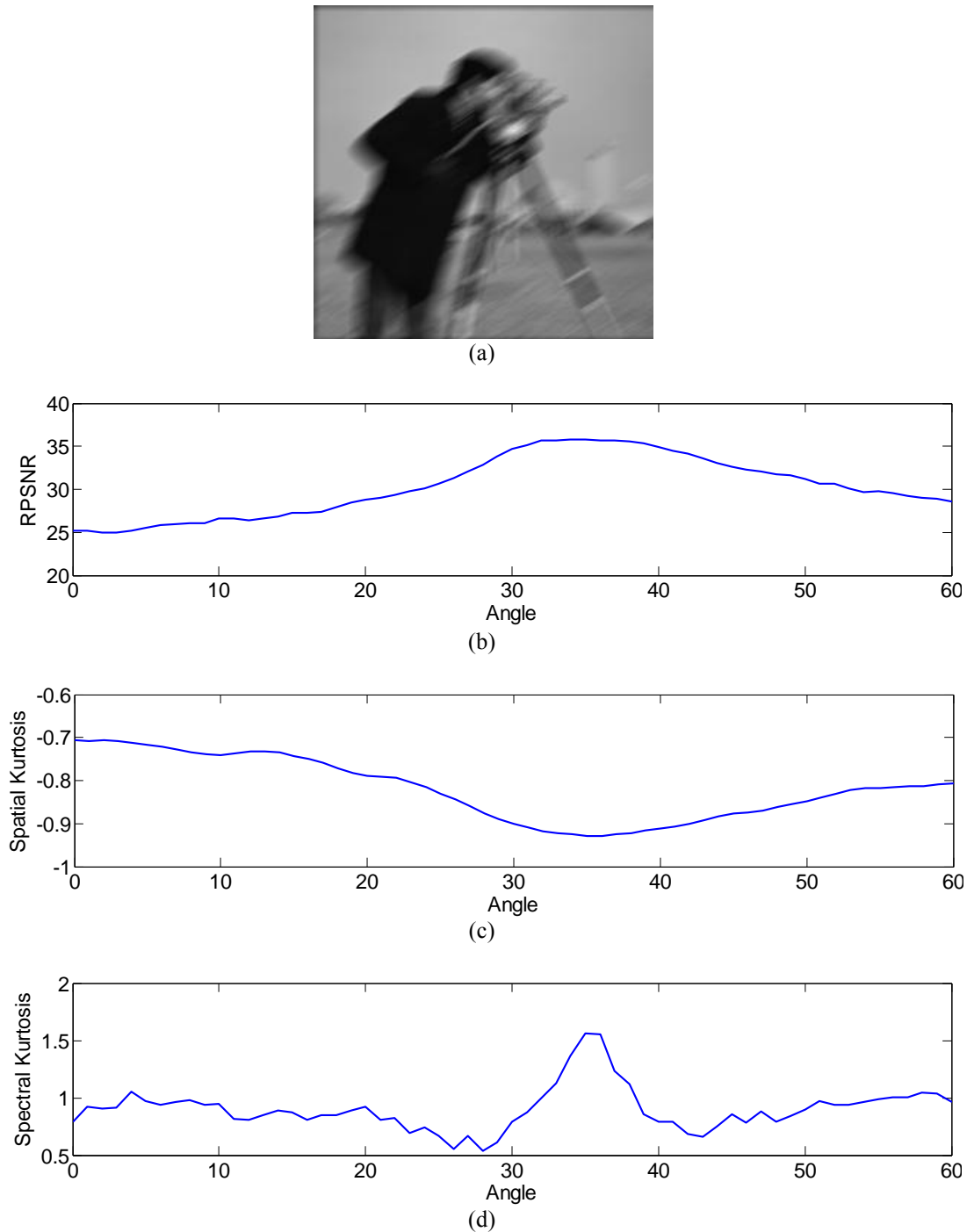
Fig. 4.7 (a) Blurred image (b) RPSNR plot (c) Spatial kurtosis plot (d) Spectral kurtosis plot.

Table 4.1 summarizes the RPSNR results for the artificially blurred Waterloo Bragzone images. In this case, motion blurred images were used and the blur angle, theta, was estimated. The estimated values are in close vicinity of the theta values used to blur the images. PSNR in decibels (dBs) has been calculated for three set of images: blurred and reblurred, original and blurred and original and deblurred. A higher value of PSNR shows image of high quality.

For the original-deblurred case, the PSF estimates produce high quality deblurred images as shown by the high PSNR values. The deblurred images when reconvolved with the estimated PSF produce the reblurred images. When the candidate PSF is near to the original PSF, the reblurred image produces a similar blurring effect as in the originally blurred image. The original blurred image and the reblurred image are compared using PSNR and shown by the blurred-reblurred pair column in Table. 4.1. The high values of PSNR depict the reblurred images are in close approximation of the original blurred images. Therefore the reblurring based BID scheme can estimate the blurring PSFs in case of motion blurred images.

Table 4.1 PSNR comparison for the RPSNR based BID scheme

| Image | Original Theta | Estimated Theta | PSNR (dB) | | | Wiener-Filter NSR Used |
			Blurred – Reblurred	*Original – Blurred*	*Original – Deblurred*	
Barbara	32.35	32	47.03	18.72	22.42	3.00E-03
Washsat	63.13	62.875	42.71	19.16	19.37	3.00E-04
Boat	123.21	122.125	46.61	18.92	22.18	3.00E-03
Cameraman	47.45	46	40.84	15.29	24.41	4.00E-03
Goldhill	11.19	11.5	51.99	19.2	25.84	4.00E-04
Lena	111.21	110.5	44.82	19.74	26.09	4.00E-04
Mandrill	175.67	176.75	32.75	17.14	19.24	4.00E-04
Peppers	85.36	85.5	32.97	18.43	18.92	3.00E-04

Table 4.2 summarizes the results for the deblurring of images artificially blurred by Gaussian blur of varying standard deviation from 1 to 5 pixels with a step size of 0.5 pixels. Results for 23 images from the Desktop Nexus image database are compiled. Variance parameter was estimated using three different IQMs i.e. BRISQUE, NIQE and RPSNR. NSR values of Wiener filter at the point of maximum IQM values are also presented. BRISQUE and NIQE estimates for the Gaussian blurring case are near to the true value of variance.

RPSNR in the Gaussian blurring case fails to correctly estimate the true variance values. The deblurred image quality for these three IQMs has been compared using PSNR, MSSIM, UQI, BRISQUE and NIQE. In the Gaussian blur case, BRISQUE

based deblurred images are estimated as the ones with the best visual quality as compared to NIQE and RPSNR. This is shown by the high values of PSNR, MSSIM and UQI and by low values of NIQE.

Table. 4.2 Artificial Deblurring Results for Gaussian blurred images using RPSNR, BRISQUE and NIQE measures. Deblurred image quality is also compared.

Image	Blur Variance	Estimated Variance			Estimated NSR			Deblurring Quality Measured By															
								PSNR			MSSIM			UQI			BRISQUE			NIQE		
		BRISQUE BID	NIQE BID	RPSNR BID	BRISQUE BID	NIQE BID	RPSNR BID	BRISQUE BID	NIQE BID	RPSNR BID	BRISQUE BID	NIQE BID	RPSNR BID	BRISQUE BID	NIQE BID	RPSNR BID	BRISQUE BID	NIQE BID	RPSNR BID	BRISQUE BID	NIQE BID	RPSNR BID
Img-01	1.00	1.00	0.90	0.50	4.00E-03	4.00E-06	5.70E-04	33.36	22.60	16.32	0.94	0.97	0.35	1.00	1.00	1.00	42.97	17.78	148.54	5.69	53.80	25.51
Img-01	1.50	1.50	1.30	0.50	1.00E-04	4.00E-07	5.97E-04	30.09	10.06	10.46	0.87	0.77	0.03	1.01	0.96	1.00	52.84	12.90	104.42	7.10	61.77	27.44
Img-02	2.00	2.10	1.80	0.50	4.00E-05	3.00E-07	7.91E-04	29.10	9.28	7.71	0.90	0.74	0.03	0.97	0.86	0.96	62.37	40.86	145.64	8.03	43.72	28.80
Img-02	2.50	2.50	2.60	0.50	1.00E-05	4.00E-07	9.58E-04	27.52	10.57	3.93	0.86	0.53	0.05	0.92	0.88	0.91	67.59	36.52	111.73	8.29	38.20	29.50
Img-03	3.00	3.10	3.40	0.50	4.00E-05	4.00E-07	9.97E-04	25.53	11.34	5.88	0.70	0.73	0.09	1.00	0.98	1.00	73.93	37.04	97.20	7.71	24.54	31.92
Img-03	3.50	3.60	3.20	0.50	9.00E-04	6.00E-03	7.31E-04	24.81	26.13	6.44	0.67	0.76	0.74	1.00	1.00	0.99	76.35	61.90	67.31	7.67	8.37	32.12
Img-04	4.00	4.10	4.00	0.50	1.00E-06	8.00E-05	9.62E-04	27.62	29.91	1.55	0.78	0.21	0.81	0.99	0.99	0.98	74.89	4.62	50.34	11.10	6.22	32.79
Img-04	4.50	4.30	4.60	0.50	1.00E-06	4.00E-03	9.77E-04	26.94	29.45	2.47	0.76	0.15	0.83	0.99	0.99	0.99	75.34	10.51	71.90	14.53	10.33	32.84
Img-05	5.00	4.20	4.90	0.50	8.00E-07	1.00E-03	2.09E-04	23.55	23.97	5.14	0.63	0.10	0.67	0.99	1.00	0.99	75.10	21.85	73.71	15.72	9.46	32.81
Img-05	1.00	1.10	0.80	0.50	8.00E-04	1.00E-03	9.45E-04	31.39	32.11	11.99	0.91	0.93	0.91	1.00	1.00	1.00	32.39	3.68	19.95	4.93	6.49	24.47
Img-06	1.50	1.30	1.10	0.50	8.00E-03	4.00E-06	9.64E-04	33.67	18.98	15.19	0.97	0.98	0.19	0.95	0.92	0.96	61.24	48.16	95.45	6.71	28.88	28.38
Img-06	2.00	1.80	2.40	0.50	1.00E-05	5.00E-06	5.47E-04	31.24	21.93	13.59	0.95	0.96	0.37	0.92	0.88	0.95	66.80	36.27	50.77	6.35	15.30	29.54
Img-07	2.50	2.90	2.30	0.50	8.00E-03	1.00E-07	8.83E-04	21.39	8.48	2.32	0.50	0.59	0.04	1.00	0.89	1.02	67.52	61.05	137.87	6.82	34.73	29.69
Img-07	3.00	3.10	3.20	0.50	1.00E-03	2.00E-07	2.10E-06	20.87	10.50	2.29	0.46	0.59	0.10	0.99	0.94	0.97	71.10	58.47	94.43	7.28	33.43	30.51
Img-08	3.50	3.40	3.40	0.50	4.00E-03	1.00E-03	9.05E-04	22.66	24.39	4.13	0.64	0.71	0.72	1.00	1.00	0.99	73.49	63.68	58.30	8.64	8.09	31.96
Img-08	4.00	3.90	4.00	0.50	1.00E-06	1.00E-04	8.73E-04	22.16	23.64	7.51	0.62	0.09	0.64	0.99	1.00	0.99	75.95	48.37	57.37	17.99	6.73	32.34
Img-09	4.50	4.20	4.30	0.50	1.00E-06	4.00E-03	1.00E-03	22.52	23.13	4.94	0.63	0.15	0.68	0.99	1.00	0.99	72.88	13.98	75.96	12.64	9.17	31.71
Img-09	5.00	4.30	4.90	0.50	8.00E-07	1.00E-03	9.97E-04	22.16	22.78	5.94	0.62	0.09	0.67	0.98	1.00	0.99	74.40	23.02	73.13	17.26	9.19	32.39
Img-10	1.00	1.10	1.00	0.50	4.00E-04	1.00E-06	5.14E-04	31.25	15.72	11.16	0.94	0.89	0.16	1.00	1.00	1.00	32.72	1.93	144.92	4.51	63.21	24.73
Img-10	1.50	1.40	1.20	0.50	8.00E-04	1.00E-06	8.06E-08	27.95	6.22	9.68	0.86	0.89	0.01	1.00	0.90	1.00	48.51	6.45	133.97	4.77	5.41	26.38
Img-11	2.00	2.00	1.90	0.50	8.00E-06	4.00E-08	7.38E-04	25.24	6.55	0.02	0.71	0.34	0.02	1.00	0.81	0.99	60.03	65.12	141.21	16.57	56.34	28.46
Img-11	2.50	2.60	2.40	0.50	1.00E-06	1.00E-08	7.41E-04	24.20	5.73	5.59	0.66	0.16	0.01	0.98	0.77	0.99	67.72	47.98	152.65	23.90	21.73	30.10
Img-12	3.00	3.10	2.50	0.50	1.00E-05	4.00E-07	9.87E-04	26.71	11.38	4.03	0.82	0.55	0.03	0.99	0.96	0.99	67.30	40.97	116.95	9.53	31.67	30.02
Img-12	3.50	3.40	3.20	0.50	1.00E-06	4.00E-07	9.97E-04	25.99	13.56	3.97	0.80	0.12	0.07	0.99	0.98	0.99	68.67	22.79	77.82	18.38	22.10	30.32
Img-13	4.00	3.40	4.10	0.50	8.00E-07	1.00E-07	9.31E-04	20.78	8.72	5.27	0.57	0.15	0.05	0.94	0.83	0.94	74.89	6.94	99.34	20.26	39.68	32.97
Img-13	4.50	4.70	4.70	0.50	1.00E-02	4.00E-07	8.97E-04	20.20	10.71	2.09	0.53	0.64	0.09	0.98	0.88	0.93	76.93	74.42	43.82	10.70	38.32	33.11
Img-14	5.00	5.00	5.10	0.50	1.00E-06	1.00E-06	8.30E-04	19.72	15.65	9.61	0.51	0.07	0.27	0.88	0.91	0.90	81.42	42.77	21.65	25.67	10.22	33.58
Img-14	1.00	1.00	1.00	0.50	4.00E-04	1.00E-06	6.00E-04	30.49	16.16	13.09	0.95	0.91	0.27	0.95	0.93	0.98	31.80	8.89	141.28	3.20	36.03	24.82
Img-15	1.50	1.30	1.80	0.50	1.00E-04	8.00E-07	6.93E-04	28.75	12.20	7.45	0.94	0.76	0.07	1.00	0.98	1.00	46.38	47.68	129.68	7.36	38.09	28.37
Img-15	2.00	2.00	2.30	0.50	1.00E-05	4.00E-07	6.72E-04	27.06	12.40	0.82	0.90	0.30	0.09	1.00	0.99	1.00	58.32	94.16	118.53	15.25	26.98	29.57
Img-16	2.50	2.40	2.60	0.50	1.00E-06	4.00E-07	9.75E-04	22.24	10.74	1.71	0.62	0.60	0.11	1.00	0.97	0.99	64.25	28.54	82.80	6.92	32.50	29.14
Img-16	3.00	3.10	2.70	0.50	4.00E-05	4.00E-03	9.92E-04	21.47	23.02	2.83	0.57	0.70	0.70	1.00	1.00	0.99	69.55	38.40	57.71	7.27	7.01	30.71
Img-17	3.50	3.30	3.80	0.50	1.00E-02	1.00E-05	9.43E-04	19.18	18.54	0.09	0.68	0.71	0.32	1.00	0.99	0.99	66.27	62.84	49.10	8.37	13.14	30.74
Img-17	4.00	3.90	4.10	0.50	4.00E-05	1.00E-07	9.25E-04	18.80	7.81	0.04	0.67	0.54	0.03	1.00	0.95	0.96	68.07	37.50	133.01	8.39	41.31	31.64
Img-18	4.00	4.00	5.10	0.50	4.00E-07	4.00E-06	9.99E-04	18.83	14.28	11.14	0.69	0.02	0.30	0.89	0.99	0.98	85.16	118.79	115.22	50.30	13.09	36.41
Img-18	5.00	4.70	5.10	0.50	4.00E-07	4.00E-03	9.87E-04	18.40	19.48	10.27	0.67	0.05	0.68	0.94	0.99	0.97	87.02	139.45	73.65	48.51	9.92	36.00
Img-19	1.00	1.00	1.30	0.50	8.00E-04	4.00E-03	5.25E-05	26.93	26.66	6.48	0.92	0.93	0.91	1.00	1.00	1.01	47.45	24.76	29.98	5.66	10.25	25.94
Img-19	1.50	1.40	1.80	0.50	4.00E-04	4.00E-06	8.45E-04	23.91	16.93	0.67	0.84	0.88	0.30	1.00	1.00	1.00	60.17	15.62	78.43	5.21	21.34	28.01
Img-20	2.00	2.00	2.20	0.50	8.00E-06	1.00E-06	8.91E-04	25.85	14.99	0.83	0.85	0.27	0.18	1.00	0.98	0.99	60.74	89.74	101.29	14.08	25.30	28.72
Img-20	2.50	2.60	2.60	0.50	4.00E-06	4.00E-07	8.48E-04	24.56	10.41	0.30	0.81	0.31	0.06	0.99	0.91	0.98	68.68	3.48	110.03	11.49	36.19	29.97
Img-21	3.00	3.00	2.90	0.50	8.00E-06	1.00E-03	8.50E-04	21.53	23.35	1.06	0.51	0.36	0.67	0.87	0.91	0.96	66.27	36.43	51.32	17.07	8.82	32.18
Img-21	3.50	3.30	3.50	0.50	4.00E-06	8.00E-03	9.83E-04	20.83	22.16	3.82	0.47	0.40	0.57	0.51	0.88	0.85	69.64	14.00	69.34	7.98	10.15	31.93
Img-22	4.00	4.00	3.90	0.50	1.00E-06	8.00E-03	9.97E-04	20.42	21.29	6.96	0.59	0.26	0.65	1.00	1.00	1.00	79.34	8.65	68.39	12.74	9.40	32.22
Img-22	4.50	4.50	4.10	0.50	1.00E-06	8.00E-02	8.47E-04	20.51	19.89	8.51	0.74	0.13	0.75	0.99	0.98	0.97	86.02	29.84	77.29	16.37	11.32	33.79
Img-23	5.00	4.70	4.60	0.50	8.00E-07	7.00E-02	8.15E-04	20.08	19.77	11.49	0.73	0.08	0.73	0.97	1.04	0.97	87.90	71.48	81.29	21.74	11.67	34.29
Mean					1.12E-03	4.38E-03	8.06E-04	**24.63**	16.97	5.93	**0.73**	0.49	0.36	**0.97**	0.95	**0.98**	66.19	**39.56**	89.66	**12.81**	23.55	30.42

Table 4.3 summarizes the results for the deblurring of artificially motion blurred images for varying PSF length and angle. The length of the blurring PSF varies as 7,9,16 and 23 pixels while the angle of the PSF varies as 11,17,25,45 and 65 degrees. Results for 23 images from the Desktop Nexus image database are compiled. Blurring parameter was estimated using three different IQMs i.e. BRISQUE, NIQE and RPSNR. NSR values of Wiener filter at the point of maximum IQM values are also presented. BRISQUE, NIQE and RPSNR estimates for the motion blurring case are near to the true value of blur parameter. The deblurred image quality for these three IQMs has been compared using PSNR, MSSIM, UQI, BRISQUE and NIQE. In the motion blur case, RPSNR based deblurred images are estimated as the ones with the best visual quality as compared to NIQE and BRISQUE. This is shown by the high values of PSNR, MSSIM, UQI and low values of BRISQUE in Table. 4.3.

Table. 4.4 summarizes the results for the deblurring of artificially blurred out-of-focus images for varying PSF radius of 2, 4,6,10 and 11 pixels. Results for 23 images from the Desktop Nexus image database are compiled. Blurring parameter was estimated using three different IQMs i.e. BRISQUE, NIQE and RPSNR. NSR values of Wiener filter at the point of maximum IQM values are also presented. BRISQUE and NIQE radius estimates for the out-of-focus blurring case are near to the true radius values. RPSNR in the out-of-focus blur case fails to correctly estimate the true radius values. The deblurred image quality for these three IQMs has been compared using PSNR, MSSIM, UQI, BRISQUE and NIQE. In the out-of-focus blur case, a single IQM among RPSNR, BRISQUE and NIQE cannot be judged as the best deblurring measure. PSNR and UQI show NIQE as the best IQM while MSSIM and BRISQUE based quality depicts BRISQUE base deblurred images as high quality images. NIQE based quality measurement shows RPSNR based deblurring estimates as high quality. In the case of out-of-focus images, deblurring results in ringing and residual blur which mars the performance of these IQMs.

Table. 4.3 Artificial Deblurring Results for motion blurred images using RPSNR, BRISQUE and NIQE measures. Deblurred image quality is also compared.

| Image | Blur Angle (A) / Blur Length (L) | | Estimated value | | | Estimated NSR | | | Deblurring Quality Measured By | | | | | | | | | | | | | | |
| | | | | | | | | | PSNR | | | MSSIM | | | UQI | | | BRISQUE | | | NIQE | | |
			BRISQUE BID	NIQE BID	RPSNR BID	BRISQUE BID	NIQE BID	RPSNR BID	BRISQUE BID	NIQE BID	RPSNR BID	BRISQUE BID	NIQE BID	RPSNR BID	BRISQUE BID	NIQE BID	RPSNR BID	BRISQUE BID	NIQE BID	RPSNR BID	BRISQUE BID	NIQE BID	RPSNR BID
Img-01	A	11	13	11	11	1.00E-03	1.00E-04	1.00E-07	31.12	28.87	16.20	0.75	0.89	0.18	1.00	0.98	0.99	16.08	45.97	132.31	6.97	10.23	24.68
Img-01	A	17	17	17	17	1.00E-05	1.00E-07	1.00E-05	23.08	14.20	23.08	0.14	0.47	0.47	1.04	0.98	1.04	44.26	128.28	44.26	14.33	17.58	16.33
Img-02	A	25	25	25	25	1.00E-06	1.00E-06	1.00E-07	12.15	16.92	12.15	0.26	0.13	0.13	0.85	0.95	0.85	89.10	80.16	89.10	21.48	20.41	23.48
Img-02	A	45	45	45	45	1.00E-05	1.00E-06	1.00E-06	17.72	15.14	15.14	0.21	0.33	0.21	0.92	0.46	0.46	52.27	63.88	63.88	12.25	17.87	19.87
Img-03	A	65	65	65	65	1.00E-05	1.00E-05	1.00E-02	23.60	23.60	28.97	0.57	0.57	0.90	1.00	1.00	1.00	22.65	22.65	24.48	12.28	12.28	6.06
Img-03	A	11	11	11	11	1.00E-07	2.00E-07	1.00E-06	12.65	13.47	17.00	0.17	0.15	0.30	0.97	0.98	0.99	153.59	153.59	143.43	37.46	38.06	21.68
Img-04	A	17	17	17	17	3.00E-03	1.00E-06	1.00E-05	27.62	14.32	21.66	0.14	0.83	0.43	0.95	0.90	0.93	9.47	96.22	53.56	3.97	23.90	15.97
Img-04	A	25	25	25	25	7.00E-04	4.00E-07	1.00E-03	25.47	12.00	25.63	0.13	0.75	0.76	0.93	0.77	0.92	14.40	92.61	12.79	6.27	17.72	7.68
Img-05	A	45	45	45	43	1.00E-03	1.00E-06	1.00E-05	27.66	16.08	21.75	0.18	0.86	0.43	1.00	0.98	1.01	7.19	153.59	50.41	5.94	39.39	17.12
Img-05	A	65	65	65	65	1.00E-05	1.00E-06	2.00E-04	20.41	13.28	24.07	0.12	0.38	0.66	1.01	0.95	1.00	61.04	77.43	65.86	13.56	36.96	10.38
Img-06	A	11	11	11	11	1.00E-03	1.00E-06	1.00E-06	27.93	16.35	26.81	0.23	0.81	0.70	0.88	0.85	0.90	23.47	82.64	29.61	5.71	24.27	13.01
Img-06	A	17	15	17	17	1.00E-03	1.00E-06	1.00E-05	24.48	12.58	17.81	0.16	0.71	0.33	0.85	0.75	0.81	27.16	95.30	48.77	5.32	19.87	17.15
Img-07	A	25	25	25	25	1.00E-07	1.00E-06	1.00E-04	15.06	18.87	26.46	0.50	0.33	0.83	0.98	0.99	0.99	94.26	75.26	35.60	16.17	12.38	10.51
Img-07	A	45	45	45	45	1.00E-06	1.00E-06	1.00E-06	22.68	16.83	23.92	0.41	0.78	0.75	0.99	0.99	0.99	35.13	60.68	31.29	7.20	13.00	11.92
Img-08	A	65	65	65	65	1.00E-02	2.00E-05	1.00E-02	23.24	19.52	23.24	0.44	0.75	0.75	1.00	0.99	1.00	21.88	50.48	21.88	6.88	11.26	8.88
Img-08	A	11	13	11	11	1.00E-05	1.00E-05	1.00E-06	15.60	17.35	13.53	0.39	0.26	0.24	0.96	0.95	0.89	52.82	33.61	55.90	10.60	11.29	15.33
Img-09	A	17	19	17	15	1.00E-04	1.00E-06	2.00E-06	26.15	19.42	20.12	0.35	0.70	0.37	1.00	1.00	1.00	32.80	64.06	69.22	6.58	11.99	12.12
Img-09	A	25	25	25	25	1.00E-06	1.00E-06	1.00E-06	17.49	17.49	17.49	0.28	0.28	0.28	1.00	1.00	1.00	75.92	75.92	75.92	15.97	15.97	17.97
Img-10	A	45	45	45	45	1.00E-04	1.00E-05	1.00E-05	20.56	17.37	17.37	0.33	0.50	0.33	0.99	0.99	0.99	24.30	37.77	37.77	8.28	11.77	13.77
Img-10	A	65	65	65	65	3.00E-02	1.00E-06	1.00E-02	20.81	13.97	21.51	0.20	0.66	0.70	0.99	0.96	0.99	35.29	69.48	26.33	7.45	15.46	7.83
Img-11	A	11	11	11	11	4.00E-03	1.00E-05	1.00E-05	30.58	25.92	25.92	0.71	0.93	0.71	0.98	0.93	0.93	24.44	60.10	60.10	3.26	13.27	15.27
Img-11	A	17	17	17	17	1.00E-03	1.00E-06	1.00E-05	27.84	23.94	23.94	0.64	0.82	0.64	0.96	0.95	0.95	34.60	38.36	38.36	8.13	9.77	11.77
Img-12	A	25	25	25	25	3.00E-07	1.00E-06	1.00E-06	14.70	16.96	16.96	0.22	0.16	0.22	0.90	0.92	0.92	81.96	74.54	74.54	16.79	15.59	17.59
Img-12	A	45	45	45	45	1.00E-03	1.00E-06	1.00E-05	23.95	14.97	17.49	0.17	0.69	0.27	0.92	0.89	0.90	21.56	63.53	55.88	4.55	14.66	12.23
Img-13	A	65	65	65	65	1.00E-02	1.00E-04	1.00E-02	27.17	26.51	27.17	0.83	0.92	0.92	0.98	0.95	0.98	20.38	27.26	20.38	5.58	6.57	7.58
Img-13	L	7	7	7	7	1.00E-04	1.00E-05	1.00E-02	28.37	24.33	26.32	0.73	0.87	0.87	0.92	0.96	0.93	52.77	76.17	9.67	9.48	13.43	6.99
Img-14	L	9	9	9	9	1.00E-06	1.00E-03	1.00E-02	17.51	27.22	24.54	0.84	0.42	0.81	0.91	0.94	0.95	75.07	15.29	13.49	12.40	3.49	5.66
Img-14	L	16	16	16	16	3.00E-04	1.00E-03	1.00E-02	23.59	23.75	21.48	0.75	0.73	0.69	0.91	0.97	0.95	13.53	8.40	24.70	4.78	3.62	5.95
Img-15	L	23	23	23	23	1.00E-05	1.00E-05	1.00E-02	14.44	19.65	20.60	0.57	0.21	0.71	0.93	0.97	0.98	66.22	31.97	36.50	10.91	5.91	10.01
Img-15	L	7	7	7	7	1.00E-04	1.00E-04	1.00E-02	26.64	26.64	28.86	0.70	0.70	0.90	1.00	1.00	1.00	87.84	87.84	3.53	8.57	8.57	5.98
Img-16	L	9	9	9	9	3.00E-03	1.00E-05	1.00E-02	25.67	21.88	24.10	0.63	0.87	0.82	1.00	1.00	1.00	4.41	45.38	6.66	4.34	6.81	6.33
Img-16	L	16	16	16	16	2.00E-03	1.00E-06	1.00E-02	22.72	21.34	21.34	0.70	0.78	0.70	0.99	0.99	0.99	11.31	31.65	31.65	4.45	4.45	6.45
Img-17	L	23	23	23	23	1.00E-06	4.00E-02	1.00E-02	12.86	17.76	18.68	0.57	0.21	0.57	0.98	0.99	0.99	105.28	43.70	33.08	24.36	12.48	11.35
Img-17	L	7	7	7	7	2.00E-02	8.00E-02	1.00E-02	25.93	21.83	27.01	0.89	0.92	0.92	0.99	0.99	1.00	19.94	28.68	17.04	9.01	10.89	10.71
Img-18	L	9	9	9	9	1.00E-02	1.00E-06	1.00E-02	24.33	16.90	24.33	0.29	0.87	0.87	1.00	1.00	1.00	48.20	112.45	48.20	8.18	21.74	10.18
Img-18	L	16	16	16	16	1.00E-05	5.00E-06	1.00E-02	14.20	12.77	20.49	0.16	0.20	0.69	0.99	0.98	1.00	69.63	59.40	46.59	33.47	47.31	11.28
Img-19	L	23	23	23	23	1.00E-05	3.00E-02	1.00E-02	13.76	17.57	18.15	0.53	0.31	0.56	0.96	0.99	0.99	89.99	53.55	46.28	12.17	10.40	12.11
Img-19	L	7	7	7	7	1.00E-02	2.00E-02	1.00E-02	26.92	25.94	26.92	0.91	0.91	0.91	1.00	1.00	1.00	19.89	24.63	19.89	6.13	7.01	8.13
Img-20	L	9	9	9	9	8.00E-02	2.00E-02	1.00E-02	23.61	26.29	27.04	0.88	0.84	0.89	0.99	0.96	0.98	46.02	31.32	24.87	5.53	4.53	6.30
Img-20	L	16	16	16	16	1.00E-06	2.00E-02	1.00E-02	13.55	23.09	23.65	0.76	0.17	0.77	0.89	0.94	0.77	60.66	40.16	33.85	18.51	5.03	6.51
Img-21	L	23	23	23	23	1.00E-03	2.00E-07	1.00E-02	19.43	9.93	18.52	0.14	0.58	0.49	0.63	0.74	0.81	19.86	153.59	25.21	7.64	29.36	14.14
Img-21	L	7	7	7	7	1.00E-03	4.00E-06	1.00E-02	28.35	21.83	25.86	0.60	0.90	0.84	1.20	1.05	1.23	38.22	96.09	9.98	8.12	18.51	8.31
Img-22	L	9	9	9	9	1.00E-04	1.00E-06	1.00E-02	23.95	24.25	24.25	0.84	0.75	0.84	1.00	1.00	1.00	30.31	18.85	18.85	8.08	3.97	5.97
Img-22	L	16	16	16	16	1.00E-05	4.00E-02	1.00E-02	16.30	20.73	22.06	0.73	0.28	0.74	0.99	1.01	1.00	35.32	46.30	33.76	16.85	6.31	7.97
Img-23	L	23	23	23	23	1.00E-06	2.00E-02	1.00E-02	12.60	19.15	19.50	0.66	0.18	0.66	0.97	0.97	0.99	134.16	44.16	34.65	21.21	9.57	10.95
Mean						4.46E-03	6.52E-03	5.37E-03	21.65	19.31	**21.98**	0.48	0.59	**0.62**	**0.96**	0.94	**0.96**	46.77	63.84	**41.78**	**11.03**	15.00	11.72

Table. 4.4 Artificial Deblurring Results for out-of-focus blurred images using RPSNR, BRISQUE and NIQE measures. Deblurred image quality is also compared.

Image	Blur Radius	Estimated Radius			Estimated NSR			Deblurring Quality Measured By															
								PSNR			MSSIM			UQI			BRISQUE			NIQE		
		BRISQUE BID	NIQE BID	RPSNR BID	BRISQUE BID	NIQE BID	RPSNR BID	BRISQUE BID	NIQE BID	RPSNR BID	BRISQUE BID	NIQE BID	RPSNR BID	BRISQUE BID	NIQE BID	RPSNR BID	BRISQUE BID	NIQE BID	RPSNR BID	BRISQUE BID	NIQE BID	RPSNR BID
Img-01	2	3	2	2	2.00E-07	1.00E-05	1.00E-02	12.44	26.90	13.35	0.95	0.54	0.05	0.97	1.00	0.99	25.74	68.59	153.42	15.52	28.04	23.47
Img-01	4	5	4	2	1.00E-07	1.00E-06	1.00E-02	10.22	16.79	12.06	0.74	0.14	0.03	0.96	1.00	0.98	32.81	74.75	138.99	17.08	23.27	20.89
Img-02	6	8	5	2	1.00E-07	1.00E-02	1.00E-02	24.21	26.62	13.57	0.77	0.82	0.06	0.94	0.94	0.92	52.45	50.63	153.59	6.41	23.18	9.16
Img-02	10	8	6	2	1.00E-07	1.00E-02	1.00E-02	23.39	22.23	13.10	0.67	0.61	0.07	0.92	0.91	0.90	53.68	63.90	146.02	7.73	26.15	8.78
Img-03	11	13	7	2	2.00E-07	1.00E-03	1.00E-02	20.19	20.99	12.99	0.57	0.38	0.41	0.96	0.98	0.98	47.24	47.70	144.15	5.69	27.72	7.05
Img-03	2	3	2	2	3.00E-07	1.00E-04	1.00E-02	15.98	30.37	13.59	0.95	0.80	0.18	0.99	0.99	0.99	39.33	32.55	153.98	9.72	29.95	12.44
Img-04	4	7	4	2	1.00E-07	1.00E-06	1.00E-02	7.45	17.26	13.15	0.84	0.12	0.01	0.79	0.99	0.97	45.48	56.26	152.86	22.21	27.02	34.68
Img-04	6	9	5	2	3.00E-04	3.00E-03	1.00E-02	21.36	29.56	13.10	0.78	0.79	0.42	0.93	0.99	0.97	51.28	23.30	50.90	5.37	35.08	8.47
Img-05	10	12	5	2	1.00E-06	1.00E-02	1.00E-02	22.95	22.54	13.60	0.60	0.57	0.07	0.98	0.99	0.97	41.80	47.40	131.25	7.07	33.15	9.72
Img-05	11	12	7	2	1.00E-07	1.00E-02	1.00E-02	23.07	22.05	13.68	0.59	0.55	0.02	0.99	0.99	0.97	44.21	60.84	151.29	7.95	30.08	9.58
Img-06	2	4	2	2	4.00E-03	1.00E-04	1.00E-02	15.56	31.95	14.57	0.98	0.75	0.15	0.92	0.93	0.87	29.84	34.82	61.60	12.93	23.33	14.61
Img-06	4	7	4	2	1.00E-06	1.00E-05	1.00E-02	9.00	22.53	14.08	0.92	0.30	0.04	0.73	0.95	0.86	52.11	43.38	153.59	18.19	27.70	25.57
Img-07	6	4	5	2	3.00E-04	2.00E-04	1.00E-02	17.42	18.10	9.59	0.42	0.22	0.12	1.01	1.00	0.92	23.35	34.32	42.22	7.32	46.76	9.89
Img-07	10	12	6	2	3.00E-06	2.00E-02	1.00E-02	19.54	18.62	12.43	0.36	0.33	0.03	0.92	0.97	0.95	35.53	59.64	116.54	8.09	32.84	10.16
Img-08	11	12	6	2	1.00E-07	1.00E-03	1.00E-02	21.12	19.42	13.30	0.55	0.39	0.06	0.98	0.98	0.98	49.22	41.90	151.45	4.47	28.84	6.17
Img-08	2	3	2	2	4.00E-03	1.00E-03	1.00E-02	18.61	32.04	13.89	0.94	0.92	0.01	1.00	1.00	1.00	28.19	14.25	53.27	4.51	21.96	9.59
Img-09	4	7	4	2	1.00E-03	1.00E-05	1.00E-02	8.15	20.44	11.59	0.68	0.32	0.01	0.86	1.00	0.97	22.55	70.00	54.64	12.13	25.92	19.34
Img-09	6	4	7	2	3.00E-04	1.00E-02	1.00E-02	22.76	23.90	12.43	0.64	0.69	0.08	1.00	1.00	0.98	32.08	57.86	47.38	6.98	27.12	5.88
Img-10	10	12	5	2	1.00E-06	1.00E-02	1.00E-02	21.59	20.85	12.67	0.60	0.56	0.09	0.98	0.99	0.98	48.28	49.36	137.35	7.17	37.09	9.91
Img-10	11	12	7	2	2.00E-07	4.00E-04	1.00E-02	20.19	19.04	12.71	0.59	0.28	0.04	0.98	0.98	0.98	49.88	47.70	151.61	7.16	32.33	5.55
Img-11	2	3	2	2	1.00E-06	1.00E-04	1.00E-02	13.71	30.31	13.30	0.93	0.82	0.12	0.97	1.00	0.97	26.49	25.66	154.01	6.83	23.70	22.10
Img-11	4	5	4	2	1.00E-07	1.00E-05	1.00E-02	11.50	21.05	10.92	0.60	0.40	0.07	0.95	1.00	0.95	29.29	50.46	151.48	12.12	32.04	16.08
Img-12	6	8	5	2	1.00E-07	1.00E-03	1.00E-02	20.96	25.71	13.22	0.78	0.66	0.42	0.98	0.99	0.98	39.58	29.58	147.93	4.14	29.10	6.45
Img-12	10	13	7	2	1.00E-06	3.00E-02	1.00E-02	23.62	23.64	13.55	0.73	0.73	0.02	0.98	0.99	0.97	44.66	72.30	132.20	9.73	29.30	11.38
Img-13	11	13	6	2	5.00E-06	1.00E-02	1.00E-02	19.61	17.93	12.38	0.41	0.31	0.09	0.91	0.89	0.89	54.98	55.42	111.26	7.90	28.57	10.85
Img-13	2	3	2	2	1.00E-06	1.00E-03	1.00E-02	19.58	33.34	14.02	0.98	0.94	0.50	0.97	0.97	0.93	31.18	24.90	154.13	5.49	31.02	8.35
Img-14	4	6	4	4	1.00E-06	1.00E-05	1.00E-07	7.68	21.41	8.62	0.14	0.44	0.02	0.82	0.95	0.86	90.79	46.37	153.58	10.90	52.63	47.57
Img-14	6	8	4	2	1.00E-06	1.00E-02	1.00E-02	19.76	20.64	11.78	0.57	0.50	0.47	0.91	0.93	0.89	40.35	37.66	153.31	5.24	30.53	8.29
Img-15	10	12	7	2	1.00E-07	1.00E-02	1.00E-02	21.69	21.17	14.34	0.72	0.66	0.09	0.99	0.99	0.98	48.89	61.26	151.16	8.01	29.21	9.91
Img-15	11	12	7	2	1.00E-06	2.00E-02	1.00E-02	21.73	20.63	13.96	0.71	0.67	0.03	0.99	0.99	0.98	50.54	70.15	133.56	9.38	32.04	10.28
Img-16	2	3	2	2	1.00E-06	1.00E-03	1.00E-02	17.22	30.63	13.85	0.94	0.94	0.40	1.00	1.00	0.99	35.81	21.35	153.72	3.95	19.38	10.42
Img-16	4	6	4	4	1.00E-07	2.00E-02	1.00E-07	20.30	24.32	8.62	0.14	0.78	0.50	0.99	1.00	0.93	86.32	49.61	153.59	5.90	52.16	7.73
Img-17	6	8	7	2	7.00E-04	2.00E-06	1.00E-02	7.08	8.89	10.31	0.65	0.03	0.01	0.88	0.95	0.98	26.27	114.89	60.99	43.52	28.31	33.67
Img-17	10	11	10	2	1.00E-06	1.00E-07	1.00E-02	6.46	8.65	12.76	0.60	0.06	0.02	0.81	0.96	0.98	38.56	78.45	137.24	56.05	29.20	34.26
Img-18	11	11	10	2	4.00E-07	1.00E-07	1.00E-02	6.23	7.77	13.18	0.61	0.02	0.05	0.76	0.90	0.96	59.57	125.53	153.39	54.93	34.44	28.05
Img-18	2	3	4	2	1.00E-06	1.00E-03	1.00E-02	18.36	13.86	15.02	0.95	0.15	0.08	0.99	0.97	0.99	24.41	144.26	154.37	43.00	27.50	21.90
Img-19	4	5	6	2	1.00E-07	2.00E-02	1.00E-02	21.88	19.50	9.90	0.70	0.48	0.04	1.00	0.99	0.97	36.33	57.79	153.83	14.48	44.93	11.89
Img-19	6	7	5	2	1.00E-07	1.00E-06	1.00E-02	7.34	9.09	10.73	0.62	0.06	0.04	0.89	0.96	0.97	49.76	138.91	153.59	56.48	33.70	50.91
Img-20	10	8	10	2	1.00E-07	2.00E-02	1.00E-02	7.97	9.33	13.15	0.65	0.04	0.01	0.79	0.86	0.94	48.42	60.03	143.86	58.81	32.47	41.30
Img-20	11	9	10	2	1.00E-07	1.00E-07	1.00E-02	7.02	8.10	12.67	0.64	0.02	0.01	0.72	0.81	0.93	48.94	70.59	145.59	70.05	43.14	30.30
Img-21	2	3	4	2	1.00E-06	1.00E-06	1.00E-02	7.12	5.72	13.27	0.91	0.01	0.03	0.68	0.65	0.78	26.42	153.59	156.05	65.28	26.89	51.49
Img-21	4	6	5	2	1.00E-07	2.00E-02	1.00E-02	20.76	22.89	10.94	0.51	0.58	0.41	0.85	0.82	0.75	35.18	49.68	153.59	12.58	49.78	11.27
Img-22	6	4	7	2	3.00E-04	1.00E-07	1.00E-02	11.03	8.35	11.29	0.58	0.04	0.02	0.99	0.94	0.99	33.72	126.12	48.13	44.03	37.23	25.52
Img-22	10	7	10	2	1.00E-04	1.00E-07	1.00E-02	7.68	9.26	13.61	0.68	0.04	0.01	0.88	0.94	0.96	57.04	70.55	62.08	59.96	28.49	33.08
Img-23	11	13	10	2	1.00E-06	1.00E-07	1.00E-02	6.47	8.10	13.20	0.67	0.02	0.01	0.78	0.90	0.96	59.42	84.85	131.78	43.33	28.34	25.29
Mean					2.45E-04	5.13E-03	9.56E-03	15.73	**19.83**	12.62	**0.68**	0.43	0.12	0.92	**0.95**	**0.95**	**42.84**	62.20	127.79	20.13	31.55	**18.43**

For different blur types (Gaussian, motion and out-of-focus), it is difficult to isolate a single measure as the best one among the non-reference IQMs just based on their deblurred image quality scores since their performance varies. In order to select among the BRISQUE, NIQE and RPSNR IQMs, the estimated NSR for the different IQMs is also analyzed. It is observed that the BRISQUE measure estimates the PSF parameters for relatively lower NSR values as compared to NIQE and RPSNR. A lower NSR value for the Wiener filter based deconvolution results in a comparatively sharper image as compared to a higher NSR value. Also, low NSR values depict the presence of deblurring noise. In accordance, the BRISQUE based deblurred images are visually much better due to the presence of sharp edges. Due to this, BRISQUE was selected as the blind IQM to be used in the later research work.

4.6. Deblurring Results for Real Blurred Images

Deblurring results of the blind IQMs for real images are presented. These include images under the effect of different types of blur including atmospheric blur, motion blur and out-of-focus blur. The deblurring results are compared to the spatial and spectral kurtosis based estimates to gauge the efficacy of the deblurring measures. The estimated PSF parameter values are given in Table. 4.5.

Table 4.5 Deblurring results for real life motion blurred images.

Image	Estimated Values					
	Spatial Kurtosis			Spectral Kurtosis		
	Length	Angle	NSR	Length	Angle	NSR
Fig. 4.7(a)	71	-2	4.00E-03	77	3	4.00E-02
Fig. 4.8(a)	19	80	4.00E-02	19	90	4.00E-02
Fig. 4.9(a)	16	161	4.00E-03	21	160	4.00E-03
	BRISQUE			NIQE		
	Length	Angle	NSR	Length	Angle	NSR
Fig. 4.7(a)	71	0	4.00E-03	73	3	4.00E-03
Fig. 4.8(a)	15	81	4.00E-02	17	87	4.00E-03
Fig. 4.9(a)	20	161	4.00E-03	17	156	4.00E-03
	RPSNR					
	Length	Angle	NSR			
Fig. 4.7(a)	77	3	4.00E-03			
Fig. 4.8(a)	19	80	4.00E-02			
Fig. 4.9(a)	21	156	4.00E-03			

Fig. 4.8 (a) shows an image under motion blur with the book title unreadable. The image was taken by an ordinary digital camera with the person holding the book moving in front of the camera. The image in Fig. 4.8(b), (d) and (e) seem to have recovered well by deblurred with PSF estimated using the spatial kurtosis, RPSNR and BRISQUE based BID schemes, respectively. In the case of spectral kurtosis and NIQE based BID scheme, the images in Fig. 4.8(c) and Fig. 4.8(f) do not recover well.

(a)

(b)

(c)

(d)

(e)

(f)
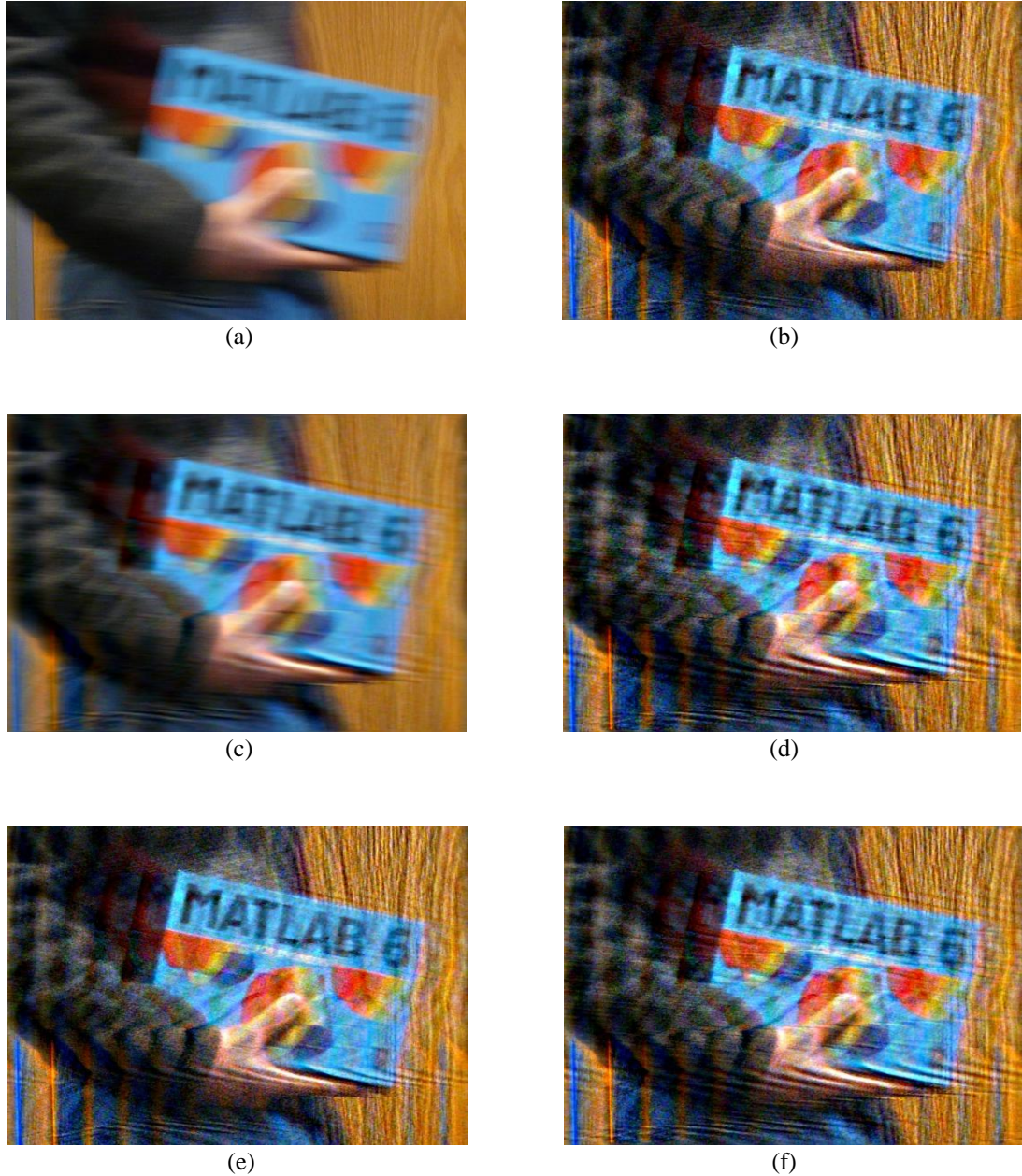
Fig. 4.8. (a) Blurred image. Deblurred using (b) Spatial kurtosis measure (c) Spectral kurtosis measure. (d) RPSNR measure (e) BRISQUE measure and (f) NIQE measure based BID scheme.

Deblurring result for another motion blurred image is shown in Fig. 4.9. A blurred

image frame extracted from a video captured by a low quality camera, depicted in Fig. 4.9(a), shows an approximate vertical motion blur with the small numbers at the bottom becoming unreadable. The blurred image contains a certain amount of noise due to poor lighting, one of the most difficult issues in deblurring. The image does not seem to have recovered well for spatial kurtosis and RPSNR based BID schemes in Fig. 4.9(b) and Fig. 4.9(d) respectively. The image was not recovered well and the digits in the image are unreadable. Reasonable recovery is visible for the spectral kurtosis and BRISQUE based BID schemes. The images in these cases present readable digits however the images appear smooth due to the presence of residual blur. The residual blur appears as a result of using a high NSR value in the Wiener filter which does not completely remove the blur. The best recovery is visible for the NIQE based BID scheme shown in Fig. 4.9(f). Deblurring in this case shows a reasonably sharper image but the kernel error among the estimated PSF and the actual blurring PSF results in the ringing visible in the deblurred image in Fig.4.9(f).

Fig. 4.9. (a) Blurred image. Deblurred using (b) Spatial kurtosis measure (c) Spectral kurtosis measure. (d) RPSNR measure (e) BRISQUE measure and (f) NIQE measure based BID scheme.

Result for another motion blurred image is shown in Fig. 4.10. Though all the IQMs except spatial kurtosis show reasonably well deblurring results, the presence of ringing artefacts suggests that error exists among the estimated PSF and the original blurring PSF. Comprehensive results on real life motion and out-of-focus blurred images are given in Appendix B.
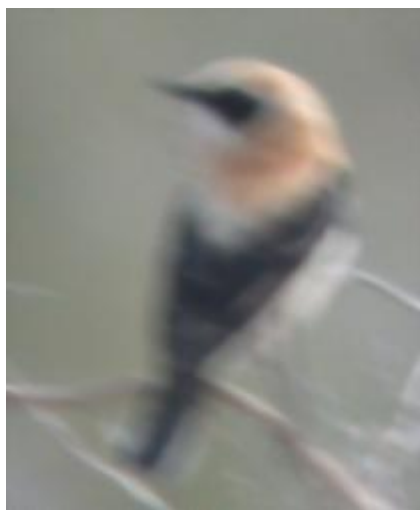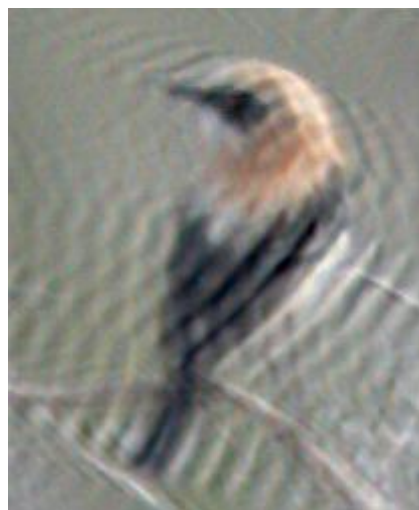
(a)   (b)

(c)   (d)
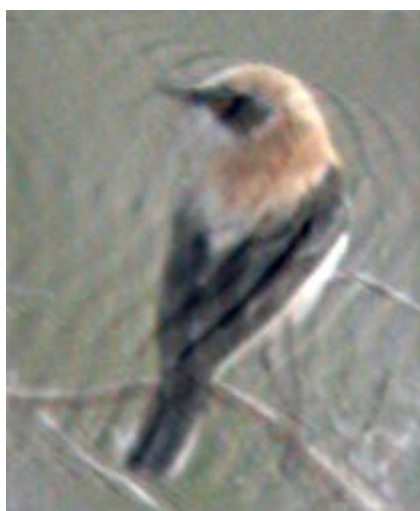
(e)   (f)

Fig. 4.10. (a) Blurred image. Deblurred using (b) Spatial kurtosis measure (c) Spectral kurtosis measure. (d) RPSNR measure (e) BRISQUE measure and (f) NIQE measure based BID scheme.

4.7. Discussion

In this chapter, the existing blind IQMs BRISQUE, NIQE and a novel full-reference blind quality measure RPSNR were investigated as alternative deblurring measures to spatial and spectral kurtosis for BID.

RPSNR based PSF estimates produce high quality deblurred images as shown by the high PSNR values of the original-deblurred pair. The deblurred images when reconvolved with the estimated PSF produce the reblurred images. It was shown that if the candidate PSF is near the original PSF, it will produce similar blurring in the reblurred image as the original blurred image (Table 4.1).

Experiments include testing of artificially blurred as well as the real blurred images. In the artificial blurring case, the three types of parametric blurs i.e. Gaussian, motion and out-of-focus blur were considered. For the Gaussian deblurring results (Table. 4.2), BRISQUE based deblurred images were estimated to have better visual quality as compared to the NIQE and RPSNR estimates. In the case of motion deblurring (Table. 4.3), RPSNR based deblurred images produced better visual quality as compared to the NIQE and BRISQUE estimates. However, for the out-of-focus deblurring (Table. 4.4), none of the IQMs i.e. RPSNR, BRISQUE and NIQE could produce better results for all the quality measures. In the out-of-focus deblurring case, the results show ringing and residual blur in the image. For the real life motion blurred images, BRISQUE based PSF estimates show high quality deblurred images as compared to spatial and spectral kurtosis, RPSNR and NIQE deblurring measures (Table. B.2).

Table 4.6 compares the computation time per iteration of the blind IQMs on a multiple core machine. Spatial and spectral kurtosis depict low computation time due to their simple computation while RPSNR depicts a slightly higher computation time, probably due to the overhead caused at the reblurring stage. NIQE shows relatively lower computation time than BRISQUE due to its implementation as code rather than executables as used in BRISQUE. On average, the IQMs show a 50 % reduction in computation time over four processor cores.

Table 4.6 Computation time per iteration for different blind IQMs over different number of cores.

IQM	Number of Cores		
	1	*2*	*4*
Spatial	99	73	44
Spectral	90	69	38
RPSNR	149	121	76
NIQE	194	127	95
BRISQUE	215	163	112

In order to single out an IQM as the deblurring measure, the NSR values of the Wiener filter corresponding to the estimated PSFs were also analyzed. It was observed that BRISQUE estimates the PSF for relatively lower NSR values, resulting in comparatively sharper image. However, this induces relatively more deblurring noise in the image. Based on the low NSR values, BRISQUE was selected as the deblurring measure for arbitrarily shaped PSF estimation BID scheme of Chapter 5.

The computational efficiency of the blind IQMs based BID schemes is also compared. Spectral kurtosis is found to be the most computationally efficient IQM for BID. This is attributed to its calculation in the frequency domain which omits iFFT during each computational iteration of the BID algorithm. However, BRISQUE is the most computationally inefficient of the IQMs for BID. This is due to the use of support vector machine for calculating the image quality, which itself takes more processing time.

4.8. Summary

In this chapter, a novel full-reference yet blind quality measure RPSNR was proposed as deblurring measure. The RPSNR deblurring measure along with BRISQUE and NIQE IQMs have been investigated as alternative deblurring measures to spatial and spectral kurtosis.

The proposed RPSNR performs well in the case of deblurring of motion blurred images. However, due to the presence of residual blur in the deblurred images, the RPSNR measure could not to correctly estimate the PSF parameter values.

The BRISQUE measure shows high quality deblurred images for real life motion blurred images; however, it was found to be computationally inefficient. The selection of IQM for further experimentation was based on the quality of deblurred images. Therefore, BRISQUE was selected as the suitable IQM for BID scheme.

In real life, the blurs are more complex as compared to the parametric blurs, which cannot be modelled correctly using the parametric PSF models presented earlier. Chapter 5 presents arbitrarily shaped PSF estimation scheme to tackle the problem of blind deblurring of images corrupted by arbitrarily shaped PSFs.

Chapter 5

Arbitrarily Shaped Point Spread Function Estimation and Blind Image Deblurring Scheme

5.1. Introduction

The research work in this chapter focuses on an interesting challenge faced in BID. It relates to the estimation of arbitrarily shaped (non-parametric or generic) PSFs of motion blur caused by camera handshake. These PSFs exhibit much more complex shapes than their parametric counterparts and deblurring in this case requires intricate ways to estimate the blur and effectively remove it. This chapter introduces a novel blind deblurring scheme visualized for deblurring images corrupted by arbitrarily shaped PSFs. It is based on GA and utilizes the BRISQUE measure as the fitness function for arbitrarily shaped PSF estimation. The proposed BID scheme has been compared with other deblurring schemes that include the single image motion deblurring scheme of Fergus et al. [17] and the single/noisy-paired motion deblurring scheme of Whyte et al. [18].

5.2. Arbitrarily Shaped PSFs

Until now, the PSF for uniform blurring has been estimated using the functional form for some common types of blur i.e. the Gaussian blur, motion blur and out-of-focus blur. In real life, especially in the case of motion blur resulting from camera handshake, the blur follows convoluted paths resulting in complex shaped PSFs [17, 45]. There exist many schemes in the literature dealing with the restoration of such images with some listed in [17, 18, 39, 41, 42, 44]. Their shape cannot be easily modelled by a simple equation or defined by a mathematical model for a set of its parameter(s). PSFs in such cases exhibit an arbitrary shape and deblurring in this case requires intricate ways to estimate the blur and effectively remove it. Arbitrarily shaped PSFs have been shown to exist in the case of atmospheric turbulence blur as well [131]. This chapter focuses on the challenging task of restoring of images blurred by arbitrarily shaped PSF resulting from motion blur due to camera handshake.

Some examples of real blurred images corrupted by arbitrarily shaped PSFs are shown in Fig. 5.1(a), with their close-ups in Fig. 5.1(b). The camera shake pictures exhibit PSFs far different from that found when linear motion was investigated. The hand sketched PSFs are shown in Fig. 5.1(c). Though modelling or defining them using a large set of parameters is not impossible, estimating the blurring PSF for a large set of blurring PSF parameter(s) values becomes challenging, computationally and in terms of convergence of the BID scheme.
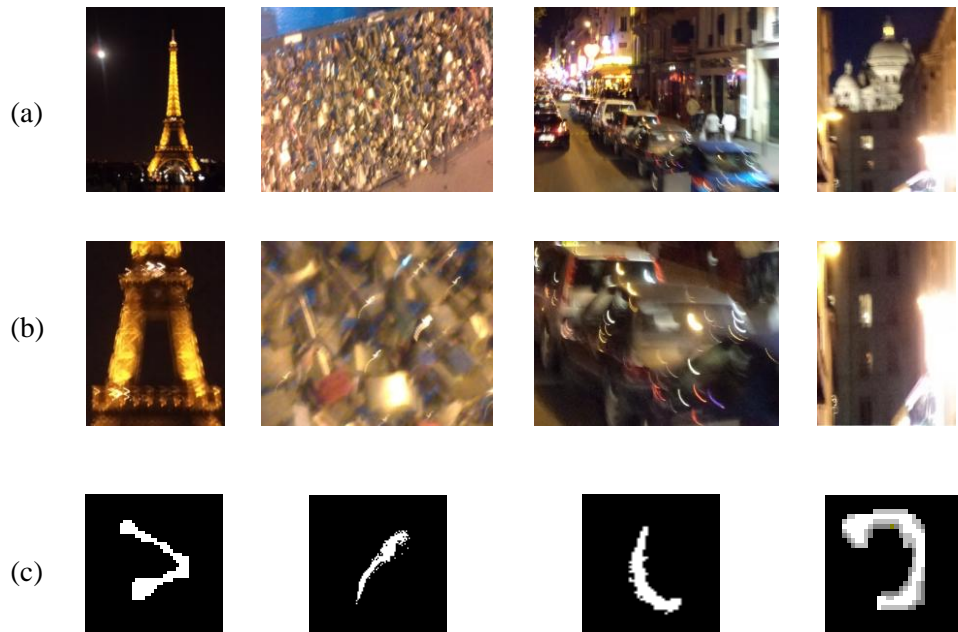
Fig. 5.1 Examples of arbitrarily shaped PSFs. Row (a) Real blurred images Row (b) Image sections and Row (c) Corresponding hand sketched PSFs.

108

5.3. Proposed Blind Deblurring Scheme for Arbitrarily shaped PSF Estimation

The main concept behind the proposed BID scheme is stated as follows:

Any parametric or non-parametric uniform PSF can be approximated by estimating its coefficients' values using a deblurring measure as feedback of deblurred image quality to the BID scheme.

A PSF can be assumed as an array of random values under the constraints mentioned below:

- The PSF has a finite support size, with a finite number of rows and columns m and $n,$ respectively.
- The energy of the PSF is maintained i.e. $\sum\limits_{m,n} h(m,n) = 1$
- The PSF is space invariant. The same blurring/averaging effect is presented by the blurring kernel at each pixel location.
- The PSF coefficients are non-negative.

During each iteration, a coefficient value is updated in the direction of improved deblurred image quality which can be calculated using any restoration measure e.g. spatial or spectral non-Gaussianity measures, non-reference or full-reference IQMs etc. The process can be evaluated for a fixed number of iterations or it can be terminated when the difference in the measure value in subsequent iterations is lower than a specified threshold value.

Fig. 5.2 shows a glimpse of the restoration process by estimating the PSF coefficients. The original PSF is depicted in Fig. 5.2 (a) while the estimation process is illustrated in Fig. 5.2 (b). From an initial set of random values, the process keeps on estimating/changing the PSF weights till the deblurring measure stops showing improvement.

(a)

(b)
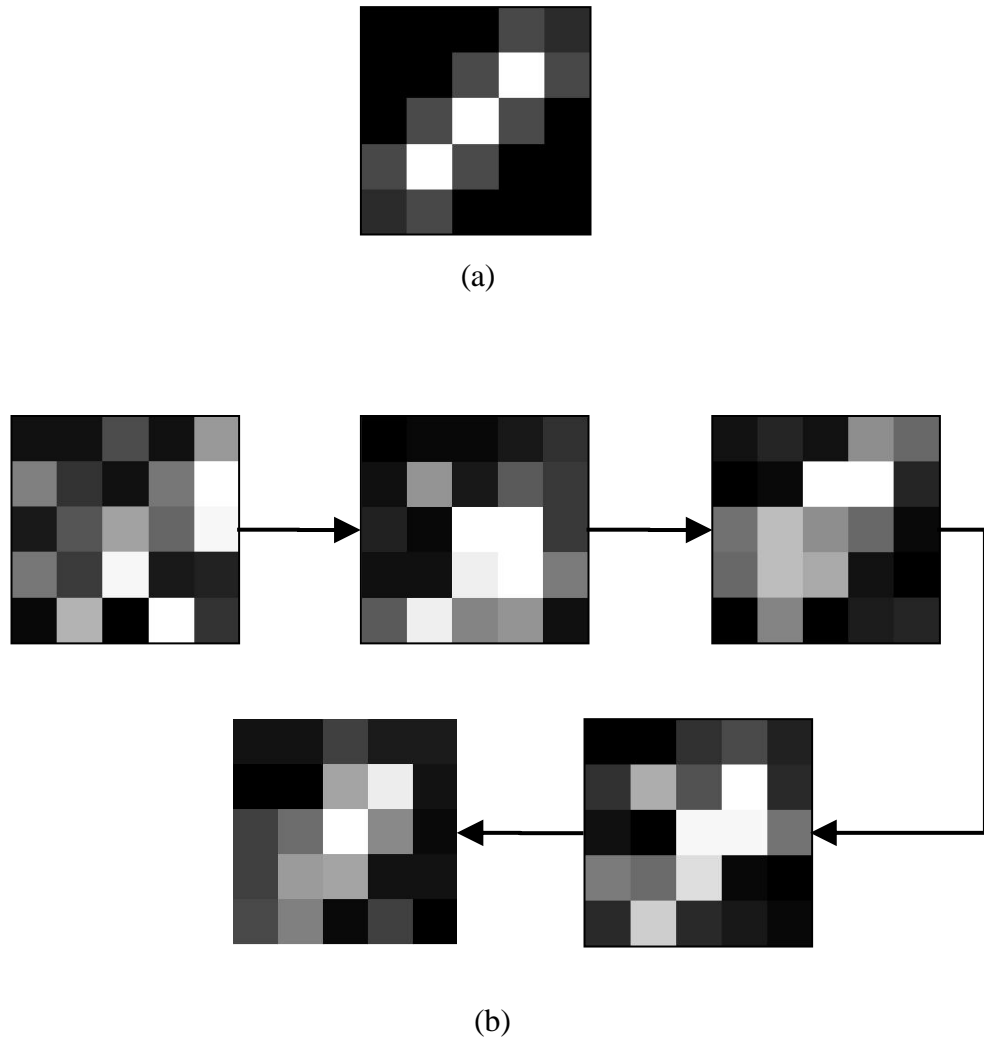
Fig. 5.2 (a) Blurring PSF (b) An overview of the PSF estimation process through different steps.

The deblurring scheme is optimized using GA. An added advantage of such a BID scheme is that the same method can easily be extended for estimating other types of blur apart from camera handshake. Also, the BID scheme based on GA is flexible and so it can be easily incorporated with any deblurring measure as the fitness function. Details of the GA based optimization are as follows:

- Step 1: Initialize the GA parameters i.e. population, size, crossover rate, mutation rate etc.
- Step 2: Generate an initial chromosome population where each chromosome contains information about all the coefficients of the finite support size PSF.
- Step 3: Perform iteration and find the restored image through Wiener filtering for all the chromosomes.
- Step 4: Calculate fitness function values for the initial population.

110

- Step 5: Select the best fitting group of chromosomes based on either roulette or threshold based selection.

- Step 6: Generate a new population from the chromosomes selected in Step 5 through crossover and mutation. Each crossover is performed with probability p_c {0.5,…,0.8} and cross over points are selected at random. Mutation involves modification of components of the individual chromosomes with probability p_m. p_m is usually a small number usually assumed in the range of {0.001,....,0.01}. Roulette wheel selection is used to select the best fitting individuals among the population.

- Step 7: Repeat the process again from Step 3 till the algorithm converges for the deblurring measure.

5.4. Experimental Setup

Test images include images from the Waterloo Bragzone grayscale image dataset as well as a collection of real life blurred images that were captured by the author. The camera used to capture the real blurred images was a Sony DSC-W310. The real life camera handshake images demonstrate a reasonable amount of noise. Noise can affect the deblurring results by changing the statistical properties of the image. Initially a self-coded GA variant was employed for optimizing the search. After MATLAB released support for GA in its optimization toolbox (see Appendix D for details), the proposed BID was successfully implemented on it and evaluated using parallel processing cores. The proposed BID scheme's estimated PSF coefficients are not exactly the same as the original PSF but are rather a near approximation of the original blurring PSF. This affects the brightness and contrast of the deblurred images thus rendering the full-reference IQMs (PSNR, MSSIM, UQI etc) invalid for quantitative image quality evaluation. Rather, non-reference IQMs BRISQUE and NIQE were used for this purpose. BRISQUE was also used as the deblurring measure for the restoration of the images due to its efficient deblurring performance depicted in chapter 4. The BRISQUE model was used over NIQE because of its exceptional predictive performance. The proposed BID scheme requires a fixed PSF size input from the user. In this regard, a method for visual judgement based PSF size estimation prior to deblurring is discussed in Section 5.5. In the case of real blurred images, the PSF size was estimated by inspecting a blur region in the image. Deblurring results for artificially blurred and real blurred images are presented below.

5.5. PSF Support Size Estimation

In order to estimate the PSF support size, a simple technique is proposed here. Initially, the GA is run for different sizes of PSF for only a few iterations. The results are then visually judged for ringing artefacts. The ringing artefacts are severe if the initial PSF estimate is bigger in size than the actual blur PSF which creates estimation error among them. The user can thus pick a PSF size which shows reduced ringing for the deblurred image. Fig. 5.3 shows the image deblurred for varying sizes of PSF. The initial blur PSF size was 8x7 coefficient matrix. The 5x5 matrix PSF depicts image sharpness as compared to the 3x3 matrix. All other bigger size matrices result in severe ringing in the deblurred image. The deblurring result for the 5x5 size estimated PSF is shown in Fig. 5.4.

3x3 PSF size	5x5 PSF size	7x7 PSF size

9x9 PSF size	11x11 PSF size

Fig. 5.3 Deblurring results for varying PSF sizes. A smaller PSF coefficient matrix results in almost no deblurring, while ringing artefacts are observed PSF sizes larger than 5x5.
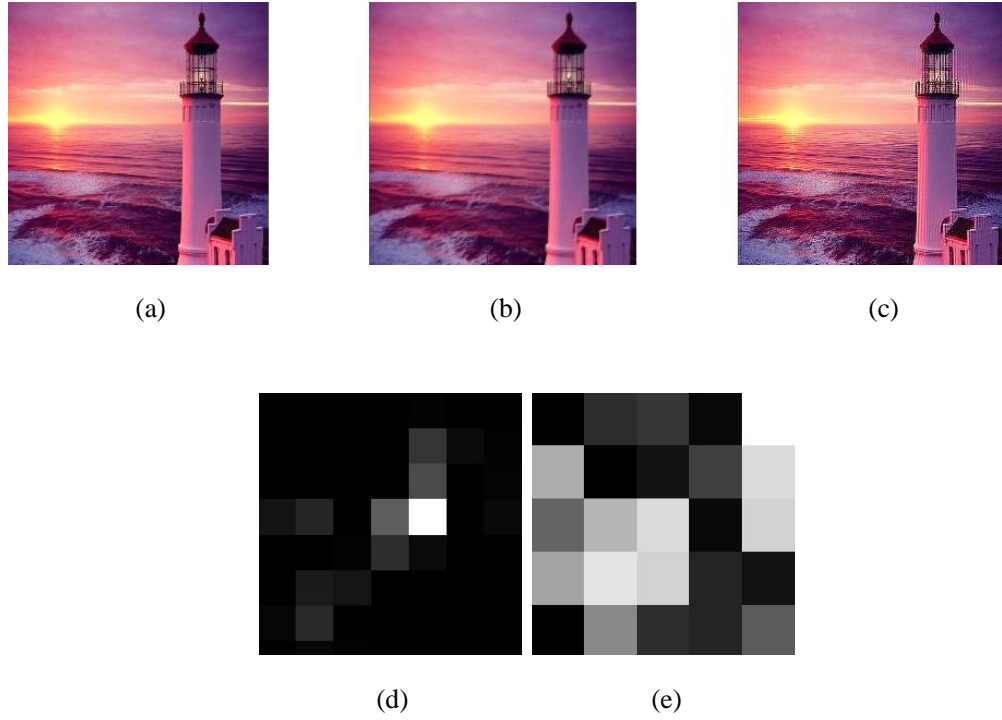
Fig. 5.4 Deblurring result for arbitrarily shaped PSF of size 5x5 pixels estimated by visual judgment of ringing artefacts. (a) Original image (b) Blurred image (c) Deblurred image (d) Blurring PSF and (e) Estimated PSF of size 5x5 pixels.

5.6. Deblurring Results for Artificially Blurred Images

Since the BID scheme can also be extended for uniform parametric blurs, the algorithm was first evaluated for the less complex parametric form blurs before testing it for arbitrarily shaped PSFs. Deblurring results for Gaussian, motion and out-of-focus blur are presented below. Detailed deblurring results for parametric and arbitrarily shaped PSF estimation are presented in Appendix C.

5.6.1. Restoration of Parametric PSF Blurred Images

The first set of tests included deblurring images blurred by Gaussian PSF. Fig. 5.5 shows the deblurring results for images blurred by different Gaussian PSFs. It can be observed that the estimated PSF takes on a rough shape of the blurring PSF as viewed in Fig. 5.5(e). Results presented here were obtained when the algorithm stopped, as the tolerance value for the fitness function was attained. The restored image appears sharper and much more detailed than its blurred counterpart.

(a) (b) (c)

(d) (e)
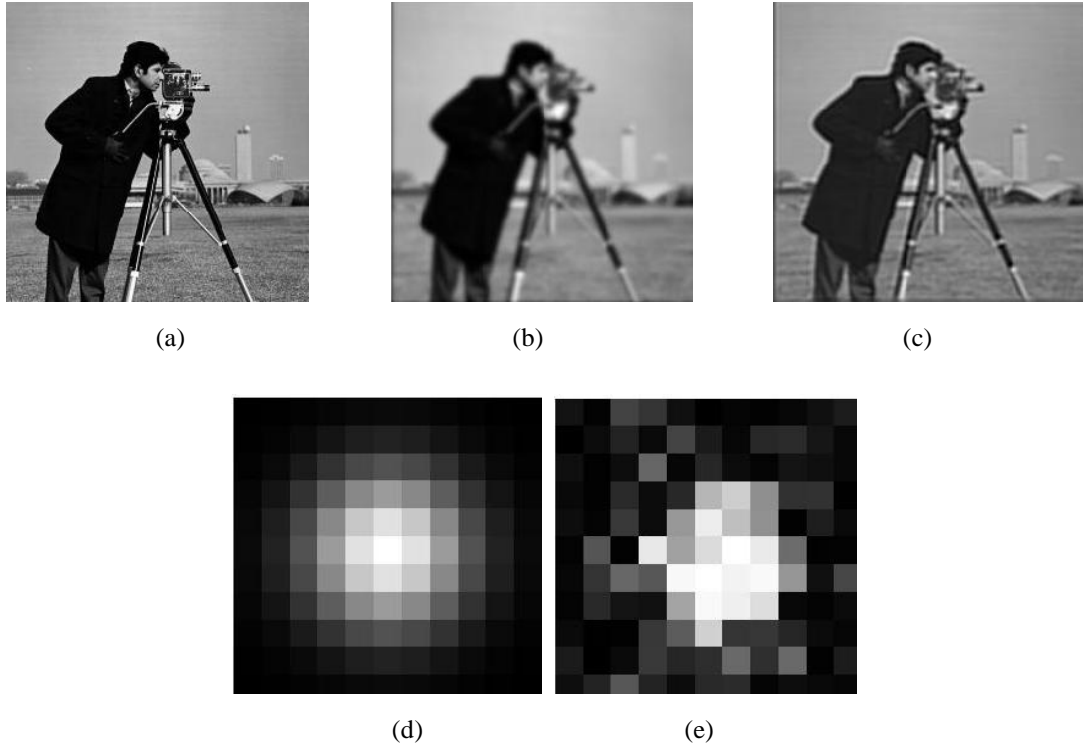
Fig. 5.5 Deblurring result for image blurred by Gaussian PSF of size 11 x 11 pixels and variance $\sigma^2=2$. (a) Original image (b) Blurred image (c) Deblurred image (d) Blurring PSF and (e) Estimated PSF.

The second set of tests included deblurring images artificially blurred by motion blur. Fig. 5.6 shows the deblurring results for the Lena image blurred by motion blur PSF of length 11 pixels and angle 23 degrees. The estimated PSF is a near approximation of the blurring kernel achieved for the fixed iterations of the deblurring algorithm.

Fig. 5.7 shows the deblurring result of the Barbara images under the influence of out-of-focus blur of radius 9 pixels. Deblurring results show the estimated PSF converging towards the original blur PSF. For large out-of-focus blur, a lot of attenuation occurs for the high frequency elements in the image and recovery in this case is not that sharp as observed for the Barbara image in Fig. 5.7 (c)

(a) (b) (c)

(d) (e)
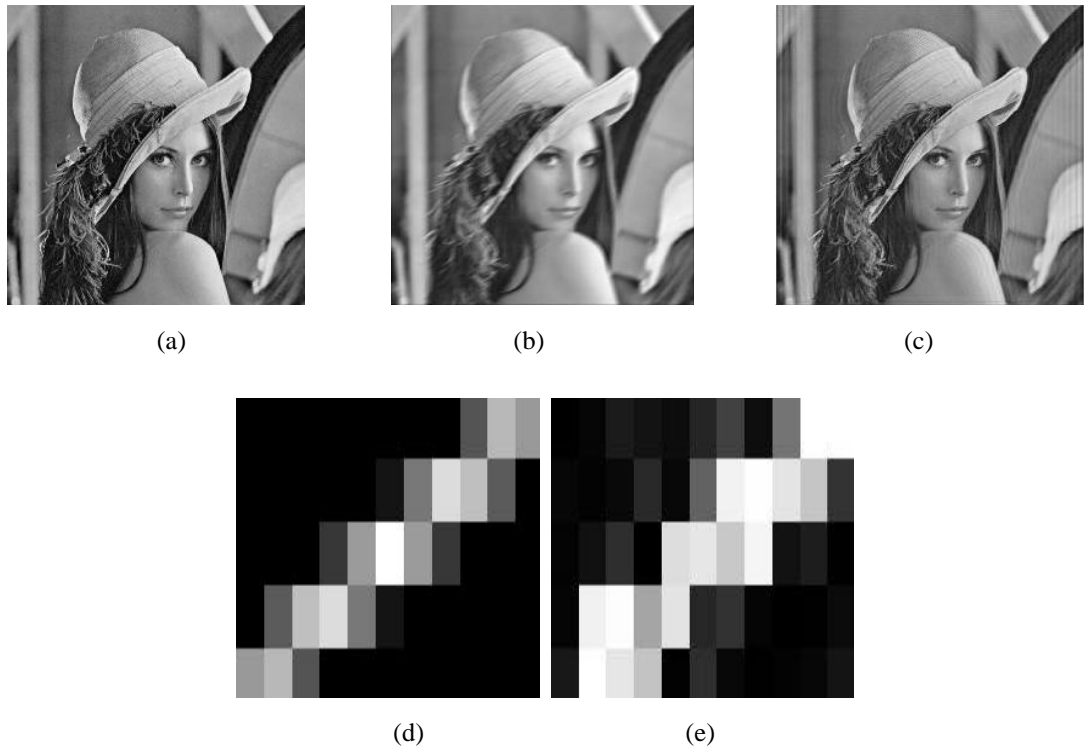
Fig. 5.6 Deblurring result for image blurred by motion blur PSF of length 11 pixels and angle 23°. (a) Original image (b) Blurred image (c) Deblurred image (d) Blurring PSF and (e) Estimated PSF.

(a) (b) (c)

(d) (e)

Fig. 5.7 Deblurring result for image blurred by out-of-focus blur PSF of radius 9 pixels. (a) Original image (b) Blurred image (c) Deblurred image (d) Blurring PSF and (e) Estimated PSF.

115

5.6.2. Deblurring Images Blurred by Arbitrarily Shaped PSFs

Arbitrarily shaped PSFs were used to blur the images and then recover using the proposed scheme. Deblurring results shown in Fig. 5.8 – 5.11 depict that the proposed algorithm was able to estimate the blurring shape/coefficients to a great extent. The deblurred images appear sharper than their blurred counterparts.

In Fig. 5.9 it can be observed that the estimated PSF was of size 5 x 5 pixels while the actual blurring kernel was of size 15 x 11 pixels. The size for the estimated PSF was selected as 5 x 5 pixels, for a bigger support size resulted in increased ringing in the deblurred image. A 5 x 5 coefficient matrix turned out as the best choice for estimating the original PSF's major coefficient values. Fig. 5.10(e) and Fig. 5.11(e) depict the estimated PSFs have slight resemble in shape to their respective blurring kernels.

| (a) | (b) | (c) |

| (d) | (e) |
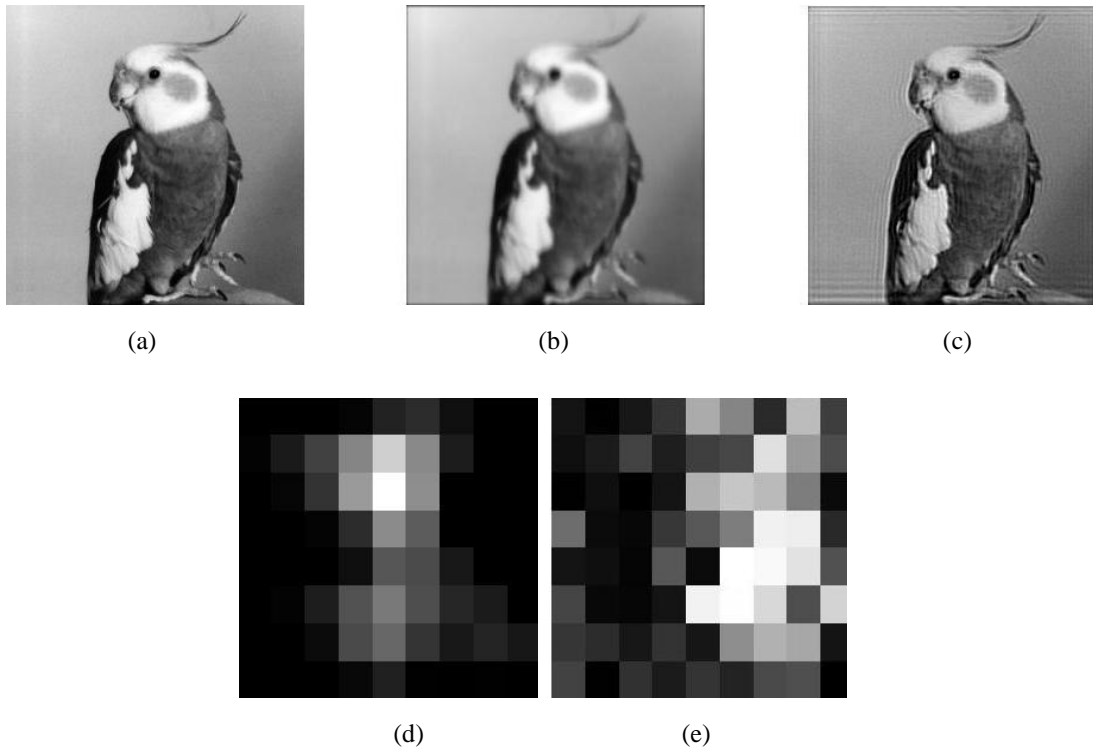
Fig. 5.8 Deblurring result for Bird image blurred by arbitrary PSF of size 9 x 9 pixels. (a) Original image (b) Blurred image (c) Deblurred image (d) Blurring PSF and (e) Estimated PSF.

(a)   (b)   (c)

(d)   (e)
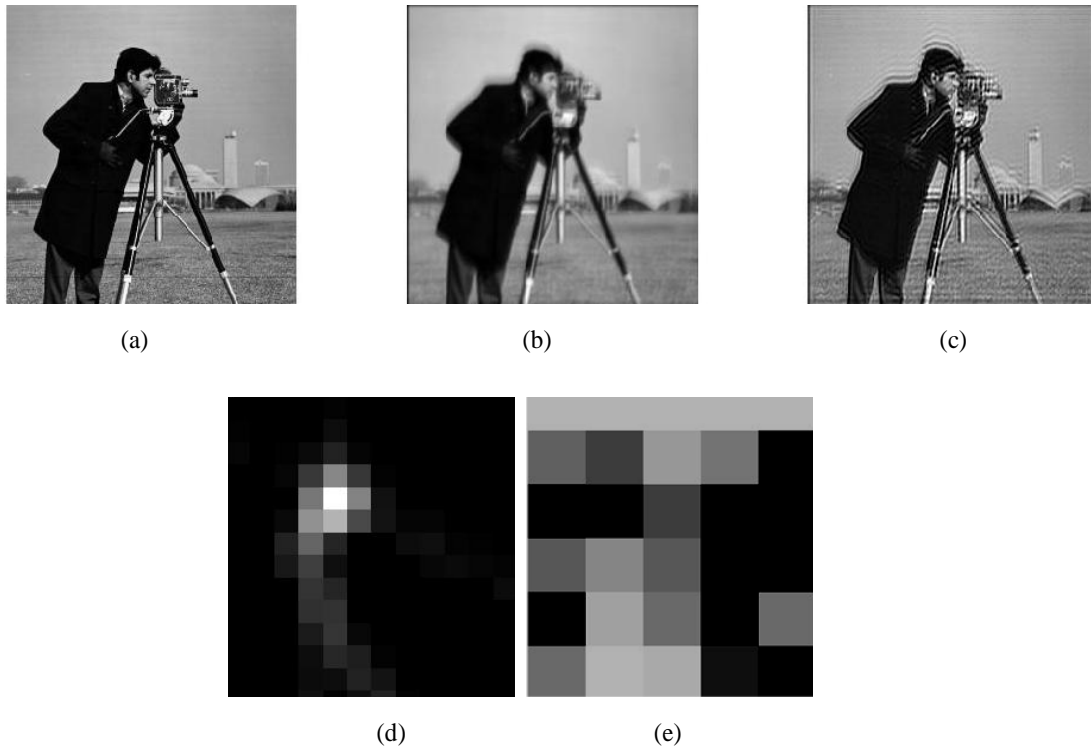
Fig. 5.9 Deblurring result for Cameraman image blurred by arbitrary PSF of size 15 x 11 pixels. (a) Original image (b) Blurred image (c) Deblurred image (d) Blurring PSF and (e) Estimated PSF.

(a)   (b)   (c)

(d)   (e)
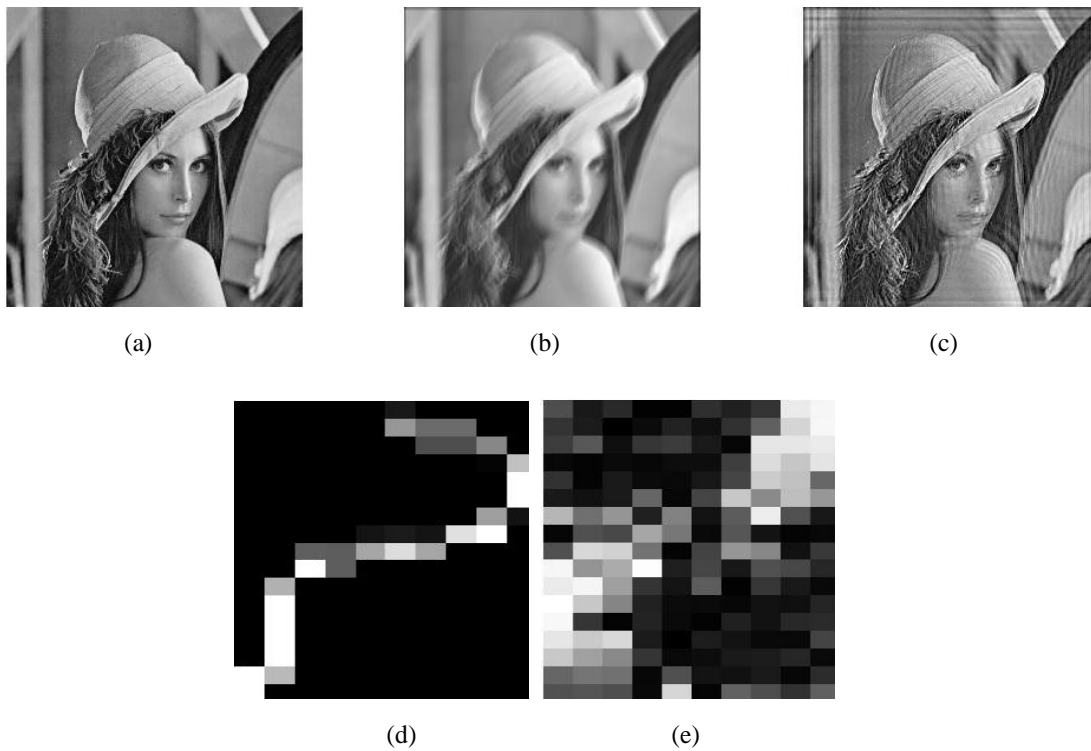
Fig. 5.10 Deblurring result for Lena image blurred by arbitrary PSF of size 16 x 10 pixels. (a) Original image (b) Blurred image (c) Deblurred image (d) Blurring PSF and (e) Estimated PSF.

(a)　　　　　　　　　　(b)　　　　　　　　　　(c)

(d)　　　　　　　　(e)
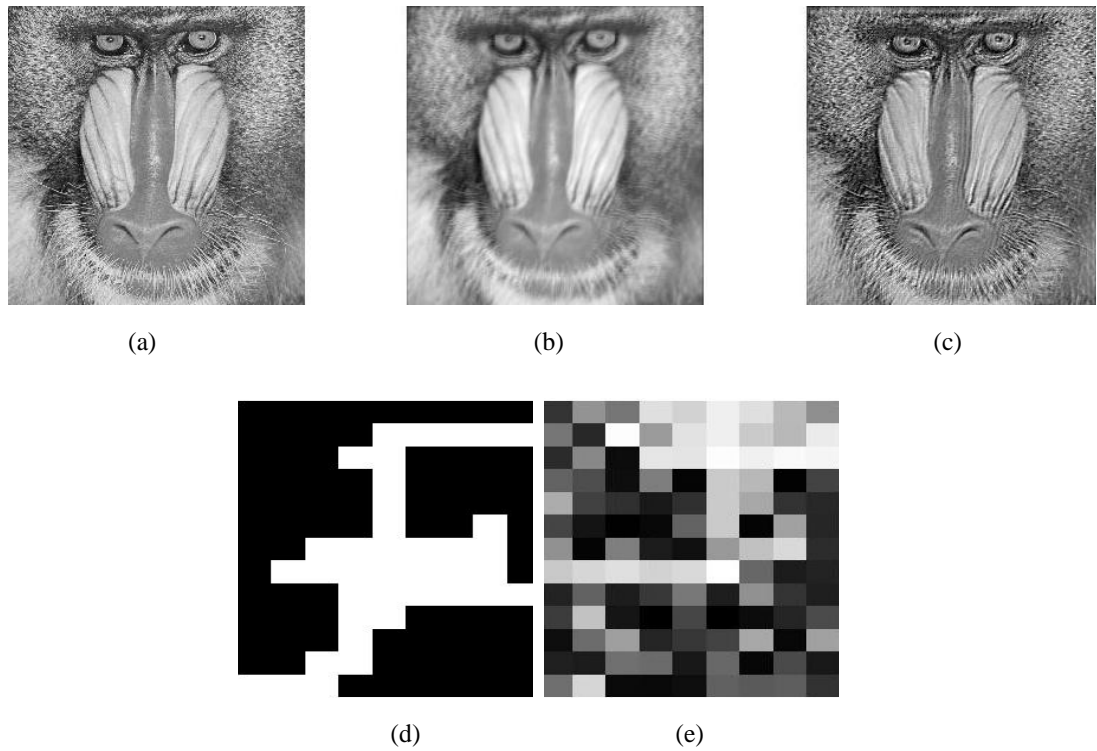
Fig. 5.11 Deblurring result for Mandrill image blurred by arbitrary PSF of size 11 x 14 pixels. (a) Original image (b) Blurred image (c) Deblurred image (d) Blurring PSF and (e) Estimated PSF.

Table 5.1 illustrates the quantitative IQMs values for the deblurred images using the arbitrarily shaped PSF estimation scheme. BRISQUE and NIQE values for the original, blurred and deblurred image are shown for comparison of deblurring quality. Low values of BRISQUE and NIQE represent high quality images. For Fig. 5.11(c), both NIQE and BRISQUE show improvement in the image. It can be seen that the ringing in the deblurred image is minimal. Though the deblurred images in Fig. 5.5 - 5.11 are recovered well as observed visually, the BRISQUE and NIQE values erroneously depict the deblurred images are of less quality. This is due to the presence of residual blur left from incomplete deblurring using the PSF estimates that are not the same as the original blurring PSFs. The tests also show that BRISQUE and NIQE IQMs may not be ideal blind IQMs and more effort is still needed to enhance their performance.

Table 5.1 Deblurring results for artificially blurred images. Deblurred image quality is evaluated using BRISQUE and NIQE IQMs.

Figure Number	Blurring Filter	Size (pixels)	Parameter Value
Fig. 5.5(d)	Gaussian	11x11	$\sigma^2=2.0$
Fig. 5.6(d)	Motion	5x11	L=11, A=23
Fig. 5.7(d)	Out-of-focus	19x19	R=9
Fig. 5.8(d)	Arbitrary	9x9	-
Fig. 5.9(d)	Arbitrary	15x11	-
Fig. 5.10(d)	Arbitrary	16x10	-
Fig. 5.11(d)	Arbitrary	11x14	-

	Image Quality Measured Using BRISQUE		
	Original	Blurred	Deblurred
Fig. 5.5	6.68	35.88	47.27
Fig. 5.6	10.26	16.67	52.07
Fig. 5.7	50.12	30.57	63.38
Fig. 5.8	14.30	14.67	39.11
Fig. 5.9	14.13	17.95	36.43
Fig. 5.10	15.45	20.77	49.80
Fig. 5.11	30.07	49.04	42.27

	Image Quality Measured Using NIQE		
	Original	Blurred	Deblurred
Fig. 5.5	5.11	4.57	6.89
Fig. 5.6	5.11	4.69	7.19
Fig. 5.7	4.98	6.12	9.66
Fig. 5.8	4.74	4.74	7.43
Fig. 5.9	5.50	5.94	7.56
Fig. 5.10	4.98	5.72	6.30
Fig. 5.11	6.42	8.85	7.94

σ^2=Variance, L=length, A=Angle, R=Radius

5.7. Restoration of Real Blurred Images

Real life blurred images were used to test the efficacy of the deblurring scheme for practical application. The images depict motion blur resulting from camera handshake. A brief discussion on the deblurring scheme of Fergus et al. [17] and Whyte et al. [18] as benchmark for comparison is provided below. These schemes were picked out due to the availability of their code. Other schemes were omitted from comparison due to their code complexity and large computation time.

The scheme from Fergus et al. estimates the blurring PSF and then deconvolves the

image using a Richardson-Lucy filter. The PSF estimation process depends on image statistics, especially pixel colour/ image gradients. Their scheme was designed to estimate in-plane motion PSF while neglecting out-of-plane (rotational) motion blur. The second scheme by Whyte et al. extends the scheme of Fergus et al. by incorporating rotational blur constraints as well as employing it for two deblurring cases. In the first deblurring case their scheme has been used to deblur a single-shot image, while in the second deblurring case, it utilizes information from a noisy pair of blurred image along with a single-shot blurred image to estimate the blurring PSF. Fig 5.12 shows the deblurring results for the Ian_1 image from the source in [132]. The blurred image is shown in Fig.5.12(a). The deblurred image using the proposed BID scheme is shown in Fig. 5.12(b) with the estimated PSF in Fig. 5.12(e). The blurred image after restoration is reasonably clear with some ringing in Fig. 5.12(b) for the proposed scheme. However, the best result in terms of visual quality is achieved for the Fergus et al. based BID scheme in Fig. 5.12(c). Whyte et al.'s scheme was unable to estimate the blurring kernel properly and the deblurred image in Fig. 5.12(d) contains large residual blur and ringing.

Deblurring results of the Basilica image are shown in Fig. 5.13. The blurred image in Fig. 5.13(a) was deblurred using the proposed BID scheme. The deblurred image and the corresponding estimated PSF are shown in Fig, 5.13(b) and Fig.5.13(e). The image seems to have recovered well as compared to the deblurred images in Fig.5.13(c) and (d) for the BID schemes of Fergus et al. and Whyte et al., respectively. Looking at the estimated PSFs in Fig. 5.13(f) and Fig.5.13(g), it can be seen the estimated PSFs are approximated for few points as compared to the estimated PSF using the proposed scheme in Fig.5.13(e).

Fig. 5.14 shows the deblurring results for the Monument image. The blurred image in Fig. 5.14 (a) was deblurred using the proposed scheme, Fergus et al. and Whyte et al. scheme in Fig. 5.14(b), (c) and (d) with their respective estimated PSFs shown in Fig. 5.14 (e), (f) and (g). In Fig. 5.14, the image seems to have recovered well, but looking it in detail, the text in the image is unreadable, as shown in Fig. 5.15

None of the BID schemes were able to estimate the PSF of the real life blurred image perfectly. For the proposed BID scheme, the rationale behind its inefficiency can be related to the lack of more extreme image and PSF constraints. However, even in the case of the deblurring schemes of Fergus et al. and Whyte et al., much more advanced image constraints and in-plane/out-plane PSF constraints fail to enhance the deblurring performance. This is probably due to blur models and image/blur

statistics constraints that leave large uncertainties in the modelling and computation of the blurring kernel [39, 45]. Also, the presence of noise in the blurred images may affect the deblurring outcome.

(a)

(b)

(c)

(d)

(e)

(f)

(g)
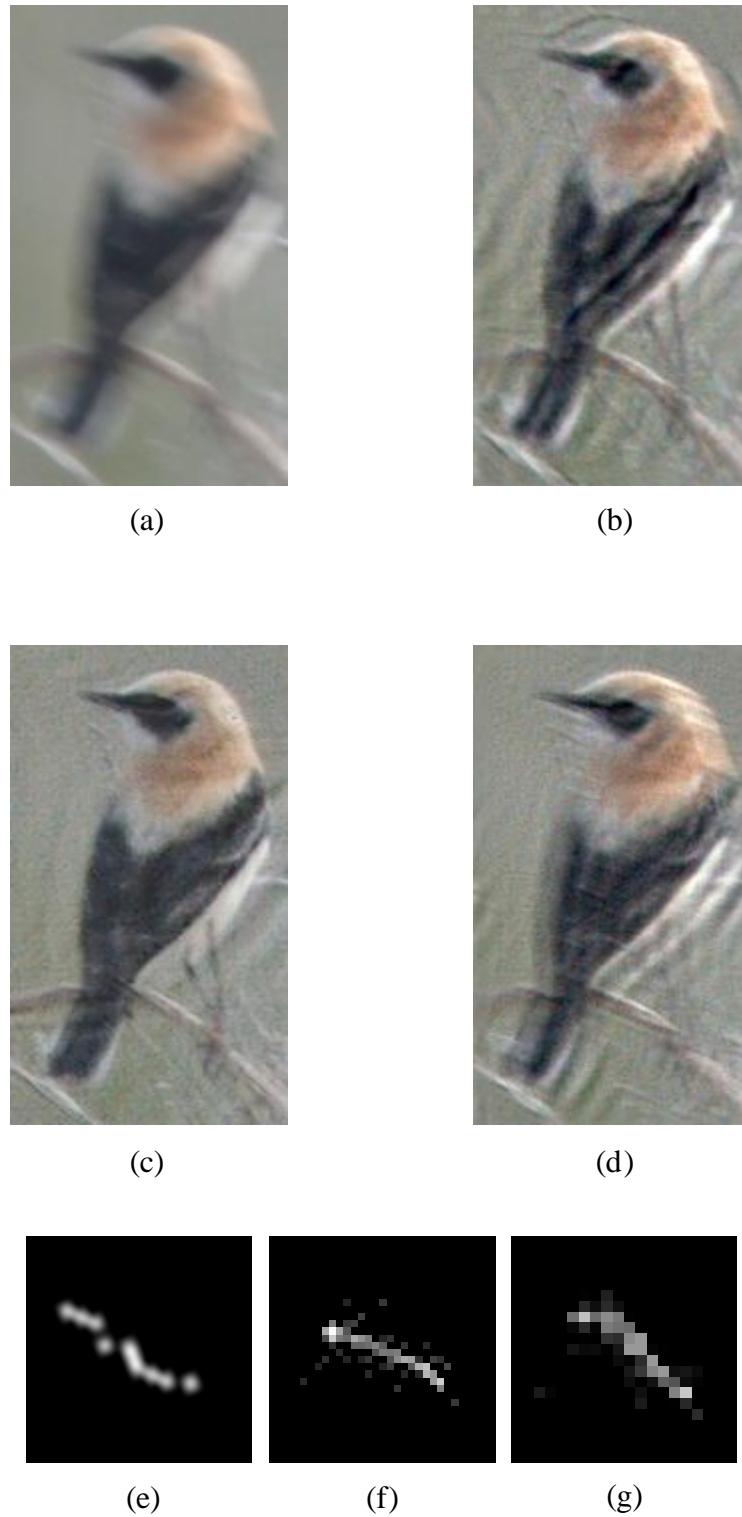
Fig. 5.12 Deblurring result for Ian_1 image blurred by arbitrary PSF resulting from camera handshake (a) Blurred image. Deblurred using (b) Proposed BID scheme (c) Fergus et al. scheme (d) Whyte et al. scheme with their respective estimated PSFs in (e), (f) and (g).
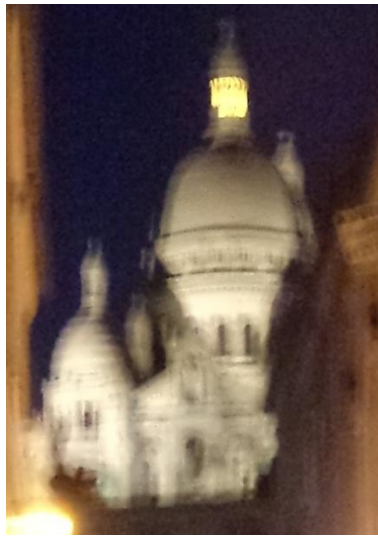
(a)

(b)

(c)

(d)
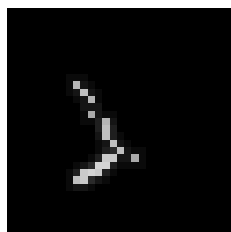
(e)
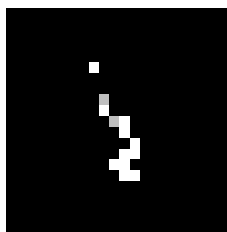
(f)
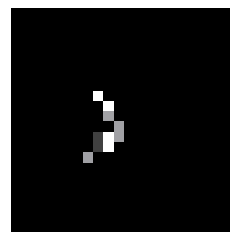
(g)

Fig. 5.13 Deblurring result for Basilica image blurred by arbitrary PSF resulting from camera handshake (a) Blurred image. Deblurred using (b) Proposed BID scheme (c) Fergus et al. scheme (d) Whyte et al. scheme with their respective estimated PSFs in (e), (f) and (g).

122

(a)

(b)

(c)

(d)
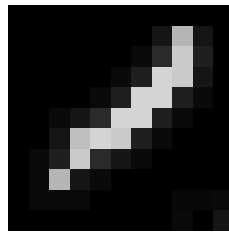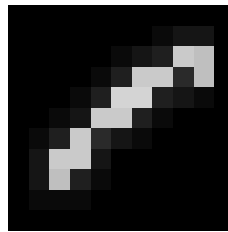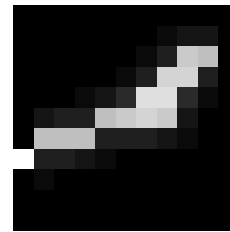
(e)   (f)   (g)

Fig. 5.14 Deblurring result for Monument image blurred by arbitrary PSF resulting from camera handshake (a) Blurred image. Deblurred using (b) Proposed BID scheme (c) Fergus et al. scheme (d) Whyte et al. scheme with their respective estimated PSFs in (e), (f) and (g).

(a)

(b)

(c)

Fig. 5.15 Deblurring results for section of Monument image using (a) Proposed BID scheme (b) Fergus et al. scheme and (c) Whyte et al. scheme. The text in the image is unreadable in all cases.

5.8. Discussion

A novel BID scheme based on GA and utilizing BRISQUE measure as the fitness function is presented for deblurring images corrupted by arbitrarily shaped PSFs. The proposed BID scheme can estimate any parametric or non-parametric PSF coefficients' values using any IQM as deblurring measure for feedback of deblurred image quality to the BID scheme. During each iteration, a coefficient value is updated in the direction of improved deblurred image quality which can be measured using the blind IQM. The process can be evaluated for a fixed number of iterations or it can be terminated when the difference in the measure value in subsequent iterations is lower than a specified threshold value.

The proposed BID scheme's estimated PSF coefficients are not exactly the same as the original PSF but are rather a near approximation of the original blurring PSF. This affects the brightness and contrast of the deblurred images thus rendering the

full-reference IQMs (PSNR, MSSIM, UQI etc) invalid for quantitative image quality evaluation. Hence, non-reference IQMs BRISQUE and NIQE were used for computation of deblurred image quality.

Initially a self-coded GA variant was employed for optimizing the search algorithm which was later replaced by MATLAB based GA in its optimization toolbox. The proposed BID was successfully evaluated using parallel processing cores. The proposed BID scheme requires a fixed PSF size input from the user. In this regard, a method for visual judgement based PSF size estimation prior to deblurring is discussed in Section 5.5. In the case of real blurred images, the PSF size was estimated by inspecting a blur region in the image.

Since the BID scheme can also be extended for uniform parametric blurs, the algorithm was first evaluated for the less complex parametric form blurs before testing it for arbitrarily shaped PSFs. Results presented here were obtained when the algorithm stopped, as the tolerance value for the fitness function was attained. The restored images appear sharper and much more detailed than its blurred counterpart.

Real life blurred images were used to test the efficacy of the deblurring scheme for practical application. The images depict motion blur resulting from camera handshake. The proposed BID scheme was compared with other deblurring schemes used as benchmark. These included the single image motion deblurring scheme of Fergus et al. [17] and the single/noisy-paired motion deblurring scheme of Whyte et al. [18]. The proposed scheme was well as the benchmark BID schemes were unable to estimate the PSF of the real life blurred image perfectly. The proposed BID scheme was probably inefficient due to the lack of more extreme image and PSF constraints. On the other hand, the deblurring schemes of Fergus et al. and Whyte et al. with much more advanced image constraints and in-plane/out-plane PSF constraints failed to enhance the deblurring performance. This could be probably due to the usage of blur models and image/blur statistics constraints that leave large uncertainties in the modelling and computation of the blurring kernel [39, 45]. The presence of image noise can also be a factor in the inefficient recovery of the blurred images.

5.9. Summary

Arbitrarily shaped PSFs resulting from motion blur and camera handshake, usually present a complex form. The problem of deblurring of images corrupted by such PSFs has been analyzed and a BID scheme is proposed. The proposed BID can

handle both parametric and arbitrarily shaped PSF estimation using a single algorithm, for single-shot blurred images, with enhanced optimization through GA. The deblurring results show effective PSF estimation capability for parametric and arbitrarily shaped PSFs in the case of artificially blurred images. For real life blurred images resulting from camera handshake, the proposed scheme as well as the benchmark schemes strive to correctly estimate the blurring kernel for image restoration. Different IQMs and restoration filters can be easily incorporated in the proposed BID in order to investigate their performance in enhancing the deblurring quality. Modelling and deblurring the complex camera handshake PSFs effectively/perfectly still remains a challenging task.

A GUI based BID toolbox was created, as it is required to readily deploy and apply the proposed BID schemes. It encompasses all the feedback IQMs based BID schemes, used in conjunction with the GA based optimization scheme. Its features are discussed in detail in chapter 6 and presented in the format of a practical lab session worksheet in order to guide the user

Chapter 6

Graphical Interface Based Blind Image Deblurring Toolbox

6.1. Introduction

A GUI enables the user to easily access and use software. It can save valuable time and avoid trouble by evaluating user desired function through a platform of function button and other easy access tools. The lack of GUI results in creating unnecessary difficulty for the user to operate the BID scheme. Most of the BID schemes visited in the literature that result from scientific research usually lack a GUI and are thus not available in the form of toolboxes or individual software. Some of the major reasons are as follows:

- BID algorithms may not be completely automated because of their dependency on such human intervention at different stage(s) of deblurring that cannot be covered by the GUI tools. In such cases multiple files of codes are rather utilized to perform the BID in multiple stages manually by obtaining result from one code file and putting it in another code file as in the case of Shan et al. [39] BID scheme.
- Most of the BID schemes usually address a limited range of the deblurring

problems i.e. either dealing with parametric or non-parametric blur, space invariant or variant blur etc. GUI development in such case would only be useful for limited users.

- BID schemes may not be computationally efficient or they may require further modifications to enhance their deblurring results and thus incorporating them in form of GUI at early stages is not desired.

The benchmark BID schemes (Shan et al. [39], Fergus et al. [17] and Whyte et al. [18]) used for comparison in this research work also lack a graphical interface. Shan et al.'s BID scheme requires command line input to Windows batch files and lacks GUI. The user has to input different parameter values to the batch file required to conduct BID on the image. Fergus et al. and Whyte et al. BID schemes use MATLAB code and require user interaction in image loading, parameter setting in code files to deblurring result presentation. **Recently presented BID schemes** In this research, a GUI toolbox for non-blind image deblurring was developed during the early stages and was regularly updated to incorporate many additional features including region based deblurring, blind IQMs for BID and parametric and non-parametric PSF estimation. After the successful use of blind IQMs for BID, the toolbox was updated to incorporate a GA based BID scheme which can use any of the blind IQMs as a fitness function. It can estimate parametric and arbitrarily shaped PSFs as well.

6.2. Key Features of the Developed GUI Toolbox

The toolbox and the related GUI have features incorporated which allow for:

- Deblurring the complete image or section of it. A moveable bounding box is provided for the user to select any or whole region of the image to deblur as shown in Fig. 6.1 and Fig. 6.2.
- Deblurring with different restoration filters: Wiener, Richardson-Lucy and Regularized. The user can select among any of these classical restoration filters and update their parameter settings.
- Sliders for setting values for the PSF parameter(s) in the case of non-blind deconvolution.
- Deblurring different types of blurs, Gaussian, motion and out-of focus blur.

- Setting values for the PSF parameters, e.g. PSF size and variance for Gaussian blur, length and angle for motion blur, and radius for out-of-focus blur for non-blind deconvolution. The parameter values can be set manually.

- Ringing reduction by using edge-taping technique applied to the image prior to deblurring. This feature is embedded in the code and is always applied to the image.

- File loading and saving and layout change. Image file can be loaded for BID and the deblurred result can be saved using a Windows based file explorer.

- The GUI can execute the code in either serial or parallel mode as desired by the user.

- The GUI allows for easy modification and amendment of the features.

The toolbox is built using MATLAB and its GUI implementation framework named GUIDE as it allows for an easy creation and updating of the GUI. GUIDE based GUI is coded by separate function allowing for easy access and incorporation of future updates. The MATLAB based GUI also supports parallel processing by simply using its distributed computing techniques. The following sections discuss briefly the design and implementation of the toolbox.

6.3. Toolbox Design

The flowchart for the toolbox is presented in Fig. 6.1 shows the workflow of the toolbox. The toolbox's functionality can be divided into three main parts: the data input, BID algorithm execution and the deblurring output section.

6.3.1. Data Input

The toolbox takes the image file in three common image formats at the moment i.e. jpeg, tiff and png. Other formats are also available as optional to the user. After the GUI loads, the user can load an image file by browsing through the computer directory and locating the image file as shown in Fig. 6.2. Once the image is loaded, the user can relocate the bounding box that selects the image section as shown in Fig. 6.3. By default, it covers the whole image. The user then needs to specify the initial PSF size used for estimation.

The user can also select among different deblurring filters i.e. Wiener, Richardson-Lucy and Regularized filter as shown in Fig. 6.4. Settings of the filter need also be input e.g. NSR for Wiener filter, number of iterations for Richardson-Lucy filter etc.

```
                    ┌──────────┐
                    │  Start   │
                    └──────────┘
                         │
                         ▼
                    ╱──────────╱
                   ╱  Load    ╱
                  ╱  Data    ╱
                 ╱──────────╱
                         │
                         ▼
          ┌──────────────────────────┐
          │  User Input: Image       │
          │  section selection,      │
          │  PSF size input          │
          └──────────────────────────┘
                         │
                         ▼
          ┌──────────────────────────┐
          │  User Input: Restoration │
          │  filter selection and    │
          │  settings input,         │
          │  Deblurring IQM          │
          │  selection               │
          └──────────────────────────┘
                         │
                         ▼
             ┌───────────────────┐
             │  User Input:      │
             │  Genetic          │
             │  Algorithm        │
             │  settings         │
             └───────────────────┘
                         │
                         ▼
             ║┌───────────────┐║
             ║│    BID        │║
             ║│  Algorithm    │║
             ║└───────────────┘║
                         │
                         ▼
          ┌──────────────────────────┐
          │  Toolbox Output:         │
          │  Estimated PSF,          │
          │  Deblurred image, IQM    │
          │  plot (optional)         │
          └──────────────────────────┘
                         │
                         ▼
          ⟨──────────────────────────⟩
          ⟨    Display               ⟩
          ⟨  deblurred image         ⟩
          ⟨  and estimated           ⟩
          ⟨    PSF                   ⟩
          ⟨──────────────────────────⟩
                         │
                         ▼
                    ┌──────────┐
                    │   End    │
                    └──────────┘
```
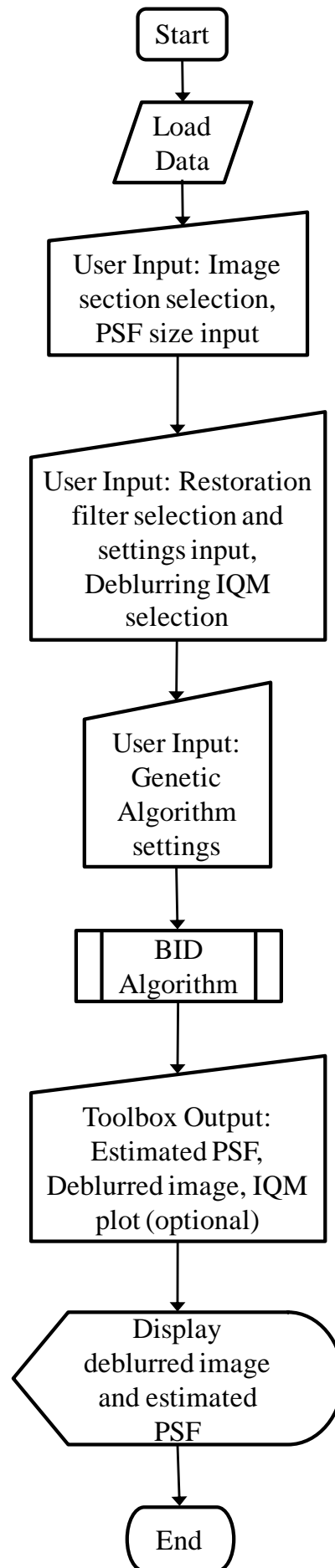
Fig. 6.1 Flowchart presenting the BID Toolbox implementation.

130
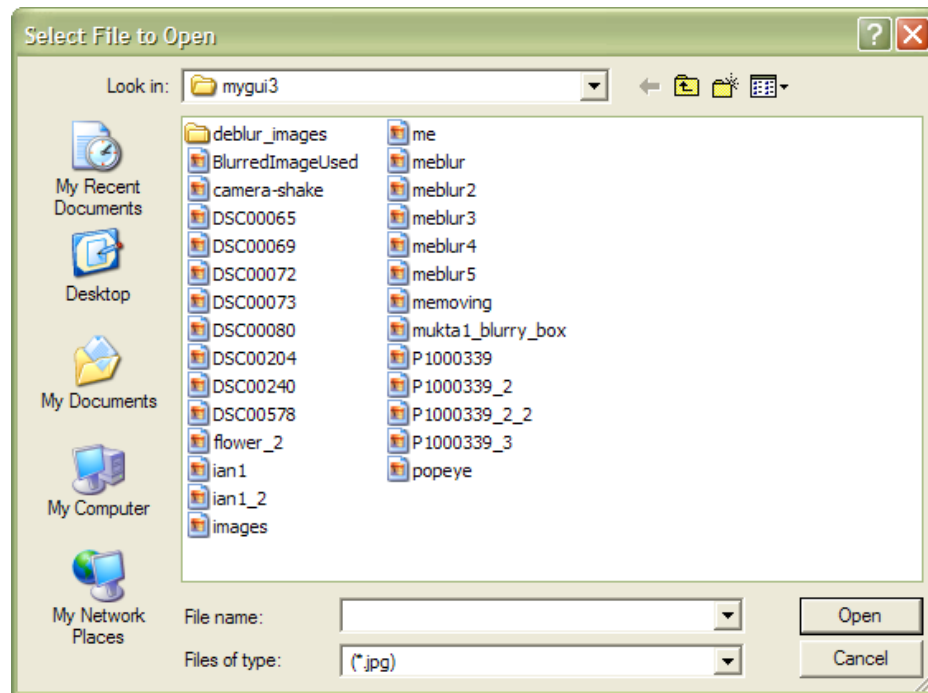
Fig. 6.2 The image loading window available in the BID Toolbox for easy selection of image data.

(a)

(b)

Fig. 6.3 Bounding box used in GUI for image region selection. (a) By default the whole image is selected (b) User specified image region for BID.

131
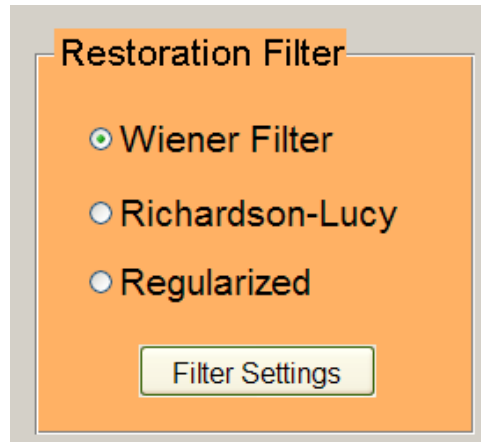
Fig. 6.4 Different filters available for BID in the GUI Toolbox.

The user has the choice of selecting among different IQMs as fitness function for the GA. List of the IQMs is given in Fig. 6.5.
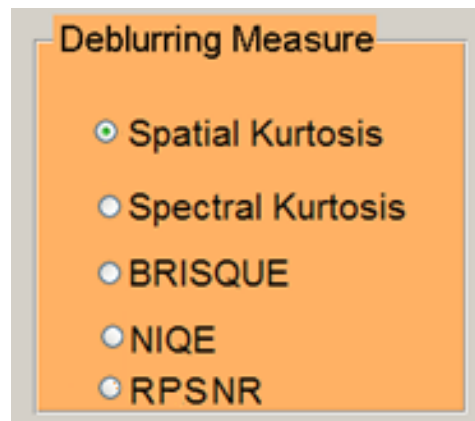
Fig. 6.5 Different deblurring measures available for BID in the GUI Toolbox.

The GA settings need to input by the user as well, if not the default values for number of iterations, initial population size, fitness function tolerance etc are used. Advanced settings of the algorithm include parameter tuning for mutation rate, crossover rate, parallel processing etc. The setup screen is shown in Fig. 6.6.
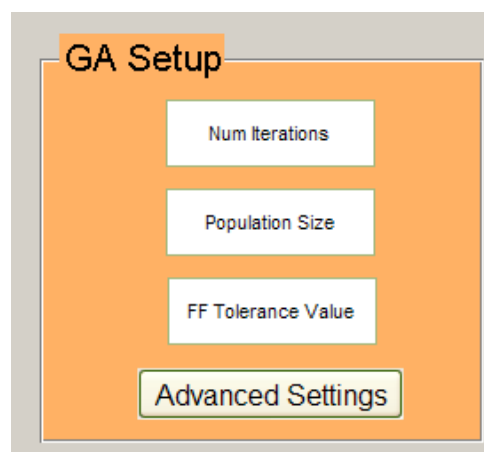
Fig. 6.6 GA setup screen for BID in the GUI Toolbox.

132

6.3.2. **Deblurring output**

Fig. 6.7 shows an overview of the GUI toolbox where the complete image is deblurred. The picture has been deblurred using a motion blur PSF of length 74 pixels and angle 0 degrees using a Wiener filter.
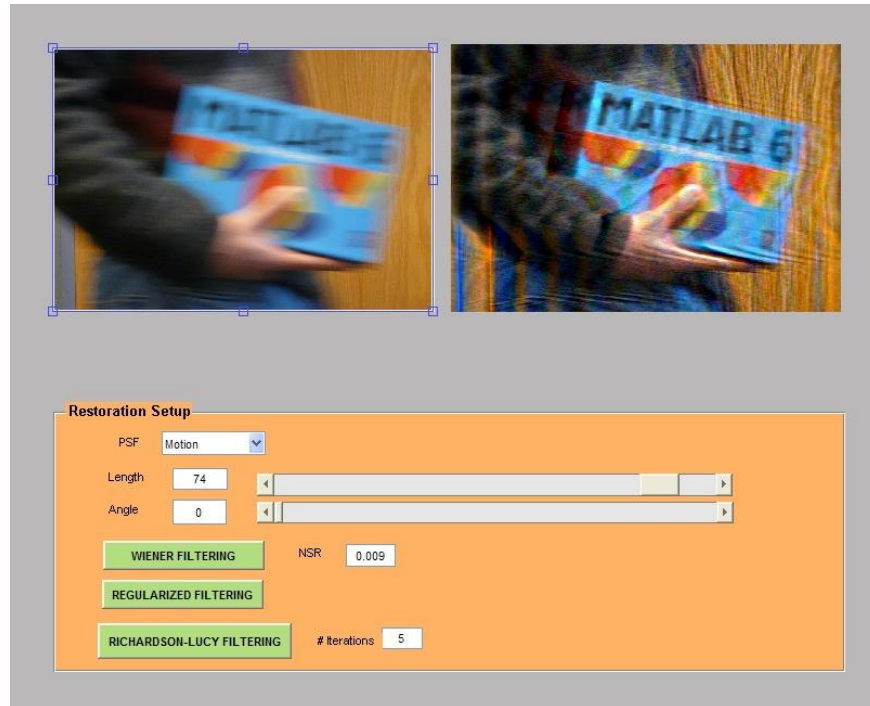
Fig. 6.7 BID Toolbox for non-blind image deblurring.

Fig. 6.8 shows the deblurring results for a section of the image. The bounding box was moved to cover the blurred title of the book in the image and deblurring was performed. This basic GUI toolbox could initially only provide manual adjustment of the PSF parameters. Later on, the GUI was updated to include the different newly proposed BID schemes and deblurring measures.

Fig. 6.9 shows the latest GUI for the BID toolbox which allows for the estimation of arbitrarily shaped PSFs. It also has features to load the blurred image and save the deblurred image. Other different options are also available in the main menu. The toolbox allows the user to select from different restoration filters and provides easy access to their settings. The deblurring algorithm is optimized through GA. The GA parameters can be set up simply. The deblurring algorithm can be optimized on a multiple core machine as well. The user can select from four deblurring measures as the fitness function for the GA. These deblurring measures are spatial and spectral kurtosis, RPSNR, BRISQUE and NIQE. By using the proposed BID scheme in Section 5.2, GA aims to estimate the PSF coefficient values for a coefficient matrix

whose size has to be input by the user. This toolbox therefore provides a single base to tackle the BID problem for images blurred by parametric and arbitrarily shaped PSFs using any of the deblurred measures.
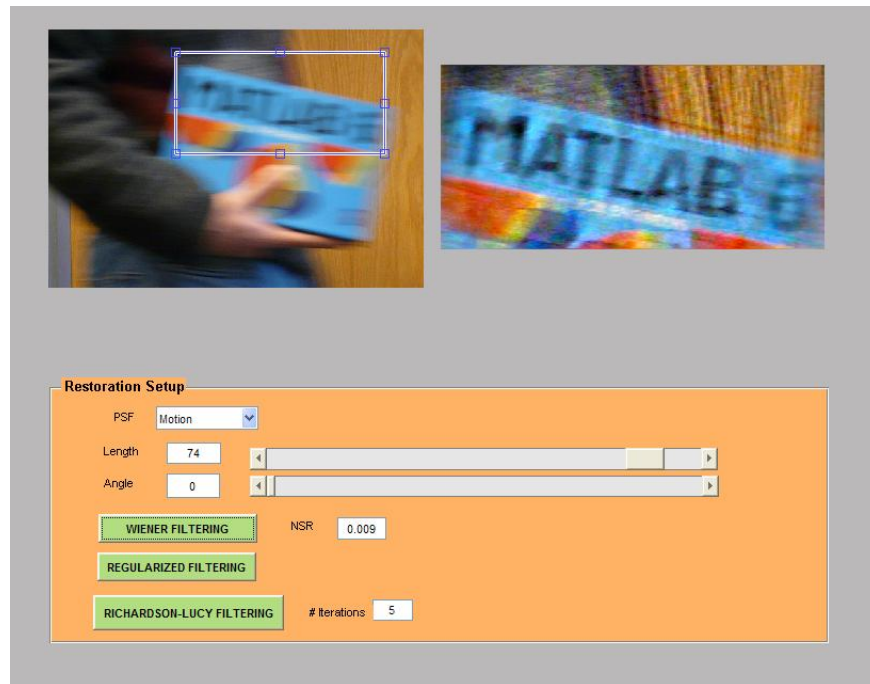
Fig. 6.8 BID Toolbox for image section deblurring. The bounding box's size and position can be adjusted by the user.
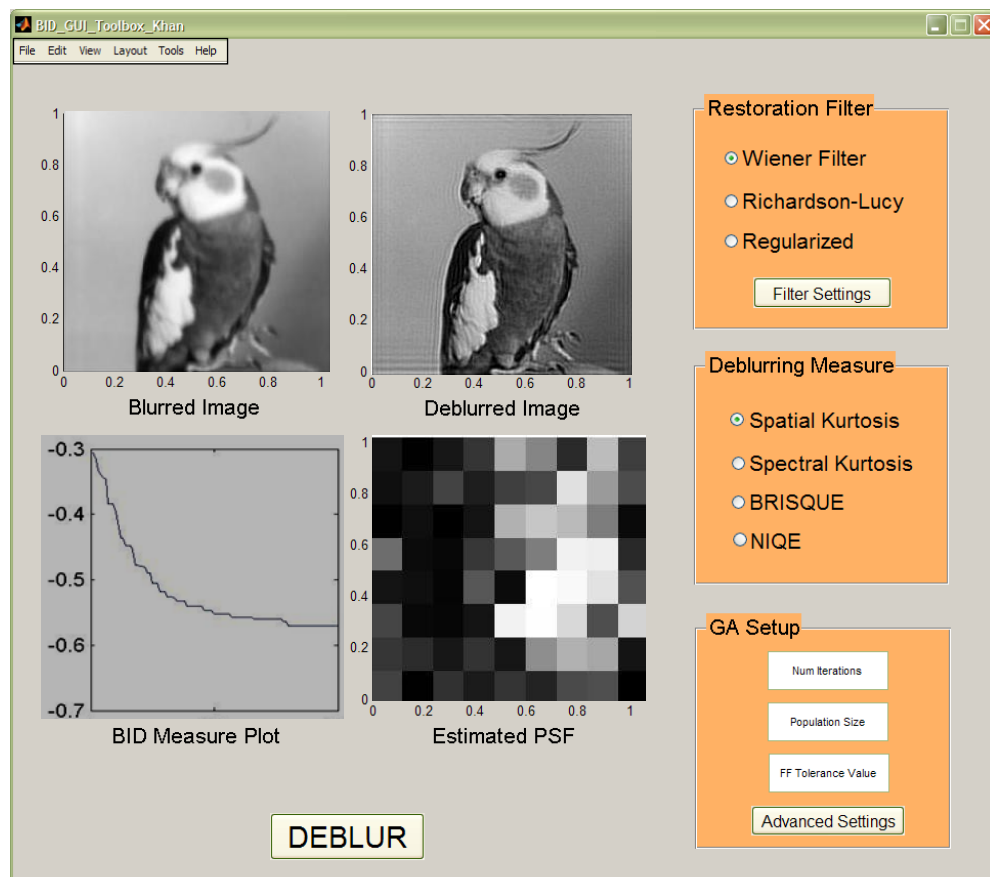
Fig. 6.9 GUI Toolbox for blind PSF estimation and image deblurring. User can select among different restoration filters, deblurring measures as well as adjust GA settings.

134

Fig. 6.10 - 6.11 shows default setups for different combinations for image deblurring. Fig. 6.10 shows the Popeye image being deblurred using a Wiener filter and the blur in the image being estimated by a parametric motion blur PSF. The GUI allows for the finite PSF size input which is set to 15x15 pixels. In this case the spectral kurtosis IQM is used for estimating the parametric motion PSF length and angle parameters. The GA is set to run for 500 iterations and a fitness value per iteration tolerance of 1⁻²². The lower and upper bounds for the estimated PSF values are set as 0.001 and 0.9 respectively. The deblurred image shows the recovery results for the Popeye image.
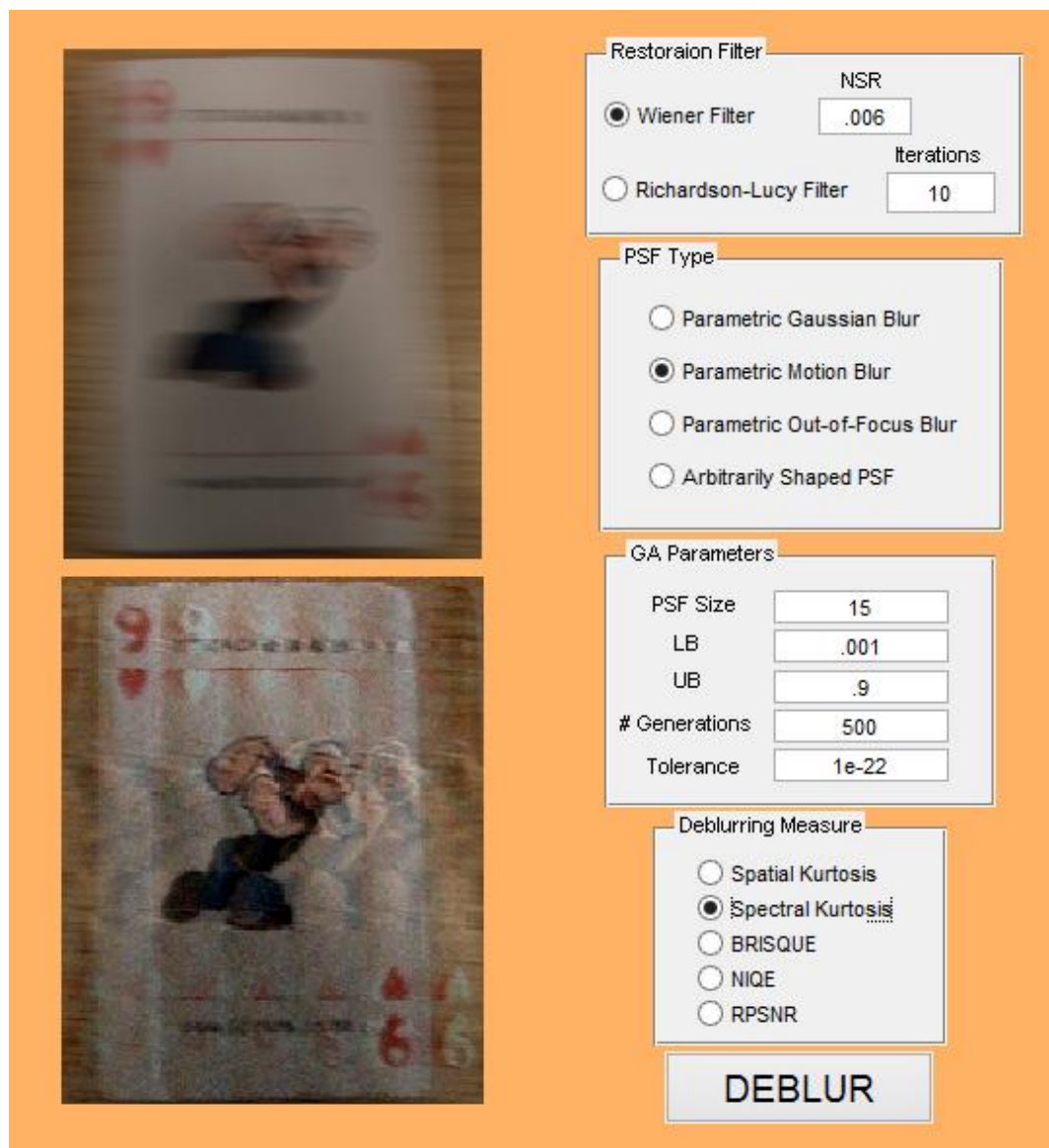
Fig. 6.10 GUI Toolbox for parametric motion PSF estimation and image deblurring. Settings are adjusted for spectral kurtosis based PSF estimation using Wiener filter.

Fig. 6.11 shows the Birdie image being deblurred using the Richardson-Lucy filter and the blur in the image being estimated by a parametric motion blur PSF. The GUI allows for the finite PSF size input which is set to 7x7 pixels. In this case the BRISQUE IQM is used for estimating the parametric motion PSF length and angle parameters. The GA is set to run for 35 iterations due to small number of estimation parameters and a fitness value per iteration tolerance of 1^{-22}. The lower and upper bounds for the estimated PSF values are set as 0.009 and 0.5 respectively. The deblurred image shows the recovery results for the Birdie image.
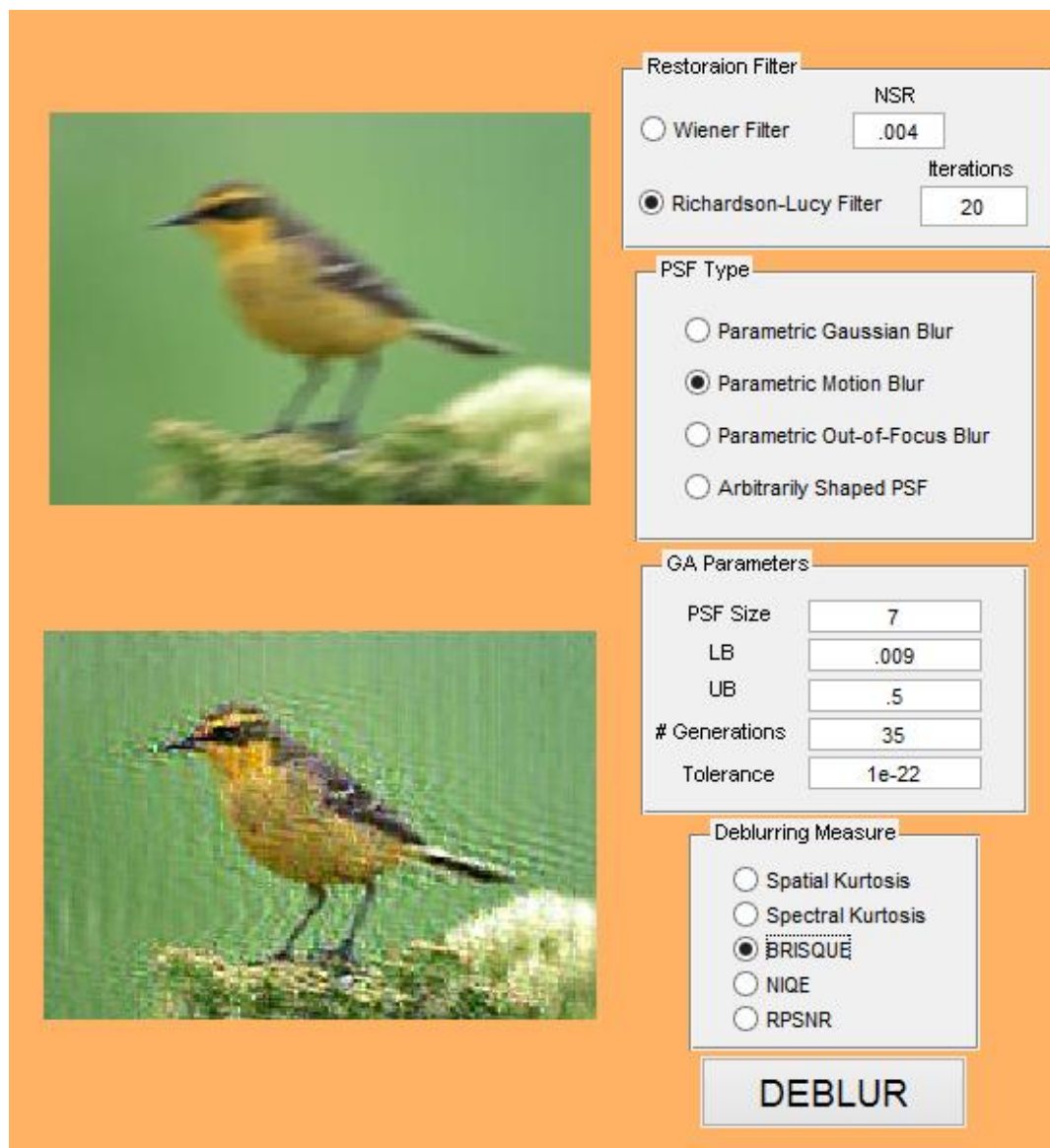
Fig. 6.11 GUI Toolbox for parametric motion PSF estimation and image deblurring. Settings are adjusted for BRISQUE based PSF estimation using Richardson-Lucy filter.

Fig. 6.12 shows the DIP book image being deblurred using the Wiener filter and the blur in the image being estimated by a parametric motion blur PSF. The GUI allows for the finite PSF size input which is set to 15x15 pixels. In this case the BRISQUE IQM is used for estimating the parametric motion PSF length and angle parameters. The GA is set to run for 500 iterations due to large number of estimation parameters and a fitness value per iteration tolerance of 1^{-22}. The lower and upper bounds for the estimated PSF values are set as 0.001 and 0.9 respectively. The deblurred image shows reasonable recovery for the blurred image.
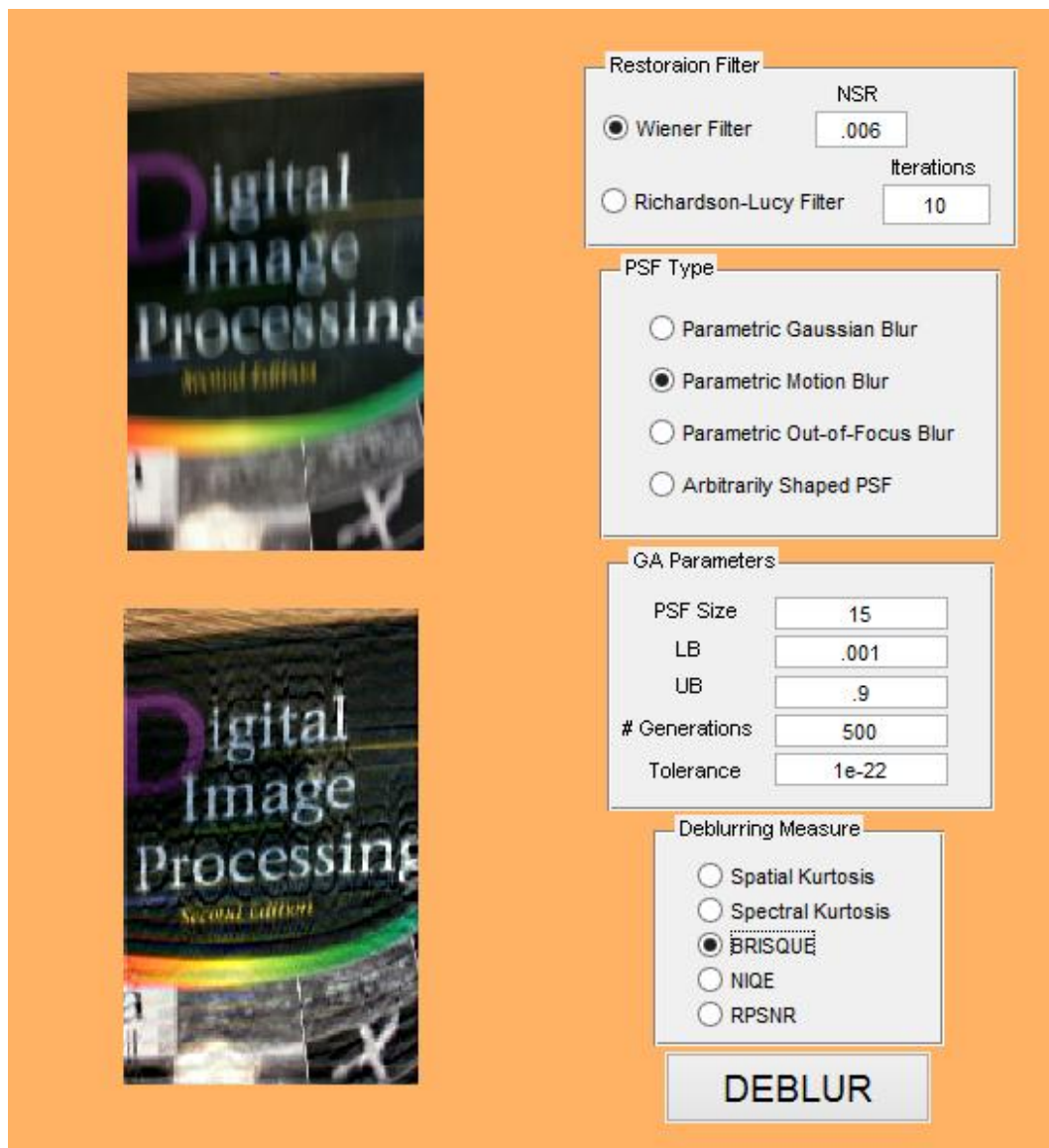
Fig. 6.12 GUI Toolbox for parametric motion PSF estimation and image deblurring. Settings are adjusted for BRISQUE based PSF estimation using Richardson-Lucy filter.

6.4. Comparison with Other BID Toolboxes

Other BID toolboxes are available and are their functionality is discussed in

comparison to the proposed BID scheme's GUI. This includes the SmartDeblur Toolbox. The toolbox allows for manual deblurring of out-of-focus and motion blurred images. The user has to manually adjust the blur parameters and search for the best parameter values to deblur the image. It allows the user to adjust motion blur length and angle parameter and radius parameter of out-of-focus blur.

The smoothness parameter allows the user the level of deblurring residual blur and the correction strength allows the level of deblurring to be applied on the blur image.
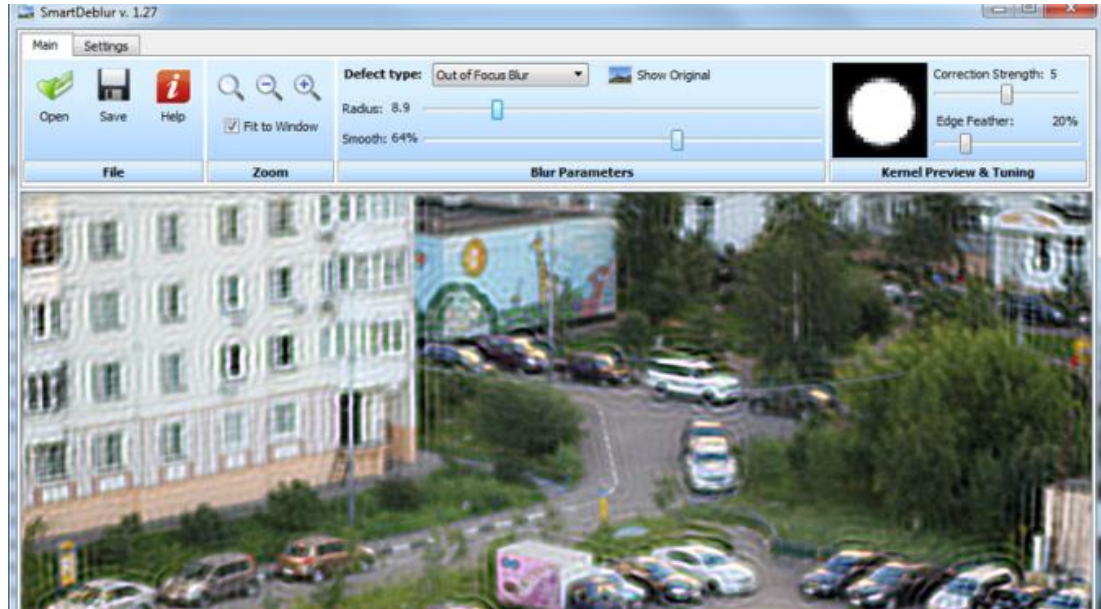
Fig. 6.13 SmartDeblur BID Toolbox for manual deblurring.

6.5. Summary

A GUI based toolbox for blind image deblurring based on IQMs and GA is developed and presented. The toolbox incorporates many features and provides a single base for parametric and non-parametric PSF estimation and deblurring. IQMs studied in this research work can be utilized along GA to automatically estimate the PSF and recover the image. The GUI was compared with other existing BID toolboxes however the main limitation of other BID schemes is their inability to function without input from the user at different processing stages. The GUI was developed with focus on functionality (automated BID scheme) and ease of usage for the users.

The present research work has been closed under the stated aims and objectives. Chapter 7 presents consolidated discussion and analysis of the research work presented before.

Chapter 7

Discussion and Analysis

This research focused on the development of blind restoration schemes for real life blurred images. The BID scheme presented in this research is designed to be robust in the estimation of parametric and non-parametric PSFs and computationally efficient. The objective was to design a BID scheme that can use an IQM to act as a feedback of image quality for the deblurred image and lead to the estimation of blurring PSF. The blind IQM used would optimize at or around the point where the true PSF is located. The blind IQMs developed and studied in this research are independent of a reference image when computing the image quality. The blind IQMs used are also independent of distortion specific features, such as ringing, noise or blur.

Blind IQMs spatial kurtosis, spectral kurtosis, RPSNR, BRISQUE and NIQE were investigated as deblurring measures for BID. A novel full-reference blind IQM, the RPSNR measure, was designed and used in this research work. BRISQUE, NIQE and spectral kurtosis are introduced for the first time as deblurring measures for BID.

7.1. Spatial and Spectral Kurtosis IQMs

Spectral kurtosis is introduced as an alternative to spatial kurtosis non-Gaussianity measure. The spatial kurtosis based BID scheme was designed and used by Yin and Hussain in [86]. The spatial kurtosis measure optimizes in the vicinity of true PSF parameter values indicating that the deblurring estimate is close to the pristine image.

It uses a Wiener filter in each iteration to generate a deblurred image estimate from the blurred image using a candidate PSF. This makes the spatial kurtosis based BID scheme computation-intensive due to the transformation of the frequency domain deblurred image, estimated by the Wiener filter, back to the time domain to calculate the spatial kurtosis. Also, spatial kurtosis is highly sensitive to outliers in the data. Due to noise amplification and ringing effects from the restoration filter the measured non-Gaussianity varies during the deblurring process, thus leading to a less precise approximation of PSF parameters. Spatial kurtosis is dependent on the statistical nature of the image i.e. for sub-Gaussian and super-Gaussian images; spatial kurtosis shows an increasing and decreasing kurtosis value respectively. Therefore, the BID scheme based on spatial kurtosis needs to be tuned accordingly for each image. Images that have normalized kurtosis value above zero are termed as super-Gaussian while images with normalized kurtosis value below zero are termed as sub-Gaussian. The above mentioned limitations make the robustness of the spatial kurtosis based BID scheme questionable especially in the deblurring case of real life blurred images with inherent noise. This limitation leads the need to develop new measures or investigate other existing measures, which are robust and computationally efficient.

The spectral kurtosis measure was presented as an efficient and robust alternative to the previously used spatial non-Gaussianity measure. The spectral kurtosis measure, unlike the spatial kurtosis measure, is calculated in the frequency domain thus omitting the use of iFFT. This saved valuable computation time during the deblurring process. The spectral kurtosis is computationally efficient with the deblurring speed almost doubled for the FFT-iFFT cycle for images larger than 256 x 256 pixels. However, MATLAB based Wiener filter implementation reduced the computational speed for the proposed BID scheme. The spectral kurtosis with a computationally efficient deblurring filter can achieve even lower execution time especially when large size images need to be deblurred or when multiple parameters of PSF need to be estimated. A BID scheme with low execution time is very critical especially when the deblurring is done online where the resources are very limited.

The spectral kurtosis IQM is independent of the statistical nature of image and always shows an increasing kurtosis value for increased blurring. This makes the spectral kurtosis based BID scheme easily automatable unlike the spatial kurtosis whose behaviour is dependent on the statistical nature of the image.

The spectral kurtosis based BID schemes for gradient descent and GA based

optimization are provided. The scheme is devised to handle any type of blur that can be modelled in a parametric form such as Gaussian, motion and out-of-focus blur. The spectral kurtosis measure was investigated for parametric blurs only. Deblurring was performed on noise free images in the artificial blurring case and with inherent image noise in the real blurred case. Gradient was computed against the blurring PSF parameter, which is optimized in the direction of increasing spectral kurtosis value till the pristine image is estimated. The scheme is simple and efficient and does not require any prior knowledge about the image or the blurring process. The algorithms and gradients are derived for a number of blurs and the performance improvements are corroborated through a set of simulations. The benefit of using such a model of estimation is that it makes the same BID algorithm easily tuneable, allowing it to estimate any of the mentioned parametric blur types using the same IQM.

In comparison with Shan et al. BID scheme [39], which can estimate parametric and arbitrarily shaped PSFs, the proposed BID scheme is designed for the estimation of parametric blurs only. In the artificial deblurring case for parametric blurs i.e. Gaussian, motion and out-of-focus blur, the proposed scheme produced better quality deblurred images as compared to the Shan et al. BID scheme. This is shown by high values of MSSIM and UQI and low values of BRISQUE and NIQE.

In the case of deblurring of real life motion blurred images, the proposed BID scheme shows better quality deblurred images for the BUILDINGS and LABEL image for BRISQUE IQM as compared to the original blurred image. The proposed scheme showed even better result as compared to Shan et al. for the BUILDINGS image. For the LABEL image, Shan et al. scheme showed better result as compared to the proposed scheme. However, for DIP_BOOK and MATLAB_BOOK images both the proposed and Shan et al. scheme further deteriorated the original blurred images.

In most of the real deblurring cases, Shan et al. BID scheme shows lower quality as compared to the original blurred image. The deblurred images of Shan et al. were marred by ringing artefacts due to kernel errors in the PSF estimation stage.

The proposed GA based BID scheme was used to enhance the search for the PSF parameter values. It was also used to compare the deblurred image quality for multiple filters i.e. Wiener filter, Richardson-Lucy filter, Regularization filter and MATLAB Iterative Blind Deconvolution (IBD) filter. Wiener filter based deblurred image estimates show better quality images as compared to other filters based on the PSNR values.

7.2. Reblurring based PSNR (RPSNR) IQM

A novel full-reference blind quality measure for BID, the RPSNR measure, was designed as an alternative deblurring measure. Reference based error computing was not previously possible in BID cases due to the unavailability of a reference image required for comparison purposes. The RPSNR measure suggests a solution to this problem by calculating error between blurred and reblurred image. RPSNR based PSF estimates produce high quality deblurred images as shown by the high PSNR values of the original-deblurred pair. The deblurred images when reconvolved with the estimated PSF produce the reblurred images. Only for the candidate PSF near to the original PSF, the reblurred image has a similar blurring effect as the originally blurred image.

The reblurring based BID scheme based on RPSNR is limited to the deblurring of motion blurred images. The deblurring results for artificially blurred Gaussian and out-of-focus images shows that the RPSNR measure could not produce global maxima near the true blur parameters. This could be due to the reblurred image depicting less difference to the original image for small PSF parameter value. This is wrongly perceived by RPSNR measure and thus results in an incorrect PSF parameter estimation.

7.3. BRISQUE and NIQE IQMs

BRISQUE based PSF estimates produce much better quality deblurred images as compared to other IQMs for artificially and real blurred images. However, BRISQUE is computationally inefficient as compared to the other IQMs due to its usage of a support vector machine for calculating the image quality. Among the non-reference IQMs, in most of the deblurring cases, BRISQUE based BID scheme shows better quality images followed by NIQE based BID scheme.

Blind IQMs spatial kurtosis, spectral kurtosis, RPNSR, BRISQUE and NIQE are investigated based on their ability in estimating parametric PSF by judging the deblurred image quality. IQMs were employed during the research work to judge the deblurred image quality and include both full-reference and non-reference IQMs. Full-reference IQMs include the PSNR, MSSIM and UQI measures whereas non-reference IQMs include spatial kurtosis, spectral kurtosis, BRISQUE, NIQE and RPSNR measures. The deblurred image quality of the IQMs is compared for artificial and real blurred images using PSNR, MSSIM, UQI, BRISQUE and NIQE.

It was difficult to isolate a single measure as the best among the non-reference IQMs just based on their deblurred image quality as their performance varies. In order to select among the multiple IQMs, the estimated NSR for the different IQMs is also analyzed. It is observed that the BRISQUE measure estimates the PSF parameters for relatively lower NSR values as compared to other IQMs. A lower NSR value for the Wiener filter based deconvolution results in a comparatively sharper image as compared to a higher NSR value. Also, low NSR values depict the presence of relatively higher noise. BRISQUE based BID gives better visual results for the deblurred images due to the presence of sharp edges and it was due to this BRISQUE was selected as the blind IQM to be used in the later research work.

7.4. BID Scheme for Arbitrarily Shaped PSFs

Real life blurred images exhibit more complex shape PSFs that cannot be modelled using the parametric models. The deblurring in this case is challenging to estimate the PSF in the blurred image and its effective removal. The estimation of arbitrarily shaped (non-parametric or generic) motion PSFs caused by camera handshake were also investigated.

A novel blind deblurring scheme was analyzed for deblurring images corrupted by arbitrarily shaped PSFs. It is based on GA optimization and utilizes the BRISQUE measure as the fitness function for arbitrarily shaped PSF estimation. An added advantage of such a BID scheme is that the same method can easily be extended for estimating other types of blur apart from camera handshake such as atmospheric turbulence blur and out-of-focus blur. Also, the BID scheme based on GA is flexible so it can be easily incorporated with any deblurring measure as the fitness function. The proposed BID scheme has been compared with other deblurring schemes that include the single image motion deblurring scheme of Fergus et al. [17] and the single/noisy-paired motion deblurring scheme of Whyte et al. [18]. The proposed BID scheme's estimated PSF is similar enough to the original PSF but not exactly the same as the original blurring PSF. This affects the brightness and contrast of the deblurred images thus rendering the full-reference IQMs (PSNR, MSSIM, UQI etc) invalid for quantitative image quality evaluation. Therefore, non-reference IQMs BRISQUE and NIQE were used for image quality evaluation.

The proposed BID scheme requires a fixed PSF size input from the user. In order to estimate the PSF support size, a simple technique based on visual judgement of ringing artefacts in the deblurred image is proposed. Initially, the GA is run for

different sizes of PSF for only a few iterations. The results are then visually judged for ringing artefacts. The ringing artefacts are severe if the initial PSF estimate is bigger in size than the actual blur PSF which creates estimation error among them. Therefore, the user can select a PSF size which shows reduced ringing for the deblurred image.

The proposed BID scheme results show that it can estimate parametric and arbitrarily shaped PSFs for artificially blurred images. However limited for the deblurring of real life blurred images due to the inherent noise in the images. Also for real life blurred images, Fergus et al. and Whyte et al. BID scheme, could not produce acceptable results.

The robustness of the proposed BID scheme is discussed as follows. For the BRISQUE IQM, the proposed BID scheme works well for artificial and real blurred images. It works well for parametric blur types for artificial and real blurred images. In the case of arbitrarily shaped PSF estimation, the proposed BID scheme based on BRISQUE works well only for artificial blurred images and fails in the case of real blurred images.

7.5. GUI based BID Toolbox

A GUI toolbox for non-blind image deblurring was developed during the early stages of the research work and was regularly updated to incorporate many additional features such as region based deblurring, blind IQMs etc. After the successful use of blind IQMs for BID, the toolbox was updated to incorporate a GA based BID scheme, which can use any of the blind IQMs as fitness function. It can estimate both parametric and arbitrarily shaped PSFs. The toolbox is built using MATLAB and its GUI implementation framework named GUIDE. It allows for an easy creation and updating of the GUI based toolbox. The GUIDE based GUI is coded by separate functions allowing for easy access and further modifications. The MATLAB based GUI also supports parallel processing by simplifying the use of its distributed computing techniques. The toolbox and the related GUI have features incorporated which allow for:

- Deblurring of complete or section of an image.
- Deblurring with different restoration filters.
- Slider bar for setting up the algorithm parameter by the user.
- Deblurring parametric and non-parametric PSFs.

- Ringing reduction through edge-taping technique.

- File loading, saving and toolbox layout change.

- Executing the BID scheme in serial or parallel mode.

The overall conclusions, achievements and future research direction are presented in Chapter 8.

Chapter 8

Conclusions, Contributions and Future Work

This research investigated the problem of blind image deconvolution and deblurring in an effort to provide efficient restoration of real life blurred images. The research work focused on the design and development of a BID scheme for real life blurred images. Though summary of each research study has been provided in the relevant chapters, a brief outline of the key findings and suggestions for possible future studies is presented here.

8.1. Conclusions

This research was an investigation to establish that the blind image deconvolution problem can be solved to a fair degree of complexity by using the information theoretic concept, where, an independent signal has certain useful information. It focused on a couple of very interesting challenges in BID and proposed new solutions for them. The challenges include; designing/investigating a robust blind image deblurring measure, estimating parametric and arbitrarily shaped PSFs, deblurring real life blurred image data, enhancing the computational efficiency and the deblurring quality of the BID scheme.

Blind IQMs were investigated as feedback deblurring measures to the BID. These

146

include; spatial kurtosis, spectral kurtosis, RPSNR, BRISQUE and NIQE index. Spatial kurtosis has been previously used for BID while existing measures, BRISQUE, NIQE and spectral kurtosis, are introduced for the first time as deblurring measures for BID. RPSNR is a novel full reference yet blind IQM designed and used in this research work.

Starting with the spatial kurtosis based BID scheme as a reference, the spectral kurtosis based BID model was designed and implemented. Some of the features of this scheme are as follows:

- The spectral kurtosis measure is calculated in the frequency domain thus limiting the need for Inverse Fourier Transform which is required for the calculation of spatial domain IQMs (spatial kurtosis, RPSNR, BRISQUE and NIQE). This makes spectral kurtosis computationally efficient. However, MATLAB's Wiener filter implementation also has other severe overheads losing the per iteration efficiency.

- Spectral kurtosis maximizes for increased blurring unlike spatial kurtosis which increases and decreases for sub-Gaussian and super-Gaussian image. This makes the BID scheme based on spectral kurtosis easily automatable.

- Experiments were carried out on a number of test images with various blurring parameters. Spectral kurtosis based BID scheme is robust as it is able to estimate the blurring parameters over a wide range of images and its performance is not marred by ringing artefacts and inherent deblurring noise in the images.

- The proposed method's deblurring ability is not limited to a single blurring function. The algorithms and gradients are derived for a number of blurs, and the performance improvements are corroborated through a set of simulations. The benefit of using such a model of estimation is that it makes the same BID algorithm easily tuneable, allowing it to estimate any of the mentioned parametric blur types using the same IQM.

- A gradient descent based scheme was utilized where the parameter(s) of the blur model were optimized in the direction of maximum spectral non-Gaussianity. The BID scheme was later replaced by the use of a GA based optimization. The GA based BID scheme was used for testing of RPSNR, BRISQUE and NIQE measure as well.

147

A novel full-reference yet blind quality measure for BID, RPSNR, was designed as an alternative to the spectral kurtosis measure.

- Reference based error computing was not previously possible in BID cases, due to the unavailability of a reference image required for comparison purposes. The RPSNR measure suggests a solution to this problem by calculating error between blurred and reblurred image.

- Deblurring results for artificial and real life motion blurred images based on the RPSNR based BID scheme are encouraging. However, the measure's performance was limited for Gaussian and out-of-focus images.

Non-reference IQMs BRISQUE and NIQE were investigated as deblurring measures alternate to the spatial and spectral non-Gaussianity measures.

- BRISQUE measure based PSF estimates depict better results for deblurring of artificially and real life blurred images as compared to other IQMs.

- From detailed testing of these measures with deblurring experimentation on the artificial and real life blurred images, BRISQUE proved to be a very robust but computationally costly PSF estimator. BRISQUE is computationally costly due to its usage of a support vector machine for calculating the image quality.

- BRISQUE based BID estimates PSF for relatively lower NSR values as compared to other IQMs resulting in a comparatively sharper image with presence of deblurring noise.

All the deblurring measures show absolute maxima at the true PSF parameter values except the spatial kurtosis measure, which maximises for super-Gaussian images and minimizes for sub-Gaussian images. This makes them a better choice in terms of an automatable measure.

In the earlier research work, parametric forms of blurs were used for Gaussian, motion and out-of-focus blur to model the blurring in the images. The IQMs were used to successfully tackle parametric blurs for both artificial and real life blurred images. The parametric model is a mere approximation of the blurring that occurs in real life blurred images. The research study was further extended to focus on the

estimation of the arbitrarily shaped PSFs that present much more complex forms than their parametric counterparts.

- A GA based novel BID scheme using BRISQUE measure as the fitness function was used to estimate the coefficients of the arbitrarily shaped PSF.

- The scheme can estimate blurs even with a large support size. The BID scheme's setup allows for the estimation of any type of PSF i.e. atmospheric turbulence blur (through Gaussian approximation), motion and out-of-focus blur in parametric form and arbitrarily shaped as well. The BID scheme was also utilized for parametric blur estimation as well.

- The proposed BID scheme's estimated PSF coefficients are not exactly the same as the original PSF but are rather a near approximation of the original blurring PSF. The proposed BID scheme estimates the PSF coefficients for limited number of iterations which produces a reasonable approximation of the original PSF coefficients.

- The proposed BID scheme requires a fixed PSF size input from the user. In order to estimate the PSF support size, a simple technique based on visual judgement of ringing artefacts in the deblurred image is proposed

- Experimentation with artificially blurred images, for parametric and arbitrarily shaped PSF, depicts excellent restoration results. However, the deblurring capability was not satisfactory when tested on real life blurred images corrupted by arbitrarily shaped PSFs and in presence of a low degree of noise.

- Other benchmark schemes used for comparison also failed to produce any viable result as they were not able to estimate the right PSF shape/coefficients.

- Full reference and non-reference IQMs were employed to gauge the deblurred image quality in the artificial blurring case. In the case of real blurred image restoration, only non-reference IQMs were employed due to unavailability of high quality image as reference.

For easy usage of the BID scheme a GUI based BID toolbox was created.

- After the successful use of blind IQMs for BID, the toolbox was updated to incorporate the proposed GA based BID scheme which can use any of the

blind IQMs as fitness function.

- It can estimate parametric and arbitrarily shaped PSFs.

- The MATLAB based GUI also supports parallel processing by simply using its distributed computing techniques.

8.2. Contributions

The research work contributed towards the image restoration field by introducing:

- New blind IQMs; spectral kurtosis, BRISQUE and NIQE as deblurring measures for the first time. A novel full-reference yet blind IQM, RPSNR, was also designed and used for BID. The measures are able to evaluate image quality for different types of situations when the reference high-quality image is not available for comparison purposes.

- A BID scheme has been developed that can handle the deblurring of images corrupted by parametric as well as arbitrarily shaped PSFs, by using a single algorithm for both cases. The scheme using BRISQUE IQM in conjunction with GA can approximate the blurring PSF coefficients for a fixed support size matrix thus giving it the flexibility to estimate any shape and size of PSF.

- The developed BID scheme is totally blind and does not require any prior knowledge about the image or the blurring process.

- The proposed BID scheme operates on a single-shot of the image for its recovery, thus making it computationally efficient and ideal for the deblurring of real life blurred images.

- The developed BID method is able to handle high level of blur with small level of noise and moderate level of blur with moderate level of noise.

- The developed BID scheme has benefited from the available parallel computing resources. On average, the IQMs show a 50 % reduction in computation time over four processor cores. MATLAB Optimization Toolbox, details in Appendix D, has been utilized for parallel code execution on a multiple core system for BID. It enables the BID schemes to be executed in less time. This is very essential especially when image deblurring includes large size images or the search space for PSF is wide.

- A MATLAB based GUI has been designed and implemented for BID which

allows the BID algorithm to be used easily by the users. Even, users unfamiliar to the field of BID can easily use the GUI toolbox without much trouble.

8.3. Future Work

This research study mainly investigated the problem of BID for real blurred images. Though good results were achieved from the proposed BID scheme(s), the research boundary may still be investigated for extending its capabilities. Some research approaches, which are out of the scope of the current research, are also suggested.

- In terms of extending this research work, new learning algorithms may be investigated for the proposed BID with focus on optimization and faster convergence rate.

- Space invariant parametric as well as arbitrarily shaped PSFs were investigated in this research work. At present, the algorithm is applicable to space invariant blur however, as the algorithm is quite adaptive it may easily be tailored to handle space variant blurs (both parametric and arbitrarily shaped PSFs) by using small windows size for the image deblurring task.

- Low level noise was handled in the deblurring of real life image data. The BID scheme's ability to handle high level noise may be enhanced by extending the developed BID scheme for blind image denoising as well. Different types of noise may be considered along with blurring in future. Knowledge from the image denoising scheme may then be incorporated with this research work to construct a unified blind image deblurring and denoising scheme.

- The arbitrarily shaped PSF estimation scheme may be further enhanced by assuming seperability for the PSF. The separable PSF may help in the reduction of computation time as well as quick convergence of the GA. The arbitrarily shaped PSF estimation technique may be investigated for photo-specific image and PSF constraints, in order to enhance the deblurring quality.

- Furthermore, a variant of the existing scheme may be designed for segmented image deblurring applications, like moving object on a stationary background or a focused object on a non-focused background.

References

[1]   Y. Bando, "Single-Shot Image Deblurring with Modified Camera Optics," PhD dissertation, The Graduate School of Information Science and Technology The University of Tokyo 2009.

[2]   Y. Bando, "Single-Shot Image Deblurring with Modified Camera Optics ", The Graduate School of Information Science and Technology The University of Tokyo., 2009.

[3]   A. Agrawal, and Y. Xu, "Coded Exposure Deblurring: Optimized Codes for PSF Estimation and Invertibility," in IEEE Conference on Computer Vision and Pattern Recognition, New York, 2009, pp. 2066-2073.

[4]   C. Y. Zhou, S. Lin, and S. K. Nayar, "Coded Aperture Pairs for Depth from Defocus and Defocus Deblurring," *International Journal of Computer Vision,* vol. 93, no. 1, pp. 53-72, May, 2011.

[5]   A. Levin *et al.*, "Image and Depth from a Conventional Camera with a Coded Aperture," *ACM Transactions on Graphics,* vol. 26, no. 3, Jul, 2007.

[6]   A. Veeraraghavan *et al.*, "Dappled Photography: Mask Enhanced Cameras for Heterodyned Light Fields and Coded Aperture Refocusing," *ACM Transactions on Graphics,* vol. 26, no. 3, July, 2007.

[7]   R. Raskar, A. Agrawal, and J. Tumblin, "Coded Exposure Photography: Motion Deblurring Using Fluttered Shutter," *ACM Transactions on Graphics,* vol. 25, no. 3, pp. 795-804, July, 2006.

[8]   S. Hiura, and T. Matsuyama, "Depth Measurement by the Multi-Focus Camera," *Proceedings of IEEE Computer Society Conference on Computer Vision and Pattern Recognition.* pp. 953-959.

[9]   M. Ben-Ezra, and S. K. Nayar, "Motion-Based Motion Deblurring," *IEEE Transactions on Pattern Analysis and Machine Intelligence,* vol. 26, no. 6, pp. 689-698, Jun, 2004.

[10]   E. Lopez-Rubio, R. M. Luque-Baena, and E. Dominguez, "Foreground Detection in Video Sequences with Probabilistic Self-Organizing Maps," *International Journal of Neural Systems,* vol. 21, no. 3, pp. 225-246, Jun, 2011.

[11]   D. L. Li, and S. Simske, "Atmospheric Turbulence Degraded-Image Restoration by Kurtosis Minimization," *IEEE Geoscience and Remote Sensing Letters,* vol. 6, no. 2, pp. 244-247, Apr, 2009.

[12]   R. Cruz-Barbosa, and A. Vellido, "Semi-Supervised Analysis of Human Brain Tumours from Partially Labelled MRS Information, Using Manifold Learning Models," *International Journal of Neural Systems,* vol. 21, no. 1, pp. 17-29, Feb, 2011.

[13]   G. H. Glover, "Deconvolution of Impulse Response in Event-related BOLD

fMRI," *Neuroimage,* vol. 9, no. 4, pp. 416-429, Apr, 1999.

[14]   T. Taxt, and J. Strand, "Two-Dimensional Noise-Robust Blind Deconvolution of Ultrasound Images," *IEEE Transactions on Ultrasonics Ferroelectrics and Frequency Control,* vol. 48, no. 4, pp. 861-866, Jul, 2001.

[15]   L. I. Shi, Z. Bao, and S. U. N. Hui, "Restoration of Aerial Multiple Blurred Images," *Optics and Precision Engineering,* vol. 17, no. 5, pp. 1161-1170, 2009.

[16]   W. Jun, and C. Danqing, "Deblurring Texture Extraction from Digital Aerial Image by Reforming a Steep Edge Curve," *Geo-spatial Information Science,* vol. 8, no. 1, pp. 39-44, 2005.

[17]   R. Fergus *et al.*, "Removing Camera Shake from a Single Photograph," *ACM Transactions on Graphics,* vol. 25, no. 3, pp. 787-794, Jul, 2006.

[18]   O. Whyte *et al.*, "Non-uniform Deblurring for Shaken Images," *International Journal of Computer Vision,* vol. 98, no. 2, pp. 168-186, Jun, 2012.

[19]   S. Cho, and S. Lee, "Fast Motion Deblurring," *ACM Transactions on Graphics,* vol. 28, no. 5, Dec, 2009.

[20]   A. Agrawal, Y. Xu, and R. Raskar, "Invertible Motion Blur in Video," *ACM Transactions on Graphics,* vol. 28, no. 3, Aug, 2009.

[21]   J. N. Caron, "Blind Deconvolution of Audio-Frequency Signals Using the Self-Deconvolving Data Restoration Algorithm (SeDDaRA)," *Journal of the Acoustical Society of America,* vol. 116, no. 1, pp. 373-378, Jul, 2004.

[22]   J. P. Ligorria, and C. J. Ammon, "Iterative Deconvolution and Receiver-Function Estimation," *Bulletin of the Seismological Society of America,* vol. 89, no. 5, pp. 1395-1400, Oct, 1999.

[23]   M. S. Ramsey, and P. R. Christensen, "Mineral Abundance Determination: Quantitative Deconvolution of Thermal Emission Spectra," *Journal of Geophysical Research-Solid Earth,* vol. 103, no. B1, pp. 577-596, Jan 10, 1998.

[24]   S. M. Jefferies *et al.*, "Blind Deconvolution in Optical Diffusion Tomography," *Optics Express,* vol. 10, no. 1, pp. 46-53, Jan 14, 2002.

[25]   S. M. Jefferies, and J. C. Christou, "Restoration of Astronomical Images by Iterative Blind Deconvolution," *Astrophysical Journal,* vol. 415, no. 2, pp. 862-874, Oct, 1993.

[26]   G. Desidera *et al.*, "Application of Iterative Blind Deconvolution to the Reconstruction of LBT LINC-NIRVANA Images," *Astronomy & Astrophysics,* vol. 452, no. 2, pp. 727-734, Jun, 2006.

[27]   W. H. Richardson, "Bayesian-Based Iterative Method of Image Restoration," *Journal of the Optical Society of America,* vol. 62, no. 1, pp. 55-59, 1972.

[28]   T. F. Chan, and C. K. Wong, "Total Variation Blind Deconvolution," *IEEE Transactions on Image Processing,* vol. 7, no. 3, pp. 370-375, Mar, 1998.

[29]   D. Kundur, and D. Hatzinakos, "Blind Image Deconvolution," *IEEE Signal Processing Magazine,* vol. 13, no. 3, pp. 43-64, May, 1996.

[30]   R. L. Lagendijk, A. M. Tekalp, and J. Biemond, "Maximum-Likelihood Image and Blur Identification - A Unifying Approach," *Optical Engineering,* vol. 29, no. 5, pp. 422-435, May, 1990.

[31]   R. A. Wiggins, "Minimum Entropy Deconvolution," *Geoexploration,* vol. 16, no. 1-2, pp. 21-35, 1978.

[32]   D. Kundur, and D. Hatzinakos, "A Novel Blind Deconvolution Scheme for Image Restoration Using Recursive Filtering," *IEEE Transactions on Signal Processing,* vol. 46, no. 2, pp. 375-390, Feb, 1998.

[33]   M. R. Banham, and A. K. Katsaggelos, "Digital Image Restoration," *IEEE Signal Processing Magazine,* vol. 14, no. 2, pp. 24-41, Mar, 1997.

[34]   P. Comon, and C. Jutten, *Handbook of Blind Source Separation (Independent Component Analysis and Applications)*: Elsevier, 2010.

[35]   D. Vigliano *et al.*, "Flexible Nonlinear Blind Signal Separation in the Complex Domain," *International Journal of Neural Systems,* vol. 18, no. 2, pp. 105-122, Apr, 2008.

[36]   A. Hyvarinen, J. Karhunen, and E. Oja, *Independent Component Analysis*: Wiley-Interscience Publication, 2001.

[37]   F. Cong *et al.*, "Single-Trial Based Independent Component Analysis on Mismatch Negativity in Children," *International Journal of Neural Systems,* vol. 20, no. 4, pp. 279-292, Aug, 2010.

[38]   L. S. Yuan, J., L. Quan, and H. Shum, "Image Deblurring With Blurred/Noisy Image Pairs," *ACM Transactions on Graphics*, 2007.

[39]   Q. Shan, J. Jia, and A. Agarwala, "High-Quality Motion Deblurring From a Single Image," *ACM Transactions on Graphics,* vol. 27, no. 3, pp. 10, Aug, 2008.

[40]   S. Cho, J. Wang, and S. Lee, "Handling Outliers in Non-Blind Image Deconvolution," in International Conference on Computer Vision, New York, 2011, pp. 495-502.

[41]   O. Whyte, J. Sivic, and A. Zisserman, "Deblurring Shaken and Partially Saturated Images," in International Conference on Computer Vision Workshops, New York, 2011.

[42]   M. Hirsch *et al.*, "Fast Removal of Non-uniform Camera Shake," in International Conference on Computer Vision, New York, 2011, pp. 463-470.

[43]   X. Yuquan *et al.*, "Single-Image Blind Deblurring for Non-Uniform Camera-Shake Blur," in Proceedings of the 11th Asian conference on Computer Vision Daejeon, Korea, 2013, pp. 336-348.

[44]   A. Gupta *et al.*, "Single Image Deblurring Using Motion Density Functions," in 11th European Conference on Computer Vision, Heraklion, Crete, Greece,

2010, pp. 171-184.

[45]   M. S. C. Almeida, and L. B. Almeida, "Blind and Semi-Blind Deblurring of Natural Images," *IEEE Transactions on Image Processing,* vol. 19, no. 1, pp. 36-52, Jan, 2010.

[46]   A. V. Oppenheim, R. W. Schafer, and T. G. Stockham, "Nonlinear Filtering Of Multiplied and Convolved Signals," *Proceedings of the Institute of Electrical and Electronics Engineers,* vol. 56, no. 8, pp. 1264-1285, 1968.

[47]   M. M. Sondhi, "Image Restoration - Removal of Spatially Invariant Degradations," *Proceedings of the IEEE,* vol. 60, no. 7, pp. 842-853, 1972.

[48]   R. C. Gonzalez, and R. E. Woods, "Digital Image Processing," *Prentice-Hall Inc*, 2002.

[49]   T. G. Stockham, T. M. Cannon, and R. B. Ingebretsen, "Blind Deconvolution through Digital Signal-Processing," *Proceedings of the IEEE,* vol. 63, no. 4, pp. 678-692, 1975.

[50]   T. G. Stockham, "Image Processing In Context of a Visual Model," *Proceedings of the IEEE,* vol. 60, no. 7, pp. 828-842, 1972.

[51]   Y. P. Zhang, and T. Ueda, "Deblur of Radially Variant Blurred Image for Single Lens System," *IEEJ Transactions on Electrical and Electronic Engineering,* vol. 6, pp. 7-16, 2011.

[52]   L. Bar, N. Sochen, and N. Kiryati, "Restoration of Images with Piecewise Space-Variant Blur," *Scale Space and Variational Methods in Computer Vision, Proceedings*, Lecture Notes in Computer Science, pp. 533-544, 2007.

[53]   M. Sorel, and F. Sroubek, "Space-Variant Deblurring Using One Blurred and One Underexposed Image," in IEEE International Conference on Image Processing, , 2009, pp. 157-160.

[54]   M. Sorel, F. Sroubek, and J. Flusser, "Recent Advances in Space-Variant Deblurring and Image Stabilization," *Unexploded Ordnance Detection and Mitigation*, NATO Science for Peace and Security Series B - Physics and Biophysics, pp. 259-272, 2009.

[55]   M. Sorel, and J. Flusser, "Space-Variant Restoration of Images Degraded By Camera Motion Blur," *IEEE Transactions on Image Processing,* vol. 17 - 2, pp. 105-116, Feb, 2008.

[56]   M. Sorel, and J. Flusser, "Restoration of Color Images Degraded By Space-Variant Motion Blur," *Proceedings of Computer Analysis of Images and Patterns*, Lecture Notes in Computer Science, pp. 450-457, 2007.

[57]   R. L. Lagendijk, and J. Biemond, "Basic Methods for Image Restoration and Identification," *The Essential Guide to Image Processing*, pp. 323-348, San Diego: Academic Press USA, 2009.

[58]   R. E. Hufnagel, and N. R. Stanley, "Modulation Transfer Function Associated With Image Transmission through Turbulent Media," *Journal of*

the Optical Society of America, vol. 54, no. 1, pp. 52-&, 1964.

[59]   R. L. Lagendijk, and J. Biemond, "Basic Methods for Image Restoration and Identification," 1996.

[60]   S. Tan, and T. Savoie, *Blind Deconvolution Techniques for Image Deblurring,* Project Report, 2002.

[61]   A. K. Jain, "Fundamentals of Digital Image Processing," *Prentice Hall Information and System Sciences Series*, pp. 565, 1989.

[62]   G. R. Ayers, and J. C. Dainty, "Iterative Blind Deconvolution Method and Its Applications," *Optics Letter,* vol. 13, no. 7, pp. 43-64, 1988.

[63]   B. L. K. Davey, R. G. Lane, and R. H. T. Bates, "Blind Deconvolution of Noisy Complex-Valued Image," *Optics Communications,* vol. 69, no. 5-6, pp. 353-356, Jan, 1989.

[64]   R. L. Lagendijk, J. Biemond, and D. E. Boekee, "Regularized Iterative Image-Restoration with Ringing Reduction," *IEEE Transactions on Acoustics Speech and Signal Processing,* vol. 36, no. 12, pp. 1874-1888, Dec, 1988.

[65]   A. N. Tikhonov, and V. Y. Arsenin, *Solutions of Ill-Posed Problems*, New York: Wiley, 1977.

[66]   B. R. Hunt, "The Application of Constrained Least-Squares Estimation to Image Restoration by Digital Computer," *IEEE Transactions on Computer,* vol. C-22, pp. 805-812, 1973.

[67]   Z. Wang, and A. C. Bovik, "A Universal Image Quality Index," *IEEE Signal Processing Letters,* vol. 9, no. 3, pp. 81-84, Mar, 2002.

[68]   T. N. Pappas, R. J. Safranek, and J. Q. Chen, *Perceptual Criteria for Image Quality Evaluation*, Amsterdam: Elsevier Science, 2005.

[69]   A. M. Eskicioglu, and P. S. Fisher, "Image Quality Measures and Their Performance," *IEEE Transactions on Communications,* vol. 43, no. 12, pp. 2959-2965, Dec, 1995.

[70]   D. Brunet, E. R. Vrscay, and Z. Wang, "On the Mathematical Properties of the Structural Similarity Index," *IEEE Transactions on Image Processing,* vol. 21, no. 4, pp. 1488-1499, Apr, 2012.

[71]   Z. Wang *et al.*, "Image quality assessment: From error visibility to structural similarity," *IEEE Transactions on Image Processing,* vol. 13, no. 4, pp. 600-612, Apr, 2004.

[72]   Z. Wang, and Q. Li, "Information Content Weighting for Perceptual Image Quality Assessment," *IEEE Transactions on Image Processing,* vol. 20, no. 5, pp. 1185-1198, May, 2011.

[73]   A. Hyvarinen, and E. Oja, "Independent Component Analysis: Algorithms and Applications," *Neural Networks,* vol. 13, no. 4-5, pp. 411-430, May-Jun, 2000.

[74] R. F. Dwyer, "Use of the Kurtosis Statistic in the Frequency-Domain as an Aid in Detecting Random Signals," *IEEE Journal of Oceanic Engineering,* vol. 9, no. 2, pp. 85-92, 1984.

[75] A. Khan, and H. Yin, "Efficient Blind Image Deconvolution Using Spectral Non-Gaussianity," *Integrated Computer-Aided Engineering,* vol. 19, no. 4, pp. 331-340, 2012.

[76] A. Khan, and H. J. Yin, "Spectral Non-gaussianity for Blind Image Deblurring," *Intelligent Data Engineering and Automated Learning - Ideal 2011*, Lecture Notes in Computer Science H. Yin, W. Wang and V. RaywardSmith, eds., pp. 144-151, Berlin: Springer-Verlag Berlin, 2011.

[77] A. Mittal, A. K. Moorthy, and A. C. Bovik, "No-Reference Image Quality Assessment in the Spatial Domain," *IEEE Transactions on Image Processing,* vol. 21, no. 12, pp. 4695-4708, Dec, 2012.

[78] A. Mittal, A. K. Moorthy, and A. C. Bovik, "BRISQUE Software Release," 2011.

[79] A. Mittal, R. Soundararajan, and A. C. Bovik, "Making a "Completely Blind" Image Quality Analyzer," *IEEE Signal Processing Letters,* vol. 20, no. 3, pp. 209-212, Mar, 2013.

[80] A. Mittal, A. K. Moorthy, and A. C. Bovik. "NIQE Software Release," http://live.ece.utexas.edu/research/quality/niqe.zip.

[81] L. D. Thede *et al.*, "A Comparison of Methods for the Optimization of VGA Colormaps," *Proceedings of Twenty-Fifth Southeastern Symposium on System Theory (SSST)*, pp. 508 - 512, 1993.

[82] Y. Gao, A. Rehman, and Z. Wang, "CW-SSIM Based Image Classification," in 18th IEEE International Conference on Image Processing, New York, 2011, pp. 1249-1252.

[83] A. Rehman, and Z. Wang, "SSIM-Based Non-Local Means Image Denoising," in 18th IEEE International Conference on Image Processing, New York, 2011, pp. 217-220.

[84] M. Haritopoulos, H. J. Yin, and N. M. Allinson, "Image Denoising Using Self-Organizing Map-Based Nonlinear Independent Component Analysis," in Neural Networks, 2002, pp. 1085-1098.

[85] Q. F. Zhang, H. J. Yin, and N. M. Allinson, "A Simplified ICA Based Denoising Method," *Proceedings of the IEEE-INNS-ENNS International Joint Conference on Neural Networks, Vol V*, pp. 479-482, Los Alamitos: IEEE Computer Soc, 2000.

[86] I. Hussain, "Non-Gaussianity Based Image Deblurring and Denoising," School of Electrical and Electronic Engineering, The University of Manchester, Manchester, 2008.

[87] J. Biemond, R. L. Lagendijk, and R. M. Mersereau, "Iterative Methods for Image Deblurring," *Proceedings of the IEEE,* vol. 78, no. 5, pp. 856-883,

May, 1990.

[88] M. I. Sezan, and A. M. Tekalp, "Survey of Recent Developments in Digital Image-Restoration," *Optical Engineering,* vol. 29, no. 5, pp. 393-404, May, 1990.

[89] M. Cannon, "Blind Deconvolution of Spatially Invariant Image Blurs With Phase," *IEEE Transactions on Acoustics Speech and Signal Processing,* vol. 24, no. 1, pp. 58-63, 1976.

[90] H. C. Andrews, and B. R. Hunt, *Digital Image Restoration*, Englewood Cliffs, N.J: Prentice Hall, 1977.

[91] A. K. Katsaggelos, and K. T. Lay, "Maximum-Likelihood Blur Identification and Image-Restoration Using the EM Algorithm," *IEEE Transactions on Signal Processing,* vol. 39, no. 3, pp. 729-733, Mar, 1991.

[92] D. C. Ghiglia, L. A. Romero, and G. A. Mastin, "Systematic-Approach to 2-Dimensional Blind Deconvolution by Zero-Sheet Separation," *Journal of the Optical Society of America a-Optics Image Science and Vision,* vol. 10, no. 5, pp. 1024-1036, May, 1993.

[93] D. B. Gennery, "Determination of Optical Transfer-Function by Inspection of Frequency-Domain Plot," *Journal of the Optical Society of America,* vol. 63, no. 12, pp. 1571-1577, 1973.

[94] T. J. Ulrych *et al.*, "Homomorphic Deconvolution of Some Teleseismic Events," *Bulletin of the Seismological Society of America,* vol. 62, no. 5, pp. 1269-1281, 1972.

[95] T. J. Ulrych, and C. Walker, "Analytic Minimum Entropy Deconvolution," *Geophysics,* vol. 47, no. 9, pp. 1295-1302, 1982.

[96] C. A. Cabrelli, "Minimum Entropy Deconvolution and Simplicity - A Non-Iterative Algorithm," *Geophysics,* vol. 50, no. 3, pp. 394-413, 1985.

[97] M. D. Sacchi, D. R. Velis, and A. H. Cominguez, "Minimum Entropy Deconvolution with Frequency-Domain Constraints," *Geophysics,* vol. 59, no. 6, pp. 938-945, Jun, 1994.

[98] R. W. Schafer, R. M. Mersereau, and M. A. Richards, "Constrained Iterative Restoration Algorithms," *Proceedings of the IEEE,* vol. 69, no. 4, pp. 432-450, 1981.

[99] M. Ben-Ezra, A. Zomet, and S. K. Nayar, "Video Super-Resolution Using Controlled Sub-pixel Detector Shifts," *IEEE Transactions on Pattern Analysis and Machine Intelligence,* vol. 27, no. 6, pp. 977-987, Jun, 2005.

[100] A. Mohan *et al.*, "Image Destabilization: Programmable Defocus using Lens and Sensor Motion," in IEEE International Conference on Computational Photography, 2009.

[101] H. Nagahara *et al.*, "Flexible Depth of Field Photography," *Proceedings of 10th European Conference on Computer Vision, IV.* pp. 60-73.

[102] P. Comon, "Independent Component Analysis: A New Concept," *Signal Processing,* vol. 36, no. 3, pp. 287-314, Apr, 1994.

[103] A. J. Bell, and T. J. Sejnowski, "An Information Maximization Approach to Blind Separation and Blind Deconvolution," *Neural Computation,* vol. 7, no. 6, pp. 1129-1159, Nov, 1995.

[104] A. J. Bell, and T. J. Sejnowski, "The "Independent Components" Of Natural Scenes Are Edge Filters," *Vision Research,* vol. 37, no. 23, pp. 3327-3338, Dec, 1997.

[105] J. F. Cardoso, "Infomax and Maximum Likelihood for Blind Source Separation," *IEEE Signal Processing Letters,* vol. 4, no. 4, pp. 112-114, Apr, 1997.

[106] A. Hyvarinen, "Fast and Robust Fixed-Point Algorithms for Independent Component Analysis," *IEEE Transactions on Neural Networks,* vol. 10, no. 3, pp. 626-634, May, 1999.

[107] J. Herault, C. Jutten, and B. Ans, "Detection de Grandeurs Primitives Dans un Message Composite par une Architecture de Calcul Neuromimetique en Apprentissage non Supervise," in Proceedings of GRETSI, 1985, pp. 1017-1020.

[108] J. F. Cardoso, "Blind Signal Separation: Statistical Principles," *Proceedings of the IEEE,* vol. 86, no. 10, pp. 2009-2025, Oct, 1998.

[109] J. F. Cardoso, "Iterative Techniques for Blind Source Separation Using Only Fourth-Order Cumulants," in European Signal Processing Conference, 1992, pp. 739-742.

[110] S. Umeyama, "Blind Deconvolution of Blurred Images By Use of ICA," *Electronics and Communications in Japan Part III-Fundamental Electronic Science,* vol. 84, no. 12, pp. 1-9, 2001.

[111] M. M. Bronstein *et al.*, "Blind Deconvolution of Images Using Optimal Sparse Representations," *IEEE Transactions on Image Processing,* vol. 14, no. 6, pp. 726-736, Jun, 2005.

[112] I. Kopriva, "Approach to Blind Image Deconvolution by Multiscale Subband Decomposition and Independent Component Analysis," *Journal of the Optical Society of America a-Optics Image Science and Vision,* vol. 24, no. 4, pp. 973-983, Apr, 2007.

[113] I. Kopriva, and D. Sersic, "Robust Blind Separation of Statistically Dependent Sources Using Dual Tree Wavelets," in IEEE International Conference on Image Processing, Vols 1-7, New York, 2007, pp. 433-436.

[114] Q. Du, and I. Kopriva, *Dependent Component Analysis for Multi-Frame Image Restoration and Enhancement*, New York: IEEE, 2008.

[115] H. J. Yin, and I. Hussain, "Independent Component Analysis and Non-Gaussianity for Blind Image Deconvolution and Deblurring," *Integrated Computer-Aided Engineering,* vol. 15, no. 3, pp. 219-228, 2008.

[116] P. Patrinos *et al.*, "Variable Selection in Nonlinear Modelling Based on RBF Networks and Evolutionary Computation," *International Journal of Neural Systems,* vol. 20, no. 5, pp. 365-379, Oct, 2010.

[117] S. Schliebs, N. Kasabov, and M. Defoin-Platel, "On the Probabilistic Optimization of Spiking Neural Networks," *International Journal of Neural Systems,* vol. 20, no. 6, pp. 481-500, Dec, 2010.

[118] I. Hussain, "Non-Gaussianity based Image Deblurring and Denoising " PhD dissertation, School of Electrical and Electronic Engineering, The University of Manchester, 2008.

[119] J. Antoni, and R. B. Randall, "The Spectral Kurtosis: Application to the Vibratory Surveillance and Diagnostics of Rotating Machines," *Mechanical Systems and Signal Processing,* vol. 20, no. 2, pp. 308-331, Feb, 2006.

[120] T. Barszcz, and R. B. Randall, "Application of Spectral Kurtosis for Detection of a Tooth Crack in the Planetary Gear of a Wind Turbine," *Mechanical Systems and Signal Processing,* vol. 23, no. 4, pp. 1352-1365, May, 2009.

[121] F. Y. Cong, J. Chen, and G. M. Dong, "Spectral Kurtosis Based On AR Model for Fault Diagnosis and Condition Monitoring Of Rolling Bearing," *Journal of Mechanical Science and Technology,* vol. 26, no. 2, pp. 301-306, Feb, 2012.

[122] J. J. G. de la Rosa, C. G. Puntonet, and A. Moreno, "Subterranean Termite Detection Using the Spectral Kurtosis," *Proceedings of IEEE Workshop on Intelligent Data Acquisition and Advanced Computing Systems: Technology and Applications.* pp. 351-354.

[123] J. Antoni, "The Spectral Kurtosis: A Useful Tool for Characterising Non-Stationary Signals," *Mechanical Systems and Signal Processing,* vol. 20, no. 2, pp. 282-307, Feb, 2006.

[124] "The Mathematical Uncertainty Principle", http://www.ams.org/samplings/feature-column/fcarc-uncertainty.

[125] W. O. Frank *et al.*, "NIST Handbook of Mathematical Functions," Cambridge University Press, 2010, p. 966.

[126] R. L. Lagendijk, R. M. Mersereau, and J. Biemond, "On Increasing the Convergence Rate of Regularized Iterative Image Restoration Algorithms," *IEEE Transactions on Acoustics, Speech and Signal Processing*, pp. 1183-1186, 1987.

[127] R. L. Lagendijk, J. Biemond, and D. E. Boekee, "Identification and Restoration of Noisy Blurred Images Using the Expectation-Maximization Algorithm," *IEEE Transactions on Acoustics, Speech and Signal Processing,* vol. 38, pp. 1180-1191, 1990.

[128] Y. L. You, and M. Kaveh, "A Regularization Approach to Joint Blur Identification and Image Restoration," *IEEE Transactions on Image Processing,* vol. 5, no. 3, pp. 416-428, Mar, 1996.

[129] "Desktop Nexus Wallpaper Image Database,"
http://www.desktopnexus.com/.

[130] R. Crane, *A Simplified Approach to Image Processing: Classical and Modern Techniques in C*: Prentice Hall PTR, USA, 1996.

[131] R. N. Tubbs, "Lucky Exposures: Diffraction Limited Astronomical Imaging through the Atmosphere.," PhD dissertation, Cambridge University 2003.

[132] R. Fergus *et al.* "Blurred Images for Blind Image Deblurring,"
http://cs.nyu.edu/~fergus/research/deblur/deblur_images.zip.

[133] "Nikon Image Stabilization,"
http://www.nikon.com/about/technology/life/imaging/stabilization/.

Appendices

Appendix A

Comprehensive Deblurring Results for Spectral Kurtosis based BID scheme

This appendix relates to the testing of spectral kurtosis based BID scheme. Fig. A.1 shows the images from Desktop Nexus image database use in experimentation. Full reference IQMs PSNR, MSSIM, UQI and non-reference IQMs BRISQUE and NIQE were used to evaluate the quality of the deblurred images. Table A.1 illustrates the deblurring results for Gaussian blurred images. A comparison of the spatial and spectral kurtosis based BID is presented. Comparison of the average quality measures for the two schemes reveals that the spectral kurtosis based BID scheme produces similar and at times better results than the spatial kurtosis based BID. For the motion blur case, tests were performed for the two blur parameters, angle and length, separately. In the first case the images were motion blurred at a certain angle and the length. The length information was assumed known. In the second case, the images were motion blurred and the angle information was assumed known. A comparison of the spatial and spectral kurtosis based BID is presented in Table A.2. Deblurring results for out-of-focus blurred images are illustrated in Table A.3.

Img-01　Img-02　Img-03　Img-04　Img-05

Img-06　Img-07　Img-08　Img-09　Img-10

Img-11　Img-12　Img-13　Img-14　Img-15

Img-16　Img-17　Img-18　Img-19　Img-20

Img-21　Img-22　Img-23　Img-24　Img-25

Img-26　Img-27　Img-28　Img-29　Img-30
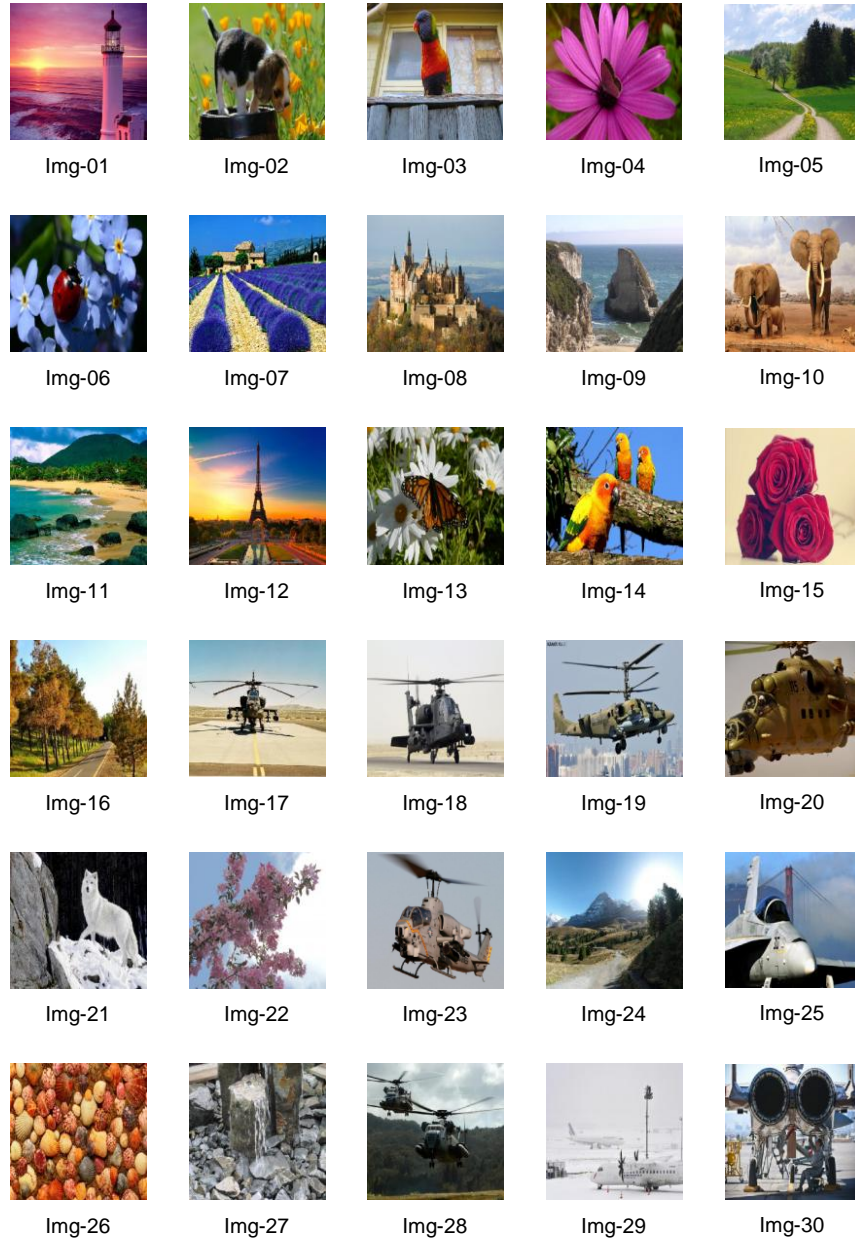
Fig. A.1. (a) Test Images from the Desktop Nexus image database used in experimentation for spectral kurtosis based BID scheme.

Table A.1: Artificial deblurring results for Gaussian blurred images using spatial and spectral kurtosis measure. Deblurred image quality is compared using full-reference and non-reference image quality measures.

Image	Blur Variance	Estimated Variance		Estimated NSR		PSNR		MSSIM		UQI		BRISQUE		NIQE	
		Spatial Kurtosis	Spectral Kurtosis	Spatial Kurtosis	Spectral Kurtosis	Spatial Kurtosis	Spectral Kurtosis	Spatial Kurtosis	Spectral Kurtosis	Spatial Kurtosis	Spectral Kurtosis	Spatial Kurtosis	Spectral Kurtosis	Spatial Kurtosis	Spectral Kurtosis
Img-01	1.00	1.30	1.05	5.00E-03	1.00E-04	32.64	35.91	0.94	0.97	0.99	1.00	27.06	17.90	7.63	5.61
Img-01	1.50	1.80	1.40	7.00E-04	7.00E-04	31.42	32.06	0.92	0.93	0.99	0.99	45.66	37.48	7.13	6.48
Img-02	2.00	2.25	2.25	7.00E-03	5.00E-04	29.88	29.88	0.88	0.88	0.99	0.99	55.11	55.11	6.64	6.64
Img-02	2.50	2.85	2.80	1.00E-04	1.00E-04	27.48	27.84	0.77	0.79	0.98	0.98	34.21	35.63	6.91	7.28
Img-03	3.00	2.95	3.15	2.00E-02	2.00E-03	26.91	26.87	0.80	0.80	0.98	0.98	67.23	68.46	8.24	8.19
Img-03	3.50	3.40	3.60	2.00E-02	7.00E-04	26.18	26.30	0.77	0.77	0.97	0.97	72.68	73.60	8.77	8.81
Img-04	4.00	4.05	4.00	8.00E-03	8.00E-03	25.88	25.88	0.76	0.76	0.97	0.97	74.50	74.48	8.95	8.96
Img-04	4.50	4.45	4.55	8.00E-03	8.00E-03	25.47	25.46	0.74	0.74	0.97	0.97	77.30	77.48	9.54	9.52
Img-05	5.00	4.90	5.05	6.00E-03	6.00E-04	25.22	25.20	0.73	0.73	0.97	0.97	79.11	78.78	9.86	9.88
Img-05	1.00	0.90	1.10	4.00E-03	4.00E-02	34.83	34.12	0.97	0.98	1.00	1.00	18.45	16.03	4.07	4.41
Img-06	1.50	1.30	1.35	5.00E-03	5.00E-03	32.17	32.41	0.97	0.97	0.99	0.99	31.13	31.50	5.32	5.39
Img-06	2.00	1.75	2.05	9.00E-05	9.00E-05	28.70	28.23	0.79	0.77	0.99	0.98	37.32	1.25	7.25	6.81
Img-07	2.50	2.30	2.40	1.00E-04	9.50E-07	28.13	28.34	0.83	0.84	0.98	0.99	36.46	37.15	6.75	6.80
Img-07	3.00	2.65	3.20	1.00E-03	2.00E-03	28.02	28.25	0.90	0.90	0.98	0.98	46.94	53.94	7.07	7.00
Img-08	3.50	3.50	3.50	8.00E-06	8.00E-06	27.32	27.32	0.87	0.87	0.98	0.98	66.68	66.68	8.00	8.00
Img-08	4.00	3.95	4.00	8.00E-07	8.00E-07	26.52	26.53	0.85	0.85	0.98	0.98	71.98	71.98	8.36	8.39
Img-09	4.50	4.30	4.25	8.00E-06	8.00E-06	25.74	25.63	0.82	0.82	0.97	0.97	76.24	76.47	8.90	8.99
Img-09	5.00	5.15	5.15	6.00E-06	6.00E-06	25.23	25.23	0.79	0.79	0.97	0.97	78.15	78.15	9.35	9.35
Img-10	1.00	1.15	0.85	4.00E-03	5.00E-02	30.38	33.42	0.97	0.96	1.00	1.00	40.75	29.34	4.31	3.73
Img-10	1.50	1.55	1.45	4.00E-03	7.00E-04	29.94	30.73	0.94	0.93	0.99	0.99	51.59	45.89	5.93	5.78
Img-11	2.00	1.85	2.05	1.00E-03	5.00E-04	28.67	26.46	0.88	0.89	0.99	0.99	36.87	45.07	6.32	6.39
Img-11	2.50	2.35	2.60	6.00E-05	2.00E-05	24.53	24.65	0.74	0.77	0.98	0.98	39.11	37.98	6.86	7.29
Img-12	3.00	3.10	3.25	2.00E-05	2.00E-03	23.12	22.87	0.66	0.65	0.96	0.96	35.00	30.79	8.50	8.58
Img-12	3.50	3.30	3.45	8.00E-06	7.00E-04	25.61	25.47	0.75	0.75	0.97	0.97	65.85	66.20	8.11	8.24
Img-13	4.00	4.00	4.00	8.00E-07	4.00E-06	24.58	24.58	0.72	0.72	0.97	0.97	72.39	72.39	9.02	9.02
Img-13	4.50	4.45	4.45	8.00E-06	7.00E-06	24.04	24.04	0.69	0.69	0.96	0.96	75.03	75.03	9.27	9.27
Img-14	5.00	5.00	5.05	6.00E-07	3.00E-06	23.50	23.40	0.67	0.67	0.96	0.96	77.94	77.90	9.52	9.52
Img-14	1.00	1.05	0.95	4.00E-02	4.00E-04	37.68	37.19	0.99	0.98	1.00	1.00	24.14	24.51	5.36	5.24
Img-15	1.50	1.50	1.55	4.00E-03	4.00E-06	35.08	35.00	0.97	0.97	1.00	1.00	24.32	24.53	5.52	5.56
Img-15	2.00	2.05	2.05	1.00E-03	1.00E-04	32.04	32.04	0.95	0.95	0.99	0.99	30.15	30.15	5.88	5.88
Img-16	2.50	2.50	2.60	6.00E-05	6.00E-05	26.09	24.46	0.82	0.82	0.99	0.99	38.04	37.00	7.00	6.87
Img-16	3.00	3.10	3.10	2.00E-05	2.00E-05	19.15	19.15	0.72	0.72	0.97	0.97	40.66	40.66	8.84	8.84
Img-17	3.50	3.40	3.40	8.00E-06	8.00E-05	28.32	28.32	0.87	0.87	0.98	0.98	63.47	63.47	8.96	8.96
Img-17	4.00	4.05	4.00	8.00E-07	8.00E-07	27.33	27.35	0.85	0.85	0.98	0.98	67.48	67.78	9.68	9.63
Img-18	4.50	4.50	4.65	8.00E-06	7.00E-07	26.30	26.44	0.83	0.82	0.98	0.98	73.24	72.58	10.25	10.32
Img-18	5.00	5.00	5.10	6.00E-07	6.00E-08	25.54	25.69	0.80	0.80	0.97	0.97	79.04	78.49	10.75	10.77
Img-19	1.00	1.05	1.10	4.00E-02	4.00E-02	36.98	35.88	0.99	0.99	1.00	1.00	42.80	41.26	6.14	6.19
Img-19	1.50	1.65	1.60	4.00E-02	4.00E-03	32.56	32.95	0.98	0.98	1.00	1.00	54.12	54.18	7.12	7.22
Img-20	2.00	1.95	2.00	4.00E-03	1.00E-03	33.48	33.49	0.98	0.98	1.00	1.00	45.08	45.36	6.89	6.83
Img-20	2.50	2.45	2.50	1.00E-03	6.00E-05	32.25	32.27	0.96	0.96	1.00	1.00	42.83	43.37	6.95	6.86
Img-21	3.00	3.10	3.10	6.00E-05	1.00E-05	29.30	29.30	0.84	0.84	0.99	0.99	44.35	44.35	6.95	6.95
Img-21	3.50	3.35	3.25	1.00E-05	1.00E-08	25.35	25.26	0.61	0.60	0.98	0.98	34.98	44.47	6.34	7.48
Img-22	4.00	4.15	4.10	8.00E-07	8.00E-07	28.76	28.78	0.90	0.91	0.99	0.99	78.28	78.48	8.70	8.66
Img-22	4.50	4.40	4.40	1.00E-08	1.00E-08	27.97	27.97	0.90	0.90	0.99	0.99	86.08	86.08	9.15	9.15
Img-23	5.00	4.95	5.05	6.00E-07	6.00E-07	27.26	27.17	0.87	0.87	0.99	0.99	89.34	88.21	9.46	9.50
Mean						28.30	**28.35**	**0.84**	**0.84**	**0.98**	**0.98**	54.43	**53.28**	7.70	**7.67**

Table A.2: Artificial deblurring results for motion blurred images using spatial and spectral kurtosis measure. Deblurred image quality is compared using full-reference and non-reference image quality measures.

Image	Blur Angle (A) / Blur Length (L)		Estimated value Spatial Kurtosis	Estimated value Spectral Kurtosis	Estimated NSR Spatial Kurtosis	Estimated NSR Spectral Kurtosis	PSNR Spatial Kurtosis	PSNR Spectral Kurtosis	MSSIM Spatial Kurtosis	MSSIM Spectral Kurtosis	UQI Spatial Kurtosis	UQI Spectral Kurtosis	BRISQUE Spatial Kurtosis	BRISQUE Spectral Kurtosis	NIQE Spatial Kurtosis	NIQE Spectral Kurtosis
Img-01	A	11	9.40	10.00	4.00E-03	9.00E-04	33.11	31.91	0.96	0.90	1.00	0.99	18.18	22.68	4.90	6.82
Img-02	A	17	16.40	16.30	4.00E-03	9.00E-04	30.31	29.37	0.91	0.85	0.99	0.99	27.69	30.69	4.30	6.33
Img-03	A	25	23.25	24.30	2.00E-03	4.00E-04	29.01	27.53	0.87	0.74	0.99	0.98	24.98	23.67	5.11	8.57
Img-04	A	45	43.00	44.00	4.00E-03	4.00E-04	27.42	26.09	0.86	0.69	0.98	0.97	32.49	40.83	4.56	6.63
Img-05	A	65	64.00	64.00	1.00E-03	7.00E-05	27.12	26.80	0.78	0.75	0.98	0.98	29.70	31.87	5.82	6.40
Img-06	A	11	11.00	11.50	8.00E-05	9.00E-04	25.63	29.11	0.74	0.91	0.98	0.99	76.17	30.83	9.85	6.11
Img-07	A	17	14.50	14.50	4.00E-03	9.00E-04	27.82	25.87	0.90	0.86	0.99	0.98	20.70	23.45	3.54	3.85
Img-08	A	25	25.00	25.00	4.00E-03	4.00E-04	26.86	24.76	0.88	0.77	0.98	0.98	24.10	21.64	3.34	6.24
Img-09	A	45	45.70	44.70	4.00E-04	4.00E-04	23.92	23.85	0.73	0.72	0.97	0.97	31.13	32.00	5.81	5.53
Img-10	A	65	64.30	64.20	4.00E-03	7.00E-04	26.24	24.47	0.86	0.78	0.98	0.98	23.53	28.03	4.20	5.25
Img-11	A	11	13.10	12.40	8.00E-04	9.00E-04	34.25	34.40	0.92	0.92	1.00	1.00	17.72	17.44	7.33	7.38
Img-12	A	17	17.35	17.00	1.00E-03	9.00E-04	31.35	31.53	0.89	0.88	0.99	0.99	20.17	19.87	7.13	7.08
Img-13	A	25	25.80	24.00	6.00E-04	9.00E-04	30.23	28.88	0.84	0.79	0.99	0.99	4.15	23.26	5.29	8.08
Img-14	A	45	45.60	45.60	4.00E-03	4.00E-04	29.92	26.51	0.90	0.76	0.99	0.98	19.57	27.08	5.06	6.92
Img-15	A	65	66.60	63.55	4.00E-03	7.00E-04	29.50	26.39	0.90	0.79	0.99	0.98	16.29	22.21	4.87	7.01
Img-16	A	11	13.00	11.00	4.00E-03	9.00E-04	37.99	36.95	0.97	0.93	1.00	1.00	14.51	19.59	5.89	9.88
Img-17	A	17	16.90	16.90	8.00E-04	9.00E-05	33.73	30.45	0.88	0.71	1.00	0.99	22.85	47.63	8.72	12.07
Img-18	A	25	25.80	23.85	8.00E-04	4.00E-04	32.42	31.26	0.86	0.78	1.00	0.99	2.75	19.27	6.19	10.16
Img-19	A	45	44.00	43.60	4.00E-03	4.00E-04	30.87	29.31	0.89	0.74	0.99	0.99	28.06	34.90	5.34	8.06
Img-20	A	65	65.00	64.00	4.00E-03	7.00E-04	30.43	29.44	0.90	0.79	0.99	0.99	23.89	25.46	5.33	7.96
Img-21	A	11	11.35	11.40	4.00E-03	9.00E-04	29.12	29.32	0.96	0.94	1.00	1.00	25.10	23.17	4.91	6.41
Img-22	A	17	17.00	16.45	4.00E-03	9.00E-04	26.67	27.08	0.89	0.88	0.99	0.99	28.41	31.14	4.52	5.03
Img-23	A	25	24.70	24.00	4.00E-03	4.00E-04	25.72	25.80	0.87	0.81	0.99	0.99	32.76	33.01	4.45	6.20
Img-24	A	45	45.00	44.00	4.00E-04	9.00E-04	24.79	25.06	0.85	0.81	0.98	0.98	33.45	33.65	5.04	5.24
Img-25	A	65	65.00	65.00	4.00E-03	6.00E-04	24.84	24.85	0.86	0.81	0.98	0.98	29.16	34.19	4.87	6.00
Img-01	L	7	7.00	7.00	4.00E-03	7.00E-04	31.53	30.22	0.93	0.86	0.99	0.99	26.47	38.12	4.74	7.33
Img-02	L	9	9.00	9.00	4.00E-03	5.00E-03	30.20	30.25	0.91	0.92	0.99	0.99	28.35	30.20	4.19	4.22
Img-03	L	16	14.50	17.50	4.00E-03	4.00E-03	25.30	26.52	0.82	0.78	0.98	0.98	36.93	38.92	5.07	5.22
Img-04	L	23	21.70	21.80	4.00E-03	4.00E-03	26.65	26.72	0.86	0.86	0.98	0.98	25.60	26.14	5.07	5.15
Img-05	L	7	6.00	7.00	4.00E-03	7.00E-04	25.50	26.77	0.85	0.87	0.99	0.99	29.34	35.82	3.95	5.79
Img-06	L	9	9.10	9.00	4.00E-03	5.00E-03	27.96	28.50	0.89	0.90	0.99	0.99	23.31	24.73	3.84	3.86
Img-07	L	16	16.00	17.10	4.00E-04	4.00E-03	23.62	23.95	0.71	0.78	0.97	0.97	32.88	29.87	5.73	5.09
Img-08	L	23	23.25	22.00	4.00E-03	4.00E-03	25.29	24.51	0.86	0.85	0.98	0.98	19.44	19.99	4.23	5.08
Img-09	L	7	7.00	7.40	4.00E-03	7.00E-04	34.54	32.47	0.95	0.88	1.00	0.99	15.88	28.49	5.08	7.33
Img-10	L	9	9.00	8.90	4.00E-03	5.00E-03	32.46	32.53	0.93	0.93	0.99	0.99	16.96	19.13	4.52	4.51
Img-11	L	16	16.00	17.00	4.00E-03	4.00E-03	29.58	27.82	0.89	0.87	0.99	0.98	21.92	23.09	5.35	5.56
Img-12	L	23	23.00	21.65	4.00E-03	4.00E-03	27.93	27.75	0.90	0.88	0.98	0.98	11.16	12.57	5.51	5.42
Img-13	L	7	6.90	6.75	4.00E-03	7.00E-04	35.88	34.85	0.95	0.89	1.00	1.00	16.83	21.10	6.14	10.54
Img-14	L	9	8.90	8.90	4.00E-03	5.00E-03	33.79	33.67	0.94	0.94	1.00	1.00	20.50	22.60	5.20	5.15
Img-15	L	16	16.35	17.00	4.00E-03	4.00E-03	30.38	29.69	0.88	0.85	0.99	0.99	30.18	30.73	5.59	6.04
Img-16	L	23	22.10	22.40	4.00E-03	4.00E-03	28.94	29.06	0.90	0.90	0.99	0.99	24.09	23.93	5.75	5.56
Img-17	L	7	6.60	6.75	8.00E-04	7.00E-04	27.53	27.92	0.91	0.89	0.99	0.99	23.04	34.69	4.58	6.00
Img-18	L	9	9.35	9.00	1.00E-03	5.00E-03	26.35	26.32	0.88	0.89	0.99	0.99	31.27	30.51	4.70	4.68
Img-19	L	16	16.00	17.00	6.00E-04	4.00E-03	24.52	23.79	0.84	0.78	0.98	0.98	33.49	34.35	4.83	5.35
Img-20	L	23	22.80	22.95	4.00E-03	4.00E-03	24.11	24.12	0.86	0.86	0.98	0.98	28.71	29.18	5.33	5.29
Mean							**28.92**	28.32	**0.88**	0.84	**0.99**	0.99	**24.97**	28.04	**5.24**	6.41

Table A.3: Artificial deblurring results for out-of-focus blurred images using spatial and spectral kurtosis measure. Deblurred image quality is compared using full-reference and non-reference image quality measures.

Image	Blur Radius	Estimated Radius		Estimated NSR		PSNR		MSSIM		UQI		BRISQUE		NIQE	
		Spatial Kurtosis	Spectral Kurtosis	Spatial Kurtosis	Spectral Kurtosis	Spatial Kurtosis	Spectral Kurtosis	Spatial Kurtosis	Spectral Kurtosis	Spatial Kurtosis	Spectral Kurtosis	Spatial Kurtosis	Spectral Kurtosis	Spatial Kurtosis	Spectral Kurtosis
Img-01	7	6.25	7.15	6.00E-04	4.00E-04	25.45	27.17	0.62	0.69	0.97	0.98	37.17	22.36	5.26	4.50
Img-02	9	9.25	9.15	4.00E-04	5.00E-04	26.13	26.55	0.68	0.72	0.97	0.97	21.17	21.47	4.17	4.33
Img-03	13	13.35	13.35	5.00E-04	6.00E-04	24.80	24.92	0.69	0.70	0.96	0.96	27.33	31.51	4.45	4.56
Img-04	17	16.95	17.10	6.00E-04	4.00E-04	23.85	23.69	0.69	0.67	0.95	0.95	31.82	22.61	5.28	4.74
Img-05	21	20.30	20.00	4.00E-04	4.00E-04	22.62	22.44	0.64	0.62	0.94	0.93	23.09	24.75	5.19	5.33
Img-06	23	21.90	21.65	4.00E-04	4.00E-04	22.33	22.05	0.63	0.60	0.93	0.93	24.37	23.40	5.13	5.43
Img-07	7	6.30	7.30	6.00E-04	6.00E-04	22.78	23.47	0.63	0.70	0.96	0.97	26.66	24.88	4.84	3.99
Img-08	9	9.00	9.00	4.00E-04	6.00E-04	22.73	23.19	0.68	0.72	0.96	0.96	17.54	21.14	4.09	3.99
Img-09	13	13.55	13.15	4.00E-04	4.00E-04	20.90	21.21	0.59	0.64	0.93	0.94	25.08	23.20	4.35	4.26
Img-10	17	17.00	17.00	4.00E-04	5.00E-04	20.14	20.26	0.62	0.64	0.92	0.92	23.96	30.12	4.52	4.75
Img-11	21	20.10	20.00	6.00E-04	4.00E-04	19.13	19.31	0.56	0.58	0.89	0.90	26.93	38.62	5.25	6.04
Img-12	23	22.00	22.00	6.00E-04	4.00E-04	18.89	18.67	0.58	0.56	0.88	0.88	41.83	29.95	6.45	5.78
Img-13	7	5.50	7.05	6.00E-04	5.00E-04	22.31	26.08	0.54	0.78	0.95	0.98	19.19	9.49	6.66	5.58
Img-14	9	9.15	9.10	4.00E-04	6.00E-04	25.57	26.31	0.74	0.80	0.97	0.98	8.42	12.10	5.09	4.97
Img-15	13	13.25	13.00	6.00E-04	4.00E-04	24.21	22.64	0.78	0.75	0.97	0.97	21.18	8.74	5.13	4.83
Img-16	17	15.00	17.00	5.00E-04	4.00E-04	19.37	23.03	0.60	0.74	0.92	0.95	17.44	13.48	5.54	4.95
Img-17	21	21.75	20.65	4.00E-04	6.00E-04	20.71	22.43	0.70	0.75	0.93	0.94	23.58	31.33	5.44	5.90
Img-18	23	23.10	23.10	4.00E-04	4.00E-04	22.29	22.29	0.73	0.73	0.93	0.93	24.50	24.50	5.51	5.51
Img-19	7	7.35	6.85	6.00E-04	6.00E-04	28.28	29.45	0.72	0.78	0.99	0.99	14.44	13.10	4.81	5.04
Img-20	9	9.35	9.35	4.00E-04	6.00E-04	27.16	27.65	0.70	0.76	0.99	0.99	11.47	16.48	4.60	4.42
Img-21	13	13.00	12.60	5.00E-04	4.00E-04	26.30	25.89	0.75	0.72	0.98	0.98	8.46	7.13	4.63	4.77
Img-22	17	18.00	17.00	6.00E-04	5.00E-04	22.30	24.42	0.61	0.74	0.96	0.97	31.49	25.42	5.90	5.48
Img-23	21	21.10	21.30	6.00E-04	6.00E-04	22.88	22.80	0.70	0.72	0.96	0.96	29.93	47.51	6.04	7.22
Img-24	23	23.50	23.25	4.00E-04	6.00E-04	22.28	22.41	0.71	0.72	0.96	0.96	49.93	50.00	7.62	7.70
Img-25	7	7.00	7.10	4.00E-04	4.00E-04	24.12	24.03	0.77	0.76	0.98	0.98	25.78	25.81	5.67	5.48
Img-26	9	9.00	9.00	6.00E-04	4.00E-04	22.92	22.85	0.76	0.74	0.97	0.97	29.69	25.85	4.89	5.17
Img-27	13	12.65	13.00	4.00E-04	6.00E-04	21.01	21.37	0.68	0.70	0.95	0.96	31.89	30.06	5.06	4.90
Img-28	17	17.00	17.00	4.00E-04	4.00E-04	19.72	19.72	0.64	0.64	0.94	0.94	36.42	36.42	5.51	5.51
Img-29	21	21.00	21.00	4.00E-04	4.00E-04	18.75	18.75	0.60	0.60	0.92	0.92	41.06	41.06	6.18	6.18
Img-30	23	22.10	22.60	5.00E-04	5.00E-04	18.11	18.31	0.55	0.57	0.90	0.91	48.50	47.67	6.99	6.54
Mean						22.60	**23.11**	0.66	**0.69**	**0.95**	**0.95**	26.68	**26.00**	5.34	**5.26**

Appendix B

# Comprehensive Deblurring Results for BRISQUE, NIQE and RPSNR Based BID Scheme

This appendix relates to the deblurring results of real life motion and out-of-focus blurred images. The images used for testing are shown in Fig. B.1 to Fig. B.9. These include images captured by the author as well as by from other sources.
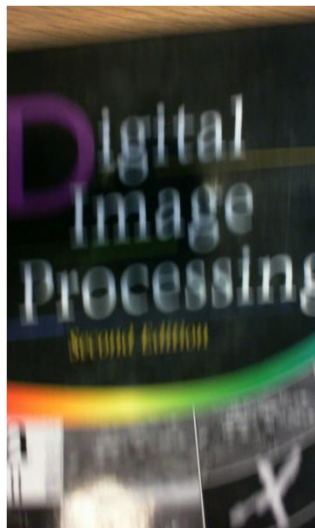

Fig. B.1. (a) Test Images with linear motion blur captured by the author.

Fig. B.2. (a) Test Images with linear motion blur from [133].
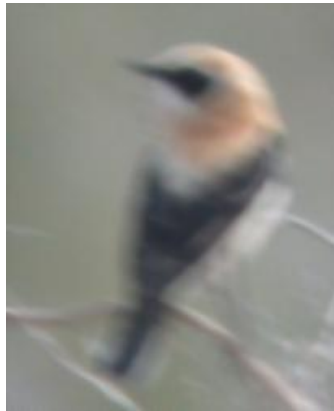
Fig. B.3. (a) Test Images with linear motion blur from [17] .

Fig. B.4. (a) Test Images with linear motion blur captured by the author.

Fig. B.5. (a) Test Images with linear motion blur captured by the author.

Fig. B.6. (a) Test Images with linear motion blur captured by the author.

Fig. B.7. (a) Test Images with linear motion blur captured by the author.

Fig. B.8. (a) Test Images with out-of-focus blur captured by the author.

Fig. B.9. (a) Test Images with out-of-focus blur captured by the author.

PSF estimation was made using spatial kurtosis, spectral kurtosis, RPSNR, BRISQUE and NIQE measures. The estimated PSF parameter values and the NSR values are given in Table B.1. Image quality values computed for spatial kurtosis, spectral kurtosis, RPSNR, BRISQUE and NIQE estimates are given in Table B.2. The deblurring results are illustrated in Fig. B.10 to Fig. B.18.

BRISQUE shows the best deblurring quality, on average, as compared to the other IQMs. RPSNR was not computed in the case of out-of-focus blur due to its inability to correctly estimate the blurring PSF parameters.

Table B.1 Deblurring results for real life motion blurred and out-of-focus blurred images.

Image	Estimated Values														
	Spatial Kurtosis			Spectral Kurtosis			RPSNR			BRISQUE			NIQE		
	Length	Angle	NSR	Length	Angle	NSR	Length	Angle	NSR	Length	Angle	NSR	Length	Angle	NSR
Fig. B-1	19	80	4.00E-02	19	90	4.00E-02	19	80	4.00E-02	15	81	4.00E-02	17	87	4.00E-03
Fig. B-2	15	13	4.00E-02	15	13	4.00E-02	15	13	4.00E-02	13	13	4.00E-02	13	10	4.00E-02
Fig. B-3	16	161	4.00E-03	21	160	4.00E-03	21	156	4.00E-03	20	161	4.00E-03	17	156	4.00E-03
Fig. B-4	26	96	4.00E-03	26	96	4.00E-03	26	98	4.00E-03	22	98	4.00E-03	25	94	4.00E-03
Fig. B-5	71	-2	4.00E-03	77	3	4.00E-02	77	3	4.00E-03	71	0	4.00E-03	73	3	4.00E-03
Fig. B-6	9	7	4.00E-03	15	13	4.00E-02	15	13	4.00E-03	13	12	4.00E-03	13	7	4.00E-03
Fig. B-7	6	90	4.00E-02	10	84	4.00E-02	10	84	4.00E-03	7	84	4.00E-03	7	85	4.00E-02
	Radius		NSR	Radius		NSR	Radius		NSR	Radius		NSR	Radius		NSR
Fig. B-8	13		4.00E-04	15		4.00E-05	/		/	13		4.00E-03	13		4.00E-03
Fig. B-9	5		4.00E-03	3		4.00E-04	/		/	4		4.00E-03	5		4.00E-03

Table B.2 Deblurring quality for real life motion blurred and out-of-focus blurred images computed using.

Image	Blurred Image Quality	Deblurred Image Quality for Paramter Estimated					Blurred Image Quality	Deblurred Image Quality for Paramter				
		Spatial Kurtosis	Spectral Kurtosis	RPSNR	BRISQUE	NIQE		Spatial Kurtosis	Spectral Kurtosis	RPSNR	BRISQUE	NIQE
		BRISQUE Values						NIQE Values				
Fig. B-1	60.44	52.60	52.60	52.60	47.73	41.97	6.73	8.39	8.39	8.39	8.71	8.12
Fig. B-2	58.11	31.12	31.12	31.12	29.46	29.46	17.21	8.13	8.13	8.13	8.57	8.57
Fig. B-3	44.99	58.10	52.82	55.20	54.59	55.20	11.23	8.45	6.64	6.40	7.32	6.40
Fig. B-4	29.77	25.79	25.79	25.79	25.74	26.71	5.78	4.41	4.41	4.41	4.46	4.36
Fig. B-5	13.78	18.43	37.45	37.45	18.43	24.17	5.25	5.34	9.07	9.07	5.34	6.17
Fig. B-6	39.85	30.09	33.76	33.76	18.76	18.76	7.01	7.74	7.49	7.49	5.21	5.21
Fig. B-7	11.10	42.34	27.96	27.96	33.83	33.78	4.54	6.03	6.21	6.21	10.18	5.51
Fig. B-8	12.47	18.75	100.82	/	3.86	3.86	9.45	6.85	16.85	/	3.72	3.72
Fig. B-9	53.12	23.69	39.28	/	7.94	23.69	8.79	6.25	8.75	/	4.57	4.25
Mean	35.96	33.43	44.62	37.70	26.71	28.62	8.44	6.84	8.44	7.16	6.45	5.81

(a)

(b)

(c)

(d)

(e)

(f)

Fig. B.10. (a) Blurred image. Deblurred using (b) Spatial kurtosis measure (c) Spectral kurtosis measure (d) RPSNR measure (e) BRISQUE measure and (f) NIQE measure.
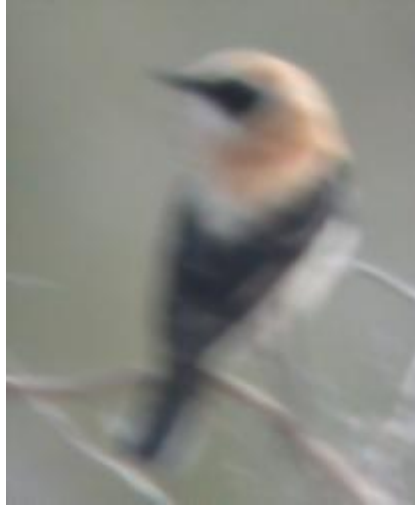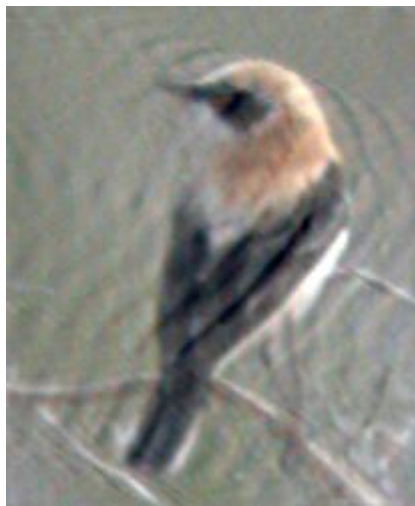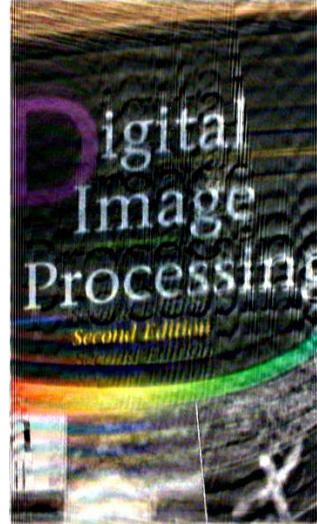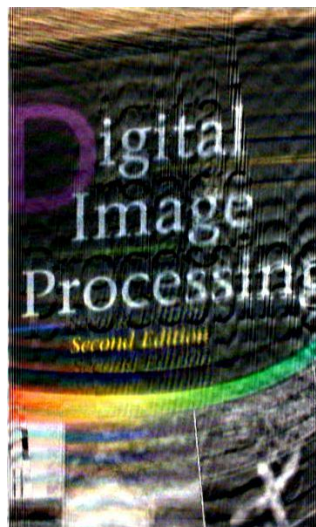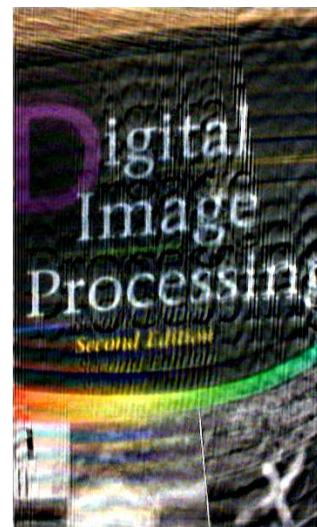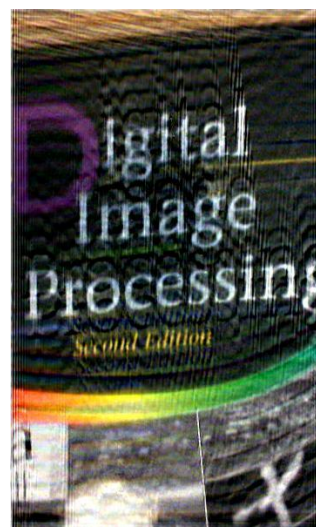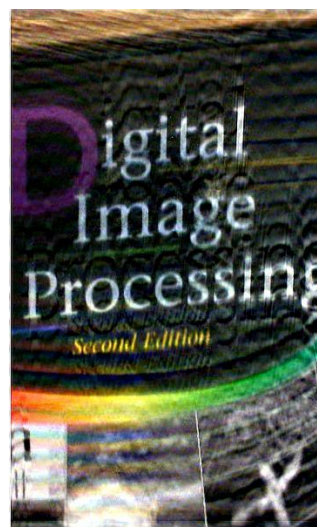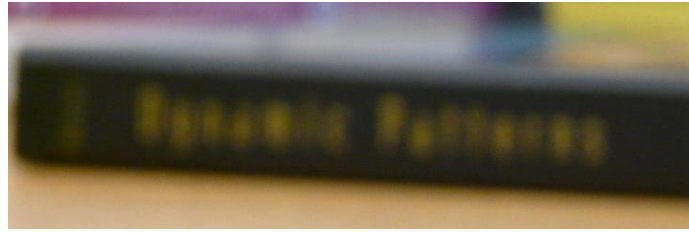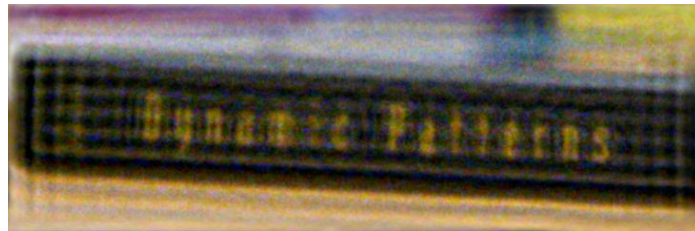
(a)

(b)

(c)

(d)

(e)

(f)

Fig. B.11. (a) Blurred image. Deblurred using (b) Spatial kurtosis measure (c) Spectral kurtosis measure (d) RPSNR measure (e) BRISQUE measure and (f) NIQE measure.
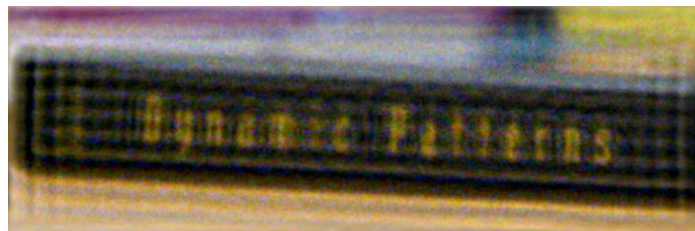
173
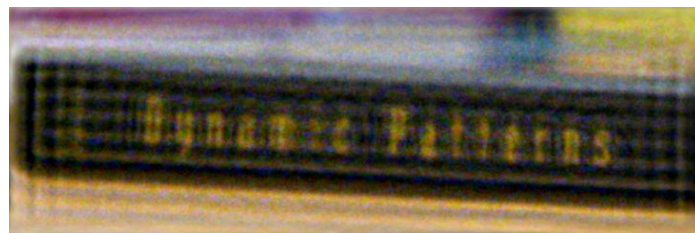
(a)　　　　　　　　　　　　(b)

(c)　　　　　　　　　　　　(d)

(e)　　　　　　　　　　　　(f)

Fig. B.12. (a) Blurred image. Deblurred using (b) Spatial kurtosis measure (c) Spectral kurtosis measure (d) RPSNR measure (e) BRISQUE measure and (f) NIQE measure.

174

Fig. B.13. (a) Blurred image. Deblurred using (b) Spatial kurtosis measure (c) Spectral kurtosis measure (d) RPSNR measure (e) BRISQUE measure and (f) NIQE measure.
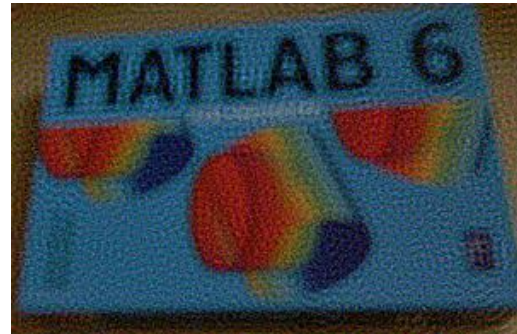
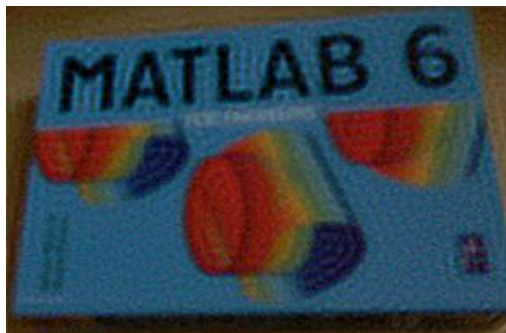(a) (b)

(c) (d)

(e) (f)

Fig. B.14. (a) Blurred image. Deblurred using (b) Spatial kurtosis measure (c) Spectral kurtosis measure (d) RPSNR measure (e) BRISQUE measure and (f) NIQE measure.

Fig. B.15. (a) Blurred image. Deblurred using (b) Spatial kurtosis measure (c) Spectral kurtosis measure (d) RPSNR measure (e) BRISQUE measure and (f) NIQE measure.

Fig. B.16. (a) Blurred image. Deblurred using (b) Spatial kurtosis measure (c) Spectral kurtosis measure (d) RPSNR measure (e) BRISQUE measure and (f) NIQE measure.

(a)

(b)

(c)

(d)

(e)

Fig. B.17. (a) Blurred image. Deblurred using (b) Spatial kurtosis measure (c) Spectral kurtosis measure. (d) BRISQUE measure and (e) NIQE measure.

Fig. B.18. (a) Blurred image. Deblurred using (b) Spatial kurtosis measure (c) Spectral kurtosis measure. (d) BRISQUE measure and (e) NIQE measure.

Appendix C

# Comprehensive Deblurring Results for Arbitrarily Shaped PSF Estimation Based BID Scheme

This appendix relates to the blind deblurring results for the BRISQUE based arbitrarily shaped PSF estimation scheme. The scheme can estimate parametric and arbitrarily shaped PSFs using a single algorithm. The deblurring results for parametric Gaussian, motion and out-of-focus blur and arbitrarily shaped PSFs is given in Table. C.1. The deblurred image quality scores computed using the BRISQUE and NIQE non-reference IQMS show that, on average, the deblurred images are of high quality. The deblurring results for blurred images along with the estimated PSFs are shown in Fig. C.1 − C.13. The deblurred images appear sharper and detailed after restoration.

Table C.1 Deblurring quality for images blurred by parametric and arbitrarily shaped PSFs. The BID scheme based on BRISQUE measure is used to estimate parametric and arbitrarily shaped PSFs using a single algorithm.

| Figure Number	Filter	Size (pixels)	Parameter Values	BRISQUE			NIQE		
				Original	Blurred	Deblurred	Original	Blurred	Deblurred
Fig. C.1	Gaussian	5x5	$\sigma^2=0.5$	14.18	25.54	18.49	4.74	4.54	4.54
Fig. C.2	Gaussian	5x5	$\sigma^2=1.0$	20.14	37.83	27.63	4.99	5.57	4.69
Fig. C.3	Gaussian	8x8	$\sigma^2=1.5$	19.91	29.71	28.26	5.32	6.65	5.17
Fig. C.4	Motion	5x5	L=5, A=45	9.42	9.55	27.44	4.98	4.37	4.92
Fig. C.5	Motion	3x17	L=17, A=6	47.88	82.44	57.99	6.85	16.93	8.47
Fig. C.6	Out-of-focus	5x5	R=2	13.76	16.29	26.08	4.53	4.57	5.03
Fig. C.7	Out-of-focus	11x11	R=5	14.18	41.78	61.01	4.74	5.66	10.34
Fig. C.8	Out-of-focus	15x15	R=7	6.68	42.03	59.13	5.11	5.74	10.45
Fig. C.9	Arbitrary	31x19	-	15.12	23.89	20.43	6.79	9.78	8.54
Fig. C.10	Arbitrary	3x3	-	11.19	61.47	14.49	3.94	15.46	4.10
Fig. C.11	Arbitrary	13x3	-	7.91	10.20	27.82	4.63	5.04	6.47
Fig. C.12	Arbitrary	19x13	-	32.31	51.34	53.03	3.56	10.20	7.36
Fig. C.13	Arbitrary	19x13	-	53.39	60.30	43.50	9.39	9.61	6.29
Mean				20.47	37.87	35.79	5.35	8.01	6.64
σ^2=Variance, L=length, A=Angle, R=Radius									

An interesting case for deblurring is that of a point filter, as shown in Fig. 5.3. The image was filtered using a point filter which basically feeds the deblurring algorithm with the same non blurred image. It was done to test the effectiveness of the algorithm in case a non-blurred image was provided. The deblurring scheme in such case still tries to find a PSF coefficient matrix that can, if possible, optimize the fitness function. A positive outcome of this behaviour is that if the original image in the artificial blurring case depicts any blurring even in its pristine form, the algorithm will try to remove it. Fig. 5.3 depicts this behaviour, where the deblurred image appears sharper than the original image.

(a)   (b)   (c)

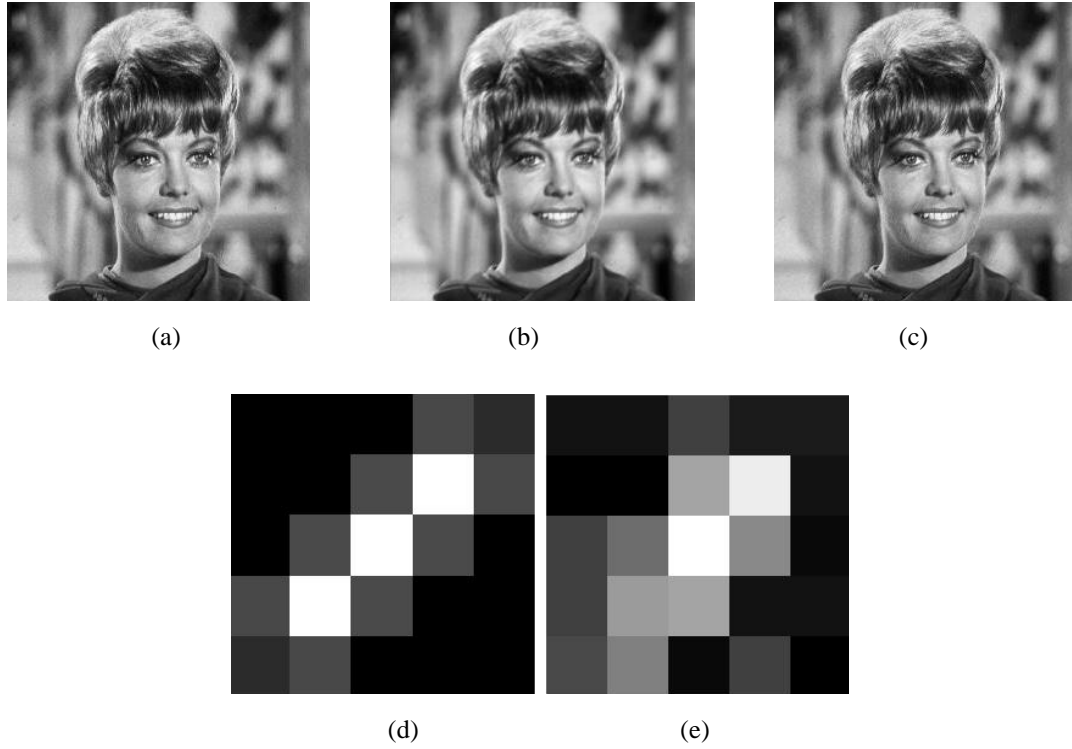(d)   (e)
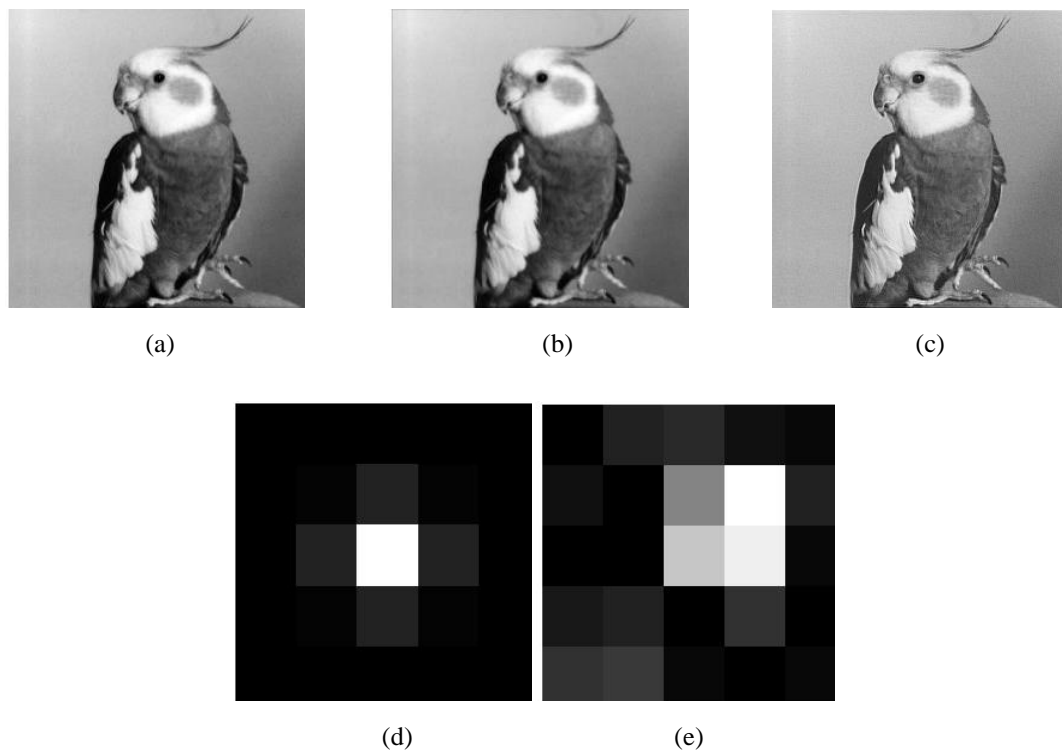
Fig. C.1 Deblurring result for image blurred by Gaussian PSF of size 5 x 5 pixels and variance 0.5. (a) Original image (b) Blurred image (c) Deblurred image (d) Blurring PSF and (e) Estimated PSF.
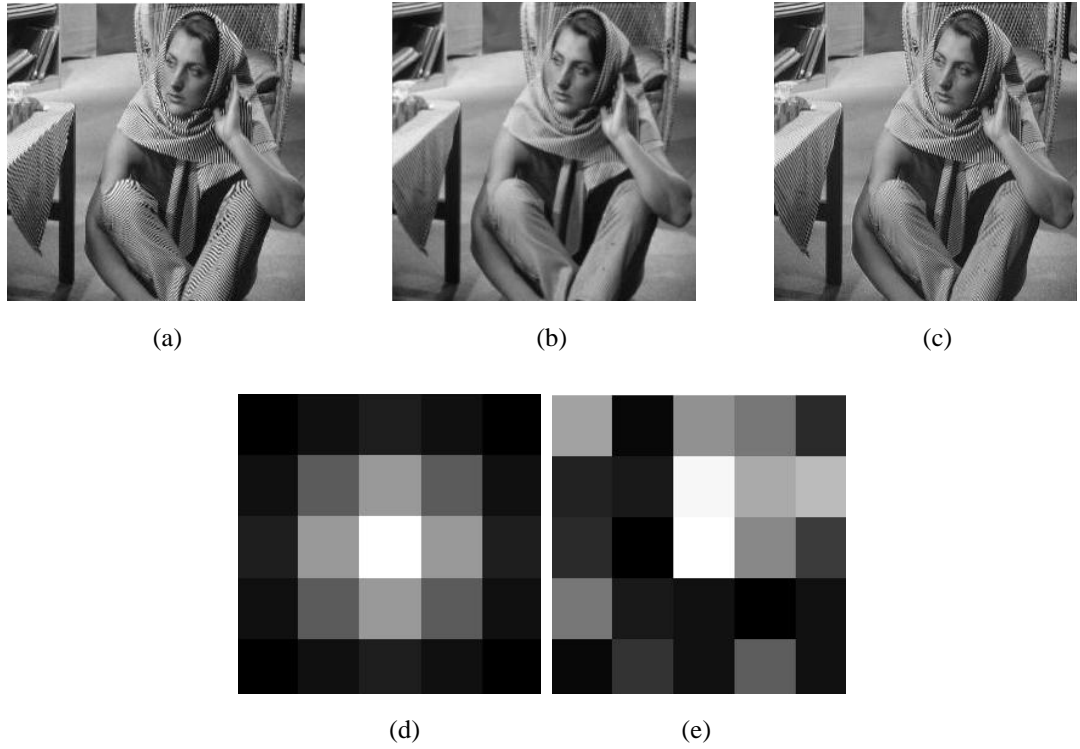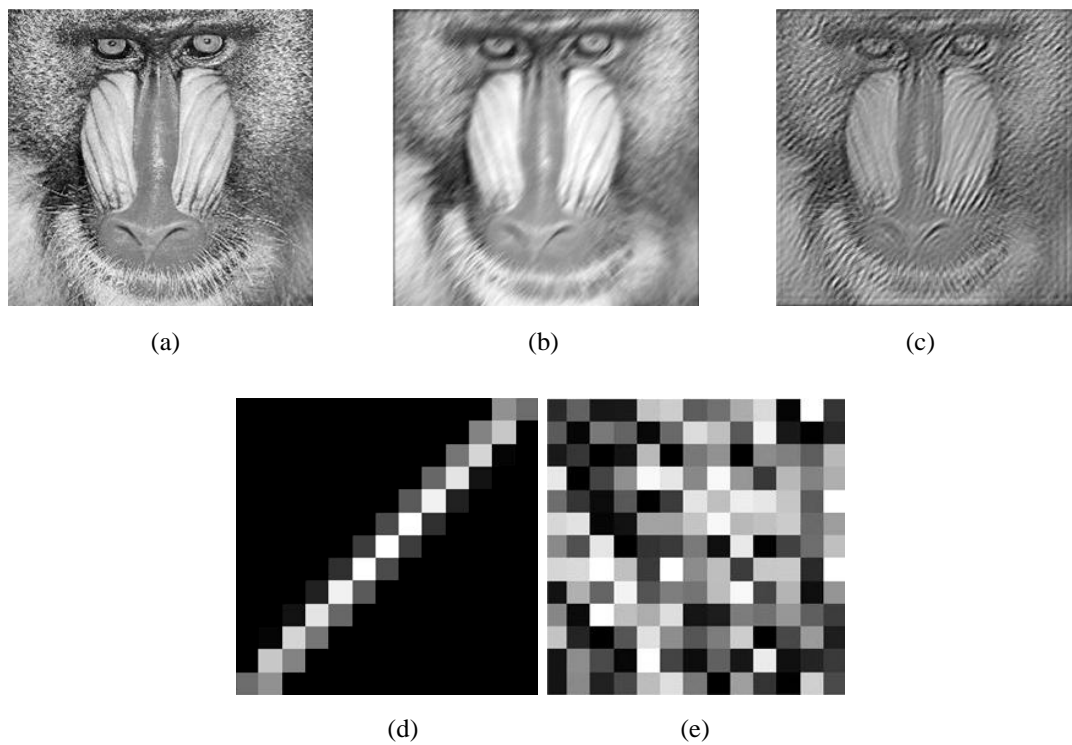
Fig. C.2 Deblurring result for image blurred by Gaussian PSF of size 5 x 5 pixels and variance 1. (a) Original image (b) Blurred image (c) Deblurred image (d) Blurring PSF and (e) Estimated PSF.
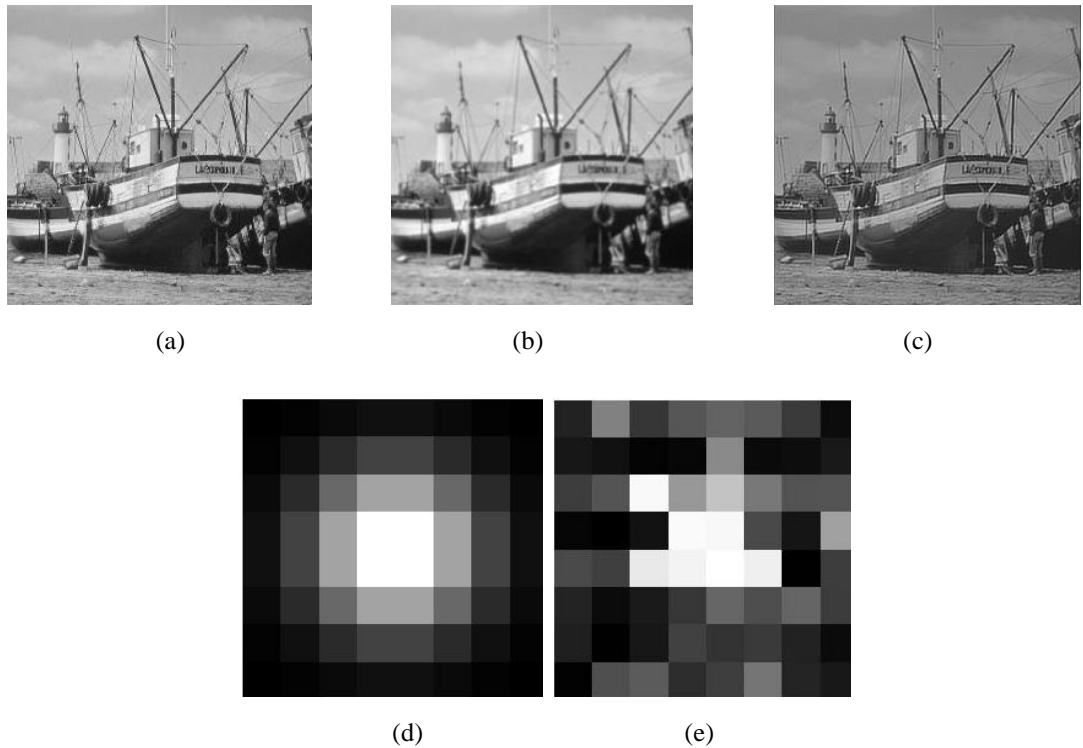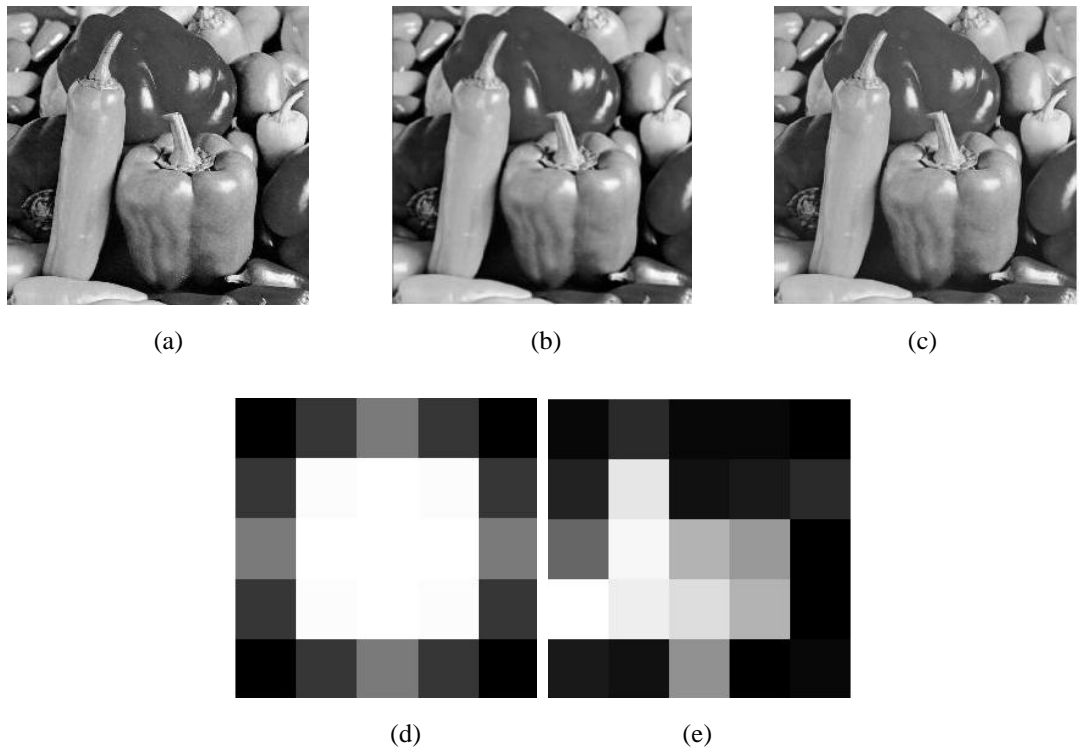

Fig. C.3 Deblurring result for image blurred by Gaussian PSF of size 8 x 8 pixels and variance 1.5. (a) Original image (b) Blurred image (c) Deblurred image (d) Blurring PSF and (e) Estimated PSF.

(a) (b) (c)

(d) (e)

Fig. C.4 Deblurring result for image blurred by motion blur PSF of length 5 pixels and angle 45°. (a) Original image (b) Blurred image (c) Deblurred image (d) Blurring PSF and (e) Estimated PSF.

In the case of the Mandrill image in Fig. 5.9, the estimated PSF, though far different in shape than the original PSF, still shows a reasonable recovery.

(a) (b) (c)

(d) (e)

Fig. C.5 Deblurring result for image blurred by motion blur PSF of length 17 pixels and angle 6°. (a) Original image (b) Blurred image (c) Deblurred image (d) Blurring PSF and (e) Estimated PSF.
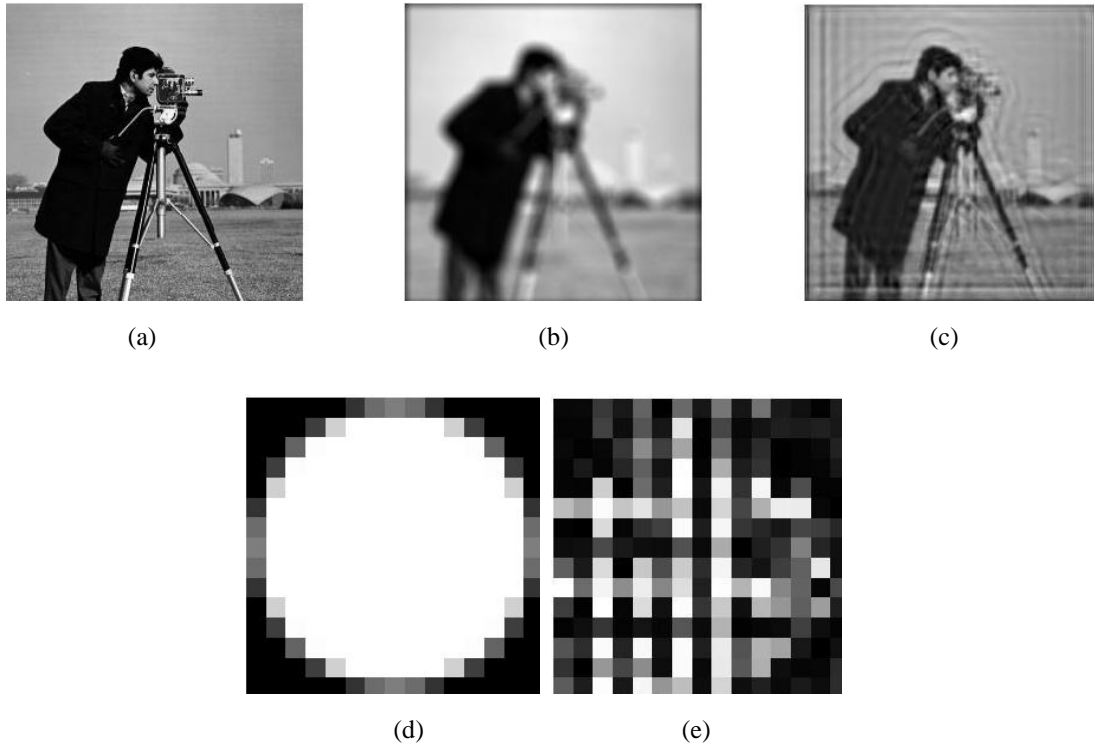
Fig. C.6 Deblurring result for image blurred by out-of-focus blur PSF of radius 2 pixels. (a) Original image (b) Blurred image (c) Deblurred image (d) Blurring PSF and (e) Estimated PSF.
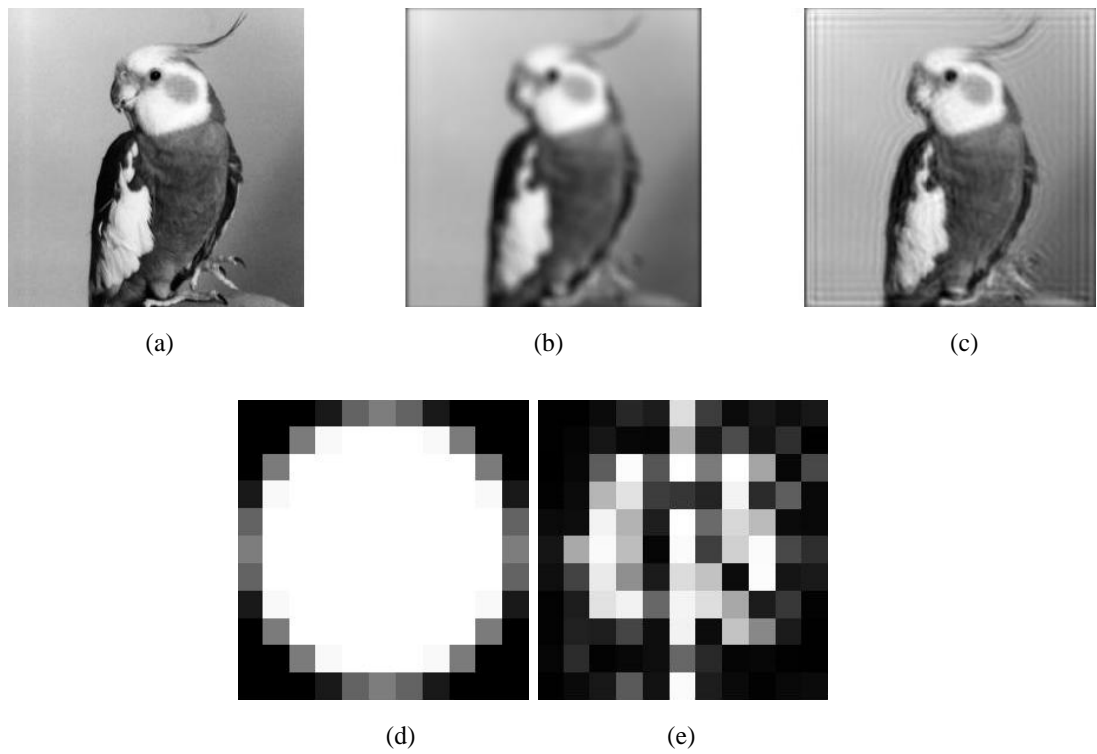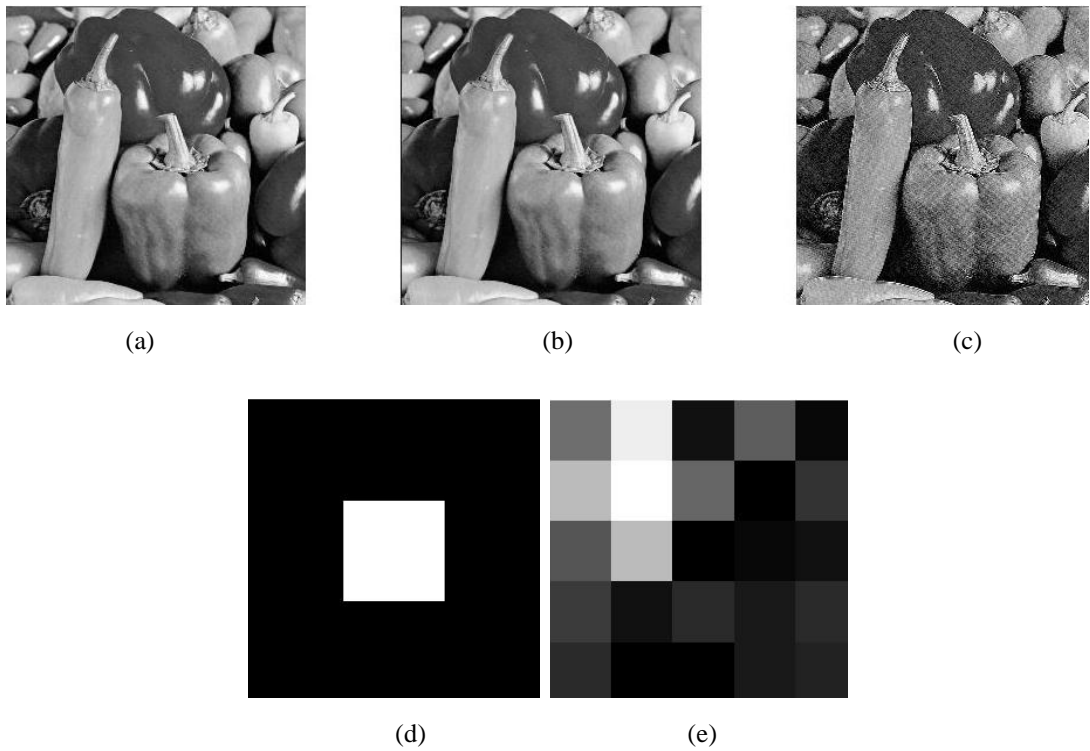

Fig. C.7 Deblurring result for image blurred by out-of-focus blur PSF of radius 5 pixels. (a) Original image (b) Blurred image (c) Deblurred image (d) Blurring PSF and (e) Estimated PSF.
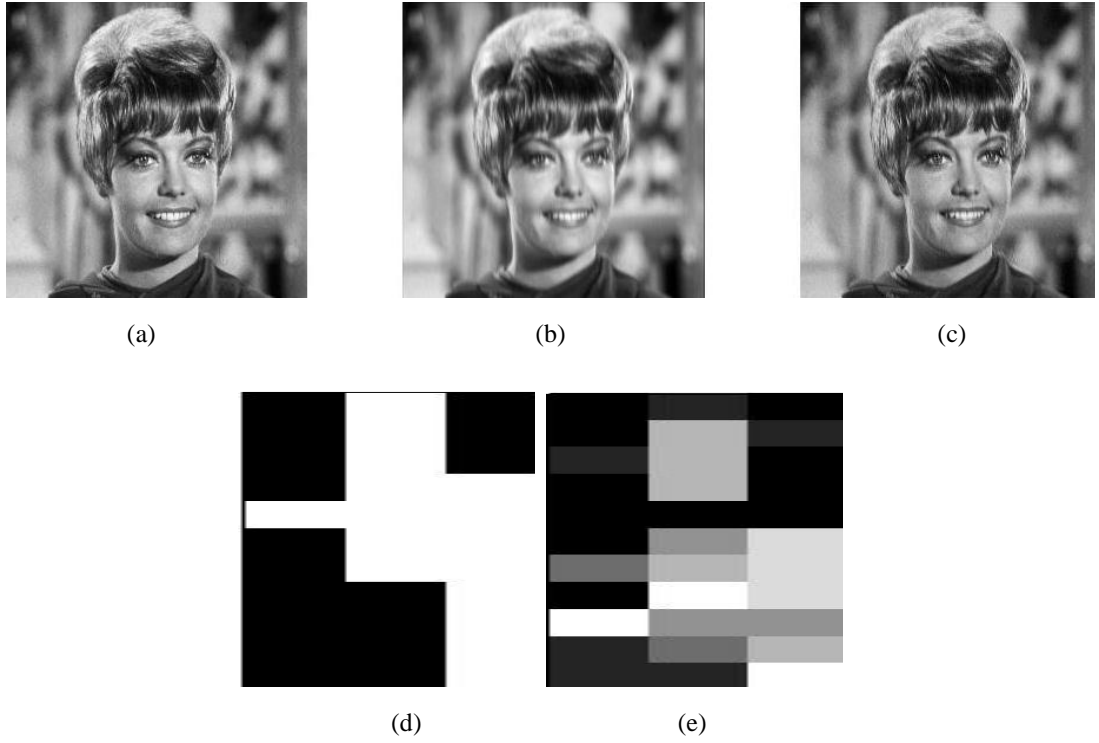
(a)　　　　　　　　(b)　　　　　　　　(c)

(d)　　　　　　　　(e)

Fig. C.8 Deblurring result for image blurred by out-of-focus blur PSF of radius 7 pixels. (a) Original image (b) Blurred image (c) Deblurred image (d) Blurring PSF and (e) Estimated PSF.


(a)　　　　　　　　(b)　　　　　　　　(c)

(d)　　　　　　　　(e)

Fig. C.9 Deblurring result for Peppers image blurred by arbitrary PSF of size 3 x 3 pixels with central element of weight 1. (a) Original image (b) Blurred image (c) Deblurred image (d) Blurring PSF and (e) Estimated PSF.
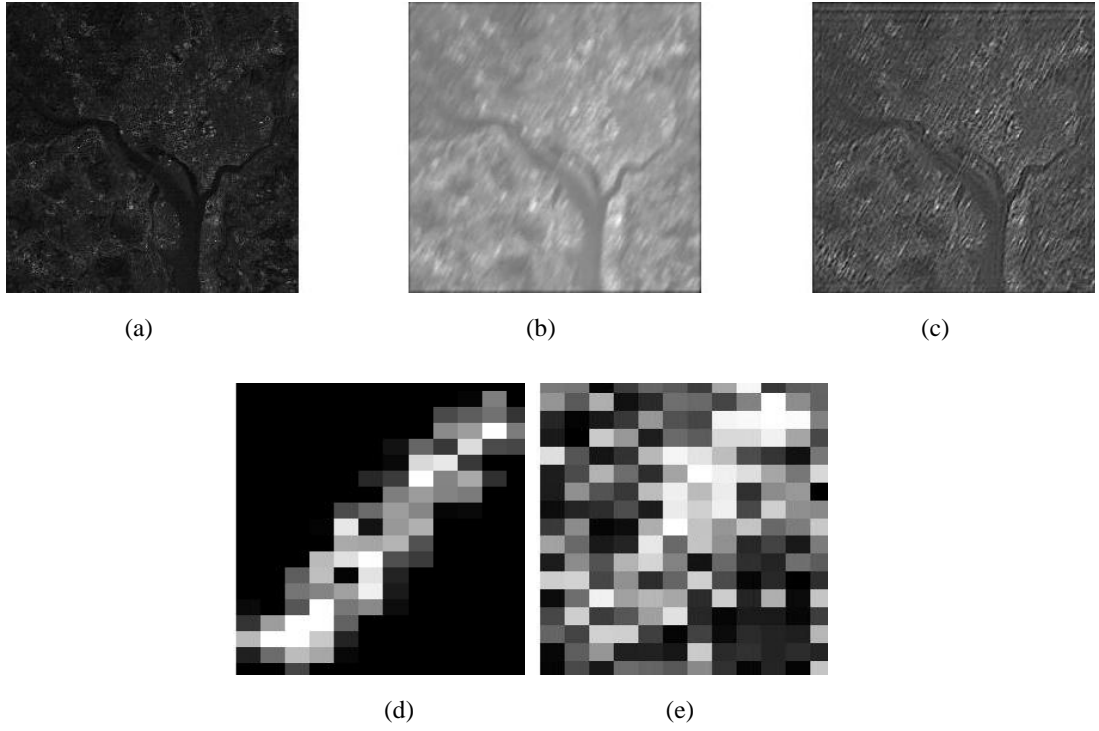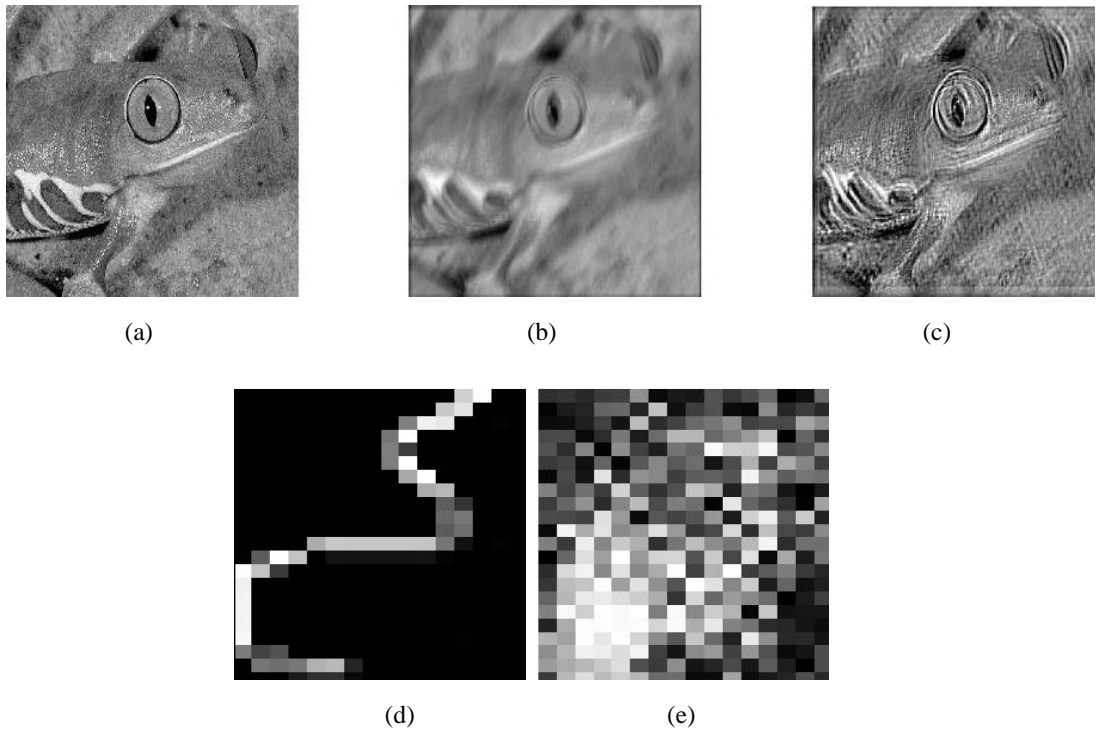
186

Fig. C.10 Deblurring result for Zelda image blurred by arbitrary PSF of size 13 x 3 pixels. (a) Original image (b) Blurred image (c) Deblurred image (d) Blurring PSF and (e) Estimated PSF.
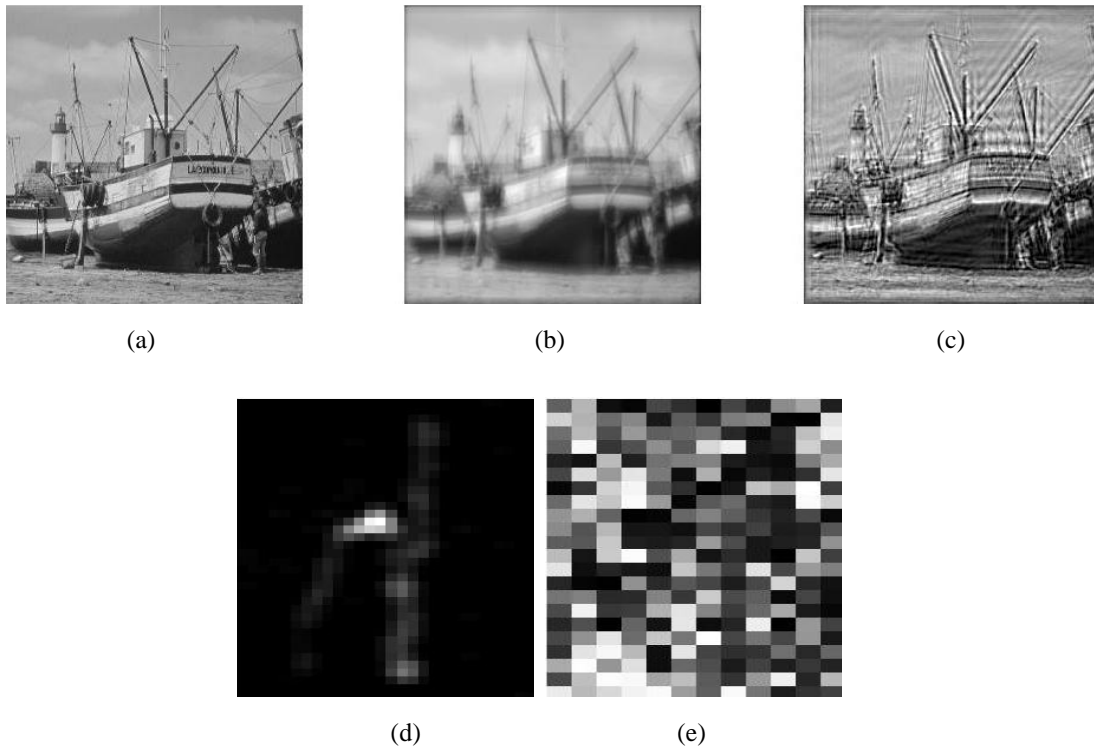
Fig. C.11 Deblurring result for Boat image blurred by arbitrary PSF of size 31 x 19 pixels. (a) Original image (b) Blurred image (c) Deblurred image (d) Blurring PSF and (e) Estimated PSF.

(a)   (b)   (c)

(d)   (e)

Fig. C.12 Deblurring result for Washsat image blurred by arbitrary PSF of size 19 x 13 pixels. (a) Original image (b) Blurred image (c) Deblurred image (d) Blurring PSF and (e) Estimated PSF.

(a)   (b)   (c)

(d)   (e)

Fig. C.13 Deblurring result for Frog image blurred by arbitrary PSF of size 19 x 13 pixels. (a) Original image (b) Blurred image (c) Deblurred image (d) Blurring PSF and (e) Estimated PSF.

Appendix D

MATLAB Optimization Toolbox

This appendix relates the usage details and some of the features of MATLAB's optimization toolbox command named *optimtool*. The toolbox was used in this research work to optimize deblurring measures using GA on multiple cores. Fig. D.1 shows the layout of the toolbox. The user input consists of entering the optimization function name, setting lower and upper bounds of the chromosome values as well as adjusting other different settings prior to simulation. It allows for the algorithm to be run on multiple cores without the trouble of coding threads or parallelizing code. By simply executing the *matlabpool* command, the user can set the number of cores/threads for the code to be executed on. The optimization can be stopped based on many factors including *number of generations reached* or *average change in fitness function less than tolerance value*. Table D.1 shows the iterative output of the fitness value for different iterations.

Below are some of the features of the optimization toolbox and their usage description.

- **Problem**

Fitness function is the objective function you want to minimize. You can specify the function as a function handle of the form @objfun, where objfun.m is a function file that returns a scalar. Number of variables (required) is the number of independent variables for the fitness function.

- **Constraints**

Linear inequalities of the form $A*x \leq b$ are specified by the matrix A and the vector b. Linear equalities of the form $Aeq*x = beq$ are specified by the matrix Aeq and the vector beq. Bounds are lower and upper bounds on the variables. Lower specifies lower bounds as a vector. Upper specifies upper bounds as a vector.
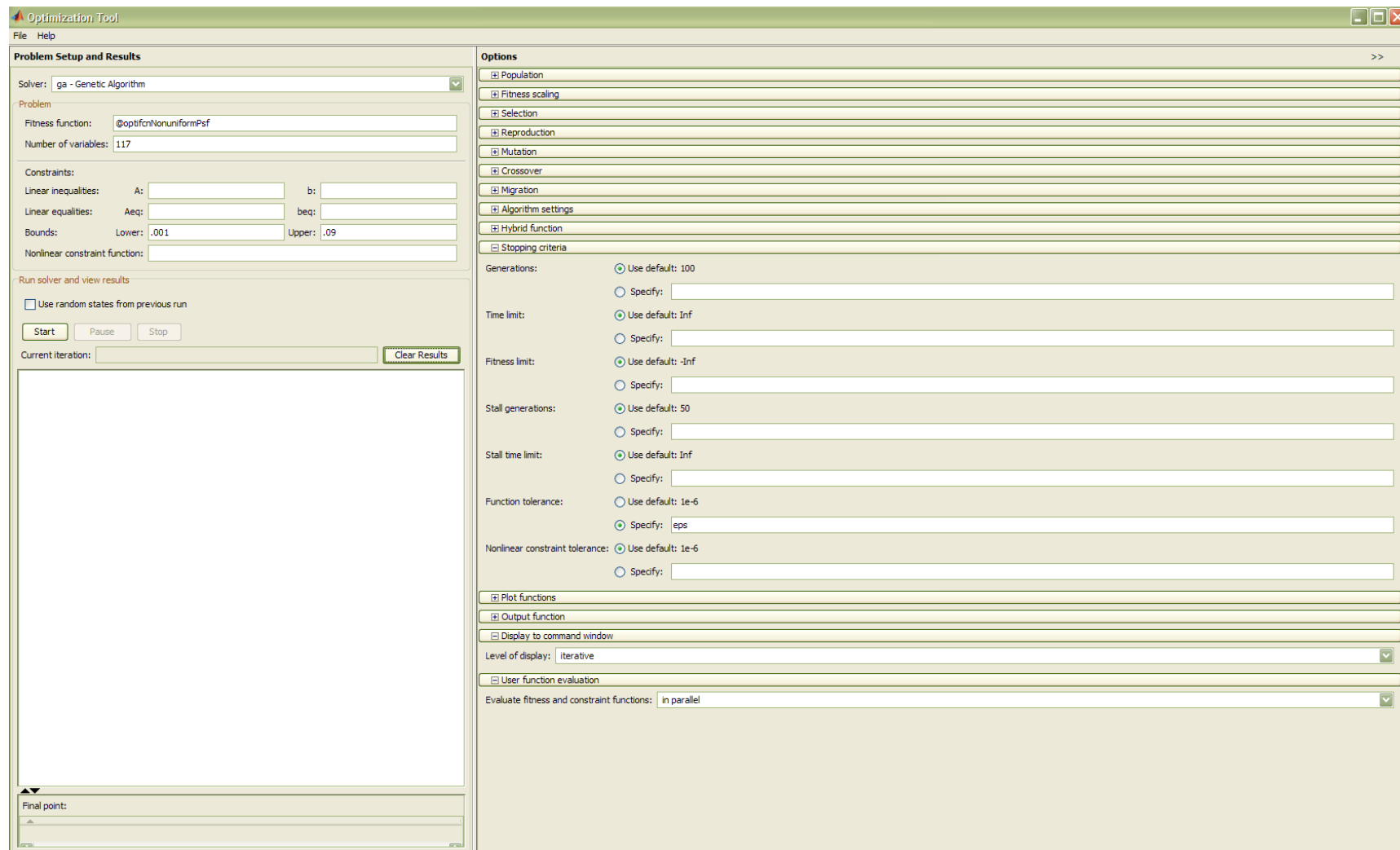
Fig. D.1. Overview of the MATLAB optimization toolbox.

- **Population**

Population options specify options for the population of the genetic algorithm.

Population type specifies the type of the input to the fitness function.

Population enables you to specify an initial population for the genetic algorithm. If you do not specify an initial population, the algorithm creates one using the Creation function. You can specify fewer than Population size individuals; if you do, the Creation function creates the rest.

Table D.1: Fitness function values depicted by the optimization toolbox for different iterations. The optimization stopped when the average change in the fitness value was less than the tolerance function value.

Generation	f-count	Best f(x)	Mean f(x)	Stall Generations
1	40	4.007	4.051	0
2	60	3.997	4.041	0
3	80	3.997	4.032	1
4	100	3.984	4.022	0
5	120	3.984	4.012	1
6	140	3.984	4.005	2
7	160	3.984	4.003	3
8	180	3.975	3.997	0
9	200	3.972	3.993	0
10	220	3.970	3.987	0
20	420	3.961	3.963	1
30	620	3.954	3.959	0
100	2020	3.877	3.881	2
150	3020	3.862	3.864	0
200	4020	3.855	3.856	0
250	5020	3.854	3.854	13
280	5620	3.854	3.854	23
281	5640	3.854	3.854	24

Optimization terminated: average change in the fitness value less than options.TolFun.

- **Selection**

The selection function chooses parents for the next generation based on their scaled values from the fitness scaling function. The selection function can be stochastic uniform, remainder, uniform, shift linear, roulette, tournament or a custom function. In this research work, roulette based selection was used to select chromosomes. Roulette function simulates a roulette wheel with the area of each segment proportional to its expectation. The algorithm then uses a random number to select

one of the sections with a probability equal to its area.

- **Reproduction**

Reproduction options determine how the genetic algorithm creates children at each new generation.

- **Mutation**

Mutation functions make small random changes in the individuals in the population, which provide genetic diversity and enable the genetic algorithm to search a broader space.

- **Crossover**

Crossover combines two individuals, or parents, to form a new individual, or child, for the next generation.

- **Stopping criteria**

Stopping criteria determines what causes the algorithm to terminate.
  - *Generations* specifies the maximum number of iterations the genetic algorithm performs.
  - *Time limit* specifies the maximum time in seconds the genetic algorithm runs before stopping.
  - *Fitness limit* — If the best fitness value is less than or equal to the value of Fitness limit, the algorithm stops.
  - *Stall generations* — If the weighted average change in the fitness function value over Stall generations is less than Function tolerance, the algorithm stops.
  - *Stall time limit* — If there is no improvement in the best fitness value for an interval of time in seconds specified by Stall time limit, the algorithm stops.
  - *Function tolerance* — If the cumulative change in the fitness function value over Stall generations is less than Function tolerance, the algorithm stops.
  - *Nonlinear constraint tolerance* specifies the termination tolerance for the maximum nonlinear constraint violation.

- **User function evaluation**

The user can evaluate the fitness function for the population in serial or parallel mode.